



UNIVERSITÀ DEGLI STUDI DI PISA
FACOLTÀ DI SCIENZE MATEMATICHE, FISICHE E NATURALI
DOTTORATO DI RICERCA IN SCIENZE CHIMICHE
XXIII CICLO
SSD CHIM/05

**Synthesis and Physico-Chemical characterization of
anion-exchange polymeric materials for
electrochemical applications**

Ph.D. Thesis

SUBMITTED BY

Antonio Filpi

SUPERVISOR

Prof. Francesco Ciardelli

EXTERNAL EXAMINER

Prof. Hubert Gasteiger

JANUARY 2011

Acknowledgements

First of all, I would like to thank my thesis supervisor, Prof. Francesco Ciardelli, for his warm encouragement and thoughtful guidance throughout my doctoral studies.

I would like to sincerely thank Acta S.p.A. for their financial support and all the instrumentation provided for electrochemical characterization. I am especially grateful to all the people that worked with me in ACTA, who have assisted and encouraged me in various ways during my research.

My thanks to Tokuyama Corp. for providing their commercial anion-exchange materials.

My thanks to Dr. Andrea Pucci for his support and precious advices. I want to express my gratitude to all the people working in the research group of the University of Pisa for their precious collaboration on the membrane synthesis.

My thanks to Dr. Hubert Gasteiger for giving me the opportunity to start my Ph.D. and reviewing my dissertation. His ideas and tremendous support during the early stages of this research had a major influence on this thesis.

The writing of a dissertation is obviously not possible without the personal and practical support of numerous people. Thus my sincere gratitude goes to all my friends for their support and patience over the last few years.

Last but not least, I wish to thank my family who have always supported me in all the choices I've made throughout my life.

Summary

In the last few years a number of new anion-exchange polymers have been developed, offering the possibility of assembling Membrane Electrode Assemblies (MEAs) to develop Anion-exchange Membrane Fuel Cells (AMFCs) and Anion-exchange Membrane-based Electrolyzers (AMEs).

The current technologies of Anion Exchange Materials (AMs) for electrochemical application shows several limitations relate to the possibility of obtaining a reasonable low cost membrane having: high ionic conductivity, chemical stability in strong alkaline media, low permeability, low water swelling and good mechanical properties.

The purpose of this study was to develop and characterize AMs based on Styrene–butadiene–styrene (SBS) copolymer, a thermoplastic material with a block structure widely employed in the rubber industry. In the present work is reported a controlled radical functionalization, initiated by benzoyl peroxide (BPO), of SBS with 4-vinylbenzyl chloride (VBC). The resulting thermoplastic polymer was converted into an anion exchange membrane via quaternization reaction with aliphatic amines, such as trimethylamine or 1,4-diazabicyclo[2.2.2]octane (DABCO). Electrochemical properties of these materials were measured and correlated with synthetic parameters. Correlations between transport properties and synthetic parameters were explained in terms of Cluster-Network morphological model. Performance of the synthesized SBS-based AMs were then evaluated in a working AMFC and compared with commercial materials. Diagnostics on AMFCs, by means of electrochemical impedance spectroscopy (EIS), were performed in order to evaluate measured performances.

Contents

SUMMARY	1
1 INTRODUCTION	1
1.1 ELECTROCHEMISTRY.....	3
1.1.1 <i>Thermodynamics</i>	4
1.1.2 <i>Transport of species in solution</i>	10
1.1.3 <i>Kinetics</i>	13
1.2 ELECTROCHEMICAL IMPEDANCE SPECTROSCOPY (EIS).....	21
1.2.1 <i>Response of Electrical Circuits</i>	21
1.2.2 <i>Impedance of Electrical Circuits</i>	25
1.2.3 <i>Equivalent circuits elements</i>	28
1.2.4 <i>Common equivalent circuit models</i>	31
1.3 ELECTROCHEMICAL APPLICATIONS	34
1.3.1 <i>Fuel cells</i>	34
1.3.2 <i>H₂/O₂ membrane fuel cells</i>	37
1.3.3 <i>Electrolyzers</i>	41
1.4 ION-EXCHANGE MATERIALS.....	43
1.4.1 <i>Structure and required properties</i>	45
1.4.2 <i>Design rules</i>	50
2 EXPERIMENTAL	53
2.1 INSTRUMENTATION	53
2.2 SOLVENTS AND CHEMICALS.....	54
2.2.1 <i>Styrene-butadiene-styrene copolymer (SBS)</i>	55
2.2.2 <i>Vinylbenzyl chloride (VBC)</i>	57
2.2.3 <i>1-Methylimidazole</i>	57
2.2.4 <i>α,α'-azo-bis-isobutyronitrile (AIBN)</i>	57
2.2.5 <i>Benzoyl peroxide (BPO)</i>	57
2.3 VBC GRAFTED SBS COPOLYMER (SBS-G-VBC)	58
2.3.1 <i>Grafting reaction</i>	58
2.3.2 <i>SBS-g-VBC extraction and purification</i>	58
2.3.3 <i>SBS-g-VBC film casting</i>	63
2.4 SBS-G-VBC QUATERNIZATION	63
2.5 ION-EXCHANGE MATERIALS CHARACTERIZATION	64
2.5.1 <i>Ion-exchange capacity (IEC)</i>	64
2.5.2 <i>Water uptake (WU)</i>	65
2.5.3 <i>Ionic conductivity</i>	65
2.6 MEMBRANE ELECTRODE ASSEMBLIES (MEAs).....	66
2.6.1 <i>Catalyst coated membranes (CCMs)</i>	66
2.6.2 <i>Gas diffusion electrodes (GDEs)</i>	66
3 RESULTS	68
3.1 ION-EXCHANGE COMMERCIAL MATERIAL CHARACTERIZATION	69
3.2 SBS BASED ANION-EXCHANGE MATERIALS	76
3.2.1 <i>SBS-g-VBC synthesis and characterization</i>	77
3.2.2 <i>SBS-g-VBC quaternization</i>	91
3.2.3 <i>Electrochemical characterization</i>	96

3.2.4	<i>Morphology and transport properties</i>	104
3.2.5	<i>Summary and future works</i>	111
3.3	ANION-EXCHANGE MEMBRANE FUEL CELL (AMFC) APPLICATIONS	113
3.3.1	<i>AMFC performances using commercial AMs</i>	113
3.3.2	<i>Electrochemical Impedance Spectroscopy in-situ diagnostics</i>	118
3.3.3	<i>AMFC performances using SBS-based AMs</i>	122
4	FINAL REMARKS	126
4.1	GRAFTING REACTION.....	126
4.2	QUATERNIZATION REACTION	127
4.3	ELECTROCHEMICAL CHARACTERIZATION	129
4.3.1	<i>Functionalization degree (FD)</i>	129
4.3.2	<i>Crosslinking ratio</i>	130
4.4	MORPHOLOGY	131
4.5	AMFC PERFORMANCES AND DIAGNOSTICS	132
4.5.1	<i>Commercial materials</i>	132
4.5.2	<i>SBS-based AMs</i>	132
4.6	FUTURE WORKS	133
5	BIBLIOGRAPHY	135

1 Introduction

Proton Exchange Membrane Fuel Cells (PEMFCs) and Proton Exchange Membrane Electrolyzers (PEM-E) have been developed over the last 20 years, however high loading of precious metal catalysts on the oxygen reduction (PEMFC)/oxygen evolution (PEM-E) side is still required due to the slow kinetics of the oxygen reduction reaction (ORR) (1) and oxygen evolution reaction (OER) (2).

Alkaline environment enable usage of first row transition metal based catalysts which are intrinsically stable and have an activity similar to platinum. A major issue related to traditional aqueous electrolyte alkaline fuel cells was the presence of mobile cations (e.g. K^+ , Na^+) which could precipitate as carbonate that block or destroy the catalyst layers (3). Using ionomer bound MEAs (Membrane Electrode Assemblies), analogous to PEMFCs, the carbonate precipitation issue would be overcome. In fact, the cationic sites (typically quaternary ammonium sites) are grafted and immobilised on the skeleton of the polymer chain. In strong alkaline environment quaternary ammonium sites degradation occurs *via* two different mechanisms: Hoffmann elimination and/or methyl and ammine direct nucleophilic displacement by hydroxide ions. Recent studies have demonstrated that the stability of ammonium sites towards alkali, can be increased by polymer crosslinking using a diamine (4).

In the last few years a number of new anion-exchange polymers (5; 6; 7; 8; 9; 10; 11; 12; 13; 14) have been developed, offering the possibility of assembling MEAs to develop Anion-exchange Membrane Fuel Cells (AMFCs) and Anion-exchange Membrane-based Electrolyzers (AMEs).

The current technologies of Anion Exchange Materials (AMs) for electrochemical application shows several limitations relate to the possibility of obtaining a reasonable low cost membrane having: high ionic conductivity, chemical stability in strong alkaline media, low permeability, low water swelling and good mechanical properties.

It has been recently discovered that the hydrogen oxidation reaction (HOR)/hydrogen evolution reaction (HER) kinetics on platinum catalyst are several orders of magnitude slower in alkaline compared to acid electrolyte (15). Therefore, the use of platinum anode catalysts in AMFCs/AMEs would require high loadings and thus become a significant cost factor unlike in PEMFCs/PEM-Es, where low Pt anode loadings are sufficient.

However transition metals oxide based catalysts, particularly spinel-type structures and transition metals alloys have been considered most promising for OER and HER (16; 17; 18; 19). Moreover other non-noble metal-based catalysts are available for AMFCs with an ORR activity comparable to Pt/C (20).

Therefore, the development of highly efficient catalysts toward HOR in alkaline electrolyte and cheap AMs having high conductivity and low water swelling are the critical challenges to make AMFCs/AMEs more practical.

The purpose of this study was to develop and characterize an AM based on Styrene-butadiene-styrene copolymer (SBS), a thermoplastic material with a block structure widely

employed in the rubber industry. It is well known how to introduce functional groups by radical grafting in SBS copolymer (21; 22; 23). In the present work is reported a controlled radical functionalization, initiated by benzoyl peroxide (BPO), of SBS with 4-vinylbenzyl chloride (VBC). The resulting thermoplastic polymer was converted into an anion exchange membrane via quaternization reaction with aliphatic amines, such as trimethylamine or 1,4-diazabicyclo[2.2.2]octane (DABCO), in the form of a thin sheet (50-100 μm).

The final properties of these SBS-based AMs will be reported in terms of ion-exchange capacity (IEC), ionic conductivity (σ), water uptake (WU). Commercial materials will be also evaluated and used as benchmarks.

The relationship between ion-exchange material structure and transport properties, such as ionic conductivity, is a critical driving force for much of the structural research on ion-exchange materials and provides the foundation for fundamental modeling work on these materials. Cluster-Network morphology model is widely used to describe the fundamental relationship between ionomer structure and electrochemical properties (24). Correlations between transport properties and synthetic parameters will be thus explained in terms of Cluster-Network morphological parameters.

Performance of the obtained SBS-based materials will be then evaluated in a working AMFC and compared with commercial AMs. Diagnostics on AMFCs, by means of electrochemical impedance spectroscopy (EIS), will be then performed in order to determine performance loss sources.

1.1 Electrochemistry

Electrochemistry is a branch of chemistry that studies chemical reactions which take place in a solution at the interface of an electron conductor (a metal or a semiconductor) and an ionic conductor (the electrolyte), and which involve electron transfer between the electrode and the electrolyte or species in solution.

If a chemical reaction is driven by an external applied voltage, as in electrolysis, or if a voltage is created by a chemical reaction as in a battery, it is an electrochemical reaction. In contrast, chemical reactions where electrons are transferred between molecules are called oxidation/reduction (redox) reactions. In general, electrochemistry deals with situations where oxidation and reduction reactions are separated in space, connected by an external electric circuit.

An electrochemical cell consists of two electrodes, or metallic conductors, in contact with an electrolyte, an ionic conductor (which may be a solution, a liquid, or a solid). An electrode and its electrolyte comprise an electrode compartment. The two electrodes may share the same compartment. The various kinds of electrode are summarized in Table 1. Any 'inert metal' shown as part of the specification is present to act as a source or sink of electrons, but takes no other part in the reaction other than acting as a catalyst for it. If the electrolytes are different, the two compartments may be joined by a salt bridge, which is a tube containing a concentrated electrolyte solution (almost always potassium chloride in agar jelly) that completes the electrical circuit and enables the cell to function. A galvanic cell is an electrochemical cell that produces electricity as a result of the spontaneous reaction occurring inside it. An electrolytic cell is an electrochemical cell in which a non-spontaneous reaction is driven by an external source of current.

Electrode type	Designation	Redox couple	Half-reaction
Metal/metal ion	$M(s) M^+(aq)$	M^+/M	$M^+(aq) + e^- \rightarrow M(s)$
Gas	$Pt(s) X_2(g) X^+(aq)$	X^+/X_2	$X^+(aq) + e^- \rightarrow X_2(g)$
	$Pt(s) X_2(g) X^-(aq)$	X_2/X^-	$X_2(g) + 2e^- \rightarrow 2X^-(aq)$
Metal/insoluble salt	$M(s) MX(s) X^-(aq)$	$MX/M, X^-$	$MX(s) + e^- \rightarrow M(s) + X^-(aq)$
Redox	$Pt(s) M^+(aq), M^{2+}(aq)$	M^{2+}/M^+	$M^{2+}(aq) + e^- \rightarrow M^+(aq)$

Table 1. Varieties of electrode

The reduction and oxidation processes responsible for the overall reaction in a cell are separated in space: oxidation takes place at one electrode and reduction takes place at the other. As the reaction proceeds, the electrons released in the oxidation $Red_1 \rightarrow Ox_1 + v e^-$ at one electrode travel through the external circuit and re-enter the cell through the other electrode. There they bring about reduction $Ox_2 + v e^- \rightarrow Red_2$. The electrode at which oxidation occurs is called the anode; the electrode at which reduction occurs is called the cathode. In a galvanic cell, the cathode has a higher potential than the anode: the species undergoing reduction, Ox_2 , withdraws electrons from its electrode (the cathode), so leaving a relative positive charge on it (corresponding to a high potential). At the anode, oxidation

results in the transfer of electrons to the electrode, so giving it a relative negative charge (corresponding to a low potential).

1.1.1 Thermodynamics

The fundamental equation for a multicomponent system establishes:

$$dU = TdS - PdV + \sum_i \mu_i dn_i \quad (1.1)$$

where U is the internal energy, V the volume, S the entropy, T the temperature in Kelvin, μ_i is the chemical potential of the species i and n_i is the number of moles of the species i . The chemical potential μ_i is defined as the change in molar internal energy with the number of moles n_i of the species i at constant volume and entropy (i.e. isochoric and adiabatic process):

$$\mu_i = \left(\frac{\partial U}{\partial n_i} \right)_{S, V, n_{j \neq i}} \quad (1.2)$$

Gibbs free energy G is defined as:

$$G = U + PV - TS \quad (1.3)$$

Differentiating equation (1.3) and combining it with equation (1.1) we obtain another form of the fundamental equation:

$$dG = VdP - SdT + \sum_i \mu_i dn_i \quad (1.4)$$

Thus, the chemical potential μ_i can be regarded as the reversible work for transferring one mole of i from vacuum to a given phase at constant pressure and temperature:

$$\mu_i = \left(\frac{\partial G}{\partial n_i} \right)_{T, P, n_{j \neq i}} \quad (1.5)$$

Euler's theorem states that if we have a function F which is homogeneous of degree 1, i.e. $F(\{\alpha y_i\}) = \alpha F(\{y_i\})$, then we can express it as the sum of its arguments weighted by the first partial derivatives:

$$F(\{y_i\}) = \sum_j y_j \left(\frac{\partial F}{\partial y_j} \right)_{y_{i \neq j}} \quad (1.6)$$

Since internal energy U is homogeneous in all its arguments (entropy, volume and number of moles) we obtain:

$$U = TS - PV + \sum_i \mu_i n_i \quad (1.7)$$

Combining equations (1.7) and (1.3) we obtain for the free energy:

$$G = \sum_i \mu_i n_i \quad (1.8)$$

which differentiated and combined with equation (1.4) gives the Gibbs-Duhem equation:

$$\sum_j n_j d\mu_j = -SdT + VdP \quad (1.9)$$

This equation shows that in thermodynamics intensive properties are not independent but related, making it a mathematical statement of the state postulate. When pressure and

temperature are variable, only 1-1, of 1, components have independent values for chemical potential and Gibbs' phase rule follows.

Partial derivative of equation (1.9) with respect to n_i gives

$$d\mu_i = \bar{V}_i dP \quad (1.10)$$

where \bar{V}_i is the partial molar volume for component i . Applying Raoult's law for ideal solutions and integrating equation (1.10) we obtain:

$$\mu_i = \mu_i^0 + RT \ln(x_i) \quad (1.11)$$

where μ_i^0 is the chemical potential of component i at standard conditions and x_i is its molar fraction. Many pairs of liquids present no uniformity of attractive forces, i.e. the adhesive and cohesive forces of attraction are not uniform between the two liquids, so that they show deviation from the Raoult's law which is applied only to ideal solutions. For real solutions we have to take in account this deviations introducing in the "active" concentration or activity a_i :

$$a_i = \gamma_i c_i \quad (1.12)$$

where γ_i is the activity coefficient. Substituting the molar fraction with the activity in equation (1.12) we obtain for real solutions:

$$\mu_i = \mu_i^0 + RT \ln(\gamma_i c_i) \quad (1.13)$$

Ion activities and Debye-Hückel theory

For a generic salt $M_n X_m$:

$$G = n \mu_+ + m \mu_- = G^{ideal} + RT \ln[(\gamma_+)^n (\gamma_-)^m] \quad (1.14)$$

It is convenient to introduce the mean activity coefficient γ_{\pm} :

$$\gamma_{\pm} = [(\gamma_+)^n (\gamma_-)^m]^{\frac{1}{n+m}} \quad (1.15)$$

Peter Debye and Erich Hückel proposed a model (25) in 1923 for calculating the activity coefficient arguing that the energy of an ion is lowered by electrostatic interactions with its ionic atmosphere. Their main assumptions were:

- Interactions are primarily coulombic;
- Electrolyte is fully dissociated at all concentrations;
- Permittivity of the electrolyte is equal to the one of the pure solvent;
- Ions are rigid charged spheres (non-polarisable);
- Electrostatic interaction is smaller than $k_B T$ (where k_B is the Boltzmann constant);

The final result yields the so-called extended Debye- Hückel equation:

$$\text{Log } \gamma_{\pm} = z_+ z_- \frac{A\sqrt{I}}{1 + a_{\pm} B\sqrt{I}} \quad (1.16)$$

where z is the integer charge of the ions, a_{\pm} is the effective hydrated radius of the ions, I is the ionic strength of the solution, A and B are constants with values of respectively 0.5085 and 0.3281 at 25°C in water (26). For diluted solutions ($I \leq 10^{-4} \text{M}$) equation (1.16) can be reduced to the Debye-Hückel limiting law:

$$\text{Log } \gamma_{\pm} = z_+ z_- A\sqrt{I} \quad (1.17)$$

Electrostatic potential of condensed phases

The electrostatic inner potential ϕ , also known as Galvani potential, determines the reversible work for transferring a positive charge unit from vacuum to the interior of the condensed phase:

$$\phi = \psi + \chi \quad (1.18)$$

where ψ is the outer or Volta potential, determined by the distance separating the unit charge from the plane of closest approach to the phase and χ is the surface potential, related to the differential work for bringing the charge to the interior of the phase.

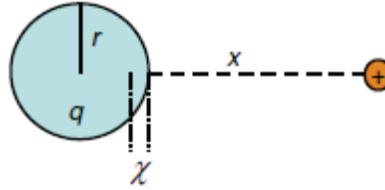


Figure 1. Diagram for a charged condensed phase having a spherical geometry

Assuming a spherical geometry (Figure 1) we obtain the following equation for the inner potential:

$$\phi = \frac{q}{4\pi\epsilon\epsilon_0(x+r)} + \chi \quad (1.19)$$

Electrochemical potential of charged species

The electrochemical potential $\tilde{\mu}_i$ is defined as the sum of chemical and electrostatic potential for a mole of the i -th compound having charge z_i :

$$\tilde{\mu}_i = \mu_i + z_i F \phi \quad (1.20)$$

where F is the Faraday constant, equal to the magnitude of electric charge per mole of electrons. On Figure 2 are sketched contributions to the electrochemical potentials.

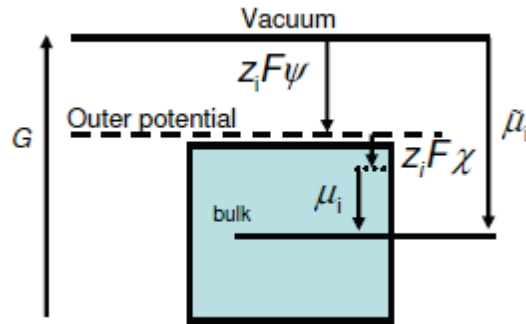


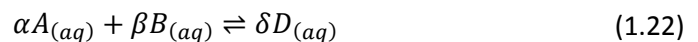
Figure 2. Contributions to the electrochemical potential

Combining equations (1.20) and (1.13) we obtain:

$$\tilde{\mu}_i = \mu_i^0 + RT \ln(\gamma_i c_i) + z_i F \phi \quad (1.21)$$

Equilibrium and the Galvani potential difference

For a general chemical process:



Gibbs free energy variation comes from equation (1.4):

$$dG = \mu_D dn_D + \mu_A dn_A + \mu_B dn_B + VdP - SdT \quad (1.23)$$

Since the process is isobaric and isothermal VdP and SdT terms are null. Moreover from balance of matter, introducing stoichiometric coefficients ν_i , moles variations dn_i should be equal to:

$$dn_i = \nu_i d\xi \quad (1.24)$$

where ξ is the extent of reaction or reaction coordinate. Combining equations (1.23) (1.24) and (1.13) we obtain:

$$dG = \left\{ \delta\mu_D^0 - \alpha\mu_A^0 - \beta\mu_B^0 + RT \left[\ln \left(\frac{c_D^\delta}{c_A^\alpha c_B^\beta} \frac{\gamma_D^\delta}{\gamma_A^\alpha \gamma_B^\beta} \right) \right] \right\} d\xi \quad (1.25)$$

Defining the reaction Gibbs free energy $\Delta_r G_{T,P}$ as:

$$\Delta_r G_{T,P} = \left(\frac{\partial G}{\partial \xi} \right)_{T,P} \quad (1.26)$$

the reaction quotient Q_r as:

$$Q_r = \frac{\prod_p a_p^{\nu_p}}{\prod_r a_r^{\nu_r}} \quad (1.27)$$

where indexes p and r refers respectively to products and reagents, and Gibbs free energy at standard conditions $\Delta_r G_{T,P}^0$ as:

$$\Delta_r G_{T,P}^0 = \sum_i \nu_i \mu_i^0 \quad (1.28)$$

equation (1.25) can be rearranged as:

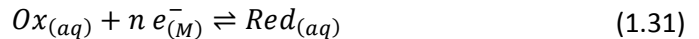
$$\Delta_r G_{T,P} = \Delta_r G_{T,P}^0 + RT \ln Q_r \quad (1.29)$$

known as Van't Hoff isotherm.

At the equilibrium $dG = 0$ or equivalently $\Delta_r G_{T,P} = 0 \Leftrightarrow \ln Q_r = -\frac{\Delta_r G_{T,P}^0}{RT}$, hence the reaction quotient has to be constant, known as equilibrium constant K :

$$K = e^{-\frac{\Delta_r G_{T,P}^0}{RT}} \quad (1.30)$$

Similarly for an electrochemical process:



Gibbs free energy variation is:

$$d\tilde{G} = \tilde{\mu}_{red} dn_{red} + \tilde{\mu}_{ox} dn_{ox} + \tilde{\mu}_e dn_e + VdP - SdT \quad (1.32)$$

which rearranged and combined with equation (1.21) gives the electrochemical reaction free energy $\Delta_r \tilde{G}_{T,P}$:

$$\Delta_r \tilde{G}_{T,P} = \Delta_r \tilde{G}_{T,P}^0 + RT \ln \frac{a_{red}}{a_{ox}} + nF \Delta_{aq}^M \phi \quad (1.33)$$

where

$$\Delta_{aq}^M \phi = \phi^M - \phi^{aq}$$

and

$$\Delta_r \tilde{G}_{T,P}^0 = \mu_{ox}^0(aq) - \mu_{red}^0(aq) + n \mu_e(M)$$

At the equilibrium $\Delta_r \tilde{G}_{T,P} = 0$:

$$\Delta_{aq}^M \phi = \Delta_{aq}^M \phi^0 - \frac{RT}{nF} \ln \frac{a_{red}}{a_{ox}} \quad (1.34)$$

where:

$$\Delta_{aq}^M \phi^0 = \frac{\Delta_r \tilde{G}_{T,P}^0}{nF} \quad (1.35)$$

equation (1.34) describes a unique relationship between the Galvani potential difference and the activity ratio of the redox species. On Figure 3 Galvani potential difference is reported for different electrode types.

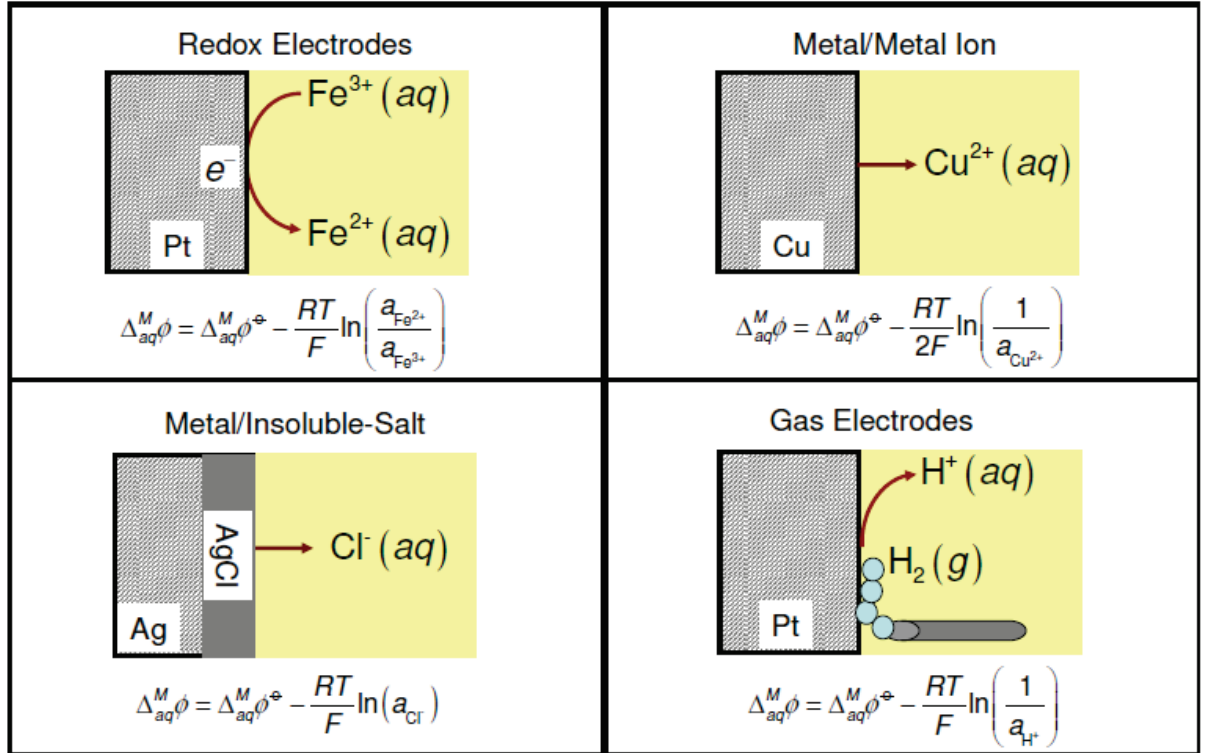


Figure 3. Galvani potential difference relationships for different electrode types

The cell potential and the electromotive force

By definition, the cell potential corresponds:

$$E_{cell} = \Delta_{aq}^M \phi(\text{cathode}) - \Delta_{aq}^M \phi(\text{anode}) \quad (1.36)$$

which combined with equation (1.34) and rearranged gives the Nernst equation:

$$E_{cell} = E_{cell}^0 - \frac{RT}{nF} \ln Q \quad (1.37)$$

where

$$E_{cell}^0 = \Delta_{aq}^M \phi^0(\text{cathode}) - \Delta_{aq}^M \phi^0(\text{anode}) \quad (1.38)$$

A cell in which the overall cell reaction is not at the equilibrium can generate electrical work. The cell potential is directly related to the magnitude of this work. In this respect, the E_{cell} is also known as the electromotive force. It follows:

$$\Delta_r \tilde{G}_{T,P} = -nF E_{cell} \quad (1.39)$$

Cells at equilibrium

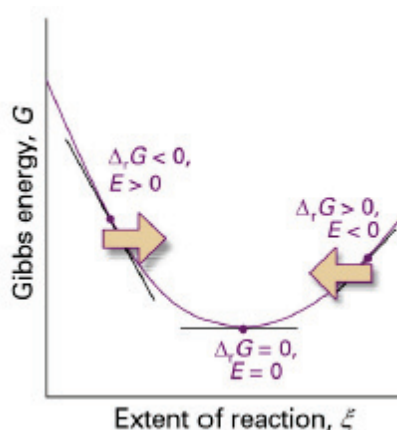


Figure 4. Gibbs free energy as a function of the extent of the reaction

The minimum in the curve reported in Figure 4 corresponds to the equilibrium state. As the Gibbs free energy of the cell reaction is zero, the cell cannot perform any external work. Consequently at equilibrium $Q = K$, equilibrium constant of the cell reaction:

$$\ln K = \frac{nFE_{cell}^0}{RT} \quad (1.40)$$

Moreover from equation (1.39):

$$E_{cell}^0 = -\frac{\Delta_r \tilde{G}_{T,P}^0}{nF} \quad (1.41)$$

Standard potentials

The cell potential is determined by the potentials at the cathode and anode. E_{cell} can be measured accurately, however, the potential at each individual electrode cannot be measured. A convention is needed:

$$\begin{aligned} H_{(aq)}^+ + e_{(M)}^- &\rightarrow \frac{1}{2} H_{2(g)} \\ \Delta_{aq}^M \phi &= \Delta_{aq}^M \phi^0 - \frac{RT}{F} \ln \frac{1}{a_{H^+}} \\ \Delta_{aq}^M \phi^0 &= 0 \end{aligned} \quad (1.42)$$

This means the half cell $Pt_{(s)} | H_{2(g)} | H^+(a_{H^+=1}, aq)$ has a Galvani potential equal to zero at all temperature. On the basis of this assumption, the standard potential for half cell reactions can be estimated by means of Bordwell thermodynamic cycles.

Temperature effects

By using the basic relation between the cell potential and the Gibbs free energy change in equation (1.39), it follows that:

$$\left(\frac{\partial E_{cell}}{\partial T} \right)_P = -\frac{1}{nF} \left(\frac{\partial \Delta_r \tilde{G}}{\partial T} \right)_P = \frac{\Delta_r \tilde{S}}{nF} \quad (1.43)$$

If we assume that $\Delta_r \tilde{S}$ is independent of temperature (i.e., $\Delta_r C_p$ is small), we can integrate equation (1.43), to give:

$$E_{cell}(T) = E_{cell}(T_0) + \frac{\Delta_r \tilde{S}}{nF} (T - T_0) \quad (1.44)$$

Note that for many redox reactions $\Delta_r \tilde{S}$ is small (less than 50 J/K). This leads to only

10^{-5} - 10^{-4} V/K change in E_{cell} ; hence, the cell potential is relatively insensitive to temperature. Finally, by noting that at constant temperature, $\Delta H = \Delta G + T\Delta S$, and using equation (1.43), we see that

$$\left(\frac{\partial \frac{E_{cell}}{RT}}{\partial T}\right) = \frac{\Delta_r \tilde{H}}{nFRT^2} \quad (1.45)$$

which is basically the Gibbs-Helmholtz equation for electrochemical equilibrium.

1.1.2 Transport of species in solution

Mass transport in electrolyte solution can be induced by three processes:

- Convection – mechanical or thermal agitation;
- Migration – gradient of an electrical field (ions);
- Diffusion – gradient of chemical potential.

Neglecting convection forces and recalling the concept of electrochemical potential of anion i ($\tilde{\mu}_i$):

$$\tilde{\mu}_i = \mu_i^0 + \underbrace{RT \ln(a_i)}_{\text{Diffusion}} + \underbrace{z_i F \phi}_{\text{Migration}} \quad (1.46)$$

Conductivity of electrolyte solutions

Ions in solution can be set in motion by applying a potential difference between two electrodes. The conductance Λ of a solution is defined as the inverse of the electric resistance R :

$$\Lambda = \frac{1}{R} \quad (1.47)$$

The SI unit of conductance is the siemens (S): $1S = 1/\Omega$. For parallel plate electrodes with area A , at the distance l it follows:

$$\Lambda = \chi \frac{A}{l} \quad (1.48)$$

where χ is the conductivity, expressed in S/m. The electrical conductivity of a solution of an electrolyte is measured by determining the resistance of the solution between two flat or cylindrical electrodes separated by a fixed distance (27). An alternating voltage is used in order to avoid electrolysis. The resistance is measured by a conductivity meter. Typical frequencies used are in the range 1-3 kHz. The dependence on the frequency is usually small (28), but may become appreciable at very high frequencies, an effect known as the Debye-Falkenhagen effect. The conductivity of a solution depends on the number of ions present. Consequently, the molar conductivity Λ_m is used:

$$\Lambda_m = \frac{\chi}{c} \quad (1.49)$$

where c is the electrolyte molar concentration. In real solutions, Λ_m depends on the concentration of the electrolyte. This could be due to:

- Ion-ion interactions: $\gamma_{\pm} \neq 1$;
- Incomplete dissociation of the electrolyte.

Strong electrolytes are fully dissociated in solution. Friederich Kohlrausch examined the conductivity of a large quantity of strong electrolytes. These results led to the Kohlrausch law:

$$\Lambda_m = \Lambda_m^0 - K\sqrt{c} \quad (1.50)$$

where Λ_m^0 is known as the limiting molar conductivity, K is an empirical constant and c is the electrolyte concentration. Moreover, Kohlrausch also found that in the limit of zero concentration, as ion-ion interactions are negligible, it can be postulated that the limiting conductivity of anions and cations are additive, i.e. the conductivity of a solution of a salt is equal to the sum of conductivity contributions from the cation and anion:

$$\Lambda_m^0 = \nu_+\lambda_+^0 + \nu_-\lambda_-^0 \quad (1.51)$$

where λ_+^0 and λ_-^0 are the limiting molar conductivity of the cation and anion, respectively, ν_+ and ν_- are the numbers of cations and anions per formula unit of electrolyte. Equation (1.51) is known as “Law of independent migration of ions”. Debye and Hückel modified their theory in 1926 and their theory was further modified by Lars Onsager in 1927. All the postulates of the original theory were retained. In addition it was assumed that the electric field causes the charge cloud to be distorted away from spherical symmetry. After taking this into account, together with the specific requirements of moving ions, such as viscosity and electrophoretic effects, Onsager was able to derive a theoretical expression to account for the empirical Kohlrausch's Law.

A weak electrolyte is one that is not fully dissociated. Typical weak electrolytes are weak acids and weak bases. The concentration of ions in a solution of a weak electrolyte is less than the concentration of the electrolyte itself. For acids and bases the concentrations can be calculated when taking in account for the degree of dissociation α :

$$\Lambda_m = \alpha\Lambda_m^0 \quad (1.52)$$

For a monoprotic acid, HA, with a dissociation constant K_a , an explicit expression for the conductivity as a function of concentration, c , known as Ostwald's dilution law, can be obtained from equation (1.52):

$$\frac{1}{\Lambda_m} = \frac{1}{\Lambda_m^0} + \frac{\Lambda_m c}{K_a (\Lambda_m^0)^2} \quad (1.53)$$

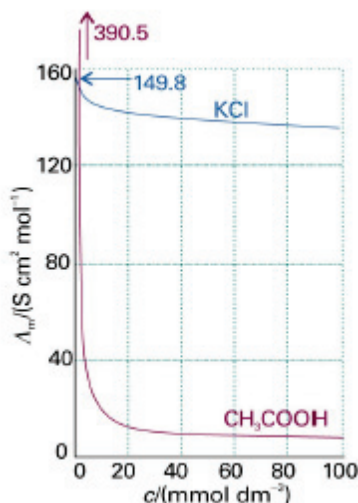


Figure 5. Concentration dependence of the molar conductivities of a typical strong electrolyte (aqueous potassium chloride) and a typical weak electrolyte (aqueous acetic acid).

On Figure 5 is reported the concentration dependence of molar conductivity of a typical strong and weak electrolytes.

The mobility of ions

Ion movement in solution is random. However, a migrating flow can be onset upon applying an electric field \vec{E} :

$$|\vec{E}| = \frac{\Delta\phi}{l} \quad (1.54)$$

where $\Delta\phi$ is the potential difference between two electrodes separated by a distance l . An ion of charge ze^- experiences a force \vec{F} :

$$|\vec{F}| = ze |\vec{E}| = \frac{ze \Delta\phi}{l} \quad (1.55)$$

\vec{F} accelerates cations to the negatively charged electrode and anions in the opposite direction. Through this motion, ions experience a frictional force in the opposite direction. Taking the expression derived by Stoke relating friction F_{fric} and the viscosity of the solvent η :

$$F_{fric} = 6\pi \eta a v \quad (1.56)$$

where a is the hydrodynamic radius of the ion and v is the drift speed, when the accelerating and retarding forces balance each other, v is defined by:

$$v = \frac{ze}{6\pi \eta a} |\vec{E}| = u |\vec{E}| \quad (1.57)$$

where u is the mobility of the ion, defined as the velocity attained by an ion moving under unit electric field:

$$u = \frac{v}{|\vec{E}|} = \frac{ze}{6\pi \eta a} \quad (1.58)$$

Finally it can be shown that:

$$\lambda = zuF \quad (1.59)$$

and equation (1.51) can be rewritten as:

$$\Lambda_m^0 = (z_+ u_+ v_+ + z_- u_- v_-)F \quad (1.60)$$

Diffusion

Conventional electrochemical processes take place at the electrode surface, creating non homogeneous composition of the electrolyte solution. A key phenomenological relationship developed by Adolf Fick in 1855 relates the diffusive flux to the concentration field, by postulating that the flux goes from regions of high concentration to regions of low concentration, with a magnitude that is proportional to the concentration. For ideal mixtures:

$$J_i = -D_i \nabla c_i \quad (1.61)$$

where J_i is the diffusion flux expressed as $\left(\frac{\text{mol}}{\text{m}^2 \text{s}}\right)$ and D_i is the diffusion coefficient, or diffusivity, expressed as $\left(\frac{\text{m}^2}{\text{s}}\right)$. In chemical systems other than ideal solutions or mixtures, the driving force for diffusion of each species is the gradient of chemical potential of this species:

$$J_i = -\frac{D_i c_i}{RT} \nabla \mu_i \quad (1.62)$$

The following mass balance can be used in order to predict how diffusion causes the concentration field to change with time:

$$\frac{\partial c_i}{\partial t} = -\nabla J_i = \nabla(D_i \nabla c_i) \quad (1.63)$$

Assuming the diffusion coefficient D to be a constant we obtain from equation (1.63):

$$\frac{\partial c_i}{\partial t} = D_i \nabla^2 c_i \quad (1.64)$$

which is analogous to the heat equation. The equilibration of the diffusion and friction forces allows establishing:

$$D_i = \frac{u_i RT}{z_i F} \quad (1.65)$$

known as Einstein equation. According to equation (1.65), typical diffusion coefficients are of the order of $10^{-9} \text{ m}^2 \cdot \text{s}^{-1}$. The fact that mobility is related to the frictional force and the diffusion coefficient allows establishing a further important expression:

$$D_i = \frac{k_b T}{6\pi\eta a_i} \quad (1.66)$$

known as Stoke-Einstein equation. Note that the ionic charge does not figure in equation (1.66). This means that the diffusion coefficient is independent of the ionic charge. Equation (1.66) is also valid for neutral molecules.

Nernst-Planck equation

Summing all contributions to mass transport in electrolyte solutions obtained before, we obtain for the flux J_i :

$$J_i = \underbrace{-D_i \nabla c_i}_{\text{Diffusion}} - \underbrace{u_i \nabla \phi}_{\text{Migration}} + \underbrace{c_i \tau}_{\text{Convection}} \quad (1.67)$$

where τ is the rate with which a volume element moves in solution. Combining equations (1.65) and (1.67) we obtain the so-called Nernst-Planck equation:

$$J_i = -D_i \nabla c_i - \frac{z_i F}{RT} D_i c_i \nabla \phi + c_i \tau \quad (1.68)$$

1.1.3 Kinetics

In order to grasp what is taking place in an electrochemical reaction, the concept of current and how the current changes when a stimulus is applied must be understood. Two types of current may flow in an electrochemical cell, faradic and non-faradic. All currents that are created by the reduction and/or oxidation of chemical species in the cell are termed faradaic currents. The current is equal to the change in charge with time, or:

$$i = \frac{\partial Q}{\partial t} \quad (1.69)$$

where i is the Faradic current, and Q is the charge given by Faraday's law. Faraday's law correlates the total charge passed through a cell to the amount of product N expressed in moles:

$$Q = nFN \quad (1.70)$$

where F is the Faraday's constant ($F = 96485 \text{ C mol}^{-1}$) and n is the number of electrons transferred per molecule of product. All other current is deemed non-faradic in nature, and is directly related to Ohm's law:

$$i_{nf} = \frac{\Delta V}{R_{\Omega}} \quad (1.71)$$

where i_{nf} is the non-faradic current, ΔV the potential difference, R is the ohmic resistance. While the resistance is applicable when considering Ohm's law in an electrical circuit, the application to an electrochemical cell requires the usage of impedance Z , which includes elements of resistance and capacitance.

Chemical reactions can be either homogeneous or heterogeneous. The first type occurs in a single phase, and its rate is uniform everywhere in the volume where it occurs:

$$\text{Rate} [\text{mol s}^{-1}] = \frac{\partial N}{\partial t} \quad (1.72)$$

Heterogeneous reactions occur at the electrode-solution interface, and they are characteristic of electrochemistry. While the expression for the reaction rate is similar to equation (1.72), it depends upon the area of the electrode, A , or the area of the phase boundary where the reaction occurs:

$$\text{Rate} [\text{mol s}^{-1} \text{ cm}^{-2}] = \frac{i}{nFA} = \frac{j}{nF} \quad (1.73)$$

where j is the faradic current density. There are four major factors that govern the reaction rate and current at electrodes:

1. Mass transfer to the electrode surface;
2. Kinetics of the electron transfer;
3. Preceding and ensuing reactions;
4. Surface reactions (adsorption).

The slowest process will be the rate determining step.

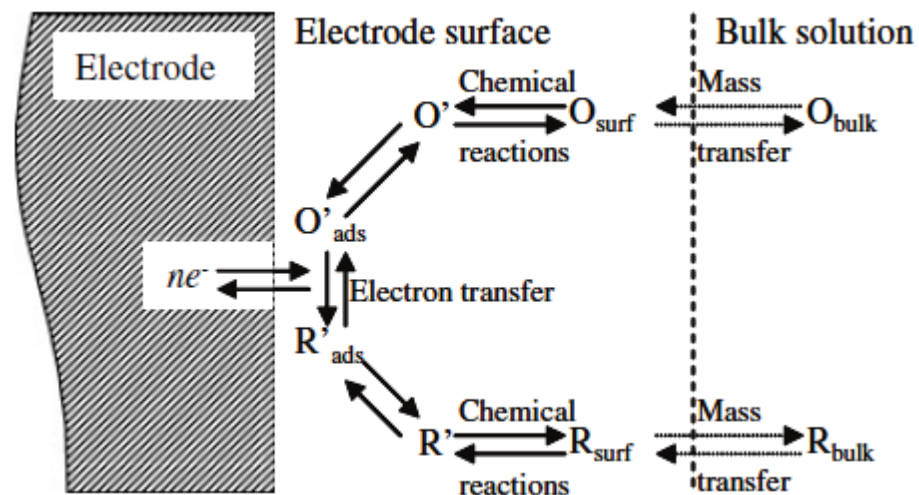


Figure 6. Processes involved in an electrode reaction

Let us consider the case of the simple reaction:



This reaction may be considered as a set of equilibria involved in the migration of the reactant to the electrode, the reaction at the electrode and the migration of the product away from the electrode surface into the bulk of the solution (Figure 6). For this reaction to proceed, O is required to move from the bulk solution near the electrode surface. This aspect of the mechanism is related to mass transfer and is governed by the Nernst–Planck equation (1.68). Mass transfer from the bulk solution towards the electrode surface could limit the rate of the reaction. When all of the processes leading to the reaction are fast, this leaves the electron transfer reaction as the limiting factor.

Near the electrode an electrochemical double-layer is formed (Figure 7): the first layer, or inner Helmholtz plane (IHP), comprises ions adsorbed directly onto the electrode due to a host of chemical interactions, the second layer, or outer Helmholtz plane (OHP) is composed of ions attracted to the surface charge via the coulomb force, electrically screening the first layer itself.

This double-layer works as an electrochemical capacitor having capacitance C_d . So the measured current is the sum of the faradic and non-faradic (capacitive) one. The non-faradaic time constant for the electrode τ [s] can be calculated by:

$$\tau = R_s C_d \quad (1.75)$$

where R_s is the solution resistance and C_d is the double layer capacitance. The double layer charging will be complete (95%) in a time frame equal to 3τ (29).

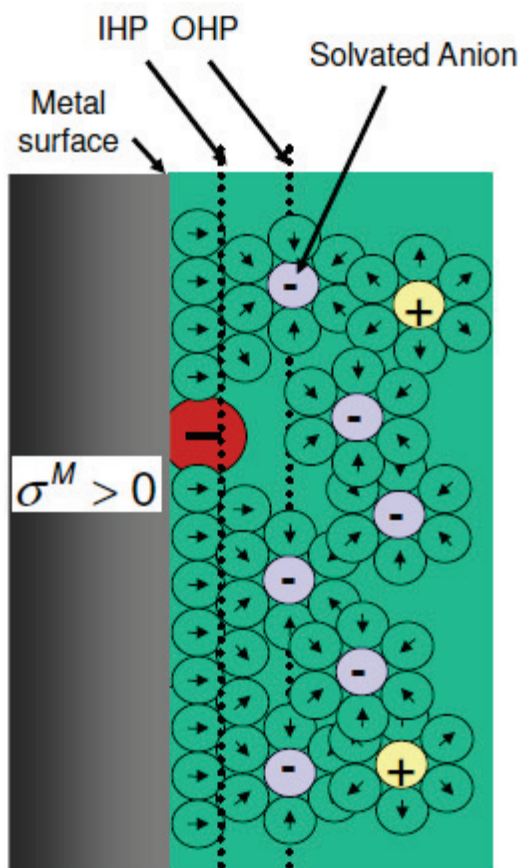
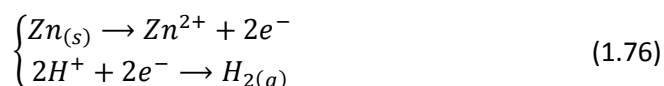


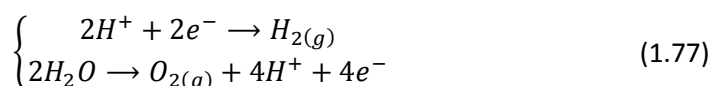
Figure 7. Simplified scheme of the electrochemical double-layer

Reversibility

Reversibility is a key concept when dealing with electrochemical reaction mechanisms. An electrochemical cell is considered chemically reversible if reversing the current through the cell reverses the cell reaction and no new reactions or side products appear. An electrochemical cell is considered chemically irreversible if reversing the current leads to different electrode reactions and new side products. This is often the case if a solid falls out of solution or a gas is produced, as the solid or gaseous product may not be available to participate in the reverse reaction. When a solid zinc electrode is oxidized in an acidic system with a platinum electrode the following two reactions take place:



When this system is reversed, by the application of a potential with a greater magnitude than the cell potential with the opposite bias, a different set of reactions occur, rendering this system chemically irreversible:



The concept of thermodynamic reversibility is theoretical. It applies to adiabatic changes, where the system is always at equilibrium. An infinitesimal change causes the system to move in one particular direction, resulting in an infinitesimal response; the analogy in electrochemistry is that a small change in potential could result in the reversal of the electrochemical process. In electrochemistry, the researcher is concerned with practical reversibility. In reality electrochemical processes occur at finite rates, and as long as the experimental parameters are set in a manner that allows for the reversal of the reaction to regenerate the original species, the processes are deemed practically reversible. For these systems the Nernst equation (1.37) holds true at all times.

Overpotential

Overpotential η is an electrochemical term which refers to the potential difference between a half-reaction's thermodynamically determined reduction potential and the potential at which the redox event is experimentally observed (29). The term is directly related to a cell's voltage efficiency. In an electrolytic cell the overpotential requires more energy than thermodynamically expected to drive a reaction. In a galvanic cell overpotential means less energy is recovered than thermodynamics would predict. In each case the extra or missing energy is lost as heat. Overpotential is specific to each cell design and will vary between cells and operational conditions even for the same reaction.

Overpotential can be partitioned into many different subcategories that are not always well defined. A likely reason for the lack of strict definitions is that it's difficult to determine how much of a measured overpotential is derived from a specific source. There is precedent for lumping overpotentials into three categories: activation, concentration, and resistance (30):

- Activation overpotential, or kinetic losses, is the potential difference above the equilibrium value required to produce a current which depends on the activation

energy of the redox event. Kinetic losses can be reduced or eliminated with the use of homogeneous or heterogeneous electrocatalysts. The electrochemical reaction rate and related current density is dictated by the kinetics of the electrocatalyst and substrate concentration.

- Concentration overpotential, or mass-transport losses, span a variety of phenomenon but all involve the depletion of charge-carriers at the electrode surface. The potential difference is caused by differences in concentration of the charge-carriers between bulk solution and on the electrode surface. It occurs when electrochemical reaction is sufficiently rapid to lower the surface concentration of the charge-carriers below that of bulk solution. The rate of reaction is then dependent on the ability of the charge-carriers to reach the electrode surface.
- Resistance overpotential, or ohmic losses, occur due to resistance to electron and ion conduction. This include "junction overpotentials" which describes overpotentials occurring at electrode surfaces and interfaces like ion-exchange membranes. This can include aspects of electrolyte diffusion, surface polarization (capacitance), and other sources of counter electromotive forces.

Kinetic losses

Assuming that the rate of diffusion of the redox species is significantly faster than the rate of electron transfer, the rate v of the electrochemical process (1.74) can be written as:

$$v = k_{ox}c_R^\ominus - k_{red}c_O^\ominus \quad (1.78)$$

where c_O^\ominus and c_R^\ominus are the concentrations at the electrode surface for respectively O and R species, k_{ox} and k_{red} are the kinetic constants for respectively oxidation and reduction reactions. It follows that the faradic current density j is given by:

$$j = nFv = nF(k_{ox}c_R^\ominus - k_{red}c_O^\ominus) \quad (1.79)$$

To a first approximation, kinetic constants can be rationalized as the average electron velocity across the interfacial region. According to the transition state theory, the electron transfer rate constants can be expressed in terms of the corresponding potential dependent activation energies $\Delta G^*(E)$:

$$\begin{cases} k_{ox} = Ae^{-\frac{\Delta G_{ox}^*(E)}{RT}} \\ k_{red} = Ae^{-\frac{\Delta G_{red}^*(E)}{RT}} \end{cases} \quad (1.80)$$

As shown in Figure 8 (left), the rate constants for oxidation and reduction at the equilibrium potential are equal ($k_{ox} = k_{red} = k^0$). Consequently, the net rate of the electrochemical reaction is zero. Changes on the potential of the electrode surface E with respect to the equilibrium potential E^0 will shift the equilibrium towards reactants or products. Kinetic overpotential η_{kin} is then:

$$\eta_{kin} = E - E^0 \quad (1.81)$$

Overpotential will affect the activation energies in a different fashion, as showed in Figure 8 (right), and a net current is generated.

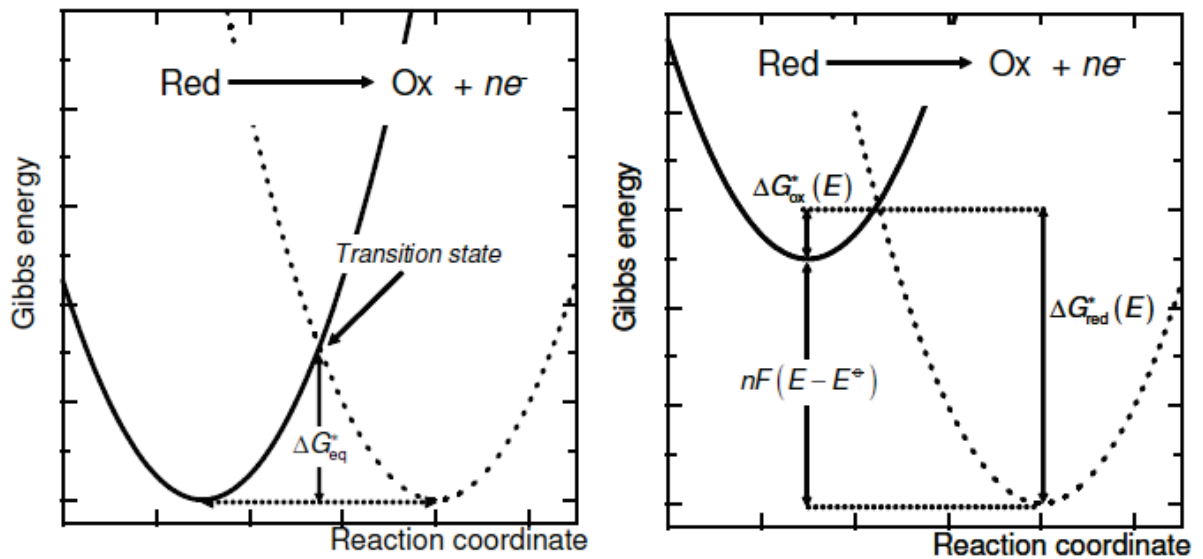


Figure 8. Potential dependent Gibbs free-energy as a function of a reaction coordinate: at the equilibrium (left), at electrode potentials E more positive than the equilibrium potential E^0 (right)

The activation energies are modified by a fraction α of the thermodynamic driving force $nF\eta_{kin}$ (31):

$$\begin{cases} \Delta G_{ox}^*(E) = \Delta G_{ox}^*(E^0) - \alpha nF\eta_{kin} \\ \Delta G_{red}^*(E) = \Delta G_{red}^*(E^0) + (1 - \alpha)nF\eta_{kin} \end{cases} \quad (1.82)$$

where α is the so-called transfer coefficient (value between 0 and 1). Combining and rearranging equations (1.79), (1.80) and (1.82) we obtain the Butler-Volmer equation (plotted in Figure 9):

$$j(E) = j_0 \left[\frac{e^{\frac{nF}{RT}\eta_{kin}}}{j_{anodic}} - \frac{e^{-(1-\alpha)\frac{nF}{RT}\eta_{kin}}}{j_{cathodic}} \right] \quad (1.83)$$

Where j_0 is known as exchange current density:

$$j_0 = nFk^0(C_R^\emptyset)^{1-\alpha}(C_O^\emptyset)^\alpha \quad (1.84)$$

As any rate constant of a chemical reaction, the exchange current density depends on temperature and reactants/products concentrations as:

$$j_0(T, C_O, C_R) = j_0(T^*, C_O^*, C_R^*) \left(\frac{C_R}{C_R^*} \right)^\gamma \left(\frac{C_O}{C_O^*} \right)^\delta e^{-\frac{E_{act}}{RT}} \quad (1.85)$$

where γ and δ are respectively the reaction order for oxidation and reduction reactions, E_{act} is the activation energy.

At a narrow potential range around the equilibrium potential (i.e. $|\eta_{kin}| \ll RT/\alpha nF$), the Butler-Volmer equation can be linearized by means of Taylor expansion:

$$\begin{cases} j \cong \frac{\eta_{kin}}{R_{ct}} \\ R_{ct} = \frac{RT}{nFj_0} \end{cases} \quad (1.86)$$

where R_{ct} is the so-called charge transfer resistance.

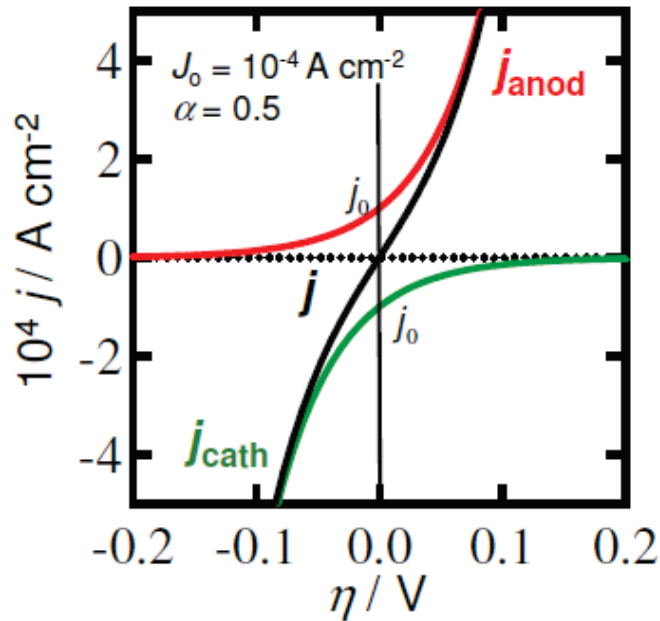


Figure 9. Current - overpotential curves for a kinetically controlled electrochemical reaction

Often the Butler-Volmer equation is written in Log_{10} form:

$$j(E) = j_0 \left[10^{\frac{\eta_{kin}}{b_{red}}} - 10^{-\frac{\eta_{kin}}{b_{ox}}} \right] \quad (1.87)$$

where b_{red} and b_{ox} are respectively the reduction and oxidation Tafel slope representing the overpotential increase required for a ten folds increase in current.

At large overpotentials, the total current is dominated by either the cathodic (reduction) or the anodic (oxidation) process. In this case, the current is expressed as:

$$\begin{cases} \text{Log}_{10}j = \text{Log}_{10}j_0 + \frac{\eta_{kin}}{b_a} & \eta_{kin} \geq b_a \\ \text{Log}_{10}j = \text{Log}_{10}j_0 - \frac{\eta_{kin}}{b_c} & \eta_{kin} \leq b_c \end{cases} \quad (1.88)$$

commonly referred to as Tafel equation. Inverting equation (1.88) we obtain the formula for the kinetic overvoltage:

$$\eta_{kin} = \pm b \text{Log}_{10} \frac{j}{j_0} \quad (1.89)$$

Mass-transport losses

Let consider the general electrochemical reaction (1.74) in which the kinetic of electron transfer is infinitely faster than the transport of species from the electrolyte to the electrode surface. For reversible systems, the Nernst equation is established “instantaneously” at the electrode surface:

$$\Delta_{aq}^M \phi = \Delta_{aq}^M \phi^0 - \frac{RT}{nF} \ln \left(\frac{c_R^*}{c_O^*} \right) \quad (1.90)$$

where c_O^* and c_R^* are the bulk concentration for respectively O and R species. Changes in the applied electrode potential E modifies the concentration ratio of the redox species at the electrode surface, creating concentration profiles, such that:

$$E = \Delta_{aq}^M \phi^0 - \frac{RT}{nF} \ln \left(\frac{c_R^\theta}{c_O^\theta} \right) \quad (1.91)$$

where c_O^\emptyset and c_R^\emptyset are the concentrations at the electrode surface for respectively O and R species. Mass-transport overpotential η_{tx} is then:

$$\eta_{tx} = V - \Delta_{aq}^M \phi = \frac{RT}{nF} \ln \left(\frac{c_O^\emptyset}{c_O^*} \right) \left(\frac{c_R^*}{c_R^\emptyset} \right) \quad (1.92)$$

The region where the concentration of the redox species depends on distance is the diffusion layer or Nernst layer. Local changes in the concentration give rise to an electrical current. The current is proportional to the rate of transformation of O to R, or vice versa. For a reversible process, the current is proportional to the flux J_O of the reactant to the electrode surface or to the flux J_R of the products away from the electrode. Recalling Fick's (equation (1.61), the faradic current for the diffusion limited step is simply:

$$i = nFAJ_O = -nFAD_O \left(\frac{\partial c_O}{\partial x} \right)_{x=0} = nFAD_R \left(\frac{\partial c_R}{\partial x} \right)_{x=0} \quad (1.93)$$

where A is the geometrical area of the electrode, D_O and D_R are the diffusion coefficients for respectively O and R species, c_O and c_R are the molar concentrations for respectively O and R species, x is the distance from the electrode surface. In order to calculate the diffusion limited current, the concentration gradient at the electrode surface ($x = 0$) should be established. Let consider the case in which the thickness of the diffusion layer (δ) is fixed:

$$i = nFAD_O \left[\frac{c_O^* - c_O^\emptyset}{\delta_O} \right] = -nFAD_R \left[\frac{c_R^* - c_R^\emptyset}{\delta_R} \right] \quad (1.94)$$

In the limit where the applied potential $V \ll \Delta_{aq}^M \phi$ we can assume an infinitely fast reduction reaction kinetics, i.e. $c_O^\emptyset = 0$, reduction current reaches the maximum value i_{red}^∞ :

$$i_{red}^\infty = \frac{nFAD_O c_O^*}{\delta_O} \quad (1.95)$$

Similarly when $V \gg \Delta_{aq}^M \phi$, oxidation current reaches the maximum value i_{ox}^∞ :

$$i_{ox}^\infty = -\frac{nFAD_R c_R^*}{\delta_R} \quad (1.96)$$

Combining equations (1.92), (1.95) and (1.96) we obtain:

$$\eta_{tx} = \frac{RT}{nF} \ln \left[\left(\frac{i_{red}^\infty - i}{i - i_{ox}^\infty} \right) \left(\frac{i_{ox}^\infty}{i_{red}^\infty} \right) \right] \quad (1.97)$$

In the case that only one of the redox species is diffusion limited, e.g. R is a gas free to leave the electrochemical cell, we obtain:

$$\eta_{tx} = \frac{RT}{nF} \ln \left(1 - \frac{i}{i_{red}^\infty} \right) \quad (1.98)$$

Ohmic losses

Resistance overpotential η_Ω is due to resistance to electron and ion conduction, according to the Ohm's law:

$$\eta_\Omega = i R_\Omega \quad (1.99)$$

where R_Ω is the sum of all resistances sources (electrode, electrolyte, ion-exchange membranes and junctions). Electrolyte resistance can be calculated from equation (1.50) or measured by means of Electrochemical impedance spectroscopy (EIS), which allow to measure whole R_Ω , as described in the next section.

1.2 Electrochemical impedance spectroscopy (EIS)

At an interface, physical properties change precipitously and heterogeneous charge distributions (polarizations) reduce the overall electrical conductivity of a system. The rate at which a polarized region will change when the applied voltage is reversed is characteristic of the type of interface: slow for chemical reactions, appreciably faster across the electrolyte. The emphasis in electrochemistry has consequently shifted from a time/concentration dependency to frequency-related phenomena, a trend toward small-signal alternating current (ac) studies. Electrical double layers and their inherent capacitive reactances are characterized by their relaxation times, or more realistically by the distribution of their relaxation times. The electrical response of a heterogeneous cell can vary substantially depending on the species of charge present, the microstructure of the electrolyte, and the texture and nature of the electrodes.

Electrochemical Impedance Spectroscopy (EIS) or ac impedance methods have seen tremendous increase in popularity in recent years. Initially applied to the determination of the double-layer capacitance (32; 33; 34; 35) and in ac polarography (36; 37), they are now applied to the characterization of electrode processes and complex interfaces. EIS studies the system response to the application of a periodic small amplitude AC signal. These measurements are carried out at different ac frequencies and, thus, the name impedance spectroscopy was later adopted. Analysis of the system response contains information about the interface, its structure and reactions taking place there. EIS is a very sensitive technique and it must be used with great care. Besides, it is not always well understood. This may be connected with the fact that existing reviews on EIS are very often difficult to understand by non-specialists and, frequently, they do not show the complete mathematical developments of equations connecting the impedance with the physico-chemical parameters. It should be stressed that EIS cannot give all the answers. It is a complementary technique and other methods must also be used to elucidate the interfacial processes.

1.2.1 Response of Electrical Circuits

Application of an electrical perturbation (current, potential) to an electrical circuit causes the appearance of a response. In this section, the system response to an arbitrary perturbation and, later, to an ac signal, will be presented.

Arbitrary Input Signal

Let us consider application of an arbitrary (but known) potential $E(t)$ to a resistance R . The current $i(t)$ is given as: $i(t) = E(t)/R$. When the same potential is applied to the series connection of the resistance R and capacitance C , the total potential difference is a sum of potential drops on each element. Taking into account that for a capacitance $E(t) = Q(t)/C$, where Q is the charge stored in a capacitor, the following equation is obtained:

$$E(t) = i(t)R + \frac{Q(t)}{C} = i(t)R + \frac{1}{C} \int_0^t i(t)dt \quad (1.100)$$

This equation may be solved using either Laplace transform or differentiation techniques (38; 39). Differentiation gives:

$$\frac{\partial i(t)}{\partial t} + \frac{i(t)}{RC} = \frac{1}{R} \frac{\partial E(t)}{\partial t} \quad (1.101)$$

which may be solved for known $E(t)$ using standard methods for differential equations.

The Laplace transform is an integral transform in which a function of time $f(t)$ is transformed into a new function of a parameter s called frequency, $\bar{f}(s)$ or $F(s)$, according to:

$$\mathcal{L}[f(t)] = \bar{f}(s) = F(s) = \int_{0^-}^{\infty} f(t)e^{-st} dt \quad (1.102)$$

The Laplace transform is often used in solution of differential and integral equations. In general, the parameter s may be complex, $s = \nu + j\omega$, where $j = \sqrt{-1}$. Direct application of the Laplace transform to equation (1.100), taking into account that $\mathcal{L}\left[\int_0^t i(t)dt\right] = \bar{i}(s)/s$, gives:

$$\bar{E}(s) = \bar{i}(s)R + \frac{\bar{i}(s)}{sC} \quad (1.103)$$

which leads to:

$$\bar{i}(s) = \frac{\bar{E}(s)}{\left(R + \frac{1}{sC}\right)} \quad (1.104)$$

The ratio of the Laplace transforms of potential and current, $\bar{E}(s)/\bar{i}(s)$ is expressed in the units of resistance, Ω , and is called impedance, $\bar{Z}(s)$. In this case:

$$\bar{Z}(s) = \frac{\bar{E}(s)}{\bar{i}(s)} = R + \frac{1}{sC} \quad (1.105)$$

It should be noticed that the impedance of a series connection of a resistance and capacitance, equation (1.105), is a sum of the contributions of these two elements: resistance, R , and capacitance, $1/sC$. For the series connection of a resistance, R , and inductance, L , the total potential difference consists of the potential drop on both elements:

$$E(t) = i(t)R + L \frac{\partial i(t)}{\partial t} \quad (1.106)$$

Taking into account that $\mathcal{L}[\partial i(t)/\partial t] = s\bar{i}(s) - i(0^+)$, and taking $i_{t=0} = 0$, one obtains the current response in the Laplace space:

$$\bar{i}(s) = \frac{\bar{E}(s)}{(R + sL)} \quad (1.107)$$

In both cases considered above the system impedance consists of the sum of two terms, corresponding to two elements: resistance and capacitance or inductance. In general, one can write contributions to the total impedance corresponding to the resistance as R , the capacitance as $1/sC$ and the inductance as sL . Addition of impedances is analogous to the addition of resistances. Knowledge of the system impedance allows for an easy solution of the problem. For example, when a constant voltage, E_0 , is applied at time zero to a series connection of R and C , the current is described by equation (1.104). Taking into account that the Laplace transform of a constant $\mathcal{L}[E_0] = E_0/s$, one gets:

$$\bar{i}(s) = \frac{E_0}{s \left(R + \frac{1}{sC} \right)} = \frac{E_0}{R} \frac{1}{s + \frac{1}{RC}} \quad (1.108)$$

Inverse transform of (1.108) gives the current relaxation versus time:

$$i(t) = \frac{E_0}{R} e^{-\frac{t}{RC}} \quad (1.109)$$

The result obtained shows that after the application of the potential step, current initially equals E_0/R and it decreases to zero as the capacitance is charged to the potential difference E_0 . Similarly, application of the potential step to a series connection of R and L produces response given by equation (1.107) which, after substitution of $\bar{E}(s) = E_0/s$, gives:

$$\bar{i}(s) = \frac{E_0}{s(R + sL)} = \frac{E_0}{R} \left(\frac{1}{s} + \frac{1}{s + \frac{R}{L}} \right) \quad (1.110)$$

Inverse transform gives the time dependence of the current:

$$i(t) = \frac{E_0}{R} \left[1 - e^{-\frac{Rt}{L}} \right] \quad (1.111)$$

The current starts at zero as the inductance constitutes infinite resistance at $t = 0$ and it increases to E_0/R as the effect of inductance becomes negligible in the steady-state condition.

In a similar way other problems of transient system response may be solved. In the Laplace space the equations (e.g. equations (1.108) and (1.110)) are much simpler than those in the time space (e.g. equations (1.109) and (1.111)) and analysis in the frequency space s allows for the determination of the system parameters. In the cases involving more time constants, i.e. more than one capacitance or inductance in the circuit, the differential equations describing the system are of the second or higher order and the impedances obtained are the second or higher order functions of s .

Alternating Voltage (av) Input Signal

In the EIS we are interested in the system response to the application of a sinusoidal signal, i.e. $E(t) = E_0 \sin(\omega t)$, where E_0 is the signal amplitude, $\omega = 2\pi f$ is the angular frequency, and f is the av signal frequency. This problem may be solved in different ways. First, let us consider application of an av signal to a series R-C connection. Taking into account that the Laplace transform of the sine function $\mathcal{L}[\sin(\omega t)] = \omega/(s^2 + \omega^2)$, use of equation (1.104) gives:

$$\bar{i}(s) = \frac{E_0 \omega}{s^2 + \omega^2} \frac{1}{R + \frac{1}{sC}} \quad (1.112)$$

Distribution into simple fractions leads to:

$$\bar{i}(s) = \frac{E_0}{R \left[\omega^2 + \left(\frac{1}{RC} \right)^2 \right]} \left[\omega^2 \frac{\omega}{s^2 + \omega^2} + \frac{\omega}{RC} \frac{s}{s^2 + \omega^2} - \frac{\omega}{RC} \frac{1}{s + \frac{1}{RC}} \right] \quad (1.113)$$

and the inverse Laplace transform, taking $\mathcal{L}^{-1}[s/(s^2 + \omega^2)] = \cos \omega t$, gives:

$$i(t) = \frac{E_0}{R \left[\omega^2 + \left(\frac{1}{RC} \right)^2 \right]} \left[\omega^2 \sin(\omega t) + \frac{\omega}{RC} \cos(\omega t) - \frac{\omega}{RC} e^{-\frac{t}{RC}} \right] \quad (1.114)$$

The third term in eqn. (15) corresponds to a transitory response observed just after application of the av signal and it decreases quickly to zero. The steady-state equation may be rearranged into a simpler form:

$$i(t) = \frac{E_0}{R \left[1 + \left(\frac{1}{\omega RC} \right)^2 \right]} \left[\sin(\omega t) + \frac{1}{\omega RC} \cos(\omega t) \right] \quad (1.115)$$

and by introducing $\tan \phi = 1/\omega RC$ the following form is found:

$$i(t) = \frac{E_0}{\sqrt{R^2 + \frac{1}{(\omega C)^2}}} \sin(\omega t + \phi) = \frac{E_0}{|Z|} \sin(\omega t + \phi) \quad (1.116)$$

where ϕ is the phase-angle between current and potential. It is obvious that the current has the same frequency as the applied potential but is phase-shifted by the angle ϕ . The value $|Z|$ has units of resistance; it is the length of a vector obtained by addition of two perpendicular vectors: R and $1/\omega C$.

Complex Notation

In order to simplify the calculations of impedances, the result obtained for the periodic perturbation of an electrical circuit may be represented using complex notation. In the latter example the system impedance, $Z(j\omega)$, may be represented as:

$$Z(j\omega) = Z' + jZ'' = R - j \frac{1}{\omega C} \quad (1.117)$$

and the real and imaginary parts of the impedance are: $Z' = R$ and $Z'' = -1/\omega C$, respectively. It should be noted that the complex impedance $Z(j\omega)$, equation (1.117), may be obtained from $Z(s)$ equation (1.105), by substitution: $s = j\omega$. In fact, this is the imaginary Laplace transform. The modulus of $Z(j\omega)$, equation (1.116), equals:

$$|Z| = \sqrt{(Z')^2 + (Z'')^2} = \sqrt{R^2 + \frac{1}{(\omega C)^2}} \quad (1.118)$$

and the phase-angle between the imaginary and real impedance equals $\phi = \arg(Z) = \tan^{-1}(-1/\omega RC)$. It may be recalled that in complex notation:

$$Z(j\omega) = |Z|e^{j\phi} = |Z|[\cos(\phi) + j \sin(\phi)] \quad (1.119)$$

Analysis of equation (1.116) indicates that the current represents a vector of the length $i_0 = E_0/|Z|$ which rotates with the frequency ω . Current and potential are rotating vectors in the time domain, as represented in Figure 10a. Using complex notation they may be described by:

$$\begin{cases} E = E_0 e^{j\omega t} \\ i = i_0 e^{j(\omega t + \phi)} \end{cases} \quad (1.120)$$

These vectors rotate with a constant frequency ω and the phase-angle, ϕ , between them stays constant. Instead of showing rotating vectors in time space it is possible to present immobile vectors in the frequency space, separated by the phase-angle ϕ . These

vectors are called phasors; they are equal to $\tilde{E} = E_0$ and $\tilde{i} = i_0 e^{j\phi}$, where the initial phase shift of the potential was assumed to be zero, see Figure 10b.

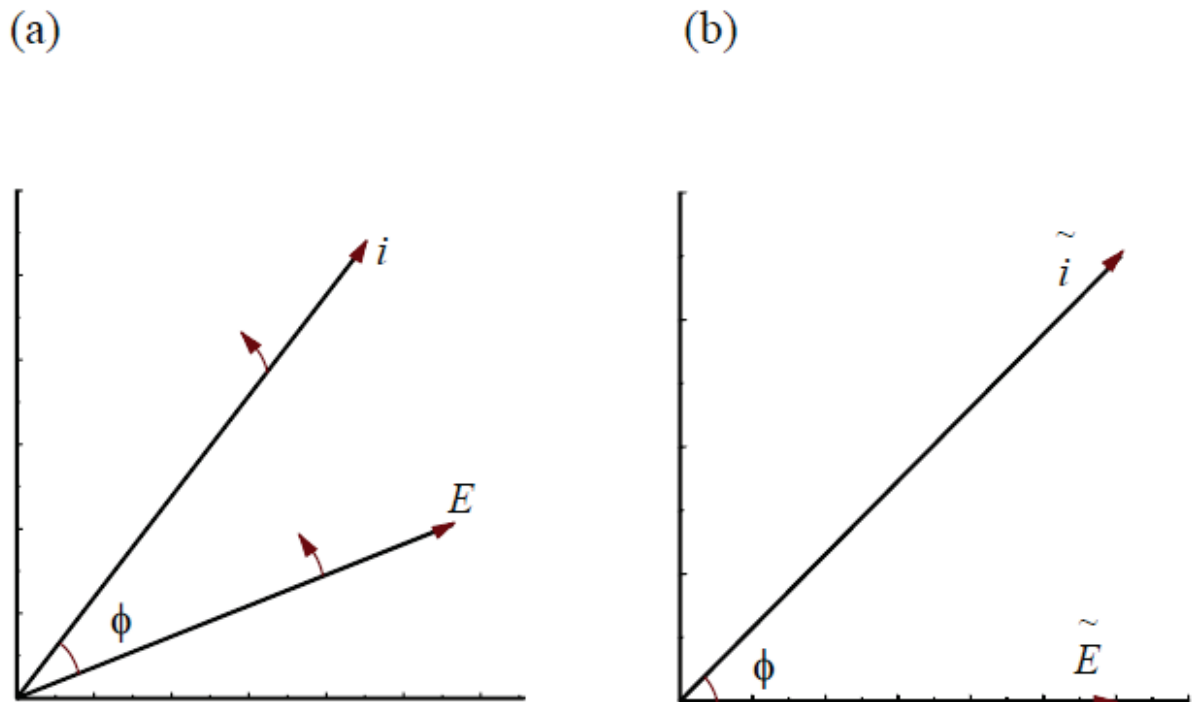


Figure 10. Representation of ac signals: (a) rotating voltage and current vectors in time space; (b) voltage and current phasors in frequency space

1.2.2 Impedance of Electrical Circuits

Electrical circuit theory distinguishes between linear and non-linear systems (circuits). Impedance analysis of linear circuits is much easier than analysis of non-linear ones. A linear system is one that possesses the important property of superposition: If the input consists of the weighted sum of several signals, then the output is simply the superposition, that is, the weighted sum, of the responses of the system to each of the signals. For a potentiostated electrochemical cell, the input is the potential and the output is the current.

Electrochemical cells are not linear: doubling the voltage will not necessarily double the current. However, Figure 11 shows how electrochemical systems can be pseudo-linear. If you look at a small enough portion of a cell's current versus voltage curve, it appears to be linear. In normal EIS practice, a small (1 to 10 mV) ac signal is applied to the cell. With such a small potential signal the system is pseudo-linear. If the system is non-linear, the current response will contain harmonics of the excitation frequency. Linear systems should not generate harmonics, so the presence or absence of significant harmonic response allows one to determine the systems linearity.

In general, for a sinusoidal signal, i.e. $E(t) = E_0 e^{j\omega t}$, the current response is:

$$i(t) = \frac{E_0}{|\hat{Z}|} e^{j(\omega t + \phi)} \quad (1.121)$$

where \hat{Z} is the complex impedance:

$$\hat{Z} = Z' + jZ'' = |Z| e^{j\phi} \quad (1.122)$$

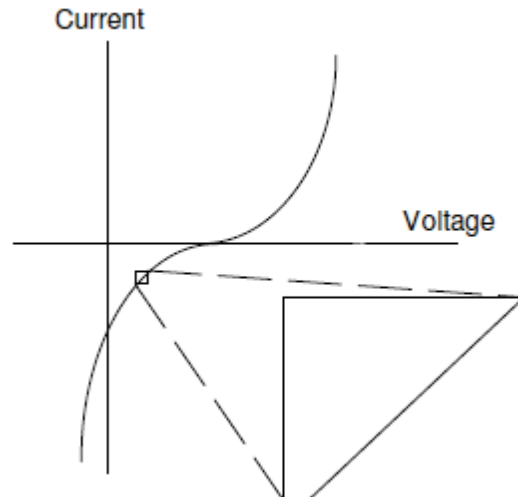


Figure 11. Current versus Voltage curve showing pseudo-linearity

For a linear systems the complex impedance may be written for any circuit by taking R for a resistance, $1/j\omega C$ for a capacitance and $j\omega L$ for an inductance, and applying Ohm's and Kirchoff's laws to the connection of these elements as shown in Table 2.

Component	Impedance
Resistor	$\hat{Z} = R$
Inductor	$\hat{Z} = j\omega L$
Capacitor	$\hat{Z} = 1/j\omega C$

Table 2. Common electrical elements

Notice that the impedance of a resistor is independent of frequency and has no imaginary component. With only a real impedance component, the current through a resistor stays in phase with the voltage across the resistor.

The impedance of an inductor increases as frequency increases. Inductors have only an imaginary impedance component. As a result, the current through an capacitor is phase shifted by -90° with respect to the voltage.

The impedance versus frequency behavior of a capacitor is opposite to that of an inductor. A capacitor's impedance decreases as the frequency is raised. Inductors also have only an imaginary impedance component. The current through an capacitor is phase shifted by 90° with respect to the voltage.

Serial and Parallel Combinations of Circuit Elements

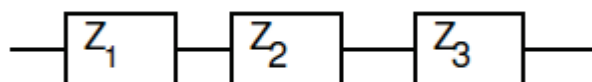


Figure 12. Impedances in series

For linear impedance elements in series (Figure 12) the total impedance is:

$$\hat{Z} = \sum_i \hat{Z}_i \quad (1.123)$$

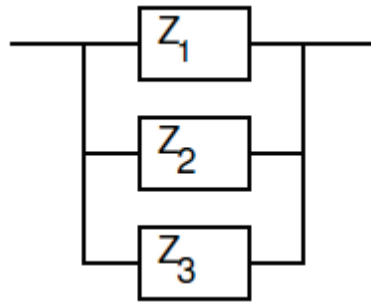


Figure 13. Impedances in parallel

For linear impedance elements in parallel (Figure 13) the total impedance is:

$$\frac{1}{\hat{Z}} = \sum_i \frac{1}{\hat{Z}_i} \quad (1.124)$$

Nyquist and Bode plots

The expression for \hat{Z} is composed of a real and an imaginary part (equation (1.122)). If the real part Z' is plotted on the x-axis and the imaginary part Z'' on the y-axis of a chart, we get a "Nyquist plot". On the Nyquist plot the impedance can be represented as an vector of length $|Z|$. The angle between this vector and the x-axis is $\phi = \arg(\hat{Z})$. Each point on the Nyquist plot is the impedance at one frequency, but you cannot tell what frequency was used to record that point.

If base-10 logarithm of the frequency is plotted on the x-axis and both the absolute values of the impedance and the phase-angle on the y-axis of a chart, we get a "Bode plot". Unlike the Nyquist plot, the Bode plot does show frequency information.

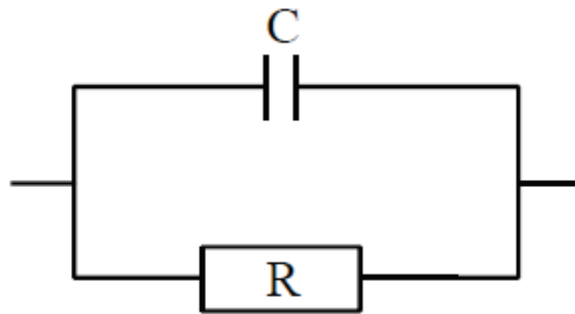


Figure 14. Parallel R-C circuit

For the parallel R-C connection in Figure 14 the total impedance is:

$$\hat{Z} = \frac{1}{\frac{1}{R} + j\omega C} = \frac{R}{1 + \omega^2 R^2 C^2} - j \frac{\omega R^2 C}{1 + \omega^2 R^2 C^2} \quad (1.125)$$

or in polar form:

$$\hat{Z} = |\hat{Z}| e^{j\phi} = \frac{R}{\sqrt{(1 + \omega^2 R^2 C^2)^2}} e^{j \tan^{-1}(\omega RC)} \quad (1.126)$$

We notice from equation (1.125) that:

$$\left(Z' - \frac{R}{2}\right)^2 + (Z'')^2 = \left(\frac{R}{2}\right)^2 \quad (1.127)$$

i.e. the Nyquist plot consists on a semicircle having radius $R/2$ and shifted on the x-axis by $R/2$, as shown in Figure 15. The frequency at the semicircle maximum equal to: $\omega = 1/RC$, the circuit's characteristic breakpoint frequency (inverse of the characteristic time constant). The semicircle is characteristic of a single "time constant".

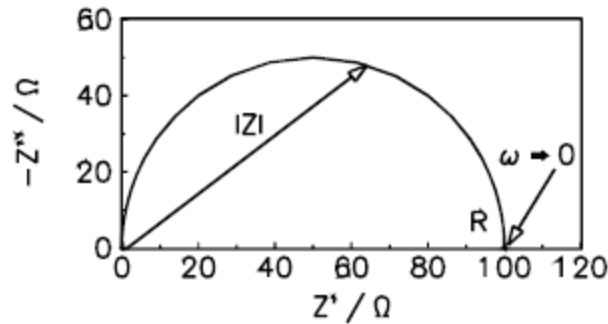


Figure 15. Nyquist plot for a parallel R-C circuit ($R=100\Omega, C=20\mu F$)

From equation (1.126):

$$\left\{ \begin{array}{l} \lim_{\omega \rightarrow 0} \log|\hat{Z}| = \log R \\ \lim_{\omega \rightarrow \frac{1}{RC}} \log|\hat{Z}| = \log \frac{R}{2} \\ \log|\hat{Z}| \approx -\log \omega C \quad \omega \gg \frac{1}{RC} \end{array} \right. \quad (1.128)$$

i.e. on the Bode plot impedance modulus would be nearly constant until the frequency is bigger than the characteristic breakpoint frequency, after which would decrease linearly (Figure 16). Moreover when the frequency is equal to the circuit's characteristic breakpoint frequency, the phase-angle is 45° .

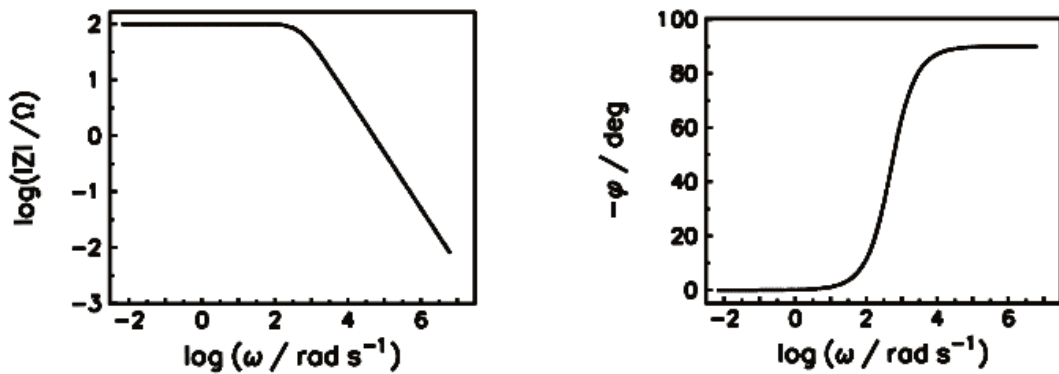


Figure 16. Bode plot for a parallel R-C circuit ($R=100\Omega, C=20\mu F$)

1.2.3 Equivalent circuits elements

EIS data is commonly analyzed by fitting it to an equivalent electrical circuit model. Most of the circuit elements in the model are common electrical elements such as resistors, capacitors, and inductors. To be useful, the elements in the model should have a basis in the physical electrochemistry of the system.

Electrolyte resistance

Solution resistance R_s is often a significant factor in the impedance of an electrochemical cell. As shown before it could be calculated using Kohlrausch law (equation (1.50)). Unfortunately, most electrochemical cells do not have uniform current distribution through a definite electrolyte area. The major problem in calculating solution resistance therefore concerns determination of the current flow path and the geometry of the electrolyte that carries the current. For this reason usually solution resistance isn't calculated from ionic conductances but calculated fitting EIS data to a model.

Double-layer capacitance

An electrical double layer exists on the interface between an electrode and its surrounding electrolyte (Figure 7). The value of the double layer capacitance C_{dl} depends on many variables and it's therefore calculated fitting EIS data to a model.

Constant phase element (CPE)

Capacitors in EIS experiments often do not behave ideally showing significant frequency dispersion. Several authors have found excellent agreement of this behavior with the dispersion shown by a CPE (40; 41). The impedance of a CPE can be expressed as:

$$\frac{1}{\hat{Z}_{CPE}} = C(j\omega)^\alpha \quad (1.129)$$

where α is an empirical exponent. For an ideal capacitor the exponent $\alpha = 1$.

Charge transfer resistance

Assuming that the rate of diffusion of the redox species is significantly faster than the rate of electron transfer, faradic current density is given by the Butler-Volmer equation (1.83), which can be linearized at a narrow potential range around the equilibrium potential by means of Taylor expansion:

$$\begin{cases} j \cong \frac{\eta_{kin}}{R_{ct}} \\ R_{ct} = \frac{RT}{nFj_0} \end{cases} \quad (1.130)$$

where R_{ct} is the so-called charge transfer resistance and j_0 is the exchange current density.

Diffusion

Mass transport in electrolyte solutions is described by the Nernst-Planck equation (1.68). In the absence of migration and convection, diffusion causes the concentration field to change with time equation (1.63). Assuming the diffusion coefficient D to be a constant equation (1.63) reduces in one dimension to:

$$\frac{\partial c}{\partial t} = D \frac{\partial^2 c}{\partial x^2} \quad (1.131)$$

From the point of view of impedance spectroscopy, solutions of the diffusion equation are required in the frequency domain. The Laplace transform of equation (1.131) is an ordinary differential equation:

$$s\bar{c} - c(t=0) = \frac{\partial^2 \bar{c}}{\partial x^2} \quad (1.132)$$

where $s = \sigma + j\omega$ is the complex frequency variable and \bar{c} is the Laplace transform of the concentration. Solutions are of the form:

$$\Delta\bar{c} = B_1 e^{-\alpha x} + B_2 e^{\alpha x} \quad (1.133)$$

where $\alpha = \sqrt{s/D}$, B_1 and B_2 are constants to be determined by the boundary conditions and $\Delta\bar{c}$ is the Laplace transform of the excess concentration:

$$\Delta c = c(x, t) - c(x, 0) \quad (1.134)$$

One boundary is usually the interface between the electrode and the electrolyte ($x = 0$). For semiinfinite diffusion into the electrode, i.e. $\Delta c \rightarrow 0$ as $x \rightarrow \infty$, $B_2 = 0$. At the electrode–electrolyte interface ($x = 0$), the solution is:

$$\Delta\bar{c}_{x=0} = \frac{\Delta\bar{i}}{nFA\sqrt{sD}} \quad (1.135)$$

where $\Delta\bar{i}$ is the diffusion limited ac current, which is equal to $-nFADd\Delta c/dx$ (equation (1.93)). For small perturbations around equilibrium, we may write:

$$\frac{\Delta E}{\Delta c} \cong \frac{\partial E}{\partial c} \quad (1.136)$$

where E is the electrode potential and $\partial E/\partial c$ represents the change in electrode potential with concentration which can be calculated differentiating equation (1.91):

$$\frac{\partial E}{\partial c} = \frac{RT}{nFc} \quad (1.137)$$

Taking the Laplace transform of equations (1.136) and substituting into equation (1.135) gives:

$$\bar{Z}(s) = \frac{\Delta\bar{E}}{\Delta\bar{i}} = \left(\frac{\partial\bar{E}}{\partial\bar{c}} \right) / nFA\sqrt{sD} = \frac{RT}{n^2 F^2 A c \sqrt{sD}} \quad (1.138)$$

which has analogies in both heat conduction and electrical circuit theory. Consider the semiinfinite transmission line composed only of resistors and capacitors (Figure 17).

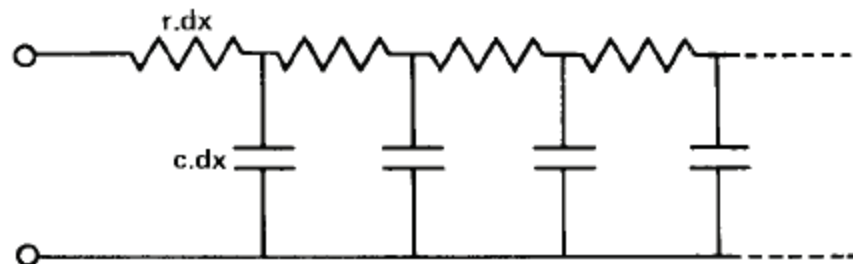


Figure 17. A resistive–capacitive transmission line which describes the behavior of a semiinfinite diffusion process

The reciprocal of the resistance per unit length is analogous to $cDAF^2n^2/RT$, and the capacitance per unit length is analogous to n^2F^2Ac/RT . Thus the reciprocal of the rc product plays the role of the diffusion coefficient. The impedance of the transmission line is:

$$\bar{Z}(s) = \sqrt{\frac{r}{sc}} \quad (1.139)$$

which is exactly the same form as equation (1.138) if appropriate substitutions are made. Setting $\sigma = 0$ and separating the real and imaginary parts in equation (1.138) gives:

$$\begin{cases} Z(j\omega) = \sigma(1-j)\omega^{-\frac{1}{2}} \\ \sigma = \frac{RT}{n^2 F^2 A c \sqrt{2D}} \end{cases} \quad (1.140)$$

called “infinite Warburg”. The complex impedance is therefore inversely proportional to the square root of frequency. In the complex plane it is a straight line inclined at $\pi/4$ to the real axis. So far, only semiinfinite boundary conditions have been considered. For many problems, however, thin samples dictate the use of finite-length boundary conditions. A constant activity or concentration is a common condition for the interface removed from $x = \delta$, where δ is the Nernst diffusion layer thickness. The equivalent circuit analog of this situation is a finite-length transmission line terminated with a resistance, and the impedance is given by the expression :

$$Z(j\omega) = \sigma(1-j)\omega^{-\frac{1}{2}} \tanh \left[\delta \sqrt{\frac{j\omega}{D}} \right] \quad (1.141)$$

called “finite Warburg”.

1.2.4 Common equivalent circuit models

The aim of the analysis of the EIS data is to elucidate the electrode process and to derive its characteristic parameters. It should be stressed here that the EIS is a very sensitive technique but it does not provide a direct measure of the physical phenomena. Other electrochemical experiments (dc, transients) should also be carried out, together with good physical knowledge of the system (solution and surface composition, thickness, porosity, presence of various layers, hydrodynamic conditions, etc.). Interpretation of impedance data requires use of an appropriate model. The modeling may be classified as: (i) physico-chemical, process or structural modeling and (ii) measurement, formal or mathematical modeling. Process modeling links measured impedances with physicochemical parameters of the process (kinetic parameters, concentrations, diffusion coefficients, sample geometry, etc.). Measurement modeling explains the experimental impedances in terms of mathematical functions in order to obtain good fit between the calculated and experimental impedances. In the latter case the parameters obtained do not necessarily have a clear physico-chemical significance. Ideally, first the measurement modeling should be carried out, the number and the nature of the circuit elements should be identified and then the process modeling should be carried out.

Such a procedure is relatively elementary for a circuit containing simple elements: R, C, and L. It may also be carried out for the circuits containing distributed elements that can be described by a closed form equation: CPE, semiinfinite or finite length diffusion, etc. However, in such cases a priori model prediction is difficult or impossible. Usually, an equivalent circuit is chosen and the fit to the experimental data is performed using the complex nonlinear least-squares technique (CNLS). However, the model deduced from the reaction mechanism may have too many adjustable parameters while the experimental impedance spectrum is simple. For example, a system with one adsorbed species, may produce two semicircles in the complex plane plots, but experimentally only one semicircle

is often identified. Another problem of data modeling is connected with the fact that the same data may be represented by different equivalent circuits (42). For example, a system displaying a capacitive loops, i.e. having one time constants, may be adequately described by the two circuits in Figure 18.

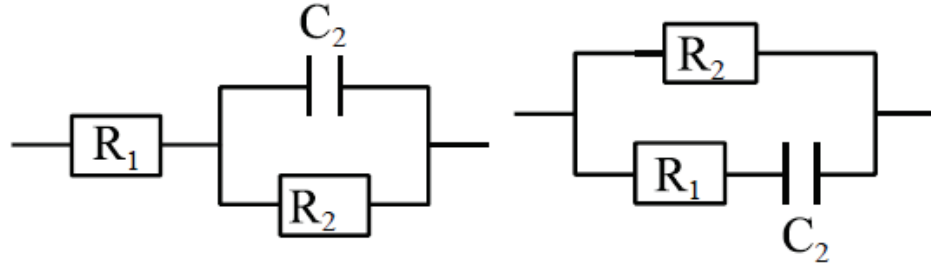


Figure 18. Alternative circuits for the impedance behavior of a system containing one capacitive loop

In the following paragraphs some common equivalent circuits models will be discussed. These models can be used to interpret simple EIS data.

Randles cell

The Randles cell is one of the simplest cell models. It includes a solution resistance, a double layer capacitor and a charge transfer resistance. In addition to being a useful model in its own right, the Randles model is the starting point for other more complex models.

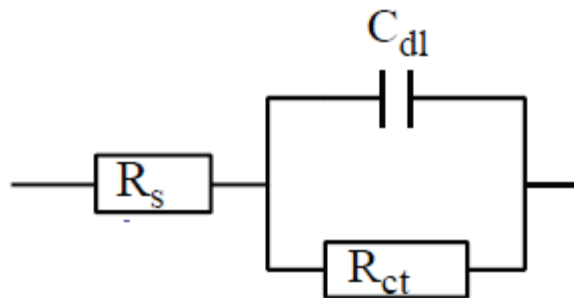


Figure 19. Randles cell equivalent circuit

The equivalent circuit for the Randles Cell is shown in Figure 19. The double layer capacity is parallel with the impedance due to the charge transfer reaction. The impedance for this circuit is:

$$Z = \left(R_s + \frac{R_{ct}}{1 + C_{dl}^2 R_{ct}^2 \omega^2} \right) - j \left(\frac{R_{ct}^2 C_{dl} \omega}{1 + C_{dl}^2 R_{ct}^2 \omega^2} \right) \quad (1.142)$$

The Nyquist plot for a Randles cell is always a semicircle (Figure 20). The solution resistance can be found by reading the real axis value at the high frequency intercept. This is the intercept near the origin of the plot. The real axis value at the other (low frequency) intercept is the sum of the charge transfer resistance and the solution resistance. The diameter of the semicircle is therefore equal to the charge transfer resistance.

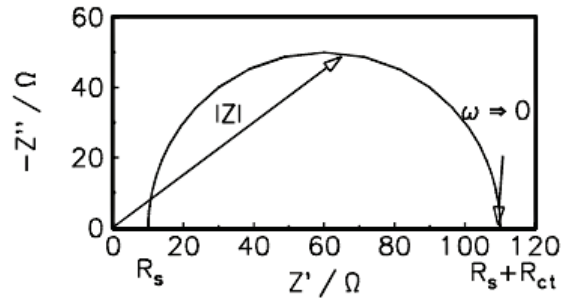


Figure 20. Nyquist plot for a Randles cell: $R_s=10\Omega$, $R_{ct}=100\Omega$, $C_{dl}=20\mu F$

Mixed kinetic and diffusion control

Let us consider a cell where polarization is due to a combination of kinetic and semiinfinite diffusion processes. This can be modeled adding a Warburg impedance R_W (equation (1.140)) in series with the charge transfer resistance on the Randles cell (Figure 21).

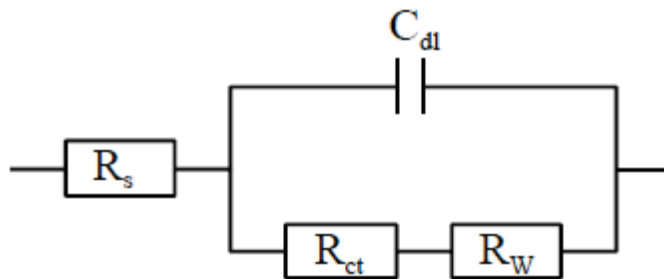


Figure 21. Mixed kinetic and diffusion controlled cell equivalent circuit

The Nyquist plot for such cell is showed in Figure 22: a semicircle is present at high frequencies, analogous to the Randles cell, followed by a 45° line at low frequencies, typical for a semiinfinite diffusion Warburg element.

Although in simple cases the process parameters may be obtained graphically, the best way to analyze the impedances is, however, by the complex nonlinear least-squares approximation technique. From such fits the following parameters may be obtained: R_s , C_{dl} , R_{ct} and the Warburg coefficient σ . It should be stressed that the Warburg impedance cannot be represented by a connection of simple R and C elements because of the non-integer power of frequency ($\omega^{-1/2}$) and it constitutes a distributed element which can only be approximated by an infinite series of simple electrical elements.

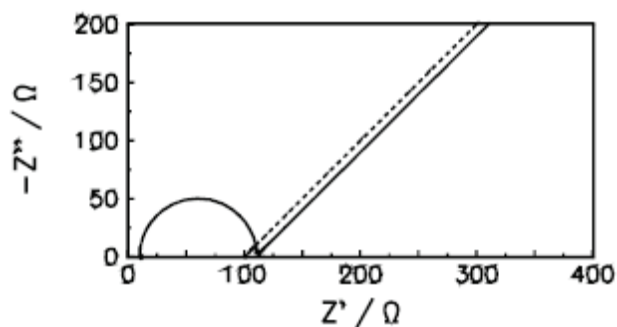


Figure 22. Nyquist plot for a mixed kinetic and diffusion controlled cell: $R_s=10\Omega$, $R_{ct}=100\Omega$, $C_{dl}=20\mu F$, $\sigma=10\Omega s^{-0.5}$

1.3 Electrochemical applications

1.3.1 Fuel cells

A fuel cell is an electrochemical cell that converts chemical energy of a source fuel directly into electric energy. The basic physical structure, or building block, of a fuel cell consists of an electrolyte layer in contact with an anode and a cathode on either side. In a typical fuel cell, fuel is fed continuously to the anode and an oxidant (often oxygen from air) is fed continuously to the cathode. The spontaneous ($\Delta_r G < 0$) electrochemical reactions take place at the electrodes to produce an ionic current through the electrolyte, while driving a complementary electric current that performs work on the load. A schematic representation of a unit cell with the reactants/products and the ion conduction flow directions through the cell is shown in Figure 23.

Though the direct use of conventional fuels in fuel cells would be desirable, most fuel cells under development today use gaseous hydrogen as a fuel. Hydrogen has a high reactivity for anode reactions, and can be produced chemically from a wide range of fossil and renewable fuels, as well as via electrolysis. For similar practical reasons, the most common oxidant is gaseous oxygen, which is readily available from air.

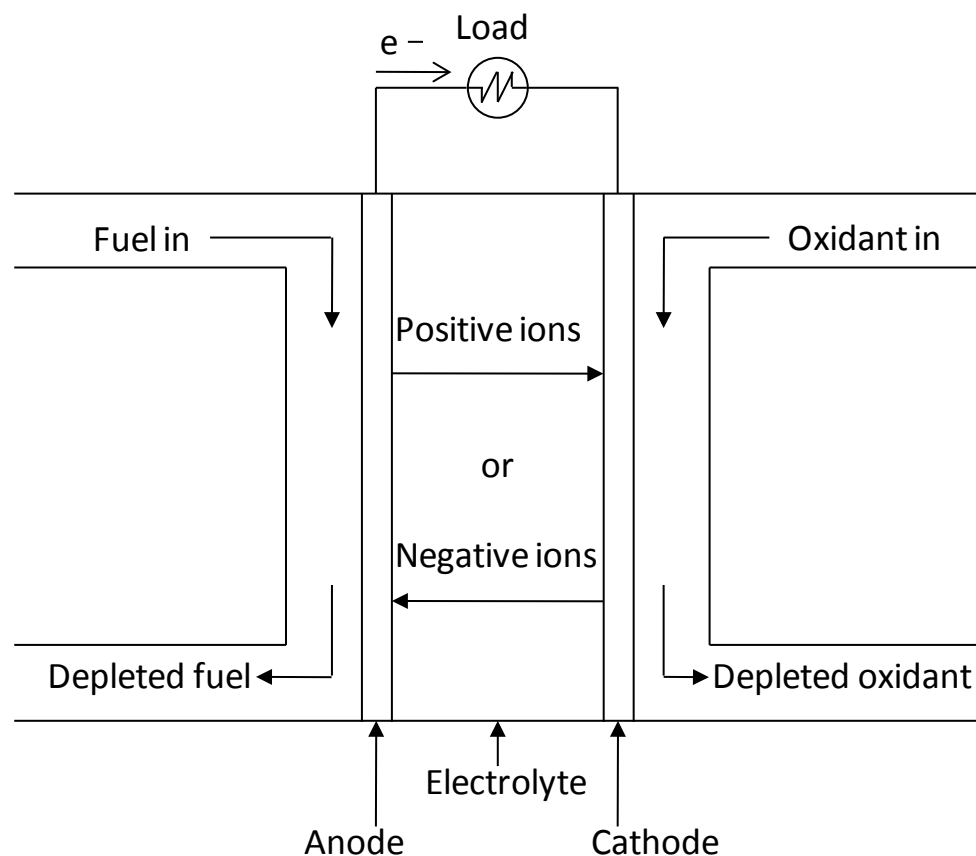


Figure 23. Fuel cell schematic

Although a fuel cell is similar to a typical battery in many ways, it differs in several respects. The battery is an energy storage device in which all the energy available is stored within the battery itself. The battery will cease to produce electrical energy when the chemical reactants are consumed (i.e., discharged). A fuel cell, on the other hand, is an

energy conversion device to which fuel and oxidant are supplied continuously. In principle, the fuel cell produces power for as long as fuel is supplied.

Fuel cell types

Fuel cells are classified according to the choice of electrolyte, which determine the type of ions that carry the current across the electrolyte:

- Alkaline fuel cells (AFC) use concentrated (85 wt%) KOH as the electrolyte for high temperature operation (250°C) and less concentrated (35-50 wt%) for lower temperature operation (<120°C). The electrolyte is retained in a matrix (e.g. asbestos), and a wide range of electrocatalysts can be used (such as Ni, Ag, metal oxides and noble metals). This fuel cell is intolerant to CO₂ present in either fuel or oxidant, reacting with the KOH to form K₂CO₃, thus that could block or destroy the catalyst layers (3). Alkaline fuel cells have been used in the space program (Apollo and Space Shuttle) since the 1960s. Advantages: circulating electrolyte establish a reliable barrier against reactant leakage from the electrodes and simplify both water and heat management. Moreover in alkaline environment a wide range of non-precious electrocatalysts can be employed. Disadvantages: if ambient air is used as the oxidant, the CO₂ in the air must be removed, increasing the size and cost of the system. In a multi-cell stack the electrolyte has to be fed into each of the cells, bridging the cells and allowing parasitic currents.
- Polymer electrolyte membrane or proton exchange membrane fuel cells (PEMFC) use a thin (≤50 μm) proton conductive polymer membrane (such as perfluorosulfonated acid polymer) as the electrolyte. The catalyst is typically platinum supported on carbon. Operating temperature is typically between 40 and 80°C. Advantages: The PEMFC has a solid electrolyte which removes corrosive cell components, provides excellent resistance to gas crossover and reduces the weight and size of the electrolyte compartment. Moreover in a multi-cell stack no parasitic current is present. Disadvantages: The low and narrow operating temperature range makes thermal management difficult, especially at very high current densities. Water management is another significant challenge in PEMFC design, sufficient hydration of the membrane has to be ensured, in order to have a good ionic conductivity, without flooding the electrodes. High loading of noble metals are required as electrocatalysts (1). In addition, PEMFCs are quite sensitive to poisoning by trace levels of contaminants including CO, sulfur species, and ammonia.
- Anion-exchange Membrane Fuel Cell (AMFC): in the last few years a number of new anion-exchange polymers (5; 6) have been developed, along with noble metal free catalysts for the Oxygen Reduction Reaction (ORR) (20), which together offered the possibility of developing AMFCs. As opposed to AFC, AMFC has no mobile cations and CO₂ tolerance is greatly improved through the so-called self purging mechanism (6; 43). Recent literature results on H₂/O₂ and H₂/Air AMFC are encouraging (44; 45). Operating temperature is typically between 40 and 80°C. Advantages: The AMFC has a solid electrolyte which removes corrosive cell components, provides excellent

resistance to gas crossover, reduces the weight and size of the electrolyte compartment and greatly improve CO₂ tolerance. In alkaline environment a wide range of non-precious electrocatalysts can be employed. Moreover in a multi-cell stack no parasitic current is present. Disadvantages: As opposed to PEMFCs, noble metal free catalysts are relatively less well studied, as well as anionic exchange materials. As for PEMFC The low and narrow operating temperature range makes thermal and water management difficult, especially at high current densities.

- Phosphoric acid fuel cells (PAFC) use concentrated phosphoric acid (100%) as the electrolyte. The matrix used to retain the acid is usually SiC and the electrocatalyst in both the anode and the cathode is platinum. Operating temperature is typically between 150 and 220°C. Advantages: PAFCs are much less sensitive to CO than PEMFCs. The operating temperature also provides considerable design flexibility for thermal management. Disadvantages: Platinum catalyst is required, the highly corrosive nature of phosphoric acid requires the use of expensive materials in a stack.
- Molten carbonate fuel cells (MCFC) have the electrolyte composed of a combination of alkali (Li, Na, K) carbonates, which is retained in a ceramic matrix of LiAlO₂. Operating temperatures are between 600 and 700°C where the carbonates form a highly conductive molten salt, with carbonate ions providing ionic conduction. Advantages: The relatively high operating temperature of the MCFC (650 °C) allows cheaper non-noble electrocatalysts usage. Moreover both CO and certain hydrocarbons are fuels for the MCFC. Disadvantages: The higher temperatures and corrosive electrolyte usage promote material problems, impacting mechanical stability and stack life. High contact resistances limit power densities to around 100 – 200 mW/cm² at practical operating voltages.
- Solid oxide fuel cells (SOFC) use a solid, nonporous metal oxide, usually Y₂O₃-stabilized ZrO₂ (YSZ) as the electrolyte. These cells operate at 800-1000°C where ionic conduction by oxygen ions takes place. Advantages: The kinetics of the cell are relatively fast, and CO is a directly useable fuel as it is in the MCFC. Thin-electrolyte planar SOFC unit cells have been demonstrated to be cable of power densities close to those achieved with PEMFC. Disadvantages: The high operating temperature places severe constraints on materials selection and results in difficult fabrication processes.

Fuel cells operating at high temperatures (PAFCs, MCFCs and SOFCs) are usually employed in stationary applications due to their long startup. In addition, the waste heat can be readily used in most commercial and industrial cogeneration applications.

On the other hand fuel cells operating at low temperatures (PEMFCs, AMFCs and AFCs) are good candidates for automotive and portable applications. On Table 3 are resumed the major differences between fuel cell types.

	AFC	PEMFC	AMFC	PAFC	MCFC	SOFC
Electrolyte	Mobilized or Immobilized KOH solution in asbestos matrix	Cation-exchange polymer	Anion-exchange polymer	Immobilized Liquid Phosphoric Acid in SiC	Immobilized Liquid Molten Carbonate in LiAlO ₂	Perovskites
Electrode	Transition metals	Carbon	Carbon	Carbon	Nickel and Nickel oxide	Perovskite
Catalyst	Platinum	Platinum	Transition metals-based	Platinum	Electrode material	Electrode material
Charge carrier	OH ⁻	H ⁺	OH ⁻	H ⁺	CO ₃ ²⁻	O ²⁻
Operating temperature	65-220°C	40-80°C	40-80°C	150-220°C	600-700°C	600-1000°C

Table 3. Fuel cell types summary

1.3.2 H₂/O₂ membrane fuel cells

Proton exchange membrane fuel cells (PEMFC) (46) are able to efficiently generate high power densities, thereby making the technology potentially attractive for certain mobile and portable applications. PEMFC technology differentiates itself from other fuel cell technologies in that a solid phase polymer membrane is used as the cell separator/electrolyte. Because the cell separator is a polymer film and the cell operates at relatively low temperatures, issues such as sealing, assembly, and handling are less complex than most other fuel cells. The need to handle corrosive acids or bases is eliminated in this system. PEMFCs typically operate at low temperatures (60°C to 80°C), allowing for potentially faster startup than higher temperature fuel cells. The PEMFC is seen as the main fuel cell candidate technology for light-duty transportation applications. While PEMFC are particularly suitable for operation on pure hydrogen, fuel processors have been developed that will allow the use of conventional fuels such as natural gas or gasoline.

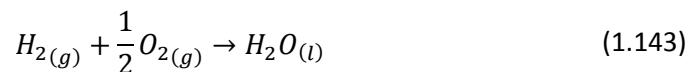
For these reasons PEMFCs have been the subject of intensive research over the last 20 years, however the main obstacle to the diffusion of this technology remains the slow kinetics of the oxygen reduction reaction (ORR) (1). Due to reasons of excessive cost and supply limitations of platinum, large-scale application of H₂/O₂ PEMFCs would require strongly reduced Pt loadings. To meet this requirement, the Pt specific power density would have to be reduced to <0.2 g_{Pt}/kW at cell voltages of ≥0.6 V (to maintain high fuel cell energy conversion efficiencies of >55%). State-of-the-art Pt loading are ≈0.4 to 0.5 mg_{Pt}/cm²_{MEA}, corresponding to Pt-specific power densities of ≈0.5 g_{Pt}/kW. Therefore, to reach the above targets, Pt loadings of ≤0.15 mg_{Pt}/cm²_{MEA} are needed, which would require improved cathode catalysts with an approximately four-fold higher activity compared to Pt/C.

In the last few years a number of new anion-exchange polymers (5; 6) have been developed, along with noble metal free catalysts which are intrinsically stable and have an

activity similar to platinum in alkaline media for the Oxygen Reduction Reaction (ORR) (20), which together offered the possibility of developing Anion-exchange Membrane Fuel Cells (AMFCs), promising the advantages of PEMFCs with reduced platinum loadings. Recent literature results on H₂/O₂ and H₂/Air AMFC are encouraging (44; 45).

Thermodynamics

Overall reaction for both H₂/O₂ PEMFC and AMFC is:



which at 25°C has the equilibrium standard potential of 1.229V. If air is used as oxygen source (≈21 vol%), the equilibrium potential can be calculated by means of Nernst equation (1.37), resulting in a decrease of the equilibrium potential of ≈ -0.01V.

Since $\Delta_r\tilde{S}$ changes below 100°C are very small (<10 J mol⁻¹ K⁻¹), the equilibrium potential at different temperatures can be calculated using equation (1.44). The equilibrium potential decreases as temperature increases ($\Delta_r\tilde{S} < 0$). However, in operating fuel cells, in general, a higher cell temperature results in a higher cell potential. This is because the voltage losses in operating fuel cells decreases with temperature, and this more than compensates for the loss of equilibrium cell potential.

The thermal efficiency of a fuel conversion device is defined as the amount of useful energy produced relative to the change in enthalpy between the product and feed streams. In the ideal case of an electrochemical converter, such as a fuel cell, the change in Gibbs free energy of the reaction is available as useful electric energy at the temperature of the conversion. The ideal efficiency of a fuel cell, operating reversibly, is then:

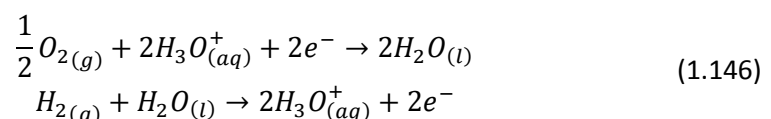
$$\eta_{ideal} = \frac{\Delta_r G}{\Delta_r H} = \frac{\Delta_r G/nF}{\Delta_r H/nF} = \frac{E_{cell}}{\Delta_r H/nF} \quad (1.144)$$

It should be noted that $\Delta_r H/nF$ has dimension of Volts, called thermoneutral potential. At 25°C and standard conditions $\eta_{ideal} = 83\%$. In an operating fuel cell it can be shown that:

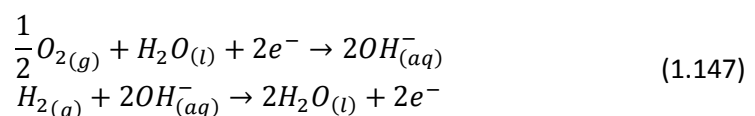
$$\eta = \frac{V_{cell}}{1.482} \quad (1.145)$$

where V_{cell} is the operating cell voltage.

For PEMFC the half reactions are:



i.e. water is produced at the cathode and the charge is carried by hydronium ions. For AMFC the half reactions are:



i.e. water is produced at the anode and the charge is carried out by hydroxyl ions. Osmotic and electroosmotic forces drag water and ions through the polymeric membrane as shown in Figure 24.

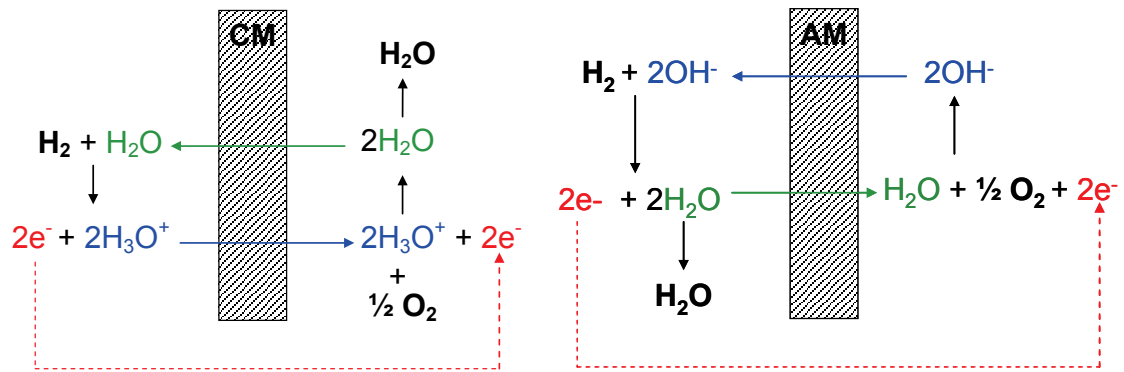


Figure 24. Schematics for H_2/O_2 PEMFC (left) and AMFC (right), showing half reactions, water, ionic and electronic flows

Cell components

Typical cell components within a PEMFC or AMFC include (Figure 25):

- the ion-exchange membrane;
- an electrically conductive gas diffusion layer;
- an electro-catalyst layer at the interface between the gas diffusion layer and the membrane;
- graphite plates that deliver the fuel and oxidant to reactive sites via flow channels and electrically connect the cells;
- gaskets to prevent leakage from the cell.

The heart of a membrane fuel cell is a polymer, ion-conductive membrane. On both sides of the membrane there is a porous electrode. The electrodes must be porous because the reactant gases are fed from the back and must reach the interface between the electrodes and the membrane, where the electrochemical reactions take place in the so-called catalyst layer, or more precisely, on the catalyst surface. Technically, the catalyst layer may be a part of the porous electrode or part of the membrane, depending on the manufacturing process. The multilayer assembly of the membrane sandwiched between the two electrodes is commonly called the membrane electrode assembly or MEA. The MEA is then sandwiched between the collector/separator plates, responsible for both conducting electrical current and separating the gases in adjacent cells in a multi-cell stack. At the same time, in multi-cell configuration they physically/electrically connect the cathode of one cell to the anode of the adjacent cell, and that is why they are also called bipolar plates. They provide the pathways for flow of reactant gases (called flow fields), and they also provide the cell structural rigidity. A critical portion of unit cells is often referred to as the three-phase interface. These mostly microscopic regions, in which the actual electrochemical reactions take place, are found where either electrode meets the electrolyte. For a site or area to be active, it must be exposed to the reactant, be in electrical contact with the electrode, be in ionic contact with the electrolyte, and contain sufficient electro-catalyst for the reaction to proceed at the desired rate. The density of these regions and the nature of these interfaces play a critical role in the electrochemical performance of both liquid and solid electrolyte fuel cells. In solid electrolyte fuel cells, the challenge is to engineer a large

number of catalyst sites into the interface that are electrically and ionically connected to the electrode and the electrolyte, respectively, and that is efficiently exposed to the reactant gases. In most solid electrolyte fuel cells, a high-performance interface requires the use of an electrode which, in the zone near the catalyst, has mixed conductivity (i.e. it conducts both electrons and ions). Usage of a solubilized ion-exchange polymer (ionomer) incorporated the catalyst layer to grant both ionic and electrical conduction inside the electrode was discovered in 1992 by Los Alamos National Lab (47).

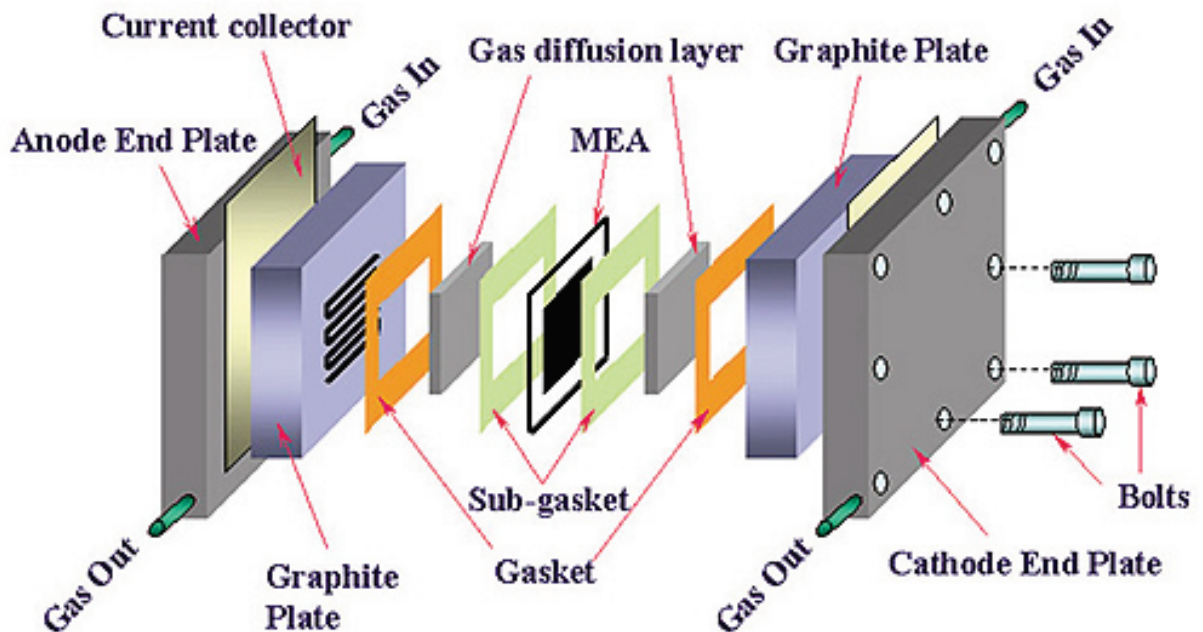


Figure 25. Single cell main components

The following processes take place inside the fuel cell:

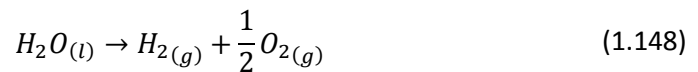
1. Gas flow through the channels;
2. Gas diffusion through porous media;
3. Electrochemical reactions, including all the intermediary steps;
4. Ions transport through ion-conductive polymer membrane;
5. Electron conduction through electrically conductive cell components;
6. Water transport through polymer membrane including both electrochemical drag and back diffusion;
7. Water transport (both vapour and liquid) through porous catalyst layer and gas diffusion layers;
8. Two-phase flow of unused gas carrying water droplets;
9. Heat transfer, including both conduction through solid components of the cell and convection to reactant gases and cooling medium.

Obviously, the design of the components and properties of materials must accommodate the above-listed processes with minimum obstruction and losses. Because in some of the components more than one process takes place, very often with conflicting requirements, the properties and the design must be optimized. For example, the gas diffusion layer must be optimized so that the reactant gas may easily diffuse, yet at the same

time that water, which travels in the opposite direction, does not accumulate in the pores. On top of that the diffusion layer must be both electrically and thermally conductive. Similar requirements may be established for almost every fuel cell component. Although a fuel cell seems to be a simple device, numerous processes take place simultaneously. It is therefore important to understand those processes, their mutual interdependence, and their dependence on the components design and materials properties. On section 1.4 will be discussed the required properties and design rules of ion-exchange materials for fuel cell applications.

1.3.3 Electrolyzers

An electrolyzer is an electrochemical cell that converts electrical energy into chemical energy: a non-spontaneous ($\Delta_r G > 0$) chemical reaction is driven by an external source of current. The result is that the chemical energy is increased. An important example of electrolysis is the decomposition of water into hydrogen and oxygen:



Fuel cells bear significant resemblance to electrolyzers since their basic physical structure is similar, as shown in Figure 26 for a water electrolyzer (acidic or alkaline).

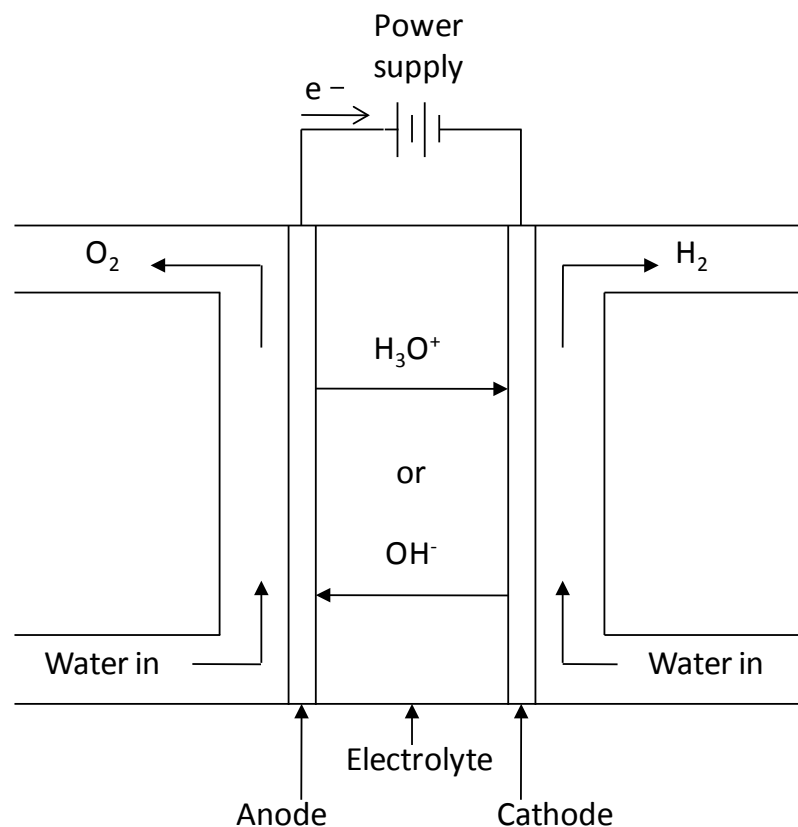


Figure 26. Water electrolyzer schematic

Since electric grid is incapable of storing more than 10% energy from renewable sources (wind, solar, etc.), water electrolysis is a good candidate for generating hydrogen as temporary energy storage to be used in an H₂/O₂ or H₂/Air fuel cell (Figure 27).

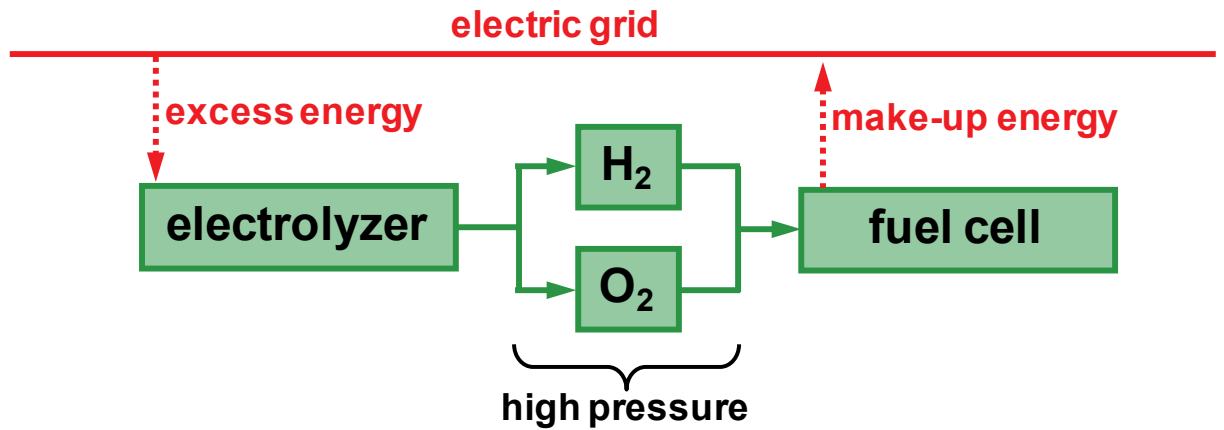


Figure 27. Water electrolysis/ H_2 - O_2 fuel cell energy storage diagram

Similarly to fuel cell, the electrolyte for water electrolysis can be either liquid (e.g. KOH solution) or solid (e.g. cation-exchange membrane). Nowadays commercially available water electrolyzers are proton exchange membrane based (PEM-E) and aqueous KOH solution based (KOH-E). On Table 4 advantages (+) and disadvantages (-) are resumed for both types.

PEM-E	KOH-E
+ High pressure H_2 (200 atm)	- Low pressure H_2
+ High purity H_2	- H_2 clean-up needed
+ Easy handling	- Concentrated KOH handling
+ High current densities (1-2 A/cm ²)	- Low current densities (0.5-1 A/cm ²)
- High precious metals loadings	+ No precious metals needed

Table 4. Advantages (+) and disadvantages (-) for both proton exchange membrane based (PEM-E) and aqueous KOH solution based (KOH-E) electrolyzers

In principle anion-exchange membrane based electrolyzers (AMEs) combine all the advantages, promising high current densities, high pressure and purity H_2 and O_2 , and no precious metals requirements for the catalyst layer. Design rules and required properties for anion-exchange materials will be discussed on the next section.

1.4 Ion-exchange materials

Electrochemists have spent many decades in a continuing search for newer, more highly conducting and more electrochemically stable electrolyte systems. Traditional electrolyte systems such as sulphuric acid and potassium hydroxide are used for their low cost and high ionic conductivity, but restricted by their extreme corrosivity and challenging confinement. With the development of single-ion conducting polymers, electrochemists have the ability to choose from a variety of polymers with both high conductivity for a given ion of interest as well as excellent stability and processability allowing the design of electrochemical devices in their most ideal formats (e.g. PEMFC and PEM-E).

Electrochemical separator membranes with fixed ion groups date back to before the 1950s with the use of polystyrene sulfonic acid and related acid-containing polymers as separators for electrochemical processes. The advantages of fixed ion group separators in the early days of usage were the same that exist today including the lack of corrosive mobile acids, high conductivity and selectivity, and thin film form leading to compact systems with low ohmic drop. The drawback of these systems was the chemical and electrochemical degradation that occurred with the instability of the C-H bonds in these early ionomers. Ionomers is a term that typically refers to single-ion conducting polymers with a fixed ion group covalently attached to the polymer. The function of the ion exchange membrane is to provide a conductive path, while at the same time separating the reactant gases. The material is an electrical insulator. As a result, ion conduction takes place via ionic groups within the polymer structure. Ion transport at such sites is highly dependent on the bound and free water associated with those sites.

A common procedure to synthesize ion-exchange materials consists in the chemical modification of a commercial polymer via free-radical graft copolymerization with polar monomers. During the propagation reactions grafting monomers grows as side chains having variable lengths (and molecular weight) attached to the polymeric matrix by covalent bonds. Side chains growing reaction occurs alongside crosslinking and homopolymer formation reactions. Starting commercial polymers are usually thermoplastic (48), granting suitable thermal and mechanical stability; it can be used either in bulk, solution, molten state or as thin film during grafting reaction.

The most common commercial perfluorinated ionomer membranes used today in numerous industrial processes throughout the world are listed in Table 5.

Trade name	Company	Membrane type
Nafion® XR resin	DuPont	Perfluorosulfonic acid
Nafion® CR resin	DuPont	Perfluorocarboxylic acid
Flemion® XR resin	Asahi Glass	Perfluorosulfonic acid
Flemion® CR resin	Asahi Glass	Perfluorocarboxylic acid
Aciplex® XR resin	Asahi Chemical	Perfluorosulfonic acid
Aciplex® CR resin	Asahi Chemical	Perfluorocarboxylic acid

Table 5. Commercial perfluorinated ionomer membranes listed by trade name

Physical structures of the Nafion[®], Flemion[®], and Aciplex[®] sulfonate (XR) and carboxylate (CR) form membranes have been shown in literature (49). Although ionomer membranes have been used for several decades in a number of commercial processes, their production volumes can only be deemed small in comparison to major commodity polymers.

Organic-based cation exchange membranes in fuel cells were originally conceived by William T. Grubb (50) in 1959. The first commercially available perfluorinated ionomer membranes were based on copolymers of tetrafluoroethylene (TFE) and perfluorovinyl ether monomers. The first use of a Nafion[®] membrane in a fuel cell was accomplished in 1966 by GE for National Aeronautics & Space Administration (NASA) (51). That initial effort eventually led to development of the perfluorosulfonic acid polymer used in today's systems. An accelerated interest in polymer electrolyte fuel cells has led to improvements in both cost and performance. Operation of PEMFC single cells under laboratory conditions similar to transportation or stationary applications have operated for over 20000 hours continuously with degradation rates of 0.7-1.0% per 1000 hours, which approaches the degradation rates needed for stationary applications. Complete fuel cell systems have been demonstrated for a number of transportation applications including public transit buses and passenger automobiles. For stationary applications, a number of demonstration systems have been developed and numerous systems have been installed, mostly in the 2 to 10 kW range. However, although these systems have collectively logged millions of kWhrs, developers have not yet demonstrated system life of more than 8000 hours with realistic catalyst loadings and realistic operating conditions, and then with degradation rates of several percent per 1000 hours. The standard electrolyte material in PEFCs belongs to the fully fluorinated Teflon[®]-based family similar to that produced by E.I. DuPont de Nemours for space application in the mid-1960s. The membrane is characterized by its equivalent weight (inversely proportional to the ion exchange capacity). A typical equivalent weight range is 800 to 1100 milliequivalents per dry gram of polymer. The type used most often in the past was a melt-extruded membrane manufactured by DuPont and sold under the label Nafion[®] 117. The perfluorosulfonic acid family of membranes exhibits exceptionally high chemical and thermal stability, and is stable against chemical attack in strong bases, strong oxidizing and reducing acids, Cl₂, H₂, and O₂ at temperatures up to 125°C (52). Nafion[®] consists of a fluoropolymer backbone, similar to Teflon[®], upon which sulfonic acid groups are chemically bonded (53; 54). Nafion[®] membranes have exhibited long life in selected applications, operating conditions, and electrochemical applications. In selected fuel cell tests and water electrolysis systems, lifetimes of over 50000 hours have been demonstrated.

Due to Nafion[®]'s expense and other engineering issues, new alternative membranes are being developed by a number of different companies. Progress in manufacturing techniques has been made. Although melt-extruded films were the norm, the industry is moving to a solution-cast film process to reduce costs and improve manufacturing throughput efficiency. In this process, the ionic form of the polymer is solubilized in alcoholic solution, such as propanol, and then fabricated into a film of desired thickness. The conversion of the non-

ionic polymer to an ionic phase, ready for use in a fuel cell, is carried out prior to the solubilization step.

Another advancement in membrane technology is that of using an internal support layer to enhance the mechanical strength of the membrane film, especially as the membrane thickness is decreased. The Primea 55 and 56 series membranes manufactured by W.L. Gore are examples of such internally-supported membranes.

The primary concern related to polymer degradation in electrochemical applications is oxidation damage. Unfortunately this phenomenon, while often mentioned, is not well documented in the technical literature to the extent that the fundamental mechanisms can be articulated. Clearly perfluorinated monomers are very stable to oxidation, as evidenced by their >10 years of continuous use in chlor-alkali cells and stability against even fluorine/nitrogen gas mixtures (55).

The excellent chemical and mechanical stability and facile cation transport valued in PEMFC industry is useful for other electrochemical applications. In general, electrolytic processes are preferred economically for production of highly oxidized or reduced products that are difficult to manufacture by chemical routes. For example, a wide range of highly oxidized gases are synthesized industrially using electrolytic processes, including chlorine dioxide, ozone, hydrogen peroxide, fluorine, nitrogen trifluoride, and dinitrogen pentoxide. The advantages of using ionomer membrane-separated processes have been explored for all of these syntheses and commercial membrane-based processes exist in certain cases. These processes utilize cell designs and catalyst layer structures similar in concept to those used in the PEMFC.

In the last few years a number of new anion-exchange polymers (5; 6; 7; 8; 9; 10; 11; 12; 13; 14) have been developed, which offer the possibility of develop Anion-exchange Membrane Fuel Cells (AMFCs) and anion-exchange membrane based electrolyzers (AMEs). The current technologies of Anion Exchange Materials (AMs) for these electrochemical applications, show several limitations relate to the possibility of obtaining a reasonable low cost membrane having: high ionic conductivity, chemical stability in strong alkaline media, low permeability to fuel crossover, low water swelling and good mechanical properties.

1.4.1 Structure and required properties

Typically, the membranes for PEM fuel cells are made of perfluorocarbon-sulfonic acid ionomer (PFSA). This is essentially a copolymer of tetrafluoroethylene (TFE) and various perfluorosulfonate monomers. The best-known membrane material is Nafion[®] made by Dupont, which uses perfluoro-sulfonylfluoride ethyl-propyl-vinyl ether (PSEPVE) as monomer. Figure 28 shows the chemical structure of perfluoro sulfonate ionomer such as Nafion[®].

In presence of water, liquid or vapour, the $-SO_3H$ groups dissociate in SO_3^- ions and H_3O^+ ions, this is why such structure is called ionomer. As a result of electrostatic interactions, these ionic groups tend to aggregate to form tightly packed regions referred to as clusters (56).

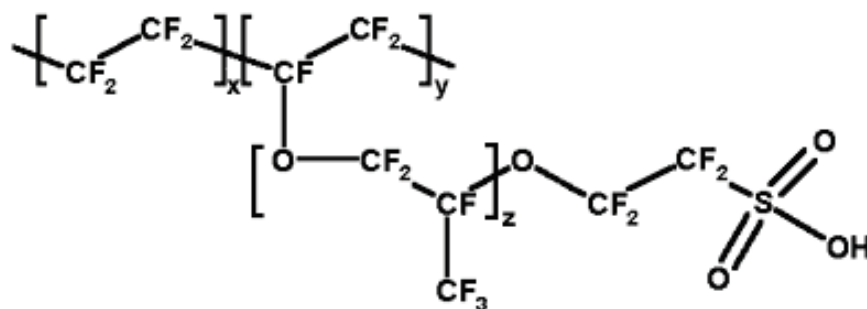


Figure 28. Structure of Nafion® polymer

The presence of these electrostatic interactions between the ions and the ion pairs enhance the intermolecular forces and thereby exert a significant effect on the properties of the parent polymer. Previous small angle x-ray scattering (57) and neutron scattering experiments clearly indicate that ionic clustering is present in Nafion®. However, details on the arrangement of matter within these clusters have not fully been realized. Although no one model has been found to provide a complete explanation of the properties and selectivities found, several, base these properties and selectivities on an extensive microphase separated morphology (56; 58). A stylized, semi-empirical view of a polar/nonpolar microphase separation in a hydrated ionomer can be seen below in Figure 29.

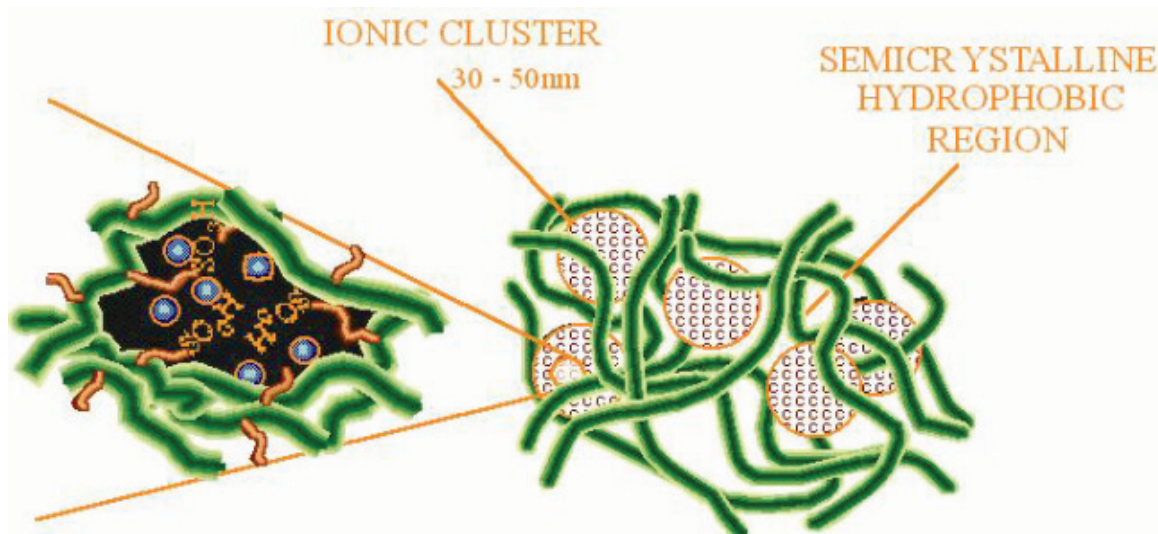


Figure 29. Stylized view of polar/nonpolar microphase separation in a hydrated ionomer

This over-simplification shows a phase separated morphology of discrete hydrophobic and hydrophilic regions. The hydrophobic region is composed of the polymer fluorocarbon backbone. Conversely, the hydrophilic region contains the ionic groups and their counter ions. From experimental means, such as, small-angle x-ray scattering (SAXS) it has been determined that the phase-separated morphology is on the order of 30-50 Å Bragg spacing (59). However, upon hydration, Nafion® with its unique ability to sorb relatively large amounts of water, can increase its dry weight by as much as 50 percent or more depending upon equivalent weight, counter ion, and temperature. Upon hydration, however, cluster diameter and the number of exchange sites are thought to increase, leading to fewer, larger clusters.

An ionomeric membrane must exhibit relatively high ion conductivity, must present an adequate barrier to mixing of fuel and reactant gases, and must be chemically and mechanically stable in the electrochemical device environment (60).

In order to grant suitable ionic conduction and mechanical stability both hydrophobic and hydrophilic regions are required. A common procedure to synthesize ion-exchange materials consists in the chemical modification of a commercial polymer via free-radical graft copolymerization with polar monomers. Consequently an anion exchange polymer for electrochemical applications should have the structure reported in Figure 30. Choice of the polymeric backbone and grafting monomer in order to improve the AM properties will be discussed in the next section.

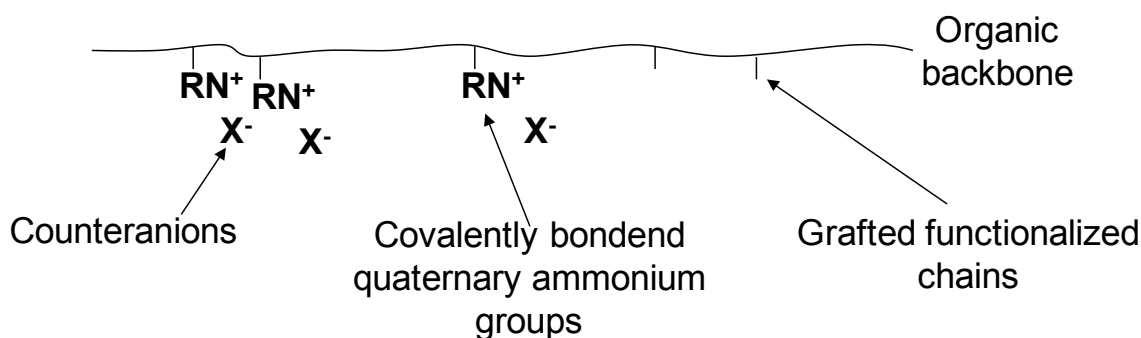


Figure 30. Anion-exchange polymer structure schematic

Key properties for these materials are the ion exchange capacity (IEC), the water uptake (WU) and the ionic conductivity (σ). On the following subsections these properties will be discussed, focusing on cation-exchange ionomers for PEMFCs (for which a vast literature is available).

Ion Exchange Capacity (IEC)

The capacity of an ion exchange polymer is defined as the number of chemical equivalents available for exchange per unit weight or unit volume of resin. The IEC is practically a measure of ionic concentration within the ionomer, usually expressed in terms of milliequivalents of ion exchange groups (IEGs) per dry gram of polymer ($\text{meq}_{\text{IEG}}/\text{g}_{\text{dry}}$) or in terms of milliequivalents of IEGs per milliliter of swollen polymer ($\text{meq}_{\text{IEG}}/\text{mL}_{\text{wet}}$). Another way for expressing the IEC is the equivalent weight (EW) expressed as dry grams of polymer per IEG equivalent.

Water Uptake (WU)

The ionic conductivity of a polymer membrane is strongly dependent on membrane structure and its water content. The water content in membrane is usually expressed as grams of water per gram of polymer dry weight, or as number of water molecules per ion exchange groups present in the polymer (λ). The maximum amount of water in the membrane strongly depends on the state of water used to equilibrate the membrane. It has been noticed that a Nafion® membrane equilibrated with liquid water takes roughly up to 22 water molecules per sulfonate group, whereas the maximum water uptake from the vapor phase is only about 14 water molecules per sulfonate group. In addition, water uptake from

the liquid phase is dependent on the membrane pretreatment. Zawodzinski et al (54) have shown that water uptake after the membrane had been completely dried out at 105°C is significantly smaller than if the membrane had been dried out at room temperature. This may be explained by the polymer morphological changes at elevated temperature. Indeed, for an experimental Dow® membrane, which has somewhat higher glass transition temperature than Nafion®, the effect of drying the membrane at 105°C is less pronounced than for Nafion® membrane. The shape of a generic isotherm for ion-exchange polymers is shown in Figure 31. It may be noticed that there are two distinct steps in water sorption from the gas phase, namely:

- At low vapor activity ($a_{\text{H}_2\text{O}}=0.15-0.75$), water uptake increases to about $\lambda = 5$;
- At high relative humidity ($a_{\text{H}_2\text{O}}=0.75-1.0$), water uptake increases sharply to about $\lambda = 14.4$.

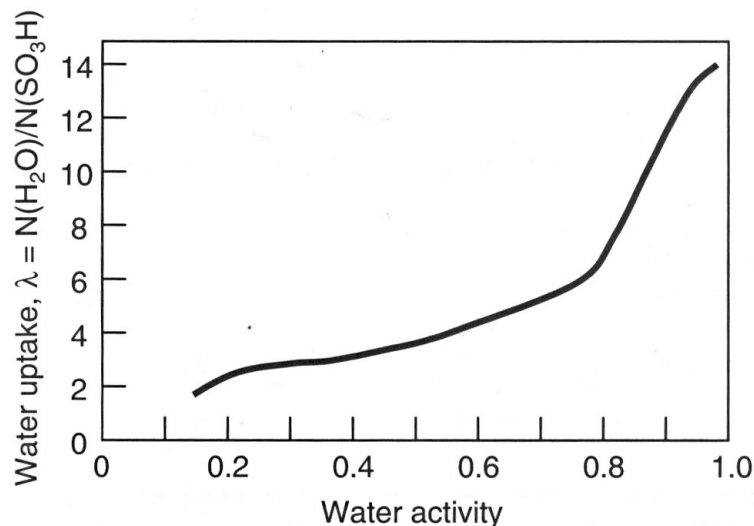


Figure 31. Water uptake in proton conductive membranes at 30°C (54)

The first step corresponds to uptake of water by solvation by the ions in the membrane, whereas the second step corresponds to water that fills the pores and swells the polymer. It is important to notice that the resulting water uptake from the fully saturated vapor phase ($a_{\text{H}_2\text{O}}=1$) is significantly lower than that from the liquid phase (also $a_{\text{H}_2\text{O}}=1$), that is, $\lambda = 14$ versus $\lambda = 22$, respectively. This phenomenon was first reported in 1903 by Schroeder, and is therefore called Schroeder's paradox (60). A possible explanation of this difference in uptake from vapor and liquid phases is that sorption from the vapor phase involves condensation of water inside the polymer, most probably on the strongly hydrophobic polymer backbone, and the resulting uptake is lower than if sorption and imbibitions occurred directly from the liquid phase (60).

Water uptake results in the membrane swelling and changes its dimensions, which is a very significant factor for fuel cell design and assembly. For Nafion® the dimensional changes are in the order of magnitude of 10%, which must be taken into account in cell design and during the installation of the membrane in the cell. In 1995, W.L. Gore and Associates, Inc. introduced the Gore-Selected membrane, a new microreinforced expanded

polytetrafluoroethylene (ePTFE) polymer electrolyte membrane targeted specifically toward PEMFC applications (61). The microreinforcements allow Fore-Select membranes to utilize ionomers that do not have sufficient mechanical properties. These membranes exhibit much higher strength, better dimensional stability, lower gas permeability, and higher conductivity than comparable nonreinforced Nafion® membranes.

Ionic conductivity

Ion conductivity is the most important function of the polymer membranes used in electrochemical applications in order to reduce ohmic overpotential, as shown in equation (1.99). Ionic conductivity is most frequently measured from alternating current impedance of a standard cell design as described in the experimental section. The charge carrier density in a Nafion® membrane of EW 1100 is similar to that in a 1M aqueous sulfuric acid solution. Remarkably, hydronium mobility in a fully hydrated membrane is only one order of magnitude lower than the hydronium mobility in aqueous sulfuric acid solution. As a result, the hydronium conductivity of fully hydrated membrane is about 0.1 S/cm at room temperature. The conductivity of PFSA membranes is a strong function of water content: for $\lambda > 5$, the relationship between water content and protonic conductivity is almost linear, on the contrary, when $\lambda < 5$ there is not enough water in the clusters around the ends of the sulphonated side chains needed for dissociation of sulphonic acid groups. Zawadzinski (62) has suggested that there are several possible ways of ionic conductivity of Nafion®-like materials (Figure 32):

- At very low water contents ($\lambda \sim 2 - 4$), hydronium ions move via vehicle mechanism;
- As the water content increases ($\lambda \sim 5 - 14$), easier movements of hydronium ions is facilitated;
- At fully hydrated membranes ($\lambda > 14$), water in interfacial regions screens weakly bound water from ion-dipole interactions, and both water and ions move freely.

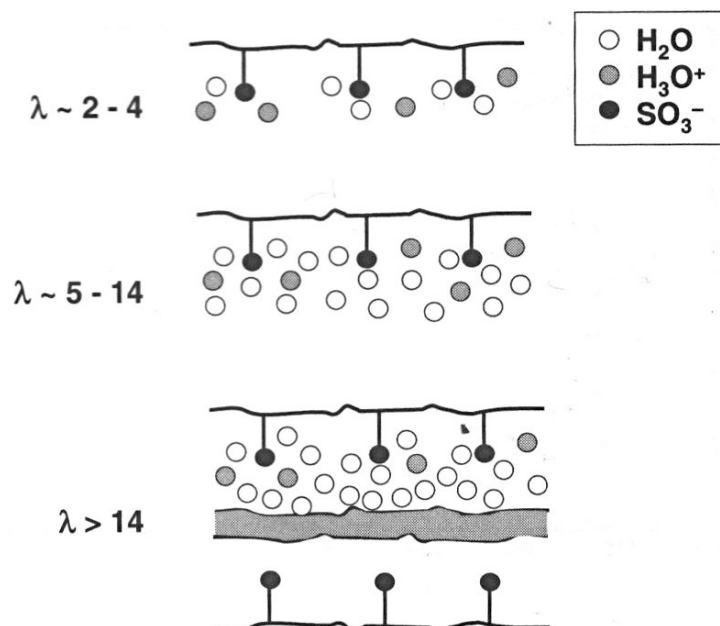


Figure 32. Mechanisms of water and hydronium ions movement through PFSA ionomer at various hydration levels, as suggested by Zawadzinski (62)

1.4.2 Design rules

Assuming the necessity of at least some water within the membrane for ion transport, and an operation temperature below 100 °C, which does allow the presence of water, it is reasonable to assume that the membranes with the best property profile will be those that “use” the water present most efficiently for ion transport. Such membranes will lose less ionic conductivity than others on decreasing relative humidity. They will also need less water for the same ionic conductivity, allowing for less swelling in the presence of liquid water, and hence less problems with mechanical durability.

H₂/O₂ fuel cells produce water, which will be present in the liquid state at temperatures below 100 °C, liquid water is also present in water electrolyzer. Thus, the membrane will be in contact with liquid water in these electrochemical applications. High water uptake and a large degree of swelling of the membrane are detrimental to its lifetime. Solubility of the membrane material in water at operating temperatures would of course be catastrophic.

On the other hand, as long as the ionic transport is based on the presence of water within the membrane and the charge carriers in the membrane are created by hydrolytic dissociation of acidic/basic groups, high ionic conductivity requires a sufficient water content of the membrane. Increasing the number of ion-exchange groups (i.e. the IEC) increases the ionic conductivity not only under fully hydrated conditions but also under dry conditions, because the membrane takes up and retains more water. At very high IEC values, the membrane materials may become water soluble. Obviously, there is a conflict between the desire for high proton conductivity, which can be achieved by a high IEC of the membrane, and the need for low water uptake and swelling, which is necessary for durability.

As discussed in the previous section both hydrophobic and hydrophilic regions are required in order to grant suitable ionic conduction and mechanical stability, i.e. the ionomeric material must be a copolymer of an hydrophobic and hydrophilic monomers. Morphology of the copolymer greatly influences the final properties of the ionomeric materials. Polymer morphology depends on the copolymer type (random or block copolymer), whether the charge is distributed on the main chain or in side chains (linear or branched copolymer) and the starting monomers hydrophobicity. On the following subsections these effects will be discussed.

Block vs. random copolymers

The requirements of a high IEC for high ionic conductivity on one side and a low IEC for good mechanical properties and low water uptake on the other side can be separated: hydrophilic and hydrophobic segments can be combined in a block copolymer. Microphase separation, which is typical for block copolymers, creates a situation in which there are hydrophilic domains formed by aggregation of ion-exchange groups (IEGs) containing chain segments and hydrophobic domains formed by aggregation of the neutral segments. The hydrophilic domains can serve as transport pathways for the ions, while the hydrophobic domains take care of the mechanical properties. Thus, the ionic transport can occur through domains with a very high local concentration of IEGs, a concentration that would make

random copolymers water soluble. In block copolymers, the formation of the hydrophobic domains prevents water solubility. Therefore, much higher IEC values can be utilized than that in conventional polymers.

In literature (63; 64; 65; 66) comparisons of the ionic conductivities and their dependence on relative humidity for membranes from block copolymers and random copolymers of similar overall composition confirm that the block copolymer membranes exhibit higher proton conductivity at comparable global IEC.

Linear vs. branched copolymers

It has been argued frequently in the literature that Nafion[®] owes its good hydronium conductivity at relatively low water uptake to its morphology (24; 54; 67). This morphology is based on Nafion[®]'s molecular structure (Figure 28): the strongly polar sulfonic acid groups are immiscible with the nonpolar fluorocarbon backbone and tend to aggregate. This is clearly facilitated by their rather flexible attachment via side chains: the acidic groups can move rather independently of the polymer main chain or backbone. Most hydrocarbon membranes, especially the fully aromatic ones, possess sulfonic acid groups (or acid groups in general), which are directly attached to the phenyl rings of the polymer backbone. These acidic groups cannot aggregate as freely as those of Nafion[®], because for a group attached in this way, a segment of the polymer backbone needs to move, and not just an independent side chain. Thus, aggregation can occur only under conditions where the whole polymer backbone is mobile enough. Also, there will always be a trade-off between the relaxed coil shape of the polymer backbone and a strained shape of the backbone, which is required to allow aggregation of the acidic groups. There is no doubt that this impedes aggregation of the acidic groups, and hence the formation of "proton transport channels" as discussed for Nafion[®]. Clearly, attaching the acidic groups to the backbone via side chains can be expected to be beneficial. However, the chemical stability of the structures involved (hydrolytic stability, stability against oxidation, and reduction) should be taken into consideration in the interest of longevity of the membranes.

In literature (68) the conductivities of membranes from two polymers, which are built from very similar building blocks, are compared: a sulfonated polyetheretherketone (S-PEEK) and a sulfonated polyparaphenylene derivative (S-PPBP).

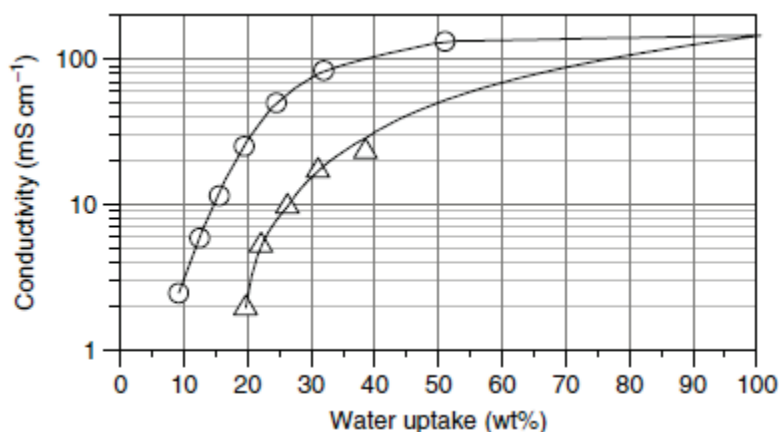


Figure 33. Side chain(circles) versus main chain(triangles) sulfonated polyimide membranes (68)

They are almost isomers of each other, but for the additional ether bridge in the S-PEEK. In the S-PEEK, the sulfonic acid groups are attached to phenyl rings in the backbone, while in the S-PPBP, the sulfonic acid groups are attached to the phenoxybenzoyl side chain. As clearly seen in Figure 33, the side chain sulfonated polymer membranes exhibit a significantly higher proton conductivity at the same water uptake.

Hydrophobicity

Block copolymers prepared by polycondensation procedures typically leads to broad molecular weight distributions, following the Schulz–Flory distribution rather than the Poisson distribution. As a result, there will be block copolymers that contain very short hydrophilic segments linked to long hydrophobic segments. Even though microphase separation takes place, these very short segments are probably not going to be able to leave the hydrophobic phase completely owing to restricted motion, which originates from their chemical link to the hydrophobic chain segments. As a consequence, there will always be a few hydrophilic segments, and hence ion-exchange groups present in the hydrophobic domains (69). These acid groups will bind some water, which is likely to add to the overall swelling of the membrane, but is not available for ionic transport in the hydrophilic phase. This will reduce the ionic conductivity and the “water efficiency” of the membrane. Therefore block copolymer membranes should be most efficient when their hydrophobic segments are as hydrophobic as possible and when the microphase separation is as complete as possible, only then the highest fraction of the absorbed water will be available in the hydrophilic domains for the actual ionic transport.

In literature (68) a comparison of the conductivities of multiblock copolymer membranes with identical hydrophilic blocks but with different hydrophobic segments shows that the conductivity increases significantly with increasing fluorine content (i.e. higher hydrophobicity) of the hydrophobic blocks.

2 Experimental

2.1 Instrumentation

FT-IR spectroscopy

FT-IR spectra were collected using a Perkin Elmer Spectrum One spectrometer. Polymer spectra were collected on films casted from a chloroform solution on a KBr plate. Since poly(vinylbenzyl chloride) (PVBC) films are brittle, FT-IR analysis was performed on pellets obtained compressing a powder mixture between samples and KBr. In order to study films morphology, spatially resolved FT-IR analysis were also performed using a Perkin Elmer GX FT-IR spectrometer coupled with a Perkin-Elmer Autoimage microscopy.

¹H-NMR spectroscopy

¹H-NMR spectra were collected using a Varian Gemini-200 spectrometer operating at 200 MHz and 25 °C. Samples were dissolved in deuterated chloroform (CDCl₃) and analyzed in 5 mm NMR tubes. Solvent signal (7.26 ppm) was used as internal reference.

¹³C-NMR spectroscopy

¹³C-NMR spectra were collected using a Varian Gemini-300 spectrometer operating at 300 MHz and 25°C. Samples were dissolved in deuterated chloroform (CDCl₃) and analyzed in 5 mm NMR tubes. Solvent signal (77.2 ppm) was used as internal reference.

Differential scanning calorimetry (DSC)

DSC analysis were performed using a Mettler-Toledo 822e calorimeter. Samples were pretreated heating a small amount (11-16 mg) from ambient temperature up to 200°C at 10°C/min and then cooled up to -120°C at -20°C/min and maintained at this temperature for 10 min. DSC analysis was therefore performed heating from -120°C up to 200°C at 10°C/min in order to calculate glass transition temperatures (T_g). Nitrogen was flowed at 80 mL/min in all the experiments.

Thermogravimetric analysis (TGA)

TGA analysis were performed using a Mettler-Toledo TGA/STDA851 thermobalance. Samples were heated from ambient temperature up to 700°C at 10°C/min. Nitrogen was flowed in all the experiments.

Elemental analysis (EA)

EA analysis were performed at the faculty of Pharmacy analytical laboratory of the University of Pisa, determining content percentage of Carbon, Hydrogen, Nitrogen and Chlorine on polymeric samples.

Gel permeation chromatography (GPC)

GPC analysis were performed using a chromatograph equipped with two Polymer Laboratories PLgel 5µm Mixed-d gel columns connected in series, a Jasco PU-1580 HPLC

pump, a Perkin-Elmer LC-75 UV/Visible detector and a Jasco 830-RI refractive index detector. Polymeric samples (4mg) were dissolved in 1mL of chloroform, filtered on 0.2 μm Teflon filters and collected on nitrogen purged tubes prior to injection. Calibration was performed using monodispersed polystyrene standards.

Scanning electron microscopy (SEM)

SEM analysis were performed at the faculty of Engineering Metal Science laboratory of the University of Pisa using a Joel JSM 5600-LV microscope equipped with a Oxford Instruments X-ray EDS microanalysis detector.

Electrochemical impedance spectroscopy (EIS)

EIS analysis were performed using a Bio-Logic SA VMP3 multi-channel potentiostat/galvanostat equipped with an impedance channel and a 4 Amps current booster.

Anion-exchange Membrane Fuel Cell (AMFC) tests

Cells were assembled using 5 cm^2 stainless steel single cell hardware from Fuel Cell Technologies and Membrane Electrode Assemblies (MEAs) prepared as described later on this section. Pt/C based electrodes were used on the anode side, whereas Pt/C or Platinum Group Metals (PGM) free catalysts from ACTA based electrodes were used on the cathode side. PTFE gasket thickness was selected to obtained an overall strain of $\approx 25\%$ to guarantee good electrical contact and sealing. H_2 and O_2 (purity of N5.0) were provided by Sol. Gas flows, humidification, temperature and cell temperature were controlled using a Scribner 850C test station. MEAs were conditioned by cycling between OCV and 200 mV cell potential for 15 minutes/step (Arbin BT-2000), till stable performance between two cycles was observed. Polarization curves were collected applying 3 minutes long constant voltage steps in 50 mV intervals, recording the last 30 seconds, from OCV to 200 mV.

2.2 Solvents and chemicals

On the following table common solvents and chemicals used without further purification are reported:

	Supplier	Purity [wt%]
Methanol	J.T. Backer	99.8
Chloroform	J.T. Backer	99.0
Acetone	Carlo Erba	99.8
Diethyl ether	Aldrich	99.7
Potassium hydroxide	Carlo Erba	98.0
Sodium hydroxide	Carlo Erba	98.0
Potassium carbonate	Carlo Erba	98.0
1-propanol	J.T. Backer	99.8
Trimethylamine water solution	Aldrich	45.0
1,4-diazabicyclo[2.2.2]octane	Aldrich	98.0

Table 6. Commonly used solvents and chemical specifications

2.2.1 Styrene-butadiene-styrene copolymer (SBS)

SBS block copolymer supplied by Softer s.p.a. (Calprene 501) has the following specifications:

Parameter	Value
Blocks average molecular weight [amu]	9300-41400-9300
Polydispersity index	1.5
Density [g/cm ³]	0.9
Styrenic percentage [mol%]	26
1,2-butadienic percentage [mol%]	11
1,4-butadienic percentage [mol%]	63

Table 7. Softer s.p.a. Calprene 501 specifications

The polymer was purified by means of precipitation on methanol of a chloroform solution of the polymer followed by Büchner filtration and vacuum drying. The purification was performed twice in order to remove stabilizers. Purified SBS was characterized by means of FT-IR, ¹H-NMR, ¹³C-NMR, GPC, EA, DSC and TGA.

FT-IR wavenumbers [cm⁻¹]: 3000-3100 (ν aromatic C-H); 1640 (ν butadienic C=C); 1380-1600 (ν aromatic C=C); 1601, 1493 and 1452 cm⁻¹ (ν aromatic rings); 1463 (δ_s CH₂); 1418 (δ =CH₂-); 994 and 911(δ vinylic C-C-H); 966 (δ internal C=C); 830 (out of plane δ aromatic C-H); 757 and 699 (δ_{as} aromatic C-H).

¹H-NMR (CDCl₃):

δ [ppm]	Hydrogen atoms
1.3-2.1	
4.8-5.1	
5.3-5.5	
6.3-7.2	

Table 8. Purified Calprene 501 SBS ¹H-NMR chemical shifts (δ)

¹³C-NMR:


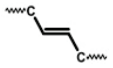
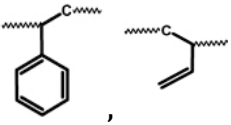
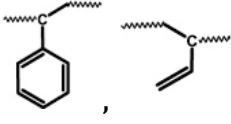
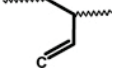
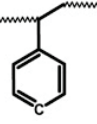
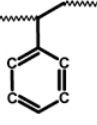
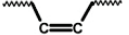
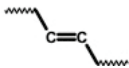
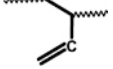
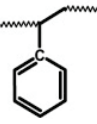
δ [ppm]	Carbon atoms
27.0	
32.5	
40.0-40.7	
43.0-43.9	
113.1-115.2	
124.9-126.0	
127.0-128.5	
129.2-129.7	
129.9-130.3	
142.3-143.2	
144.5-146.5	

Table 9. Purified Calprene 501 SBS ¹³C-NMR chemical shifts (δ)

GPC [amu]: Two peaks are detected. Main peak (99% area ratio), relative to SBS triblock copolymer, show a weight average molecular weight $\overline{M}_w = 220800$ and number average molecular weight $\overline{M}_n = 216300$. Second peak (1% area ratio), relative to SB diblock copolymer impurity, show a weight average molecular weight $\overline{M}_w = 74800$ and number average molecular weight $\overline{M}_n = 74400$.

EA [wt%]: Carbon 89.6, Hydrogen 10.4

DSC: Two glass transition temperatures are detected. Lower T_g at -87°C is relative to the butadienic block. Higher T_g at 69°C is relative to styrenic blocks.

TGA: Degradation temperature (T_d) at 430°C .

2.2.2 Vinylbenzyl chloride (VBC)

VBC supplied by Aldrich (98% purity) is shipped with two stabilizers that need to be removed:

- 1) 4-tert-butylcatechol (≥ 10 ppm), added to prevent oxygen oxidation and subsequent radical promoted crosslinking;
- 2) Nitromethane (≥ 500 ppm), added to prevent Friedel-Craft reactions.

In order to remove stabilizers 60 mL of VBC were washed twice with 25 mL of a NaOH water solution (25 wt%), the two immiscible phases were then separated using a separatory funnel. Organic phase is then neutralized and vacuum distilled in a Claisen tube (1 mmHg, 59°C). Purified VBC is then stored at -20°C in a nitrogen atmosphere.

2.2.3 1-Methylimidazole

The chemical supplied by Aldrich (99% purity) is purified by vacuum distillation (35 mmHg) and stored at room temperature.

2.2.4 α,α' -azo-bis-isobutyronitrile (AIBN)

The chemical supplied by Aldrich (98% purity) is purified by recrystallization from methanol, dried and stored at -20°C .

2.2.5 Benzoyl peroxide (BPO)

The chemical supplied by Aldrich (70% purity) is purified by recrystallization from methanol, dried and stored at -20°C .

2.3 VBC grafted SBS copolymer (SBS-g-VBC)

2.3.1 Grafting reaction

Synthesis were conducted in a three-neck polymer cylindrical reactor equipped with a mechanical stirrer and a Teflon paddle. Reactor was connected to a Schlenk line (vacuum/nitrogen). Purified SBS (2g) was added to the reaction vessel, followed by 8mL purified VBC addition against a flow of inert gas (N₂). Reactor was then heated at 80°C by means of a vertex controlled oil bath and stirred until complete dissolution of the SBS copolymer. Heating was then switched off until room temperature is reached.

In the meanwhile a certain amount of initiator (see Table 19) was added in a Schlenk tube together with 1.2 mL of purified VBC under nitrogen flow. After sealing, initiator was dissolved at 0°C in an ice bath. VBC dissolved initiator was then added to the reaction vessel at room temperature under nitrogen flow using a glass syringe connected to a silicone tube, taking care to keep the silicone tube end close to the inner solution surface. At this point 9.2 mL of VBC were added to the reactor, having a VBC to polymer weight ratio of 5. Initiator added reactants were then heated at 80°C, by means of a vertex controlled oil bath, under nitrogen atmosphere and stirring speed of 250 rpm; reaction was carried out under these conditions for 2h.

Since after few minutes viscosity of the reacting solution start to increase, stirring speed was reduced in order to ensure an homogeneous mixing. After 2h reaction was stopped cooling the reactor at room temperature and adding 80 mL of a chloroform solution where 7g of 2,6-di-tert-butyl-p-cresol (BHT), a radical inhibitor, were previously dissolved. Reacted solution was stirred at room temperature for 12 h in order to quench left-over free-radicals. Quenched solution was then filtered on a porous septum in order to remove solid particles traces, mainly consisting in crosslinked SBS.

Products (grafted SBS, unreacted SBS and VBC homopolymer) were then precipitated in methanol and filtered on a Büchner funnel. Filtered products were then redissolved in chloroform, reprecipitated in methanol and filtered again on Büchner funnel. Filtered and purified products were then dried under vacuum until a constant weight was obtained.

On Table 19 are reported all the batches with respective initiator type and amounts.

2.3.2 SBS-g-VBC extraction and purification

In order to separate SBS-g-VBC grafted copolymer from poly(vinylbenzyl chloride) (PVBC) homopolymer byproduct a two steps extraction was performed.

First step consists on dissolving in chloroform previously purified products mixture and dropwise addition of the solution on a magnetic stirred acetone containing flask. After all the chloroform solution was added to the flask, stirring was switched off and the mixture was left to settle for 12h. Afterwards mixture was centrifuged in order to separate solid fraction, consisting on grafted and unreacted SBS copolymer, from solubilized fraction, consisting on PVBC homopolymer. Residual fraction is dried at room temperature at open air and then

under vacuum. Dried residual fraction is then dissolved in chloroform and casted on a PTFE Petri dish under chloroform saturated atmosphere, obtaining a $\approx 100 \mu\text{m}$ thick film.

Second purification step consists on a acetone extraction of the dried film, previously cut in narrow strips, conducted in a Kumagawa extractor for 6h, in order to remove PVBC traces left from the previous purification step.

Purified residual product was then dried under vacuum and stored in polyethylene container inside a laboratory dryer on a dark environment. Extracted phases coming from first and second steps purification were collected and dried under vacuum in order to be characterized.

Residual and extracted phases will be labeled preceding batch name respectively by "R-" and "E-" prefixes (e.g. R-SBS-F7 refers to the residual phase of the SBS-F7 batch).

Residual phases characterization

FT-IR wavenumbers [cm^{-1}]: 3000-3100 (ν aromatic C-H); 1640 (ν butadienic C=C); 1380-1600 (ν aromatic C=C); 1601, 1493 and 1452 cm^{-1} (ν aromatic rings); 1463 (δ_s CH_2); 1418 (δ $=\text{CH}_2$ -); 1265 (δ_w $\text{CH}_2\text{-Cl}$); 994 and 911 (δ vinylic C-C-H); 966 (δ internal C=C); 830 (out of plane δ aromatic C-H); 757 and 699 (δ_{as} aromatic C-H); 675 (ν C-Cl).

$^1\text{H-NMR}$ (CDCl_3):

δ (ppm)	Hydrogen atoms
1.5-1.9	
4.5	
5.0	
5.5	
6.3-7.2	

Table 10. Residual phases $^1\text{H-NMR}$ chemical shifts (δ)

¹³C-NMR:


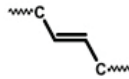
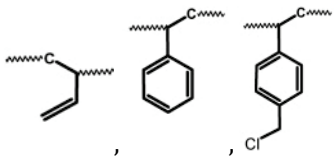
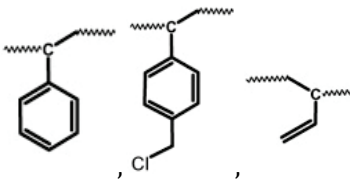
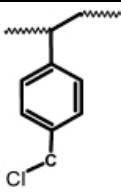
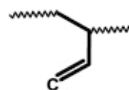
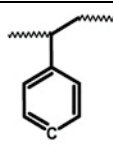
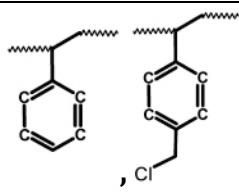
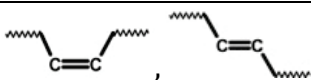
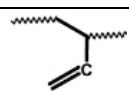
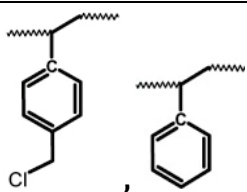
δ (ppm)	Carbon atoms
27.0	
32.9	
40.0-41.0	
43.5-44.0	
46.0-46.5	
114.0-114.2	
125.5-126.0	
127.5-128.2	
129.0-130.4	
142.5-143.0	
145.2-145.8	

Table 11. Residual phases ¹³C-NMR chemical shifts (δ)

GPC [amu]: Chromatogram analysis will be performed on Section 3.2.1, on the next table results for residual phases are reported.

	R-SBS-F7	R-SBS-F9	R-SBS-F10	R-SBS-F12	R-SBS-F13	R-SBS-F14	R-SBS-F15	R-SBS-F17
Area % 1 st peak	1.1	1.1	2.3	2.2	1.7	1.1	2.2	1.2
Mw 1 st peak	78000	78700	102900	101200	91100	75800	85900	94700
Mn 1 st peak	70500	69800	51300	51900	71800	70400	55500	62900
ID 1 st peak	1.1	1.1	2.0	2.0	1.3	1.1	1.6	1.5
Area % 2 nd peak	45.5	45.2	43.7	55.0	53.4	47.3	47.9	58.1
Mw 2 nd peak	225300	230800	232800	260800	236700	250800	228200	259600
Mn 2 nd peak	219100	222400	225600	246500	220000	244700	205200	245600
ID 2 nd peak	1.0	1.0	1.0	1.1	1.1	1.0	1.1	1.1
Area % 3 rd peak	53.4	53.7	54.0	42.8	44.9	51.6	49.9	40.7
Mw 3 rd peak	368500	399100	382800	465500	449000	438500	426000	472100
Mn 3 rd peak	166300	191900	179600	250300	230100	212700	182900	228700
ID 3 rd peak	2.2	2.1	2.1	1.9	2.0	2.1	2.3	2.1

Table 12. Weight average molecular weights obtained for some residual phases by deconvolution analysis of GPC chromatograms

TGA: Degradation temperature (T_d) between 445°C and 455°C.

EA [wt%]: Carbon, hydrogen and chlorine percentage was determined by elemental analysis for some residual phases and are reported on the following table:

	C [wt%]	H [wt%]	Cl [wt%]
R-SBS-F13	88.2	9.3	3.2
R-SBS-F15	86.6	9.3	4.1
R-SBS-F23	87.5	8.0	4.5

Table 13. Elemental composition of some residual phases

Extracted phases characterization

FT-IR wavenumbers [cm^{-1}]: 3000-3100 (ν aromatic C-H); 1380-1600 (ν aromatic C=C); 1265 (δ_w CH₂-Cl); 830 (out of plane δ aromatic C-H); 675 (ν C-Cl).

¹H-NMR (CDCl₃):

δ (ppm)	Hydrogen atoms
1.3-2.2	
4.5	
6.0-8.0	

Table 14. Extracted phases ¹H-NMR chemical shifts (δ)**¹³C-NMR:**

δ (ppm)	Carbon atoms
40.0-41.0	
43.5-44.0	
46.0-46.5	
127.5-128.2	
145.2-145.8	

Table 15. Extracted phases ¹³C-NMR chemical shifts (δ)

GPC:

BPO initiator						
Batch	E-SBS-F7	E-SBS-F12	E-SBS-F17	E-SBS-F20	E-SBS-F24	E-SBS-F25
initiator [%]	0.46	0.8	0.6	0.9	0.7	0.5
Mw [amu]	33500	60900	69500	88300	114700	126600
Mn [amu]	19800	35500	38300	50000	67300	74800
ID	1.7	1.7	1.8	1.8	1.7	1.7

AIBN initiator			
Batch	E-SBS-F19	E-SBS-F18	E-SBS-F21
initiator [%]	0.4	0.6	0.8
Mw [amu]	106700	104000	110900
Mn [amu]	49800	47500	55800
ID	2.1	2.2	2.0

Table 16. Extracted phases GPC analysis**2.3.3 SBS-g-VBC film casting**

Purified residual phase (≈ 800 mg) was dissolved in 60mL of chloroform in a flask at room temperature. The solution was poured in a glass Petri dish (9 cm diameter) and moved in a chloroform saturated chamber left to evaporate at room temperature, obtaining a casted film (100-150 μm thickness).

2.4 SBS-g-VBC quaternization

Residual phases casted films were quaternized with a tertiary amine in order to convert chloromethylene groups in quaternary ammonium salts. DABCO, trimethyl amine and 1-methylimidazole were used as tertiary amines.

Quaternization reaction was performed in a flask equipped with a Allihn condenser and heated with a vertex controlled oil bath. Polymer film was soaked in 100 mL of methanol solution of the envisaged tertiary amine. Reaction was carried out at 60°C for 72h.

FT-IR wavenumbers [cm^{-1}]: 3000-3100 (ν aromatic C-H); 1640 (ν butadienic C=C); 1380-1600 (ν aromatic C=C); 1601, 1493 and 1452 cm^{-1} (ν aromatic rings); 1463 (δ_s CH₂); 1418 (δ =CH₂-); 994 and 911 (δ vinylic C-C-H); 966 (δ internal C=C); 830 (out of plane δ aromatic C-H); 757 and 699 (δ_{as} aromatic C-H); 1456 (δ_s N-C-H); 1313 (δ_w N-C-H); 1058 (ν_s C-N).

$^1\text{H-NMR}$ (CDCl_3):

δ (ppm)	Hydrogen atoms
1.5-1.9	
3.5	
5.0	
5.5	
6.3-7.2	

2.5 Ion-exchange materials characterization

Deionized liquid water ($\rho \geq 10 \text{M}\Omega \cdot \text{cm}$) was used in all experiments. A multi-channel potentiostat/galvanostat, having an impedance channel and a 4A current booster (VMP3 from Bio-Logic SA) was used to perform electrochemical impedance spectroscopy measurements. Water Uptake, Ionic Exchange Capacity, in-plane and through-plane conductivities were also measured for Nafion[®] 115, serving as benchmark for cation-exchange materials, and using 0.5M H_2SO_4 in place of KOH to exchange to the H-form; Nafion[®] ionomer bonded Pt/C electrodes were used in this case for through-plane conductivity measurements.

2.5.1 Ion-exchange capacity (IEC)

The IEC of anion-exchange materials (AM) was determined by acid-base back-titration: an AM piece was pretreated in 1M KOH at 50°C for 1h in order to exchange to the OH-form, the piece was then washed under exclusion of air using N_2 -degassed water and soaked for 30 min in a exact amount of a standardized HCl solution, where OH^- (the counteranion of the ion-exchange groups, IEGs) is neutralized. Excess of HCl was backtitrated with standardized KOH using visual or potentiometric end-point detection.

2.5.2 Water uptake (WU)

A tailed flask containing continuously N₂-degassed water was used. The temperature control was ensured using a thermostatic oil bath and the weight of an AM piece (either a membrane or the ionomer cast as membrane) was determined by a four-digits analytical balance. Dry weight of the AM piece was measured after 24h equilibration at 60°C in an oven. The AM was pretreated in 1M KOH (or 1M KCl) at 50°C for 1h in order to exchange it into the OH-form (Cl-form). Wet weight values were measured after 30 min equilibration in the tailed flask at the envisaged temperature. The water uptake, as mass percentage, was calculated using the following equation:

$$WU(\text{wt}\%) = \frac{W_{\text{wet}} - W_{\text{dry}}}{W_{\text{dry}}} \cdot 100 \quad (2.1)$$

where W_{wet} and W_{dry} are the wet and dry AM piece weight, respectively, averaged over 3 measurements, at each temperature.

2.5.3 Ionic conductivity

In-plane conductivity (σ_{IP})

In-plane conductivity was measured using a Bekttech PTFE 4-probe flow-cell, assembled with a 5 cm² cell hardware supplied by Fuel Cell Technologies, allowing in-situ AM exchange to the OH-form (Cl-form) flowing a 1M KOH (or 1M KCl) solution. This was followed by removal of the excess electrolyte via a continuous flow of N₂-degassed water, such that the AM cannot get contaminated by bicarbonate ions which are present in air-exposed deionized water. Figure 34 (a) shows a typical Nyquist plot obtained for such measurements: the high-frequency arc represents a parallel RC circuit coming from membrane bulk resistance and capacitance, while the low-frequency arc is an artifact coming from Pt-wire/AM interfacial impedance (70). AM resistance was calculated by fitting the impedance data to an RC circuit between 100 kHz and 10 kHz (i.e. before the low-frequency arc) to prevent artifacts.

Through-plane conductivity (σ_{TP})

Through-plane conductivity was measured using a 5 cm² cell hardware supplied by Fuel Cell Technology allowing in-situ ion exchange, analogous to the in-plane tests, again carefully avoiding air exposure of the AM materials. Pt based anion-exchange ionomer based membrane electrode assemblies (MEAs), prepared as described later on this section, were used. Figure 34 (b) shows a typical Nyquist Plot obtained for such measurements: at high frequency, a transmission line shows up (i.e., a 45° line), coming from the ionic resistance of the electrode, while at low frequencies the graph approaches a vertical line, due to the electrode capacitance. The contact resistance was measured using a cell assembled without the membrane ($R_{\text{contact}} \approx 5\text{m}\Omega$). Membrane resistance was calculated extrapolating the 45° line to the real axes and subtracting the measured contact resistance.

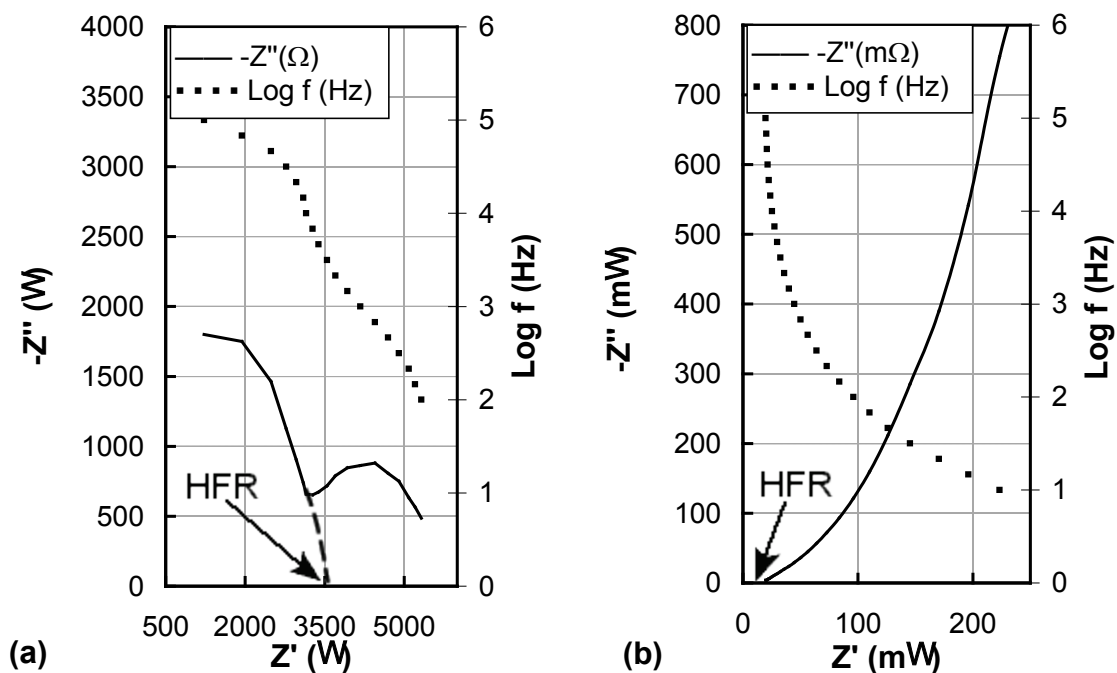


Figure 34. (a) 4-probe impedance spectra for an in-plane conductivity measurement, in flowing N_2 -degassed deionized liquid water ($\rho \geq 10 M\Omega\text{-cm}$), of a cast AM piece having width of 1.15 cm and wet thickness of 120 μm . Frequency range 100 kHz – 100 Hz, voltage amplitude 10 mV. **(b)** Impedance spectra for a through-plane conductivity measurement in flowing N_2 -degassed deionized liquid water ($\rho \geq 10 M\Omega\text{-cm}$), of a cast AM of 5 cm^2 area and a wet thickness 40 μm . Anion-exchange ionomer bonded Pt/C electrodes were used, having a loading of 0.66 $\text{mg}_{\text{Pt}}/\text{cm}^2_{\text{MEA}}$, using SGL carbon paper (25BC) with a microporous layer as diffusion medium. Frequency range 100 kHz – 10 Hz, voltage amplitude 5 mV

2.6 Membrane electrode assemblies (MEAs)

2.6.1 Catalyst coated membranes (CCMs)

For AMFC testing and anion-exchange measurements, anion-exchange membrane and alcohol solubilized ionomer were used, whereas Nafion[®] 115 membrane (Fuel Cell Scientific) and a solution of Nafion[®] in a mixture of lower aliphatic alcohols and water (Aldrich) were used for cation-exchange measurements. CCMs were prepared either using a 40 wt% Pt on Vulcan catalyst (BASF) or a transition metal based catalyst supported on carbon (Acta) (20). The catalyst was mixed with a certain amount of water, alcohol, and ionomer solution, and then sonicated to obtain a homogeneous ink. The obtained ink was coated on a decal and transferred to the membrane by hotpressing to obtain CCMs. SGL carbon paper (25BC) with a microporous layer was used as diffusion medium.

2.6.2 Gas diffusion electrodes (GDEs)

An R-SBS-F37 film (FD 11.6%), previously quaternized in methanol with trimethylamine, was dissolved in methanol at 120 $^{\circ}\text{C}$ in an autoclave for 1h, obtaining a 4wt% ionomer solution. An ink was prepared dispersing Pt/C 40wt% (BASF[®]) catalyst into a portion of the ionomer solution (50 wt% Ionomer to Carbon ratio). The ink was then casted on SGL BC-25 support using a Mayer rod, obtaining a catalyst layer having 0.4 $\text{mg}_{\text{Pt}}/\text{cm}^2$ loading. Two square pieces

(5 cm²) of the catalyst coated support were assembled with a DABCO quaternized R-SBS-F37 membrane (1M DABCO in methanol), obtaining a GDE.

3 Results

In the last few years a number of new anion-exchange polymers (5; 6; 7; 8; 9; 10; 11; 12; 13; 14) have been developed, offering the possibility of assembling MEAs to develop Anion-exchange Membrane Fuel Cells (AMFCs) and Anion-exchange Membrane-based Electrolyzers (AMEs).

The current technologies of Anion Exchange Materials (AMs) for electrochemical application shows several limitations relate to the possibility of obtaining a reasonable low cost membrane having: high ionic conductivity, chemical stability in strong alkaline media, low permeability, low water swelling and good mechanical properties.

It has been recently discovered that the hydrogen oxidation reaction (HOR)/hydrogen evolution reaction (HER) kinetics on platinum catalyst are several orders of magnitude slower in alkaline compared to acid electrolyte (15). Therefore, the use of platinum anode catalysts in AMFCs/AMEs would require high loadings and thus become a significant cost factor unlike in PEMFCs/PEM-Es, where low Pt anode loadings are sufficient.

However transition metals oxide based catalysts, particularly spinel-type structures and transition metals alloys have been considered most promising for OER and HER (16; 17; 18; 19). Moreover other non-noble metal-based catalysts are available for AMFCs with an ORR activity comparable to Pt/C (20).

Therefore, the development of highly efficient catalysts toward HOR in alkaline electrolyte and cheap AMs having high conductivity and low water swelling are the critical challenges to make AMFCs/AMEs more practical.

For cation exchange materials, as reported in the first chapter, a block copolymer having side chain ionic functionalities has favorable combination of high conductivity and low swelling compared to random copolymers having ion-exchange groups in the main chain. Styrene–butadiene–styrene (SBS) copolymer is a cheap thermoplastic material with a block structure widely employed in the rubber industry and it is well known how to introduce functional groups by radical grafting in the polybutadiene block (21; 22; 23) making it a good candidate to produce low-cost AMs having good properties for electrochemical applications.

The purpose of this research was to develop and characterize AMs based on SBS copolymer, obtained by radical grafting of 4-vinylbenzyl chloride in polybutadiene blocks of SBS and subsequent conversion of grafted benzyl chloride functionalities to quaternary ammonium salts via nucleophilic substitution reaction with tertiary amines, as described in the experimental section.

Once protocols to measure main properties for an AM are developed and validated for commercial ion-exchange materials, tuneable synthetic parameters (i.e. functionalization degree and quaternization conditions) will be correlated to mechanical and transport properties in order to improve and study the morphology of these novel SBS-based AMs.

Performances will be measured for H₂/O₂ AMFC application using both commercial and SBS-based AMs. At last, Electrochemical Impedance Spectroscopy (EIS) diagnostics will be performed in order to evaluate measured performances.

3.1 Ion-exchange commercial material characterization

Commercial anion-exchange membrane A-201 and anion-exchange ionomer AS-4 from Tokuyama were characterized in terms of thermodynamic and transport properties in order to evaluate their suitability to be used in AMFCs and use these values as reference to develop SBS-based AMs. Thermodynamic and transport properties will be compared to the commercial cationic exchange membrane Nafion®115 in order to validate the developed analytical protocols. Tokuyama A-201 membranes are shipped as dry films having 28 μm thickness and A4-size. Tokuyama AS-4 ionomer is shipped as 5 wt% solution of the polymer in 1-propanol. A film of the commercial ionomer, having thickness of 130 μm , has been casted from the shipped solution in a PTFE petri dish (Figure 35), the solvent was evaporated for 3 days in a 1-propanol saturated atmosphere at room temperature.

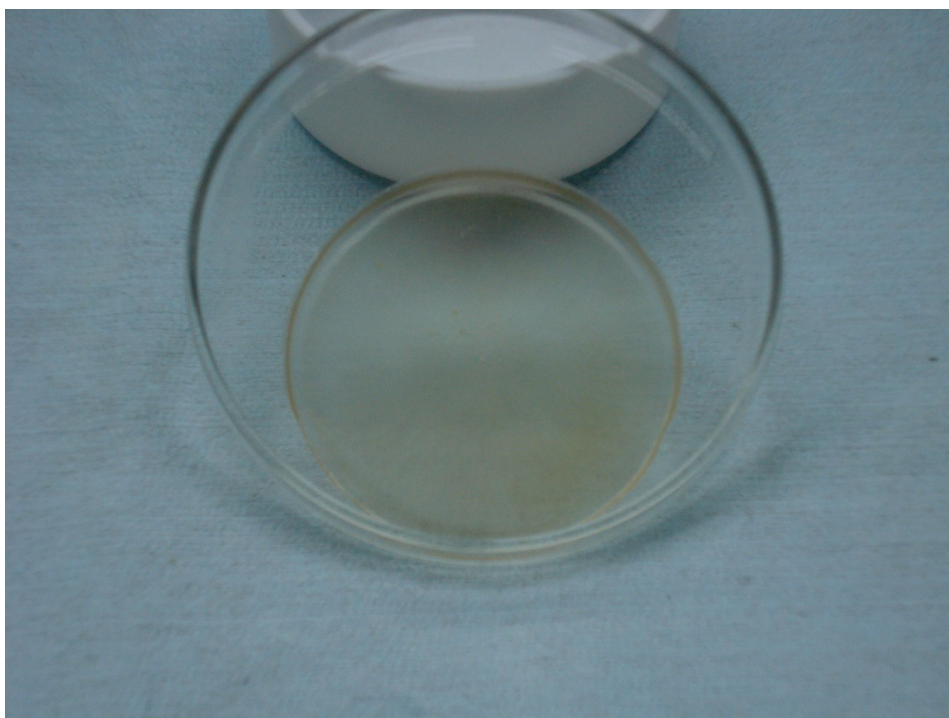


Figure 35. Tokuyama AS-4 film casted from the shipped ionomer solution

Ion Exchange Capacities (IECs) were measured as described in the experimental section, mean values over 5 titrations are compared with the values reported in data sheets on Table 17.

Sample	IEC [meq/g _{polymer}]	
	Experimental	Data sheet
Nafion®115	0.87±0.04	0.95±1.05
Tokuyama A-201	1.84±0.03	1.9
Tokuyama AS-4	1.44±0.04	1.5

Table 17. Ionic Exchange Capacity for commercial ionomeric materials

Experimental values for IEC are comparable with data sheets reported ones. Since the density of Tokuyama materials ($\approx 1,1 \text{ g/cm}^3$) is nearly half compared to Nafion® 115 ($\approx 2 \text{ g/cm}^3$), volumetric IECs are nearly the same: $\approx 2 \text{ meq/cm}^3$ for Tokuyama A-201, $\approx 1,8$

meq/cm³ for Nafion[®] 115, $\approx 1,6$ meq/cm³ for Tokuyama AS-4, suggesting that similar conductivities could be obtained for the three materials.

Figure 36 shows Water Uptake (WU), expressed as mass percentage, in liquid water as function of temperature for the three ion-exchange materials. Water uptake measured for Nafion[®] 115 is comparable with literature reported values (71; 72). While the Tokuyama membrane A-201, in the OH-form, has an higher WU compared to Nafion[®] 115, their volumetric swelling are essentially the same since Nafion[®] density is nearly two fold larger than Tokuyama A-201 one. Therefore, the anionic membrane from Tokuyama is expected to be promising for fuel cell and electrolyzer applications, where low volumetric swelling is required for mechanical stability. Moreover, WU variations with temperature of the anionic membrane in the OH-form are rather small, such that the thickness of a pre-swollen membrane will not change significantly during conductivity measurements as a function of temperature. Thus, all conductivity measurements will be referenced to the pre-swollen membrane thickness. Contrary to the Tokuyama membrane, solubilized ionomer AS-4 has a very high WU at 30°C, at higher temperature casted film swelling wasn't measurable due to mechanical fault.

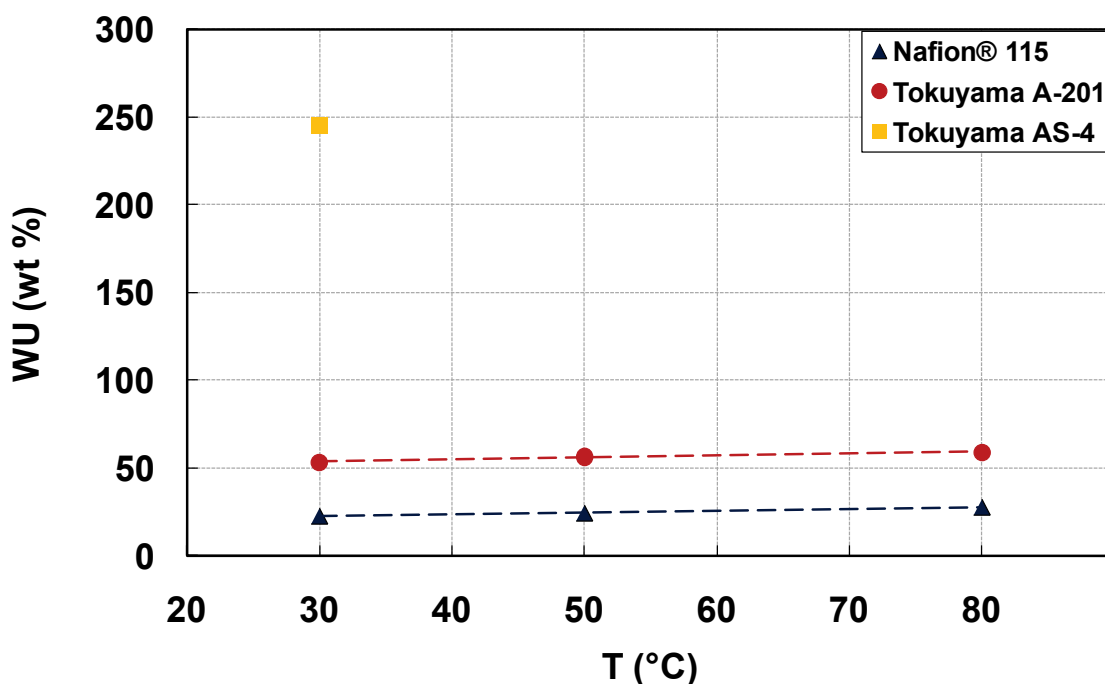


Figure 36. Water uptake as mass percentage of Tokuyama materials (OH-form) and Nafion[®] 115(H₃O⁺-form), measured in liquid water at different temperatures. The mean error over a set of 5 measurements at each temperature is ≈ 3 units of wt % for Tokuyama A-201 values, ≈ 5 units of wt % for Tokuyama AS-4 value, and ≈ 1 unit of wt % for Nafion[®] 115 values

Since most anion-exchange materials are prepared and supplied in their chloride-form, WU in this ionic form was also examined. The chloride-form of the Tokuyama A-201 membrane exhibits significantly lower WU (see Figure 37), probably due to the different polarizability and ionic-radii of chloride and hydroxyl ions. Since the differences between the OH-form and the Cl-form are quite significant, the evaluation of anion-exchange membranes and ionomers should always be done in the OH-form, especially if inferences are to be

drawn with regards to the suitability of a new anion-exchange material for AMFC and Anion-exchange Membrane Electrolyzer (AME) applications, which require the OH-form.

A more fundamental parameter to characterize the WU is the so-called λ -value, expressing the mean number of water molecules per ion-exchange group. Being independent of the IEC and density of the material, it allows for a better comparison between different materials. The WU expressed as λ was calculated using the following equation:

$$\lambda = \frac{WU(\%) \cdot 10}{IEC \cdot MW_{water}} \quad (3.1)$$

where WU(%) is expressed as mass percentage, IEC is expressed as meq/g_{polymer}, and MW_{water} is water molecular weight.

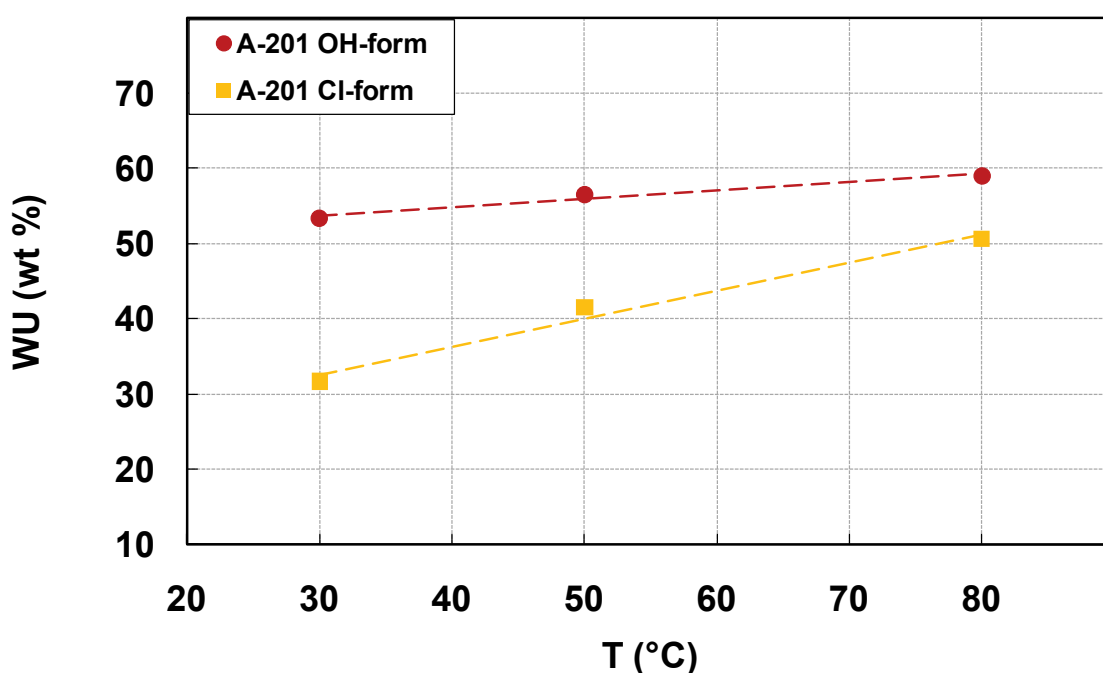


Figure 37. Water uptake as mass percentage of Tokuyama membrane A-201, measured in liquid water at different temperatures. The mean error over a set of 5 measurements at each temperature is ≈ 3 units of wt % (both OH-form and Cl-form)

In terms of λ WU values for the Tokuyama A-201 in the OH-form are close to Nafion® 115, as shown in Figure 38. Water swelling for the Tokuyama ionomer AS-4, in terms of λ , is 6-fold larger, suggesting differences in either backbone structure (in terms of chemical structure and/or molecular weight) or crosslinking ratio.

Figure 39 shows the in-plane (full lines) and through-plane (dashed lines) conductivities of Tokuyama A-201 and Nafion® 115, measured and calculated as described in the experimental section. Conductivity data are referenced to thickness of the pre-swollen films. Early literature (73) shows in-plane conductivities for Nafion® 117 comparable with measured ones at low temperatures, at temperatures higher than 50-60°C the authors reported a drop in conductivity. On the contrary, more recent literature (71) shows increase in 1100EW Nafion® conductivity up to 100°C and better compare with data reported in Figure 39.

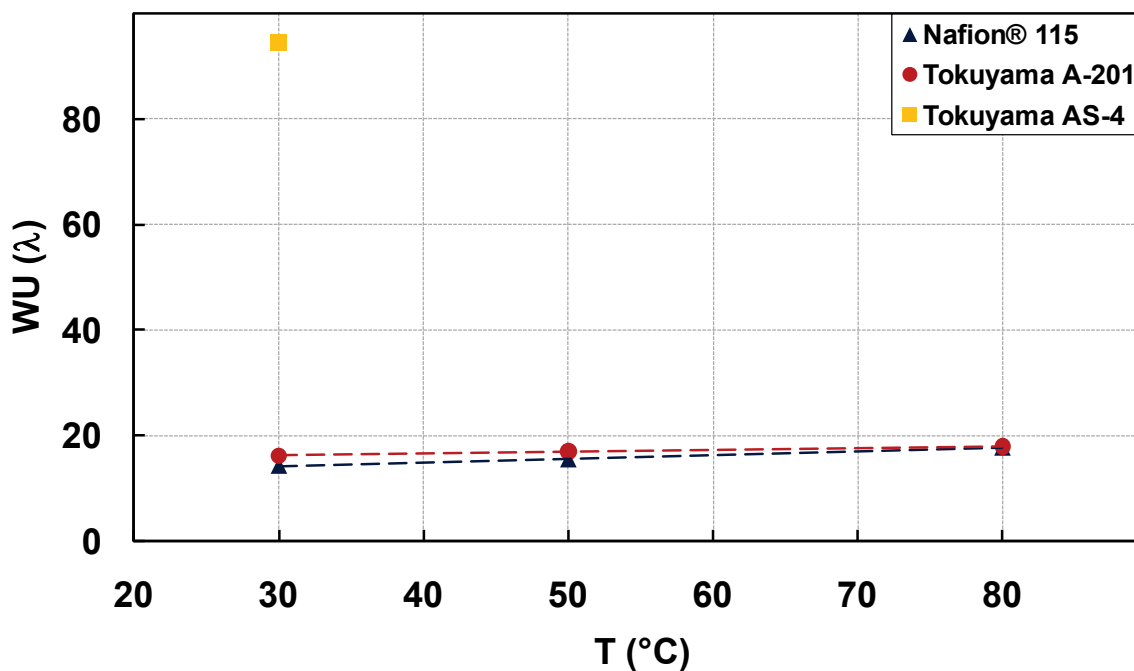


Figure 38. Water uptake in terms of λ (i.e. water molecules per ion-exchange group) of Tokuyama materials (OH-form) and Nafion® 115(H₃O⁺-form), measured in liquid water at different temperatures. The mean error, over a set of 5 measurements at each temperature is $\approx 0,9$ units of λ for Tokuyama A-201 values, ≈ 2 units of λ for Tokuyama AS-4 value, and $\approx 0,3$ units of λ for Nafion® 115 values

As explained by the authors it is important to correct measured data with swollen membrane thickness and control gases relative humidity during the tests. Both Nafion® 115 and Tokuyama A-201 exhibit isotropic behavior, having the same conductivities for in-plane and through-plane. Gardner et al. (74) suggested that the normal component of the conductivity depends strongly on the pressure applied on the membrane; correcting through-plane conductivity data to zero pressure they reported an in-plane to through-plane conductivity ratio of 4, yet to be confirmed by other authors. Whilst the conductivities for the Tokuyama membrane in the OH-form is only half compared to Nafion® 115, this result is very encouraging since these values are already high enough to develop AMFC and AMEs with sufficiently low ohmic losses at high current densities. For example, a conductivity of ≈ 0.07 S/cm at 80°C for the 40 μ m thick swollen A-201 would correspond to ohmic losses of only ≈ 60 mV at 1 A/cm². In addition, considering that the conductance at infinite dilution of OH⁻ ion in water is nearly half compared to H₃O⁺ ion, and that the two materials have nearly the same volumetric IEC, the conductivity of Tokuyama membrane is quite excellent.

Also, the conductivity of the Tokuyama membrane in the OH-form compares favorably with the literature, which reports OH⁻ conductivities of ≈ 30 mS/cm at 50°C in H₂O_{liquid} (44) vs. the ≈ 50 mS/cm shown in Figure 39. In-plane conductivity was also measured for the ionomer casted film: both bicarbonate and hydroxyl forms are comparable with the membrane. Above 50°C the hydroxyl form was not stable, preventing further measurements. High conductivities and swelling suggest either low crosslinking or low molecular weight of the polymer. Due to a non-disclosure agreement (NDA) thermal measurements (e.g. TGA, DSC)

or molecular weight measurements (e.g. GPC) could not be carried on these materials to confirm these hypothesis.

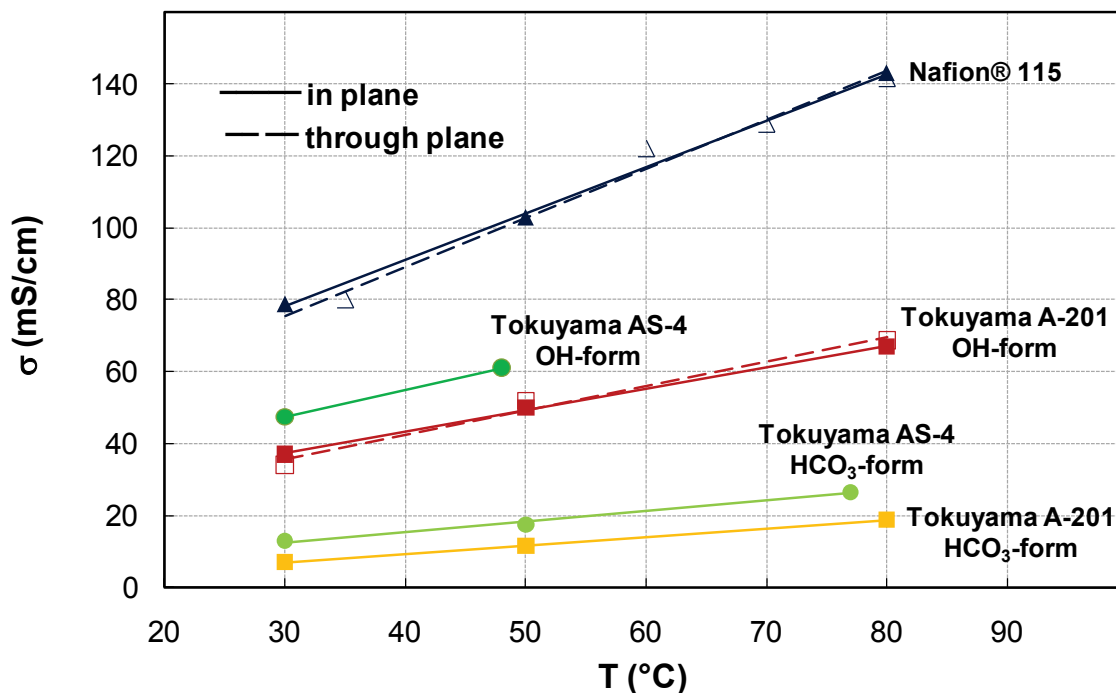


Figure 39. In-plane (full-lines and filled symbols) and through-plane (dashed-lines and empty symbols) conductivities of Tokuyama A-201, Tokuyama AS-4 and Nafion® 115 in liquid water vs. temperatures. The mean error, over a set of 3 measurements at each temperature is ≈ 2 mS/cm for in-plane values, and ≈ 3 mS/cm for through-plane values. Conductivity data are referenced to thickness of the pre-swollen films

Since bicarbonate ions contamination can occur, as discussed in the experimental part, conductivity for the HCO₃-form of anion-exchange materials was also measured. It is ≈ 4 -fold lower than that of the OH-form, consistent with the approximately 4-fold lower equivalent ionic conductance of bicarbonate compared to hydroxide.

To figure out the influence of CO₂ contained in the air on ionic conductivity, a piece of Tokuyama A-201 membrane has been converted to the OH-form and equilibrated in deionised water exposed to air for 1 day. The conductivity of the air exposed-form, reported in Table 18, is exactly the same as the in-situ exchanged HCO₃-form. This suggests that bicarbonate formed by the absorption of CO₂ from air can replace the hydroxide ions from the membrane. Therefore, it is clear that measurements of anion-exchange membrane properties are affected by air exposure, which must be avoided in experimental procedures, as was done in our experiments in a flow cell using carefully N₂-degassed water. This may also explain why essentially identical conductivities are reported for the hydroxide and carbonate form of anion-exchange membranes in the literature (6).

air exposed-form	HCO ₃ -form	OH-form
7 mS/cm	7 mS/cm	37 mS/cm

Table 18. Effect of CO₂ contained in air on the IP conductivity in liquid water of Tokuyama A-201 at 30°C.

Figure 40 shows the Arrhenius plot of the conductivity of Tokuyama A-201 membrane in the OH-form and Nafion® 115 in the proton form. Both of them show a linear behavior with

temperature, yielding activation energies of ≈ 11 kJ/mol, suggesting a similar transport mechanism. Calculated activation energy for Nafion® 115 is of the same magnitude of literature (71; 75) reported ones.

Polymeric membranes to be used in fuel cells or electrolyzers should prevent gas supplied or generated in one side to pass through it, reaching the other one (crossover). Figure 41 shows H₂ permeability for Tokuyama A-201 (OH-form) and Nafion® 115 at 30°C and fully humidified; it has been measured electrochemically as described in the experimental section.

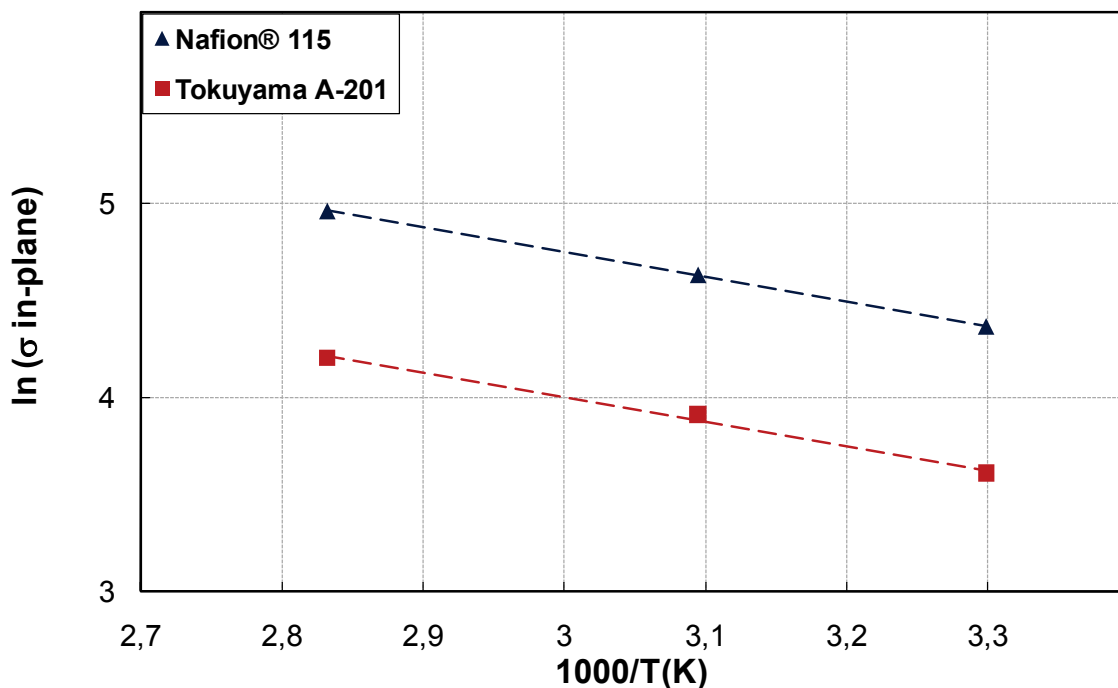


Figure 40. Arrhenius plot for in-plane conductivity in liquid water for Tokuyama A-201 (OH-form) and Nafion® 115 (based on the data shown in Figure 39)

Permeability measured for Nafion® 115 is $1.4 \cdot 10^{-13}$ mol·cm·s⁻¹·cm⁻²·kPa⁻¹, comparing well with literature (76) and in agreement with datasheet for Nafion® 212 ($<4 \cdot 10^{-10}$ mol·cm·s⁻¹·cm⁻²·kPa⁻¹), a membrane having the same equivalent weight as Nafion® 115. Hydrogen crossover measured for Tokuyama membrane is nearly one forth compared to Nafion® 115, making this material suitable for AMEs development.

Overall, the balance between conductivity, water uptake and H₂ crossover of Tokuyama commercial membrane A-201 is quite excellent and compares very well to Nafion® 115. At the same time, while the conductivity of the solubilized anion-exchange ionomer is essentially identical with that of the anionic membrane (shown in Figure 39), its water uptake is several times higher.

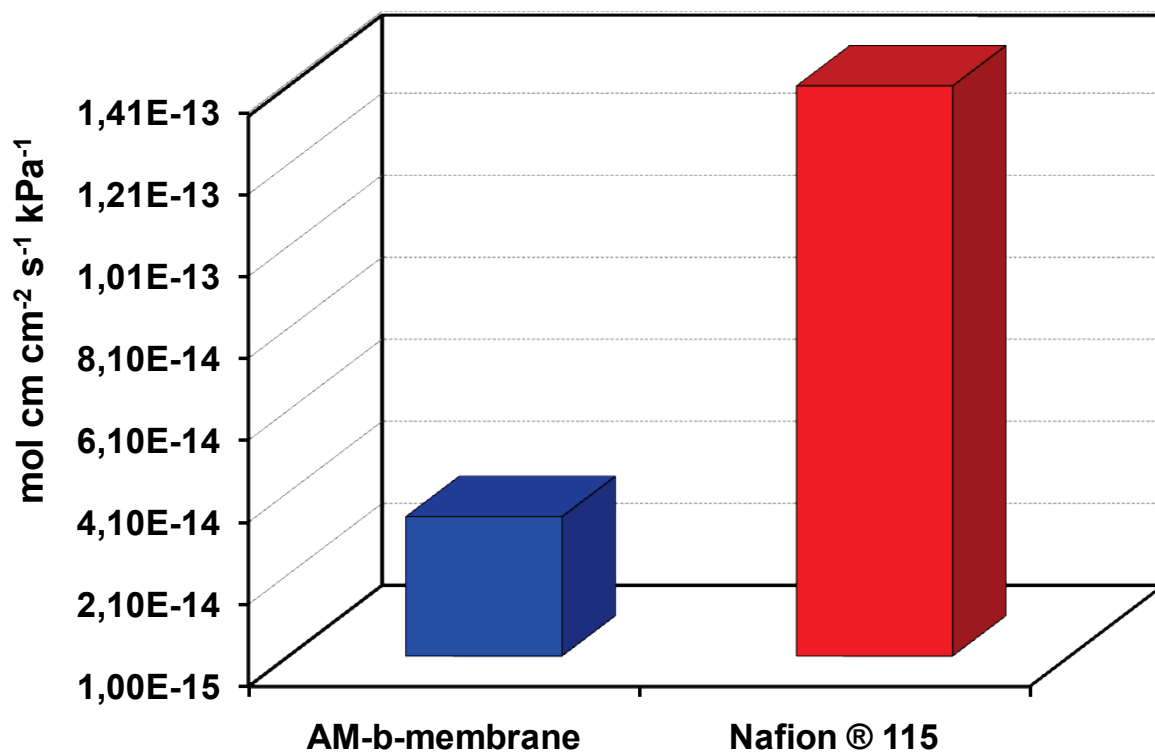


Figure 41. H₂ permeability at 30°C and 100% Relative Humidity for Tokuyama A-201 (OH-form) and Nafion® 115

3.2 SBS based anion-exchange materials

A common procedure to synthesize ion-exchange materials consists in the chemical modification of a commercial polymer via free-radical graft copolymerization with polar monomers. During the propagation reactions grafting monomers grows as side chains having variable lengths (and molecular weight) attached to the polymeric matrix by covalent bonds. Resulting polymer have the so-called comb-type (77) structure (Figure 42).

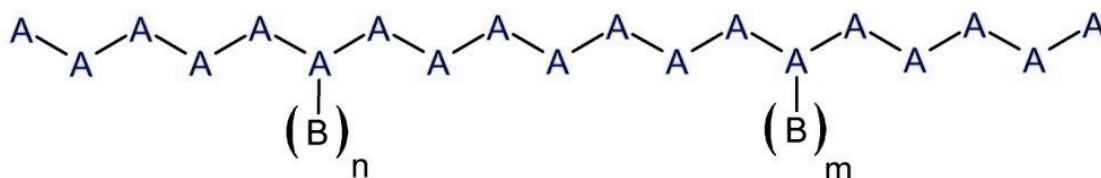


Figure 42. Comb-type copolymer structure obtained by graft copolymerization of B monomers on A polymer

Side chains growing reaction occurs alongside crosslinking and homopolymer formation reactions. Starting commercial polymers are usually thermoplastic (48), granting suitable thermal and mechanical stability; it can be used either in bulk, solution, molten state or as thin film during grafting reaction.

Ion-exchange materials are prepared mainly through graft copolymerization promoted by high energy radiation, for instance AMs prepared by electron beam grafting of thermoplastic fluoropolymer poly(ethylene-co-tetrafluoroethylene) (ETFE) are emerging in recent literature (5; 44). However, grafting copolymerization promoted by chemical initiators are promising; using this technique chemical modification of polymeric matrixes has been made in order to improve their chemico-physical properties. For instance SBS compatibility with other polymers, such as polyurethanes, has been improved grafting maleic anhydride or N-carbamyl maleamic acid (NCMA) in butadienic block (78). Examples of grafting functionalization via in-situ free-radical copolymerization promoted by chemical initiators are: methyl methacrylate on SBS (79), vinyl monomers (styrene, benzyl methacrylate and benzyl acrylate) on polybutadiene (PB) (80; 81; 82) or on polyisoprene (PIP) (83). Chemical initiators used in these grafting functionalizations are the same commonly used in radical polymerization, i.e. peroxides (e.g. benzoyl peroxide, BPO) and azocompounds (e.g. α,α' -azo-bis-isobutyronitrile, AIBN). An initiator is chosen according to grafting monomer and reaction conditions. Moreover radicals coming from peroxides decomposition, such as BPO, remove an allylic hydrogen atom, while radicals produced by azocompounds such as AIBN simply adds to double bonds.

It is well known how to introduce functional groups by radical grafting in SBS copolymer (21; 22; 23). In the next section is reported a controlled radical functionalization, initiated either by benzoyl peroxide (BPO) or α,α' -azo-bis-isobutyronitrile (AIBN), of SBS with 4-vinylbenzyl chloride (VBC). The resulting thermoplastic polymer, SBS-g-VBC, via quaternization reaction with tertiary amines, such as 1,4-diazabicyclo[2.2.2]octane (DABCO) or trimethylamine (TMA), is converted into an anion-exchange membrane in the form of a thin sheet (50-100 μm). The final properties of these AMs were determined in terms of ion-

exchange capacity (IEC), ionic conductivity (σ), water uptake (WU) and performances in a fuel cell apparatus.

3.2.1 SBS-g-VBC synthesis and characterization

Free-radicals are atoms, molecules, or ions with unpaired electrons on an open shell configuration. Free radicals may have positive, negative or zero charge. Even though they have unpaired electrons, by convention, metals and their ions or complexes with unpaired electrons are not radicals (84). The unpaired electrons cause radicals to be highly chemically reactive, promoting radical addition on molecules having multiple bonds (such as ethylene, styrene, vinyl chloride and butadiene) or atom removal via radical transfer reaction (such as allylic hydrogen removed from polybutadiene). Grafting reaction can be conducted using radical initiators giving raise to free radicals via thermal decomposition, reduction-oxidation reaction or photodegradation. Common radical initiators are benzoyl peroxide (BPO), which homolitically dissociate at temperature higher than $\approx 40^\circ\text{C}$, and α,α' -azo-bis-isobutyronitrile (AIBN), giving raise to free radicals at temperature higher than $\approx 50^\circ\text{C}$, as shown in Figure 43.

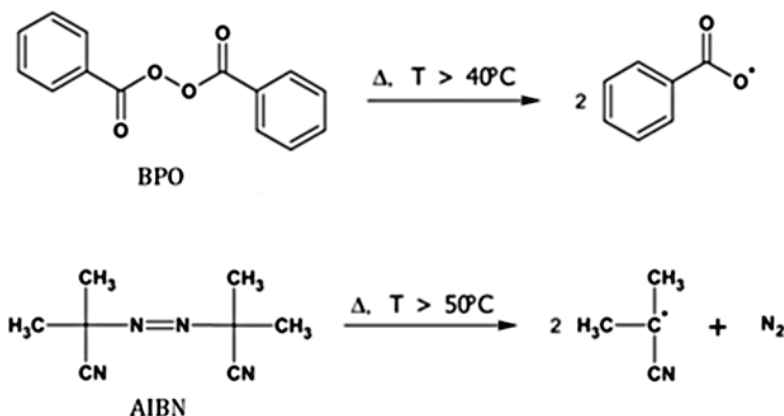


Figure 43. Thermal decomposition of benzoyl peroxide (BPO) and α,α' -azo-bis-isobutyronitrile (AIBN)

In literature (80; 81; 82; 83) are reported lots of studies on experimental and kinetics of free radical graft copolymerization on polydienic matrices, such as polybutadiene and polyisoprene. These studies shows that using a peroxide as radical initiator most likely the reaction mechanism starts with allylic hydrogen removal by primary radical (BPO $^{\bullet}$). Assuming that radical grafting on SBS proceed via the same mechanism VBC units are most likely bonded to butadienic units (showed in red on Figure 44).

Commercial monomer 4-chloromethyl-styrene was grafted via free-radical graft copolymerization to a commercial thermoplastic block Styrene–butadiene–styrene copolymer (SBS, Calprene 501) to obtain the comb-type thermoplastic material SBS-g-VBC, as described in the experimental section. The reaction has been conducted in bulk phase, weight ratio between the VBC monomer and SBS matrix was 5 to 1 (i.e. the minimum ratio for which VBC was able to solubilise the polymer).

The reaction was performed at 80°C for 2 and a half hours, using different quantity of radical initiator, expressed as molar percentage of the initiator over the polymer, in order to establish a relationship between its quantity and VBC grafting degree on SBS. Either AIBN or BPO were used in different syntheses as radical initiators.

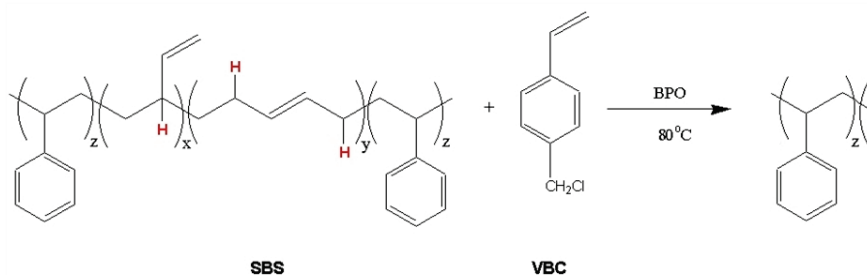


Figure 44. Grafting of VBC on SBS matrix via free radical copolymerization initiated by BPO

Grafting reactions were performed using a molar percentage of radical initiator in the range of 0.25÷1.20% for BPO, or 0.4÷1.20% for AIBN (Table 19). Maximum percentage was such that crosslinking between butadienic units was negligible.

Sample	BPO initiator			AIBN initiator		
	mg	mmol	mol%	mg	mmol	mol%
SBS-F7	33.4	0.14	0.46	-	-	-
SBS-F8	18.2	0.07	0.25	-	-	-
SBS-F9	33.4	0.14	0.46	-	-	-
SBS-F10	21.8	0.09	0.30	-	-	-
SBS-F11	50.9	0.21	0.70	-	-	-
SBS-F12	58.1	0.24	0.80	-	-	-
SBS-F13	50.9	0.21	0.70	-	-	-
SBS-F14	87.2	0.36	1.20	-	-	-
SBS-F15	58.1	0.24	0.80	-	-	-
SBS-F16	58.1	0.24	0.80	-	-	-
SBS-F17	43.6	0.18	0.60	-	-	-
SBS-F18	-	-	-	29.5	0.18	0.60
SBS-F19	-	-	-	19.7	0.12	0.40
SBS-F20	65.4	0.27	0.90	-	-	-
SBS-F21	-	-	-	39.4	0.24	0.80
SBS-F22	-	-	-	59.0	0.36	1.20
SBS-F23	61.7	0.26	0.85	-	-	-
SBS-F24	50.9	0.21	0.70	-	-	-

Table 19. Grafting reactions of VBC on SBS performed using different type and amount of radical initiators

During grafting of VBC on SBS, propagation reactions may lead to the formation of the envisaged grafted copolymer (SBS-g-VBC), or to the formation of poly(vinylbenzyl chloride) (PVBC) homopolymer. Hence, a mixture of the grafted copolymer SBS-g-VBC, having different functionalization degrees, and PVBC homopolymer is formed. This is confirmed by the FT-IR spectra of the obtained mixtures (Figure 45) : typical bands for both butadienic on SBS (blue wavenumbers on Figure 45) and chloromethylenic on VBC (red wavenumbers on Figure 45) are detected. FT-IR bands attribution has been discussed in the experimental section.

In order to separate the SBS-g-VBC copolymer from PVBC the mixture was washed with acetone. In fact this solvent is able to completely solubilize the homopolymer, leaving unreacted SBS and its grafted derivative, SBS-g-VBC, on the solid phase. Once acetone is removed, extracted homopolymer (PVBC) was stocked in order to be analyzed.

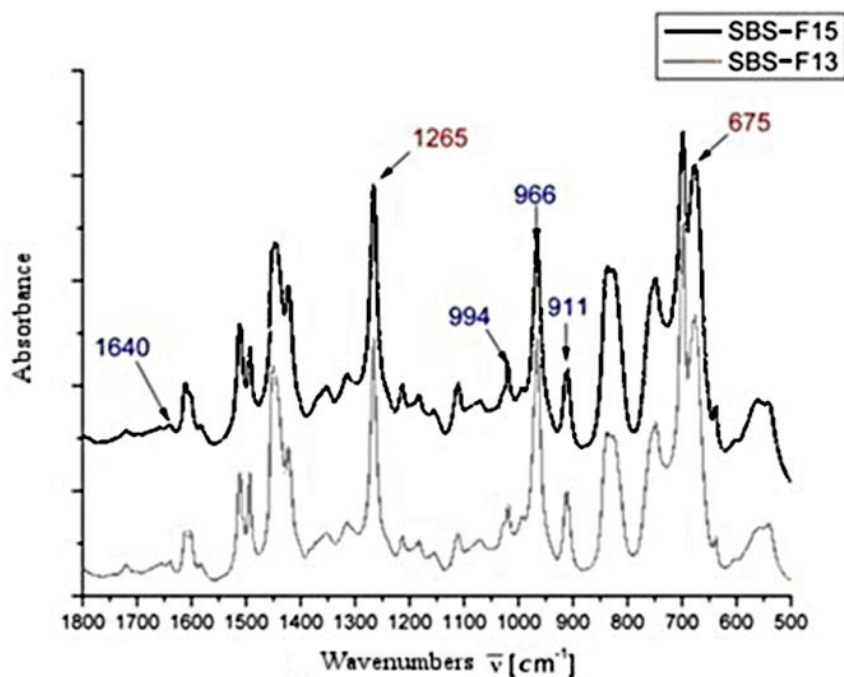


Figure 45. FT-IR spectra of grafting reaction products SBS-F13 and SBS-F15

Solid phase after the extraction with acetone is composed by unreacted SBS and its grafted product; in order to further purify the envisaged product, residual phase has been dissolved using chloroform and reprecipitated adding methanol, then separated and dried out.

Sample	Residual phase wt%	Extracted phase wt%	Initiator mol%
SBS-F8	40	60	0.25 BPO
SBS-F9	37	63	0.46 BPO
SBS-F10	38	62	0.30 BPO
SBS-F11	42	58	0.70 BPO
SBS-F12	41	59	0.80 BPO
SBS-F13	44	56	0.70 BPO
SBS-F14	49	51	1.20 BPO
SBS-F15	48	52	0.80 BPO
SBS-F16	59	41	0.80 BPO
SBS-F17	44	56	0.60 BPO
SBS-F18	38	62	0.60 AIBN
SBS-F19	39	61	0.40 AIBN
SBS-F20	56	44	0.90 BPO
SBS-F21	38	62	0.80 AIBN
SBS-F22	37	63	1.20 AIBN
SBS-F23	58	42	0.85 BPO

Table 20. Weight percentage ratio of residual (SBS-g-VBC) and extracted (PVBC) phases of SBS grafting reaction products using acetone as extracting solvent

Extracted and residual phases were weighted in order to measure reaction products ratio (Table 20). This table shows a different behavior of the reaction products ratio respect

to radical initiator amount, depending on its type. Using BPO the residual phase percentage increases as we increase radical initiator amount. On the other hand, reactions conducted using AIBN do not show net change in reaction products ratio varying the initiator amount. These trends are plotted in Figure 46: a positive correlation subsist between obtained residual phase and starting radical initiator percentage using BPO as free radical source, slightly negative correlation is on the contrary observed for AIBN initiator. These data suggest that BPO promotes VBC grafting on SBS matrix over its homopolymerization, the opposite trend is observed for AIBN.

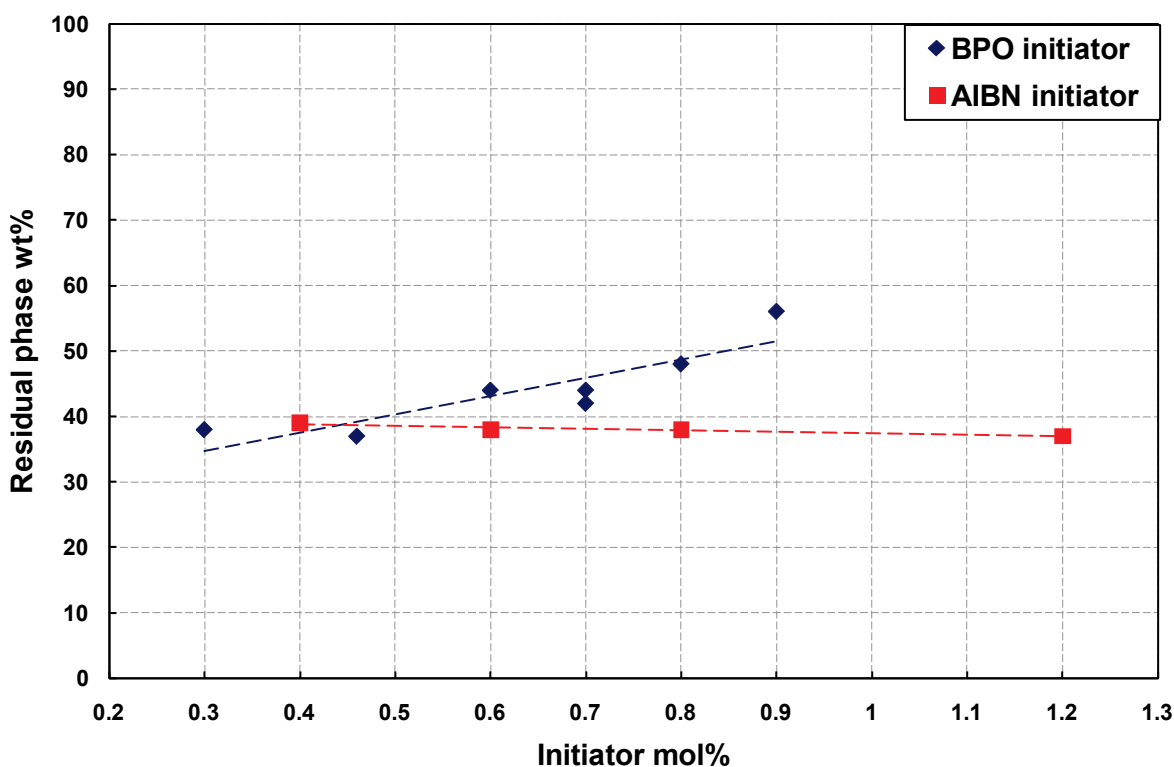


Figure 46. Correlation between obtained residual phase (SBS-g-VBC) and starting free radical initiator quantity, after extraction using acetone

Both residual and extracted phases were characterized via FT-IR, $^1\text{H-NMR}$, $^{13}\text{C-NMR}$, SEC and elemental analysis in order to ensure the complete separation of the grafted copolymer from the homopolymer by-product. The residual phase, composed by the envisaged grafted copolymer and unreacted SBS matrix, was furthermore characterized by thermal analysis (TGA) and scanning electron microscopy (SEM).

FT-IR spectroscopic analysis

Infrared absorption spectra were acquired after acetone extraction for both extracted and residual phases. On Figure 47 extracted phases FT-IR spectra, overlapped using different colors, are compared with the pure homopolymer: having no differences on main absorption peaks at 1265 cm^{-1} ($\delta\text{ CH}_2\text{-Cl}$), 828 cm^{-1} ($\delta\text{ C-H aromatics}$) and 675 cm^{-1} ($\nu\text{ C-Cl}$), we can conclude that the extracted phases are fully composed by PVBC. On Figure 48 residual phases FT-IR spectra, overlapped using different colors, are compared with both pure SBS (Calprene 501) and pure PVBC ones: typical absorption bands for both butadienic and chloromethylenic groups are present on residual phases spectra suggesting that grafting

reaction of VBC on SBS matrix occurred and that after an extraction using acetone grafted copolymer and homopolymer are separated.

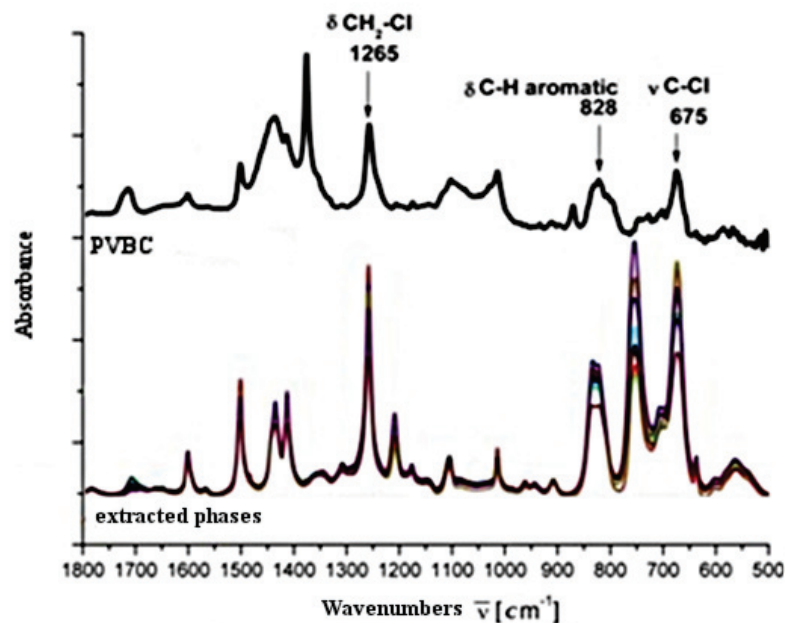


Figure 47. FT-IR spectra comparison ($1800\text{-}500\text{ cm}^{-1}$) between acetone extracted phases and PVBC

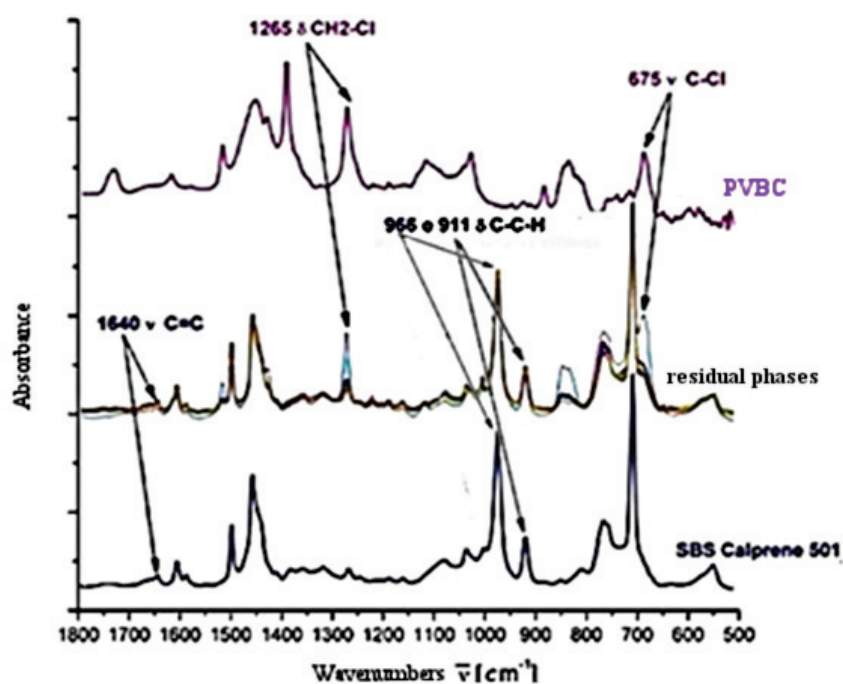


Figure 48. FT-IR spectra comparison ($1800\text{-}500\text{ cm}^{-1}$) between SBS, residual phases and PVBC

¹H-NMR spectroscopic analysis

Spectra for both SBS-F23 acetone extracted phase and PVBC homopolymer are reported on Figure 49: since same signals are observed in both spectra we can conclude that the extracted phase is composed by PVBC only. On Figure 50 are reported $^1\text{H-NMR}$ spectra for SBS-F23 residual phase (R-SBS-F23), SBS copolymer (Calprene 501) and PVBC: signals from both SBS matrix and chloromethylenic groups ($\delta=4.5\text{ ppm}$) can be observed, confirming that VBC grafting on SBS matrix occurred.

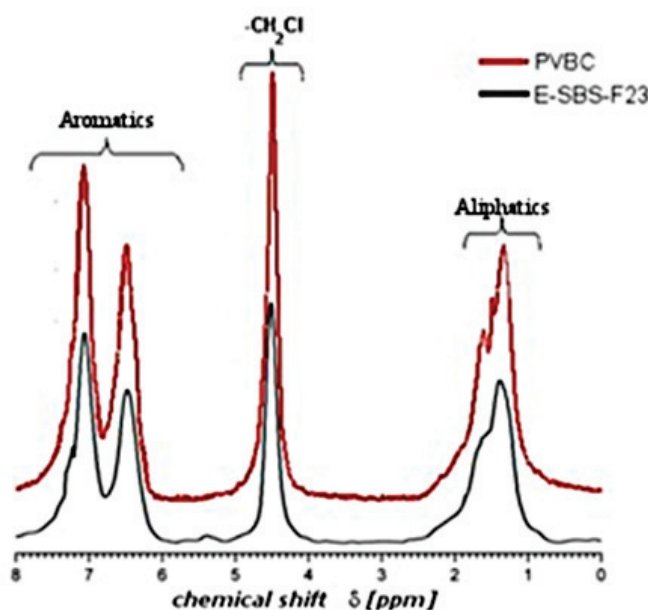


Figure 49. $^1\text{H-NMR}$ spectra comparison between PVBC and SBS-F23 acetone extracted phase (E-SBS-F23)

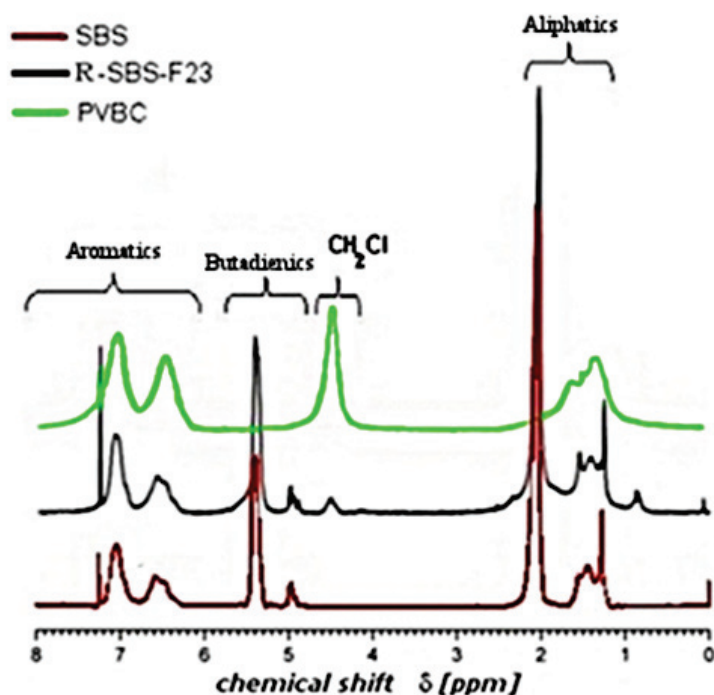


Figure 50. $^1\text{H-NMR}$ spectra comparison between PVBC, SBS and SBS-F23 residual phase (R-SBS-F23)

Thus both $^1\text{H-NMR}$ and FT-IR spectroscopies report that chemical promoted free-radical grafting of VBC on SBS matrix occurred along with VBC homopolymerization and that after an extraction with acetone those products are completely separated.

Integrating the different signals observed on $^1\text{H-NMR}$ spectra of residual phases it is possible to calculate each fragment contribution, thus to extrapolate how much VBC is grafted on the SBS matrix.

On Figure 51 is reported a typical $^1\text{H-NMR}$ spectra of a residual phase, signals have been divided into four groups:

- Group A ($\delta=7.1$ and 6.5 ppm): styrenic and VBC aromatic protons;
- Group B ($\delta=5.4$ ppm): 1,4-butadienic and 1,2-butadienic protons;

- Group C ($\delta=4.9$ ppm): 1,2-butadienic protons;
- Group D ($\delta=4.5$ ppm): VBC aliphatic protons.

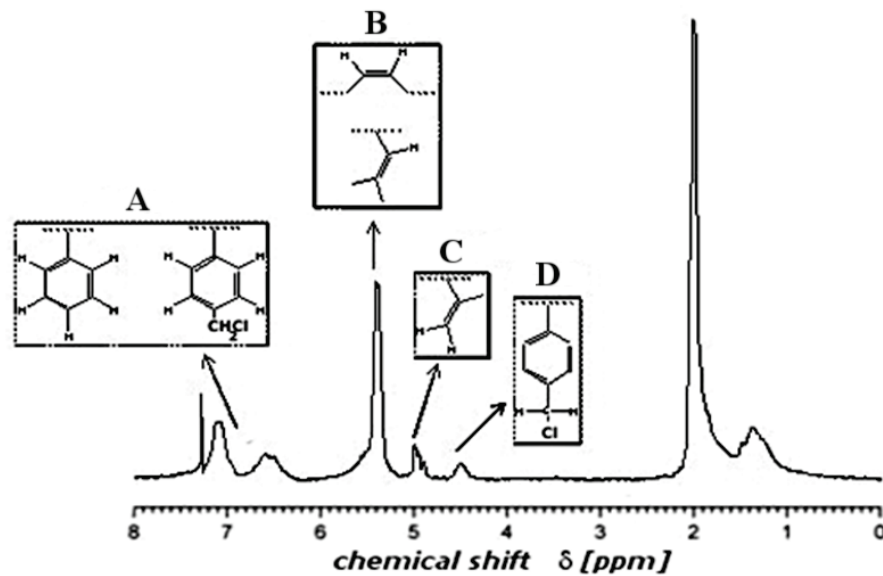


Figure 51. $^1\text{H-NMR}$ spectra of a residual phase (SBS-g-VBC) and its signals attribution

Integrating signals for each fragments and taking into account their equivalent protons, it is possible to obtain each fragment relative contribution:

$$\begin{aligned}
 \text{VBC mol\%} &\propto \frac{D_{\text{area}}}{2} \\
 \text{1,2-butadiene mol\%} &\propto \frac{C_{\text{area}}}{2} \\
 \text{1,4-butadiene mol\%} &\propto \left(B_{\text{area}} - \frac{C_{\text{area}}}{2} \right) \cdot \frac{1}{2} \\
 \text{styrene mol\%} &\propto \left(A_{\text{area}} - \frac{D_{\text{area}}}{2} \cdot 4 \right) \cdot \frac{1}{5}
 \end{aligned} \tag{3.2}$$

Normalizing monomeric contributions in equations (3.2) we obtain the following equations to calculate monomeric composition of the grafted copolymer (expressed as molar percentage):

$$\begin{aligned}
 \text{VBC mol\%} &= \frac{10D_{\text{area}}}{4A_{\text{area}} + 10B_{\text{area}} + 5C_{\text{area}} + 2D_{\text{area}}} \cdot 100 \\
 \text{1,2-butadiene mol\%} &= \frac{10C_{\text{area}}}{4A_{\text{area}} + 10B_{\text{area}} + 5C_{\text{area}} + 2D_{\text{area}}} \cdot 100 \\
 \text{1,4-butadiene mol\%} &= \frac{10B_{\text{area}} - 5C_{\text{area}}}{4A_{\text{area}} + 10B_{\text{area}} + 5C_{\text{area}} + 2D_{\text{area}}} \cdot 100 \\
 \text{styrene mol\%} &= \frac{4B_{\text{area}} - 8A_{\text{area}}}{4A_{\text{area}} + 10B_{\text{area}} + 5C_{\text{area}} + 2D_{\text{area}}} \cdot 100
 \end{aligned} \tag{3.3}$$

Grafted VBC molar percentage (VBC mol%), defined in equation (3.3), will be referred as functionalization degree (FD). Once the monomeric composition for a batch has been

calculated using equations (3.3), it is possible to estimate the theoretical Ionic Exchange Capacity (IEC_{th}), expressed as millimoles of ion-exchange groups per gram of polymer, that the grafted copolymer should have after a quaternization reaction between grafted VBC groups and a tertiary amine. Theoretical IEC can be estimated using following formula:

$$IEC_{th} = \frac{VBC \text{ mol}\%}{\sum_i i \text{ mol}\% \cdot MW(i)} \cdot 1000 \quad (3.4)$$

where IEC_{th} is the theoretical ion-exchange capacity, expressed as millimoles of ion-exchange groups per gram of polymer, i is one of the four fragments and $MW(i)$ its molecular weight. This value is approximate and can vary from the measured IEC since different molecular weights for the VBC fragments should be considered on the calculation, based on the amines used during the quaternization reaction. On Table 21 monomeric composition and approximate theoretical ion-exchange capacity for each batch is reported: increasing radical initiator percentage the functionalization degree (FD) increases as well, moreover at the same radical initiator percentage batches using BPO have an higher FD compared to the AIBN ones. For radical initiator percentages higher than 1.1 mol% the residual phase, after acetone extraction, was only partially soluble in chloroform suggesting that crosslinking reactions between different SBS matrix chains occurred. Crosslinking reaction explains the small FD changes for BPO percentages >1.1 mol%.

Sample	initiator	1,4-butadiene	Butadiene1,2	Styrene	VBC (FD)	IEC_{th}
	mol%	mol%	mol%	mol%	mol%	mmol/g _{polymer}
SBS	0	60.0	10.0	30.0	0.0	0.0
R-SBS-F9	0.46 BPO	58.6	7.0	30.0	4.4	0.6
R-SBS-F10	0.30 BPO	62.2	6.6	27.5	3.7	0.5
R-SBS-F11	0.70 BPO	58.3	9.4	25.9	6.4	0.9
R-SBS-F13	0.70 BPO	57.4	7.5	28.1	7.0	0.9
R-SBS-F14	1.20 BPO	54.5	9.3	27.7	8.5	1.1
R-SBS-F15	0.80 BPO	57.7	8.0	25.8	8.5	1.1
R-SBS-F16	0.80 BPO	57.0	8.2	26.7	8.1	1.0
R-SBS-F17	0.60 BPO	57.9	9.2	27.6	5.3	0.7
R_SBSF18	0.60 AIBN	61.9	7.7	28.4	2.0	0.3
R_SBSF19	0.40 AIBN	63.3	7.8	27.9	1.0	0.1
R-SBS-F20	0.90 BPO	53.9	7.1	28.6	10.4	1.3
R_SBSF21	0.80 AIBN	62.8	8.3	25.8	3.1	0.4
R_SBSF22	1.20 AIBN	62.7	8.1	24.7	4.5	0.6
R-SBS-F23	0.85 BPO	53.9	7.3	29.2	9.6	1.2
R-SBS-F37	0.95 BPO	54.2	8.3	25.9	11.6	1.4

Table 21. Residual phases (SBS-g-VBC) monomeric composition calculated from ¹H-NMR data

Functionalization degree data from Table 21 were plotted versus free radical initiator percentage for both AIBN and BPO in Figure 52: grafting efficiency for BPO at the same molar percentage is higher than AIBN. Therefore BPO initiator promotes grafting reaction of

VBC on SBS more than VBC homopolymerization (Figure 46) and the obtained grafted product has an higher FD compared to the grafted copolymer obtained using the same amount of AIBN.

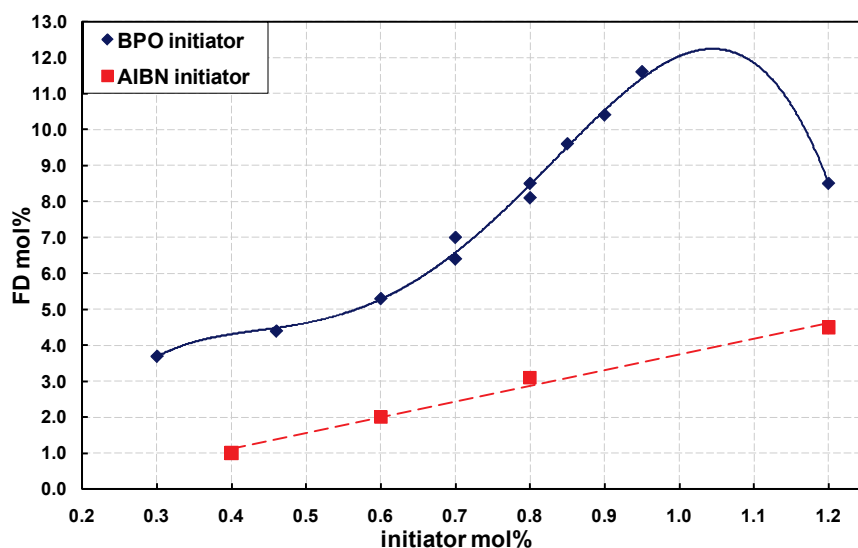


Figure 52. Functionalization degree (FD) as function of free radical initiator percentage in the reaction feed

¹³C-NMR spectroscopic analysis

Carbon-13 NMR analysis confirmed the results obtained by both FT-IR and ¹H-NMR spectroscopies: extracted phases show ¹³C-NMR signals typical for PVBC homopolymer, residual phases show raw SBS signals together with chloromethylenic carbons signals. On Figure 53 is showed the ¹³C-NMR spectra of SBS-F23 residual phase together with signals assignment.

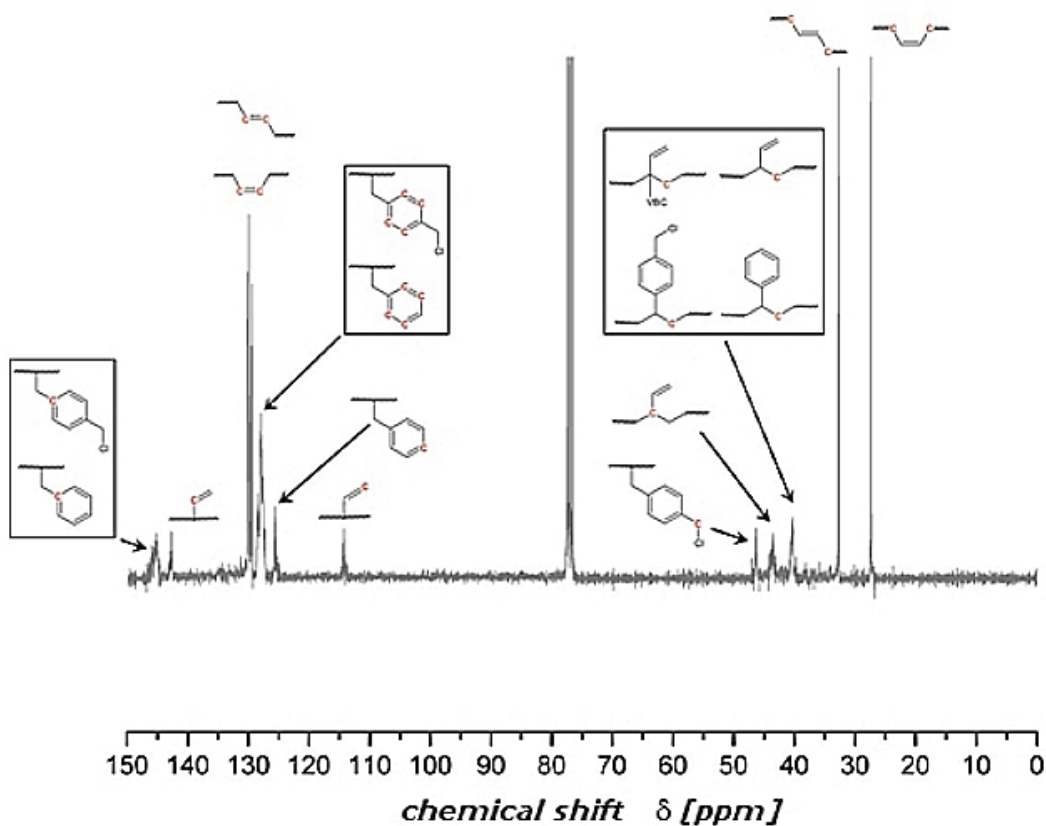


Figure 53. ¹³C-NMR spectra of a residual phase and its signal assignments.

Gel permeation chromatography (GPC) analysis

Both residual (SBS-g-VBC) and acetone extracted (PVBC) phases were characterized by means of gel permeation chromatography in order to determine their molecular weights. GPC chromatograms of acetone extracted phases show a broad monomodal distribution of molecular weights with an asymmetrical (fronting) shape (Figure 54).

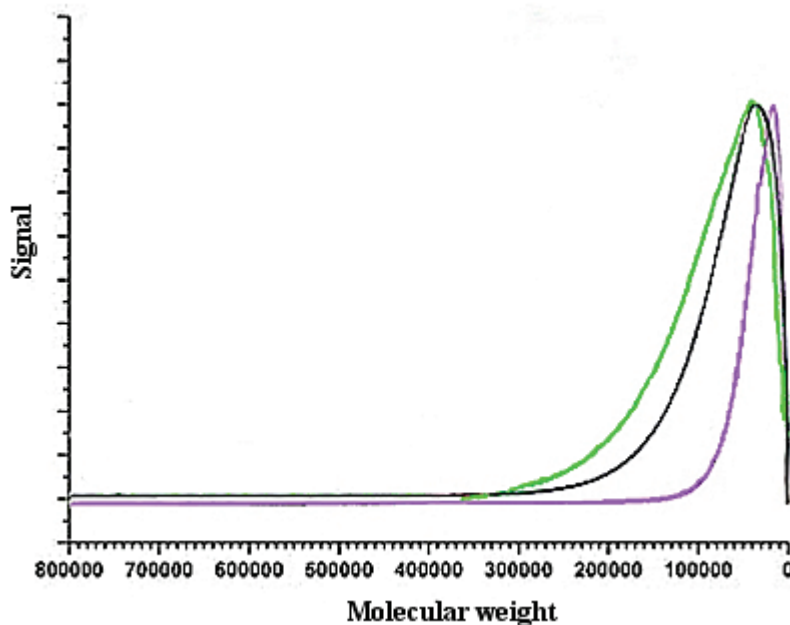


Figure 54. GPC chromatograms for three acetone extracted phases using an UV detector set at 250nm

Plotting the weight average molecular weight \overline{M}_w of extracted phases as function of BPO initiator percentage (Figure 55) a positive correlation is observed. Considering that homopolymer yield decreases with BPO percentage (Table 20), increasing the initiator amount decreases free radicals amount on the bulk environment, probably due to an higher kinetics of allylic hydrogen removal of butadienic units, also suggested by an increased VBC grafting degree on SBS matrix (Figure 52).

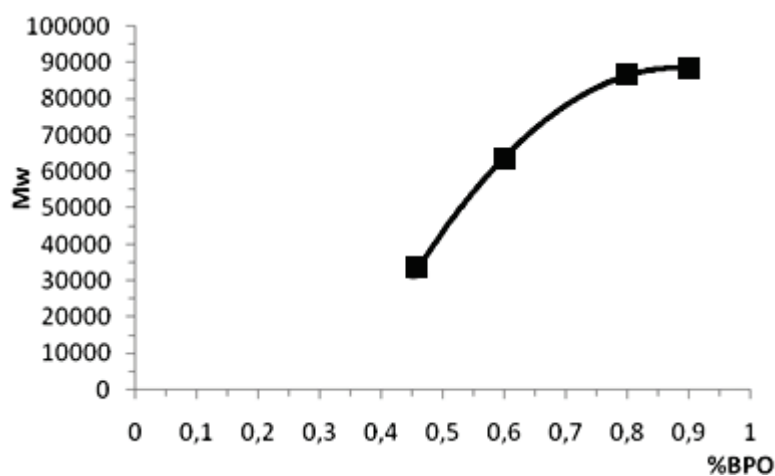


Figure 55. PVBC weight average molecular weight (\overline{M}_w) as function of BPO initiator percentage

On the contrary using AIBN as free radical source the weight average molecular weight is nearly independent from the initiator percentage obtaining homopolymers having $\overline{M}_w \approx 10700$ amu.

On Figure 56 a comparison between residual phases and raw SBS (Calprene 501) GPC chromatograms is reported: residual phases show an asymmetric broad peak, having a maximum at the same molecular weight as the SBS matrix.

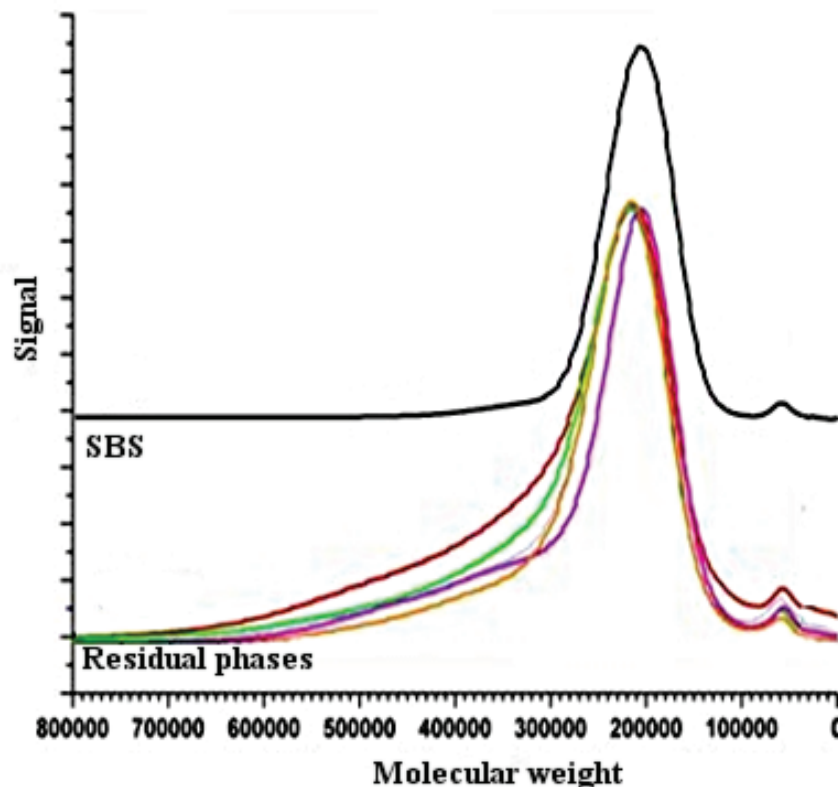


Figure 56. GPC chromatograms of SBS (Calprene 501) and residual phases using an UV detector set at 250nm

The shape of residual phases GPC peaks suggest a polymodal distribution, therefore a deconvolution analysis was performed. The analysis showed that the chromatogram is composed by three overlapped peaks (green curves on Figure 57). The two deconvoluted curves having lower molecular weights have same distribution and \overline{M}_w as the SBS matrix. Considering that the residual phase is composed by a mixture of unreacted SBS and its VBC grafted product, the third peak having higher molecular weight (400000) comes from the grafted copolymer (SBS-g-VBC). By means of deconvolution it was possible to obtain weight average molecular weight of the grafted copolymer fraction of the residual phases for each batch. On Figure 58 weight average molecular weight (\overline{M}_w) and functionalization degree of SBS-g-VBC are plotted against free radical initiator molar percentage: increasing BPO amount both FD and \overline{M}_w increases, moreover the shape of the two curves is similar, confirming thus that the residual phase is composed by a mixture of raw SBS and its VBC grafted derivative.

Similar results were obtained for residual phases obtained using AIBN free radical initiator: residual phases are composed by a mixture of raw SBS and its VBC grafted derivative, small changes were observed in FD and \overline{M}_w varying initiator percentage.

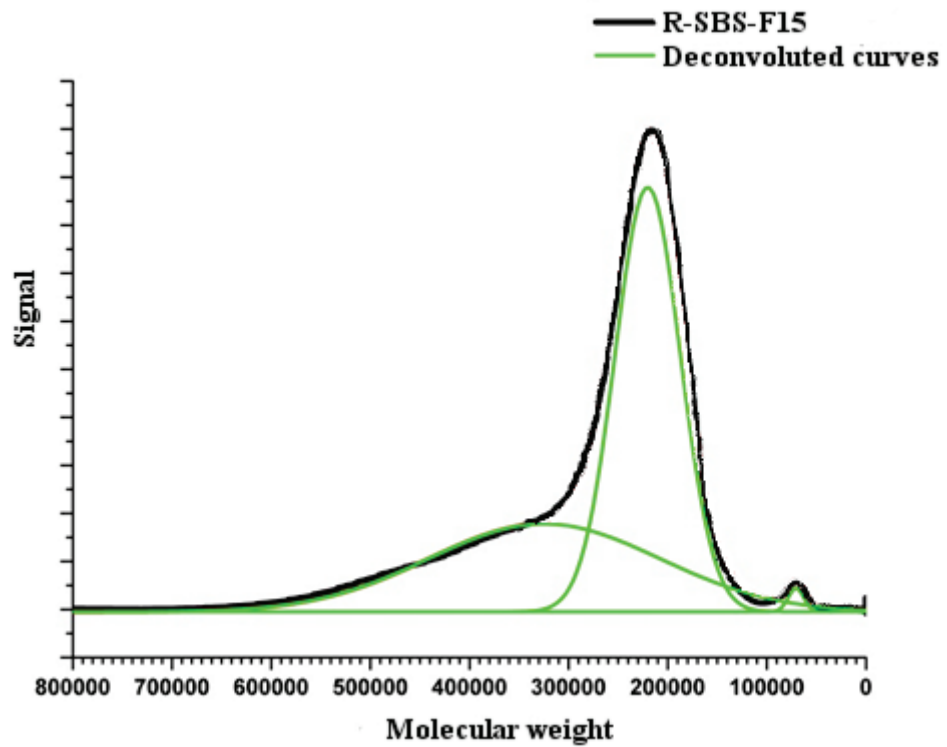


Figure 57. SBS-F15 residual phase GPC chromatogram and its deconvoluted curves

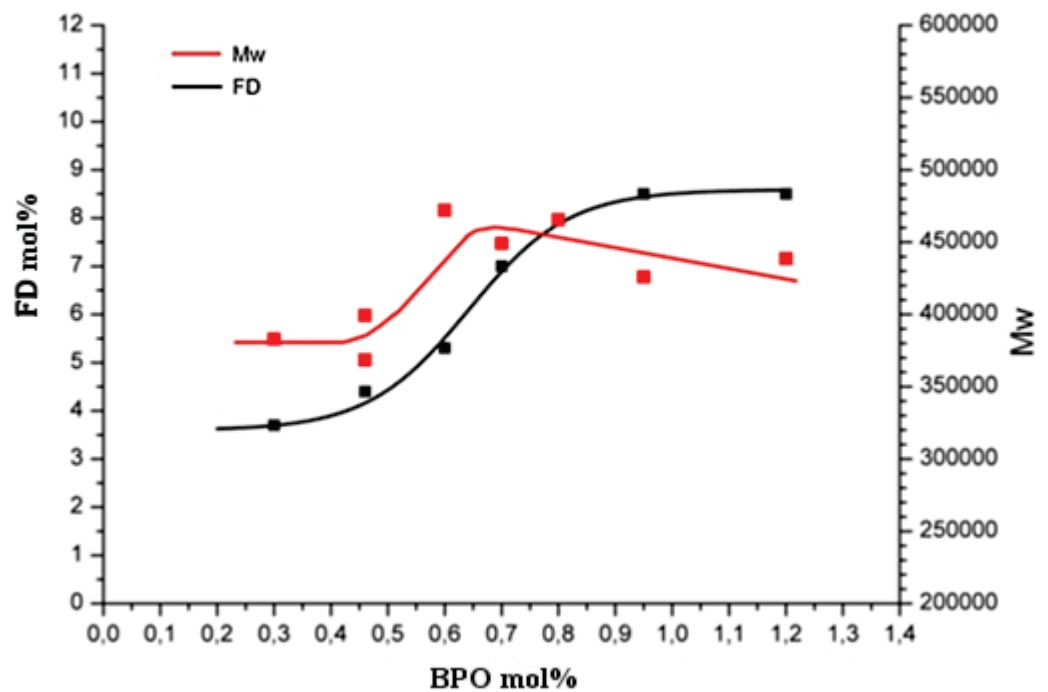


Figure 58. Functionalization degree (FD) and weight average molecular weight (\overline{M}_w) of SBS-g-VBC as function of Benzoyl peroxide (BPO) molar percentage.

Thermogravimetric analysis (TGA)

SBS matrix and residual phases of two batches (SBSF13 and SBSF15) were characterized by means of Thermogravimetric analysis, showing one decomposition temperature (T_d).

On Figure 59 decomposition temperatures of 3 batches are plotted against BPO percentage used for the grafting reaction, exhibiting a positive correlation. Considering that higher BPO percentage produces a grafted copolymer having higher functionalization degree (Figure 52), the positive correlation can be explained in terms of thermal stabilizing effect of VBC fragments which can delocalize free radicals generated on polymer matrix during the heating.

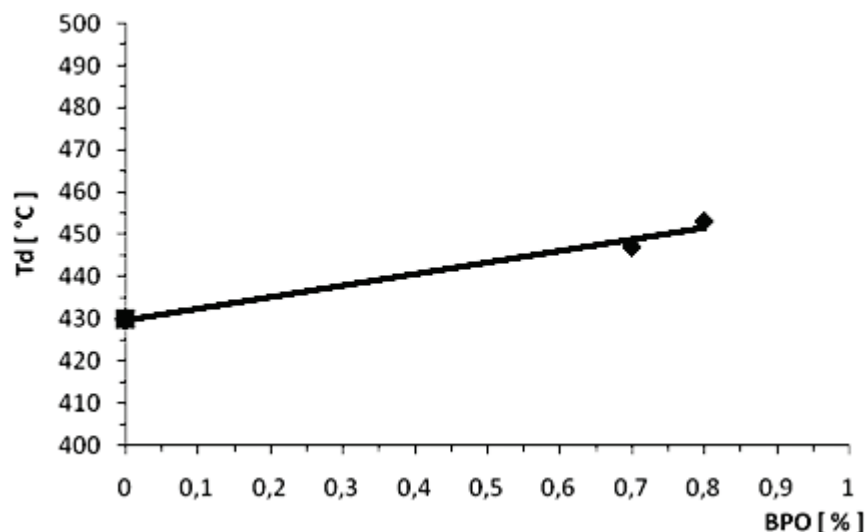


Figure 59. Decomposition temperature (T_d) of SBS and VBC grafted derivatives as function of BPO molar percentage

Elemental analysis

From residual phases monomeric composition, calculated by equation (3.3) from $^1\text{H-NMR}$ data, their elemental compositions has been calculated. SBS matrix and three residual phases were characterized by means of elemental analysis (Carbon, Hydrogen and Chlorine) in order to compare these data with $^1\text{H-NMR}$ ones. On Table 22 a comparison is reported, showing comparable results for the two techniques.

Sample	Elemental analysis			$^1\text{H-NMR}$		
	C	H	Cl	C	H	Cl
	wt%	wt%	wt%	wt%	wt%	wt%
SBS	89.6	10.4	0.0	90.4	9.6	0.0
R-SBS-F13	88.2	9.3	3.2	87.6	9.0	3.3
R-SBS-F15	86.6	9.3	4.1	87.0	9.0	4.0
R-SBS-F23	87.5	8.0	4.5	86.8	8.8	4.4

Table 22. Elemental analysis and $^1\text{H-NMR}$ data comparison for the SBS matrix and three residual phases

Scanning electron microscopy (SEM)

Residual phases were solubilized in chloroform (≈ 13 g/L) and casted on a glass petri dish; by slow evaporation in a chloroform saturated environment at room temperature films having thickness of ≈ 100 μm were obtained. Scanning electron microscopy (SEM) coupled with energy dispersive X-ray spectroscopy (EDS) was used in order to evaluate films morphologies. Micrographs of a film prepared using the residual phase of batch SBS-F23 show an homogeneous structure having no microscopic defects (Figure 60).

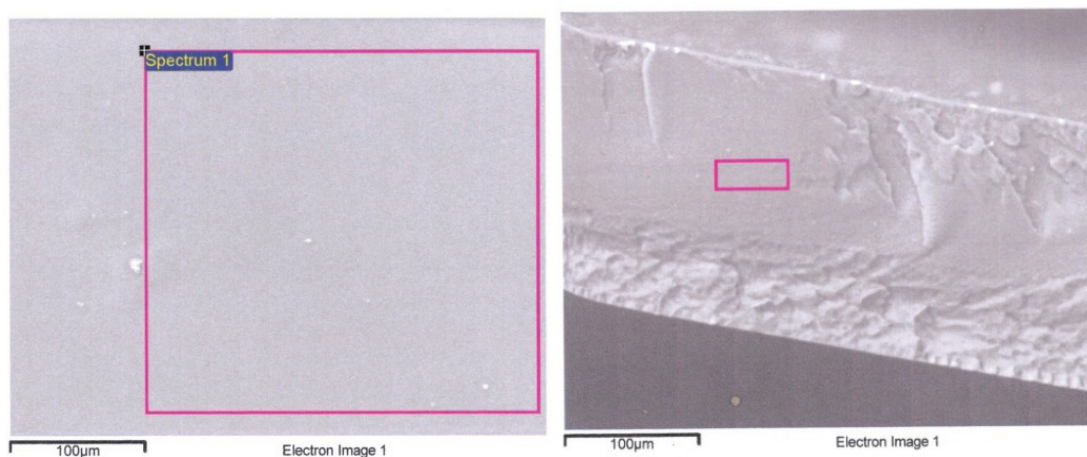


Figure 60. SEM micrographs of surface (left) and fracture (right) for R-SBS-F23 film

Energy dispersive X-ray spectroscopy showed a chlorine percentage for R-SBS-F23 comparable with $^1\text{H-NMR}$ and elemental analysis, moreover its distribution is homogeneous across the film fracture (Figure 61).

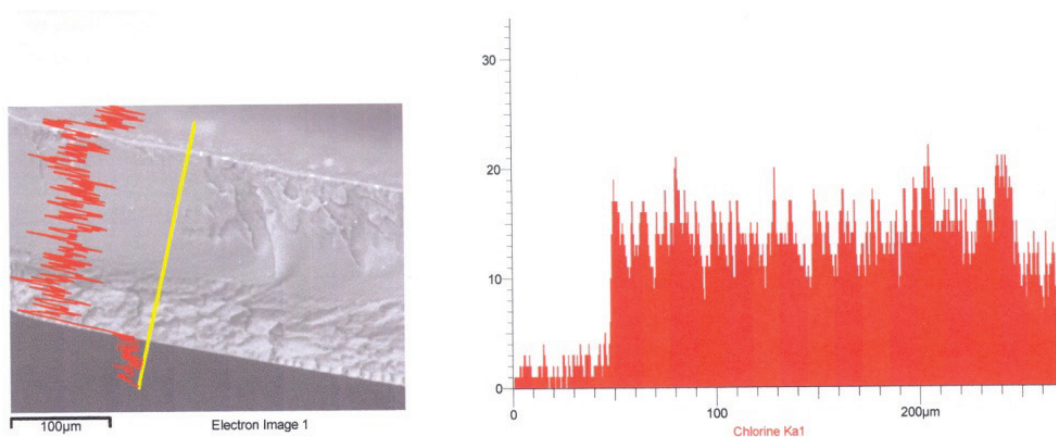


Figure 61. SEM microscopy (left) of R-SBS-F23 film showing the scanning line (yellow) for EDS chlorine analysis. Chlorine distribution (right) across the film fracture.

FT-IR microscopy

FT-IR microscopy is a technique that merges optical microscopy with spatially resolved FT-IR spectroscopy, facilitating inspection of restricted regions of the examined sample and giving thus hint of physical and chemical composition homogeneity. Optical micrograph of SBS-F17 residual phase film (Figure 62) shows an homogeneous surface, 40 FT-IR spectra were collected along the blue line marked on the micrograph and reported on the right, this set of spectra show spatial chemical homogeneity of the casted film, confirm the energy dispersive X-Ray results.

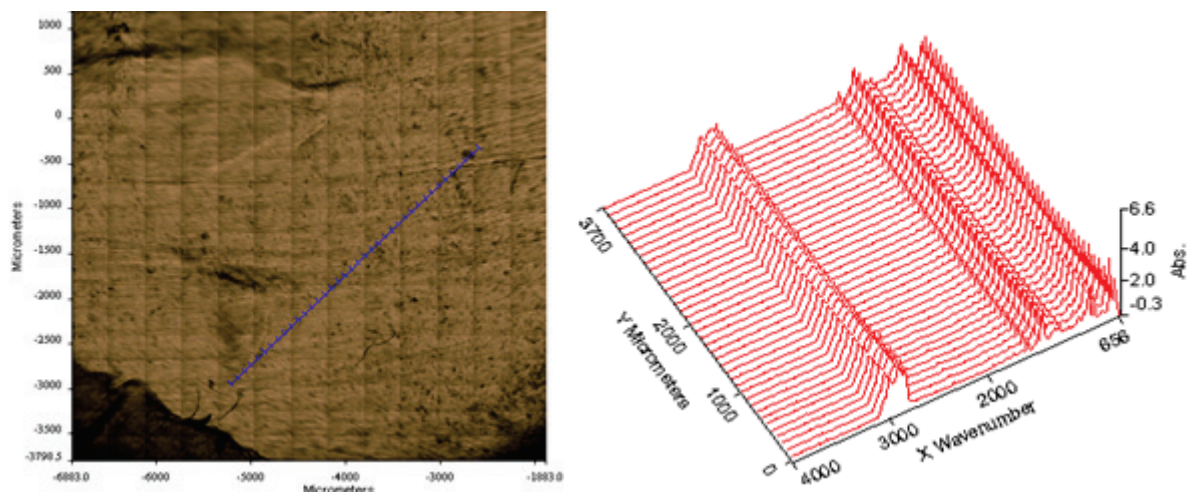


Figure 62. Surface optical micrograph (left) of R-SBS-F17 film. Spatially resolved FT-IR spectra (right) collected along the blue line sketched on the left micrograph

3.2.2 SBS-g-VBC quaternization

To ensure anionic conduction properties the polymer matrix must incorporate cationic functionality. A quaternary ammonium group grafted onto the polymer matrix exhibits the best thermal and chemical stabilities(85).

In an alkaline medium quaternary ammonium groups can be very sensitive to Hoffman degradation (86), leading to the formation of a tertiary amine and a non-charged olefin.

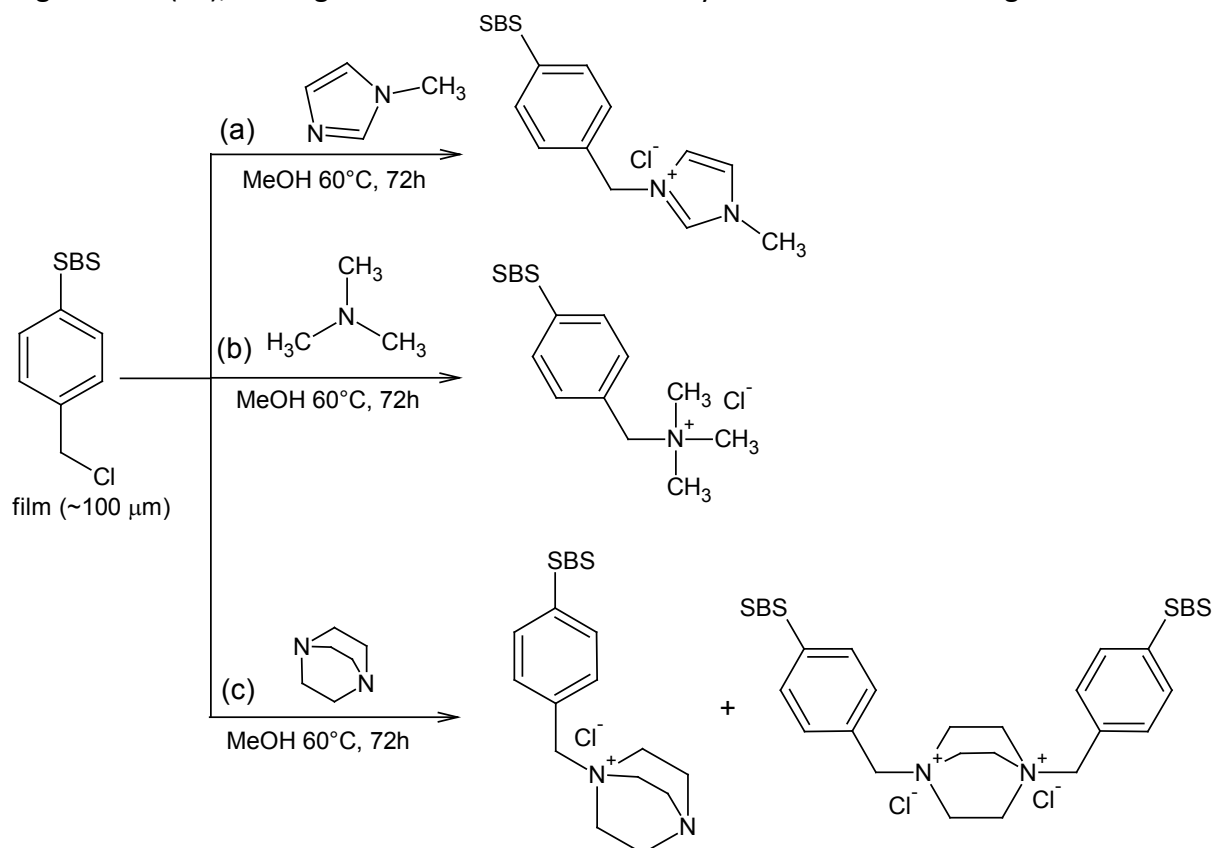


Figure 63. Quaternization reactions between grafted chlorobenzyl groups and (a) N-methylimidazole, (b) trimethylamine and (c) DABCO

This reaction implies the presence of an hydrogen atom in beta position respect to the nitrogen atom of the quaternary ammonium group and need an anti-periplanar (180°) or

syn-periplanar (0°) conformation, easily obtained at room temperature due to the low rotational barrier between the conformations. Benzyl chloride groups grafted onto the SBS matrix can be converted into quaternary ammonium groups via quaternization reaction with a tertiary amine. In order to avoid Hoffmann degradation reaction chosen tertiary amine should have no β -hydrogens (such as trimethylamine), or an high rotational barrier (such as strained cyclic amines). An interesting tertiary amine is the 1,4-diazabicyclo[2.2.2]octane (DABCO): even though there are several β -hydrogens its bicyclic structure prevents interconversion between conformers, moreover being a diamine can produce crosslinked structure during the quaternization reaction (Figure 63 c).

Films of the residual phases, having thickness of $\approx 100 \mu\text{m}$, were prepared and reacted with 1M methanol solution of DABCO for 72h at 60°C . In order to better understand crosslinking effect on electrochemical properties, residual phase films of batch SBS-F16 were quaternized using mixtures of DABCO and N-methylimidazole (Figure 63 a), whereas residual phase films of a new batch (SBS-F37, FD 11.6%) were quaternized with 1M methanol trimethylamine solution (Figure 63 b) and methanol DABCO solutions having concentrations between 1wt% and 5wt%.

FT-IR spectroscopic analysis

Comparing FT-IR spectra before and after quaternization reaction with DABCO for SBS-F10 residual phase film (Figure 64) peak at 1265 cm^{-1} , associated to $\text{CH}_2\text{-Cl}$ wagging, disappears whereas new peaks at 1313 and 1058 cm^{-1} show up, attributable to amine absorptions. Same behavior is observed for all the residual phases. Some of the characteristic absorptions for DABCO cannot be noticed on quaternized R-SBS-F10 FT-IR spectra since stronger peaks are already present before the quaternization.

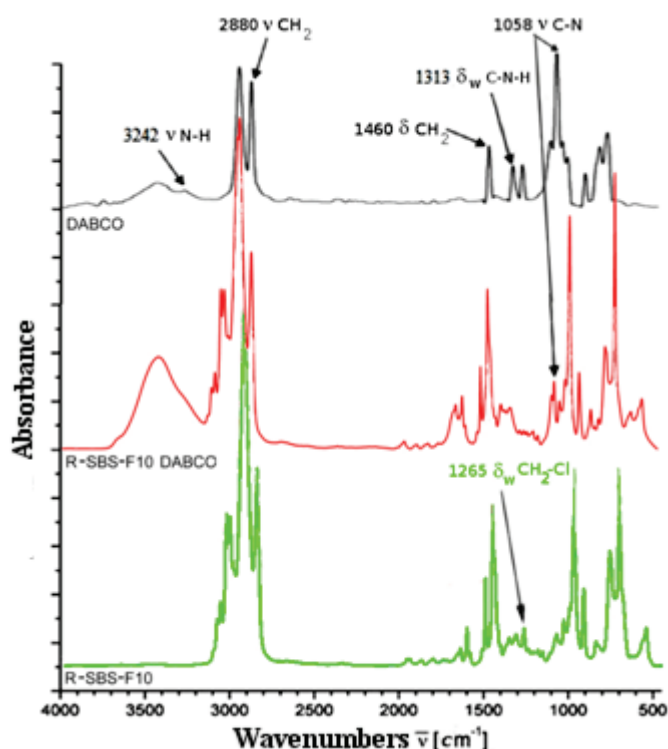


Figure 64. R-SBS-F10 FT-IR spectra before and after quaternization with DABCO

For the same reason weak bands between 1313 and 1460 cm^{-1} relative to quaternary ammonium salt absorption, as reported in literature (87), are not detectable.

A similar behavior can be observed using trimethylamine (Figure 65) or N-methylimidazole for the quaternization reaction.

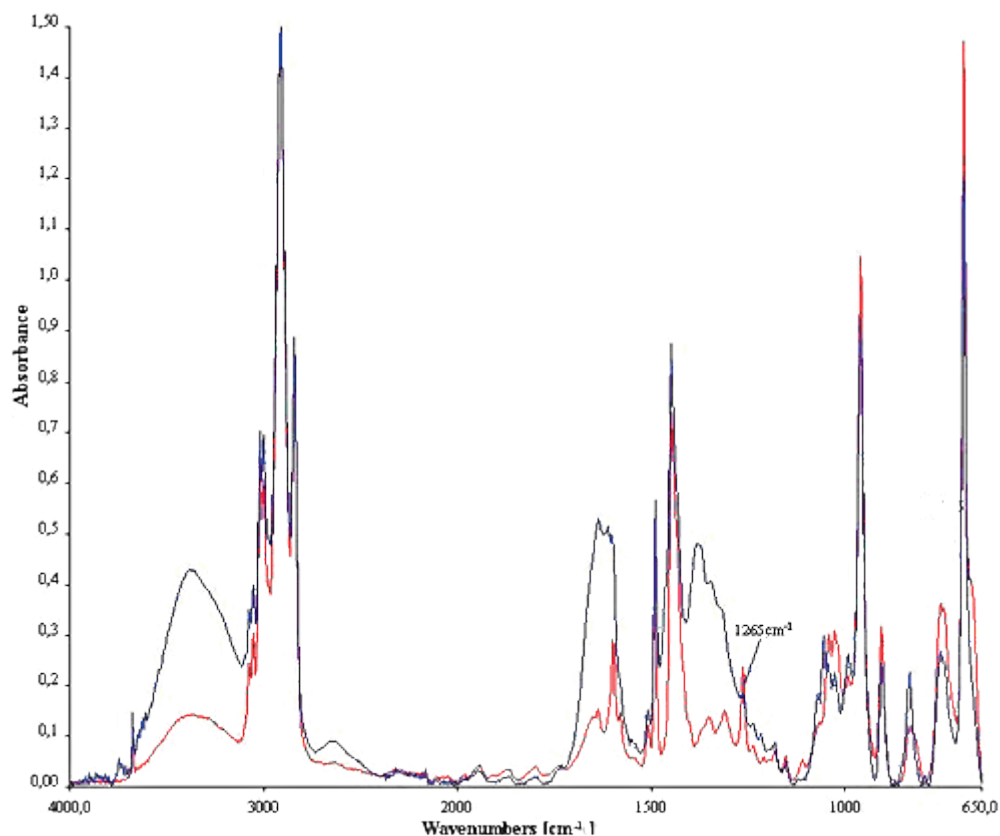


Figure 65. R-SBS-F37 FT-IR spectra before (red line) and after (blue line) quaternization with TMA

For all the quaternized films CH_2Cl wagging absorption at 1265 cm^{-1} disappears, confirming thus that the reactions were all complete having no chloromethylenic units left.

¹H-NMR spectroscopic analysis

Since films quaternized with DABCO were not soluble in common deuterated solvents due to crosslinking, NMR analysis was not performed on these samples.

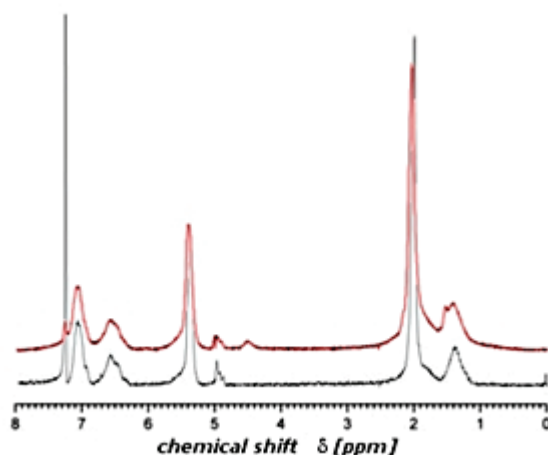


Figure 66. R-SBS-F37 ¹H-NMR spectra before (red line) and after (black line) quaternization with TMA

On the contrary, residual phases quaternized with TMA are all soluble in CDCl_3 . On Figure 66 is reported a comparison of $^1\text{H-NMR}$ spectra before and after TMA quaternization of a R-SBS-F37 film: signal at 4.5 ppm related to chloromethylene units disappears, confirming that quaternization was complete, as already stated by FT-IR analysis.

Scanning electron microscopy (SEM)

After the quaternization reaction the polymer assumes a positive charge, increasing its swelling in polar solvents such as methanol or water. An excessive swelling may change the film morphology. Micrographs of an R- SBS-F23 DABCO quaternized film show an homogeneous structure both for its surface and fracture (Figure 67). Similar results were obtained for the hydroxyl form of the membrane, exchanged as described in the experimental section.

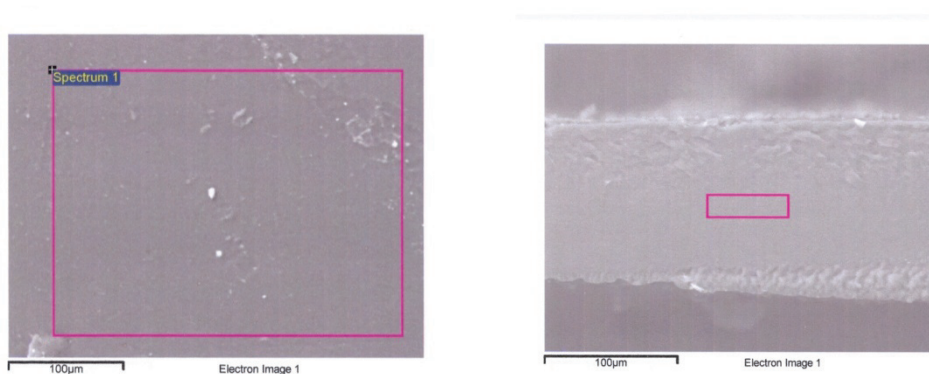


Figure 67. SEM micrographs of surface (left) and fracture (right) for R-SBS-F23 film quaternized with DABCO

FT-IR microscopy

In order to confirm morphological and chemical homogeneity optical micrograph coupled with spatially resolved FT-IR spectra were collected for R-SBS-F17 DABCO quaternized film (Figure 68): film surface is smooth meaning that quaternization reaction and subsequent higher solvent swelling didn't damage its structure, moreover from the FT-IR spectra it's clear that the reaction was evenly complete all over the surface.

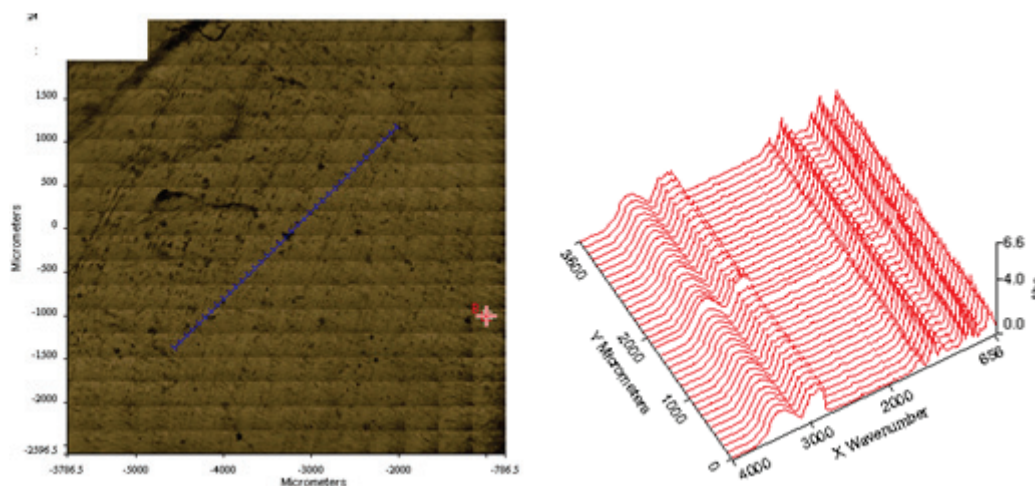


Figure 68. Surface optical micrograph (left) of DABCO quaternized R-SBS-F17 film. Spatially resolved FT-IR spectra (right) collected along the blue line sketched on the left micrograph

Thermal analysis (TGA, DSC)

Thermogravimetric curve of DABCO quaternized R-SBS-F11 film shows two decomposition temperatures (Figure 69). First decomposition temperature at 270.5°C (6.50% weight loss) is most likely due to quaternary ammonium decomposition. Second decomposition temperature at 447.5°C (88.28% weight loss) is due to SBS matrix degradation, as already stated discussing TGA analysis for unreacted residual phases (Figure 59). Since decomposition temperatures are far above the operating temperature range (25-80°C) of the considered electrochemical applications, the membrane is thermally stable.

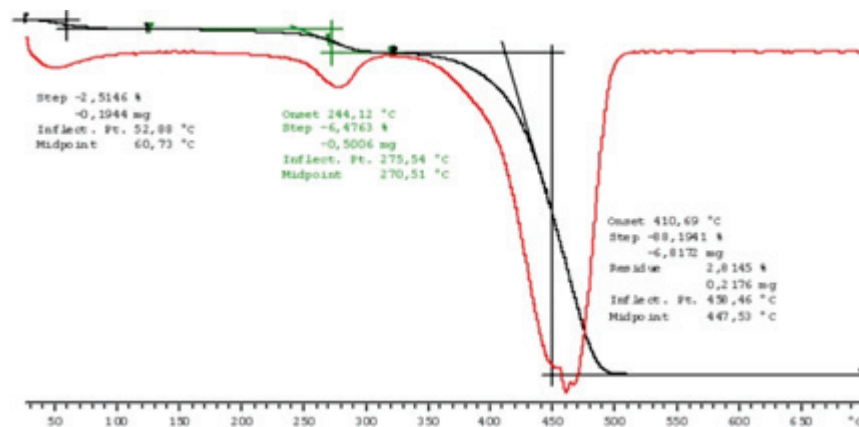


Figure 69. DABCO quaternized R-SBS-F11 film (Cl-form) TGA curve

Thermogravimetric analysis was performed on the same film after KOH solution conditioning, in order to determine how hydroxyl counterion modifies the membrane thermal stability. Also in this case (Figure 70) two decomposition temperatures are found at 264.7°C and 445.9°C, confirming that the membrane is thermally stable at the operating condition for the considered electrochemical applications.

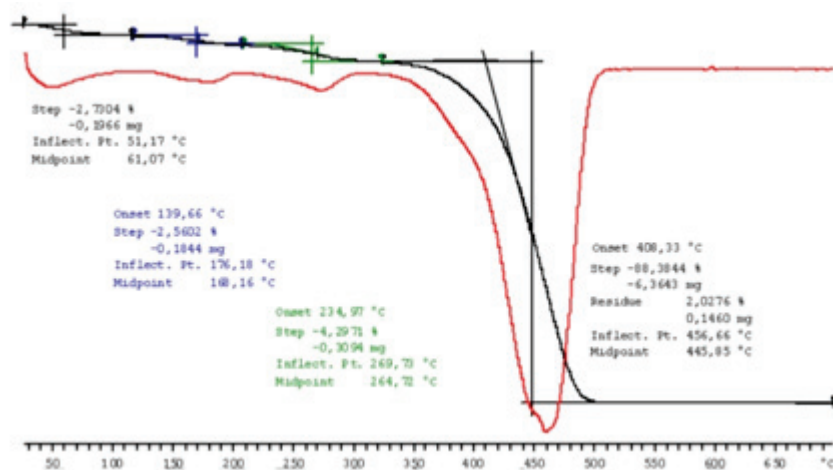


Figure 70. DABCO quaternized R-SBS-F11 film (OH-form) TGA curve

Thermal properties were furthermore investigated by means of Differential Scanning Calorimetry (DSC), comparing glass transition temperatures (T_g) of raw SBS with DABCO quaternized derivative both in chloride and hydroxyl forms. DSC curves for different samples have similar shape, showing two glass transition temperatures: lower one relative to butadienic block (T_{g1}), higher one relative to styrenic blocks (T_{g2}). A typical DSC curve is showed on Figure 71 for DABCO quaternized R-SBS-F11 (Cl-form).

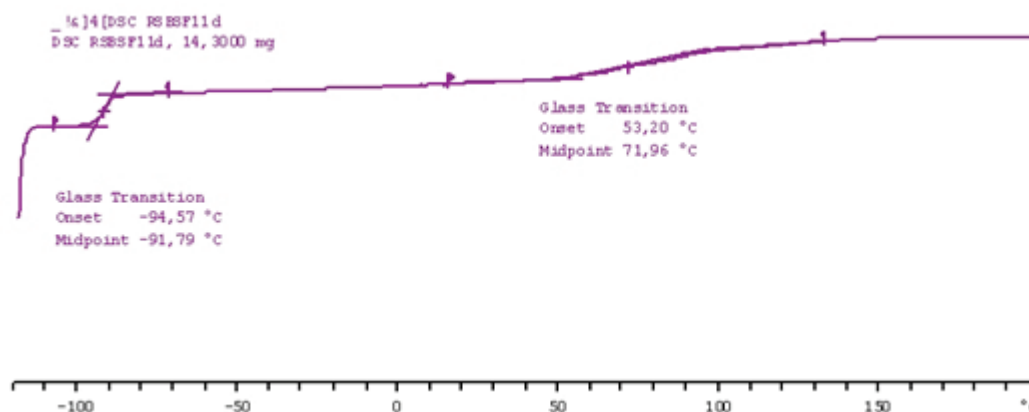


Figure 71. DABCO quaternized R-SBS-F11 film (Cl-form) DSC curve

Glass transition temperatures comparison for raw SBS (Calprene 501) and DABCO quaternized R-SBS-F11 (both chloride and hydroxyl forms) is reported on Table 23. Grafting reaction and subsequent DABCO quaternization do not affect thermal properties: butadienic block glass transition temperature (T_{g1}) changes of 5°C aren't sensible, suggesting that VBC grafting and subsequent DABCO quaternization on this block didn't stiffen the polymer chain. Since crosslinking tends to increase the glass transition temperature, this result suggest that quaternized R-SBS-F11 has a very low crosslinking ratio after quaternization with 1M DABCO solution in MeOH. Similar behavior is observed for all the samples quaternized with 1M DABCO solution in MeOH.

Sample	Tg1 [°C]	Tg2 [°C]
SBS (Calprene 501)	-87	69
R-SBS-F11 + DABCO (Cl-form)	-92	72
R-SBS-F11 + DABCO (OH-form)	-92	67

Table 23. Glass transition temperature comparison between raw SBS (Calprene 501) and DABCO quaternized R-SBS-F11 both in chloride and hydroxyl forms

3.2.3 Electrochemical characterization

In the previous paragraphs was described a synthetic protocol to develop an anion-exchange material based on the triblock commercial copolymer SBS by means of free radical grafting of VBC units on the butadienic block of SBS, separation of the grafted SBS-g-VBC copolymer from the PVBC homopolymer and subsequent quaternization of the SBS-g-VBC copolymer using mono or diamines, performed in order to convert grafted chlorobenzyl groups into quaternary ammonium salts.

Benzoyl peroxide (BPO), as free radical initiator, showed a higher yield in SBS-g-VBC product compared to α,α' -azo-bis-isobutyronitrile (AIBN) more suitable to produce VBC homopolymer (Figure 46). Separation of PVBC homopolymer from the envisaged grafted copolymer via acetone extraction was complete (FT-IR, $^1\text{H-NMR}$, $^{13}\text{C-NMR}$ and GPC data). Moreover the functionalization degree (FD), calculated by $^1\text{H-NMR}$ data and confirmed by elemental analysis, of the for residual phases is highly tunable being positively correlated to the percentage of radical initiator. Quaternization reactions were performed using amines not sensible to Hoffman degradation (DABCO, TMA and N-methylimidazole). Quaternization

reactions completeness was confirmed by $^1\text{H-NMR}$ and FT-IR spectroscopies. Diamines such as DABCO introduce a certain crosslinking degree between different chains, in fact the resulting films were not soluble in chloroform and other common solvents. The introduced crosslinking should help to obtain materials having better mechanical properties. Furthermore, the resulting membranes are thermally stable at the envisaged operating temperature range (TGA and DSC data) and physically and chemically homogeneous (SEM and FT-IR microscopies data).

In the first chapter were discussed the required properties, mainly high through plane conductivity and low water uptake, of an ion-exchange membrane for the considered low temperature electrochemical applications and the design rules in order to optimize these properties. These discussions lead to the conclusion that at the same ion-exchange capacity (IEC) values and polymer molecular weight (M_w) a block copolymer matrix having side chain ionic functionality is preferable over a random copolymer having ionic charge onto the main chain.

Summarizing, the reported three-steps synthetic protocol (i.e. VBC grafting, purification, quaternization reaction) leads to a chemically and thermally stable anion-exchange membrane based on a cheap commercial SBS triblock copolymer complying with the design rules.

Functionalization Degree (FD) optimization

As mentioned before the FD can be easily tuned varying free radical initiator molar percentage during the grafting reaction (Figure 52).

Electrochemical parameters were evaluated as described in the experimental section for membranes prepared using R-SBS-F13, R-SBS-F16 and R-SBS-F37 films after being quaternized with 1M solution of DABCO in methanol. Electrochemical parameters obtained for the Tokuyama A-201 commercial membrane were used as benchmark values in order to optimize FD value.

Ion exchange capacities (IECs) are compared with the approximated values calculated from $^1\text{H-NMR}$ data in Table 24.

Sample	FD [mol%]	IEC _{exp} [meq/g _{polymer}]	IEC _{th} [meq/g _{polymer}]
Tokuyama A-201	-	1.84±0.04	-
R-SBS-F13+DABCO	7.0	0.52±0.05	0.9
R-SBS-F16+DABCO	8.1	0.82±0.05	1.0
R-SBS-F37+DABCO	11.6	1.21±0.04	1.4

Table 24. SBS-based membranes ion-exchange capacities measured by back titration (IEC_{exp}) and calculated from $^1\text{H-NMR}$ data (IEC_{th}). Tokuyama A-201 membrane IEC_{exp} is reported as benchmark

The films show a lower experimental value for IEC, obtained by back titration, compared to the $^1\text{H-NMR}$ calculated ones. Since incomplete quaternization (IR, NMR) and thermal degradation (TGA) of the membranes should be excluded, the difference is probably due to inaccurate molecular weight used in the calculation: the calculated IEC_{th} is just indicative, especially for DABCO, since we do not know the exact crosslinking ratio in order to evaluate

the quaternized molecular weight of VBC fragments to be used in equation (3.4). However experimental and calculated IECs are positively correlated, hence calculated values give a good hint on the real IEC. The three synthesized membranes exhibit a lower IEC compared to the benchmark; the gap doesn't change considering the volumetric swelling since polymer densities are similar (1.1 g/cm^3 for the benchmark, 0.94 g/cm^3 for the SBS-based membranes).

On Figure 72 is reported an histogram of Water Uptake (WU) data for the hydroxyl form of the considered SBS-based films: increasing the FD water swelling increases as well. This trend was predictable: an higher FD (i.e. higher IEC) would result in a comb-type polymer having more side chains or longer side chains. In either case charge density of the butadienic block would be higher, increasing thus its hydrophilicity and the water swollen at the equilibrium. This data suggest that increasing the ion-exchange groups concentration newly bonded ionic groups are reachable by the solvent, hence, an higher ionic conductivity is expected increasing the FD. Nevertheless IECs of the SBS-based membrane are lower compared to the benchmark, their swelling is slightly higher but still promising.

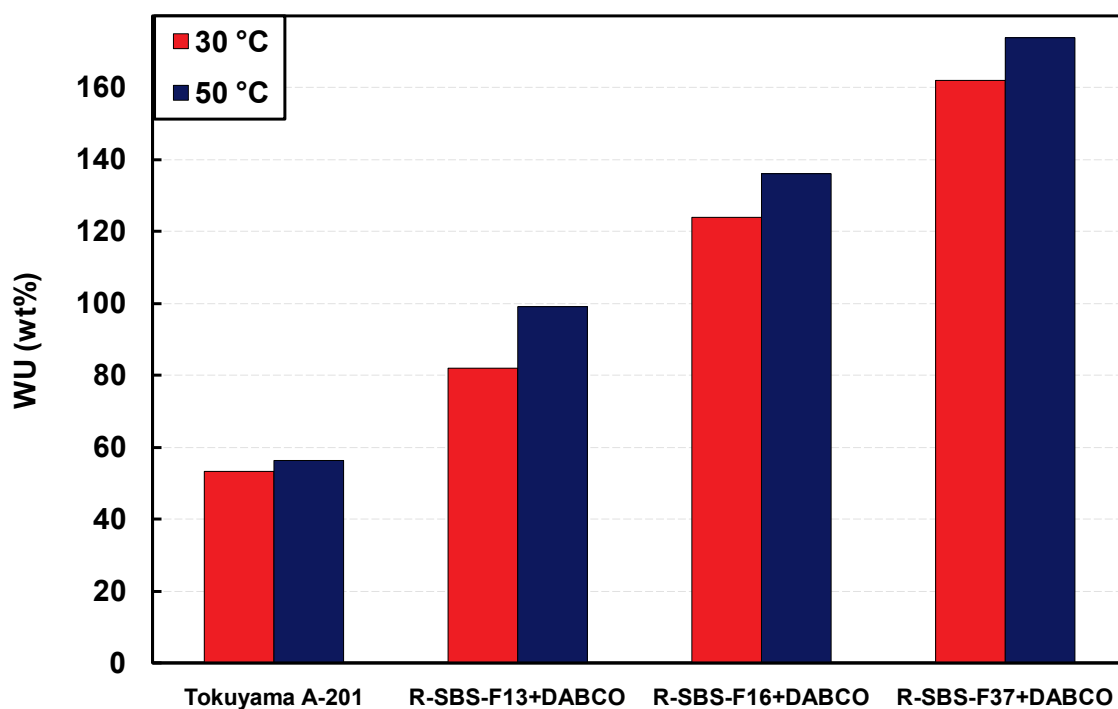


Figure 72. Water uptake (WU) comparison, expressed as wt%, at different temperatures of three DABCO quaternized SBS-based membranes (OH-form) having different FD. Tokuyama A-201 swelling (OH-form) is reported as benchmark

On Figure 73 in-plane ionic conductivities, measured at 30°C, are reported for both bicarbonate and hydroxyl forms of the three SBS-based and benchmark membranes: as suggested by WU data analysis increasing the FD ionic conductivity increases as well. Nevertheless R-SBS-F37 based membrane IEC is lower than the Tokuyama benchmark membrane one, its ionic conductivity at 30°C is higher in both bicarbonate and hydroxyl forms. Moreover, ionic conductivities for bicarbonate forms are ≈ 4 -fold lower than that of the hydroxyl form, consistent with the approximately 4-fold lower equivalent ionic

conductance in water of bicarbonate ions compared to hydroxide, suggesting an ion transport mechanism similar to the one that occur in water.

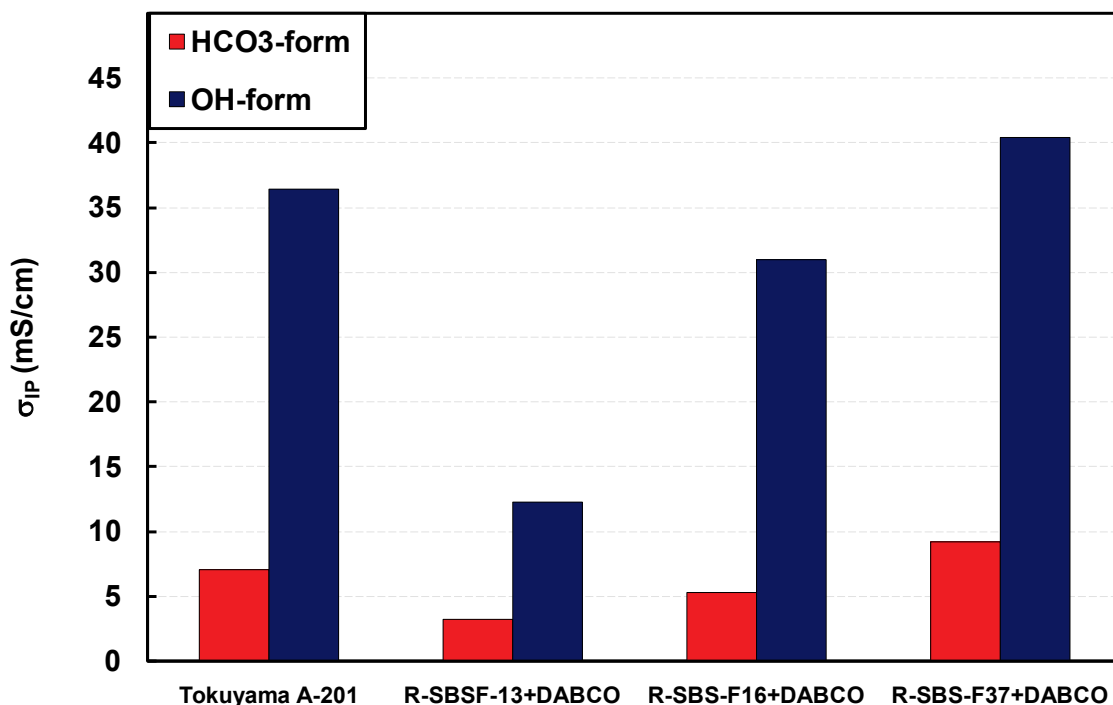


Figure 73. In-plane conductivities (σ_{IP}) comparison at 30°C, both in hydroxyl (blue bars) and bicarbonate (red bars) forms, of three DABCO quaternized SBS-based membranes having different FD. Tokuyama A-201 in-plane conductivities (both hydroxyl and bicarbonate forms) at 30°C are reported as benchmark

Best trade-off between ionic conductivity and water swelling was found for R-SBS-F16 based membrane, having FD 8.1 mol%, which conductivity is comparable with the benchmark material and water uptake is slightly higher but still acceptable. In order to check whether the membranes show an isotropic behavior, through-plane conductivity at 30°C was measured for the bicarbonate form of the three SBS-based membranes. Data reported on Table 25 confirm the isotropic behavior.

Sample	FD [mol%]	σ_{IP} [mS/cm]	
		HCO ₃ -form	HCO ₃ -form
R-SBS-F13+DABCO	7.0	3.2	3.3
R-SBS-F16+DABCO	8.1	5.3	5.5
R-SBS-F37+DABCO	11.6	9.2	9.1

Table 25. In-plane and through-plane conductivities comparison at 30°C for the bicarbonate form of the three DABCO quaternized SBS-based membranes, having different functionalization degree

Thus, a positive correlation between the FD, tunable during the synthesis, of the synthesized DABCO quaternized SBS-g-VBC based membranes and both water swelling and ionic conductivity, has been found. Moreover, simply tuning the FD of these SBS-based membranes ionic conductivities higher than the commercial benchmark membrane has been obtained (R-SBS-F37), though water uptake has yet to be reduced. Finally, the synthesized SBS-based membranes show an isotropic behavior.

Crosslinking optimization (amines mixing)

Other than FD another tunable parameter during the described SBS-based membrane synthesis is the crosslinking ratio. Its tuning can be achieved modifying the quaternization reaction conditions. A first attempt was made quaternizing four R-SBS-F16 films with a solution obtained mixing different amounts of 1M DABCO (diamine) solution in methanol and 1M N-methylimidazole (monoamine) solution in methanol, as reported in Table 26. On the same table x_{link} is the theoretical crosslinking percentage, calculated assuming that DABCO quaternization always give raise to crosslinking and quaternization probability with an amine type is given by the normalized product of its concentration and the number of amine groups per molecule:

$$x_{link} = \frac{2 \cdot DABCO\%}{100 + DABCO\%} \cdot 100 \quad (3.5)$$

where DABCO% is the volumetric percentage of the 1M DABCO solution in methanol, used to prepare the quaternizing solution. For simplicity the theoretical crosslinking percentage has been used as label to distinguish between the membranes obtained using the respective amines solution mixture (e.g. R-SBS-F16 50% for the membrane having a theoretical crosslinking percentage equal to 50%).

Sample	DABCO 1M solution [vol%]	N-methylimidazole 1M solution [vol%]	x_{link} %
R-SBS-F16 100%	100	0	100
R-SBS-F16 75%	60	40	75
R-SBS-F16 50%	33.3	66.7	50
R-SBS-F16 25%	14.3	85.7	25

Table 26. Composition of the solutions used to quaternize four R-SBS-F16 casted films and resulting theoretical crosslinking (x_{link}), calculated using equation (3.5)

Complete quaternization was confirmed by means of FT-IR spectroscopy: CH_2Cl wagging absorption at 1265 cm^{-1} disappears for all the samples. Ionic exchange capacities (IECs) are reported in Table 27. Since all the examined membranes have the same FD (8.1 mol%), IEC values should be the same for all the samples, in fact all data are within experimental errors (ca. $\pm 0.05 \text{ meq/g}_{\text{polymer}}$).

Sample	FD [mol%]	IEC_{exp} [meq/g _{polymer}]
R-SBS-F16 100%	8.1	0.82
R-SBS-F16 75%	8.1	0.85
R-SBS-F16 50%	8.1	0.83
R-SBS-F16 25%	8.1	0.79

Table 27. Ionic exchange capacities measured for the four R-SBS-F16 based membranes, obtained by quaternization reaction using methanol solutions containing different amounts of DABCO and N-methylimidazole, as reported in Table 26

On Figure 74 water uptake data, expressed as weight percentage, are reported against theoretical crosslinking percentage (x_{link}) at both 30°C and 50°C: even though the crosslinking

percentage is a pure theoretical data, based on the arguable assumption of complete crosslinking by DABCO, a perfectly negative linear correlation is observed. Thus, even though the real crosslinking is not known, varying this theoretical value modify in a different scale the real crosslinking ratio.

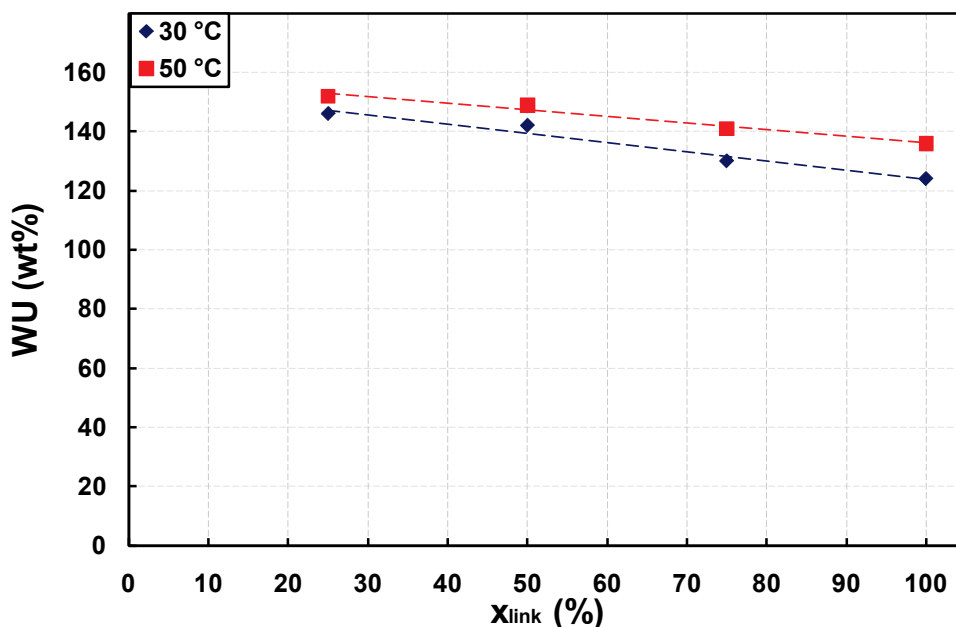


Figure 74. Water uptake (WU) comparison, expressed as wt%, at different temperatures of DABCO/ N-methylimidazole quaternized SBS-based membranes (OH-form) having different theoretical crosslinking percentage (x_{link})

In-plane conductivities at 30°C, for both bicarbonate and hydroxyl forms are plotted against x_{link} percentage on Figure 75: a negative linear correlation between the theoretical parameter and conductivity is found and confirm a change on the real crosslinking ratio.

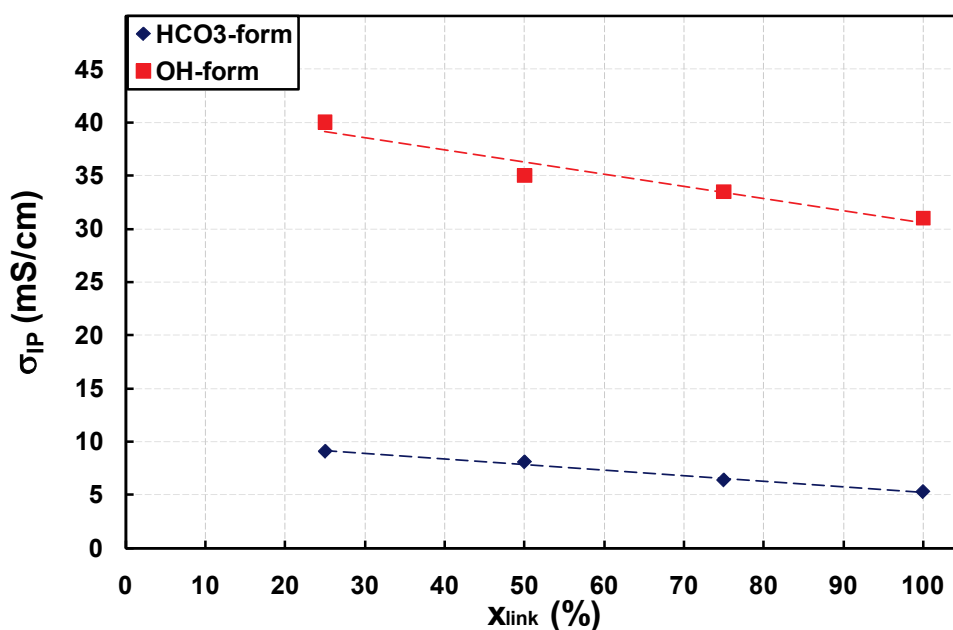


Figure 75. In-plane conductivities (σ_{IP}) comparison at 30°C, both in hydroxyl (blue bars) and bicarbonate (red bars) forms, of DABCO/ N-methylimidazole quaternized SBS-based membranes having different theoretical crosslinking percentage (x_{link})

Therefore the crosslinking ratio can be effectively modified mixing DABCO with a monoamine, such as N-methylimidazole or trimethylamine, in order to tune the electrochemical parameters. Moreover, even though the actual value of the crosslinking is not known, a theoretical value can be defined as in equation (3.5) in order to define a new scale inside the crosslinking window affected by amine solution mixing prior to quaternization reaction.

Crosslinking optimization (DABCO concentration)

Even though crosslinking ratio can be tuned mixing DABCO with a monoamine, as reported in the previous paragraph, the assumption previously made in order to estimate the crosslinking percentage is arguable, since a chlorobenzyl group may react with amine groups coming both from a one-side quaternized DABCO molecule, leading to crosslinking, or with an unreacted DABCO molecule, coming from the solution (see Figure 63 c). In literature (88) is reported that an important parameter to tune DABCO crosslinking during the quaternization reaction is its molar fraction relative to the chlorobenzyl groups: lower the relative molar fraction, higher the crosslinking degree. Thus, in principle, there's no need to mix DABCO with a monoamine in order to tune the resulting crosslinking ratio: DABCO concentration is correlated to this parameter.

In order to verify and study this correlation five R-SBS-F37 films have been quaternized with methanol solutions of DABCO having concentration ranging from 1wt% to 5wt%. A sixth R-SBS-F37 film was quaternized using a trimethylamine (TMA) solution in methanol (5 wt%) in order to obtain a crosslinking-free membrane. Amine solutions used for R-SBS-F37 quaternization reactions are reported in Table 28, along with ion-exchange capacities of the obtained membranes. All the IEC data are within experimental error (ca. ± 0.05 meq/g_{polymer}), complete quaternization was confirmed by means of FT-IR spectroscopy.

Batch	Amine solution	IEC _{exp}
	in methanol	[meq/g _{polymer}]
#0	TMA (5 wt%)	1.20
#1	DABCO (1 wt%)	1.18
#2	DABCO (2 wt%)	1.22
#3	DABCO (3 wt%)	1.21
#4	DABCO (4 wt%)	1.25
#5	DABCO (5 wt%)	1.18

Table 28. Ionic Exchange Capacity data for R-SBS-F37 based membranes obtained quaternizing the grafted copolymer with the reported amine solutions

For the membrane obtained by quaternization reaction with trimethylamine (batch #0) an in-plane conductivity at 30°C in liquid water of the bicarbonate form of 12 mS/cm and a water uptake at the same temperature of ≈ 300 wt% were measured. These values, being relative to a membrane having same FD and no crosslinking, can be used as reference values for the data reported in Figure 76 where in-plane conductivities and water uptake of the bicarbonate form of DABCO quaternized R-SBS-F37 based membranes are plotted against

DABCO concentration. As expected both water swelling and conductivities are positively correlated with DABCO concentration, confirming that decreasing its value increase the crosslinking ratio of the resulting membranes. Contrarily to the case where crosslinking was tuned by mixing DABCO with a monoamine the way water uptake and conductivity increase with DABCO concentration are different: while water swelling increases linearly, conductivity increases asymptotically to the crosslinking-free value, having a value which is compared to the reference one at 3wt% of DABCO concentration. Compared to the crosslinking free membrane (batch #0), the membrane obtained using 3wt% of DABCO shows a decrease in water swelling and conductivity of two third and one third respectively.

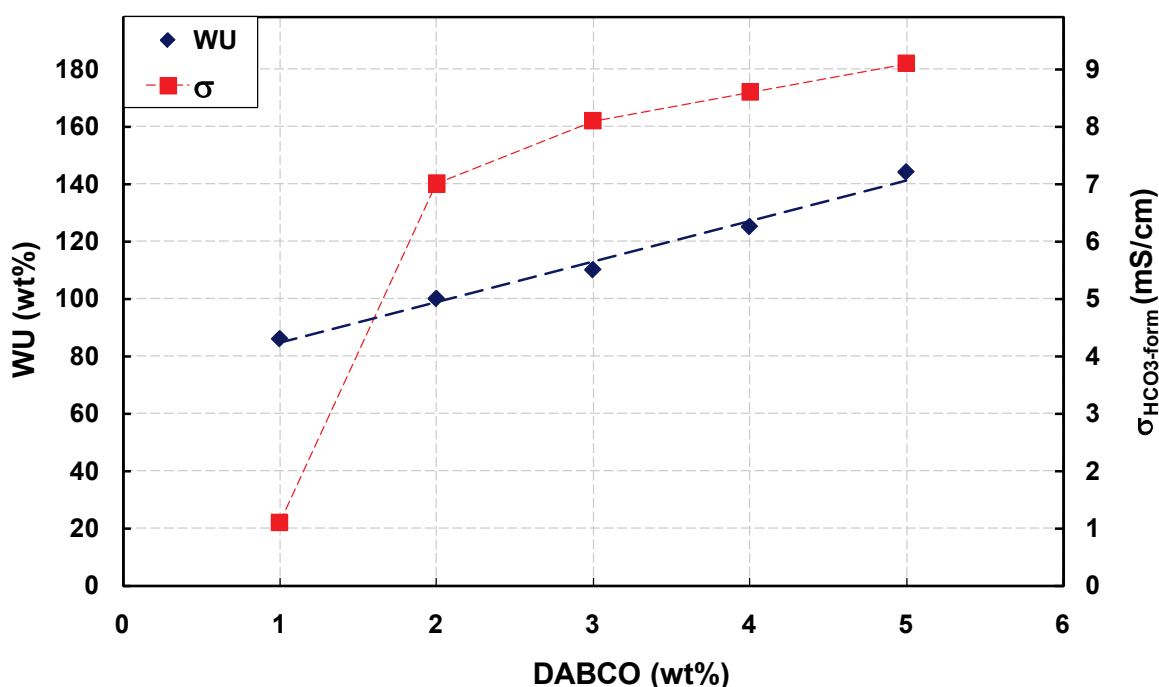


Figure 76. In-plane conductivities ($\text{HCO}_3\text{-form}$) in liquid water and water swelling (expressed as wt%) at 30°C of R-SBS-F37 based membranes as function of DABCO concentration during the quaternization reaction

These data suggest that tuning crosslinking degree using different concentration of DABCO in the quaternizing solution would result in a large water swelling decrease, with a small decrease in ionic conductivity. Thus, together with the FD, the DABCO concentration can be tuned in order to efficiently obtain an SBS-based membrane having high ionic conductivity and low water swelling.

In-plane conductivities in liquid water for the bicarbonate form of the six batches were measured in the range between 15°C and 50°C. These values are correlated by an Arrhenius-like equation:

$$\ln \sigma_{\text{HCO}_3}(T) \propto \frac{E_a}{RT} \quad (3.6)$$

where σ_{HCO_3} is the in-plane conductivity of the bicarbonate form, E_a is the activation energy, R is the universal gas constant and T is the absolute temperature. In Figure 77 calculated activation energies are reported for the six batches: the values are of the same order of magnitude of free ions in water solution (e.g. 14.6 kJ/mol for a 0.1M KCl solution), suggesting an analogous transport mechanism inside these water swollen membranes.

Moreover the activation energy decreases as the DABCO concentration increases, confirming a decrease on the crosslinking ratio. Similar values (11 kJ/mol) were obtained for Nafion® and the benchmark Tokuyama membranes (Figure 40).

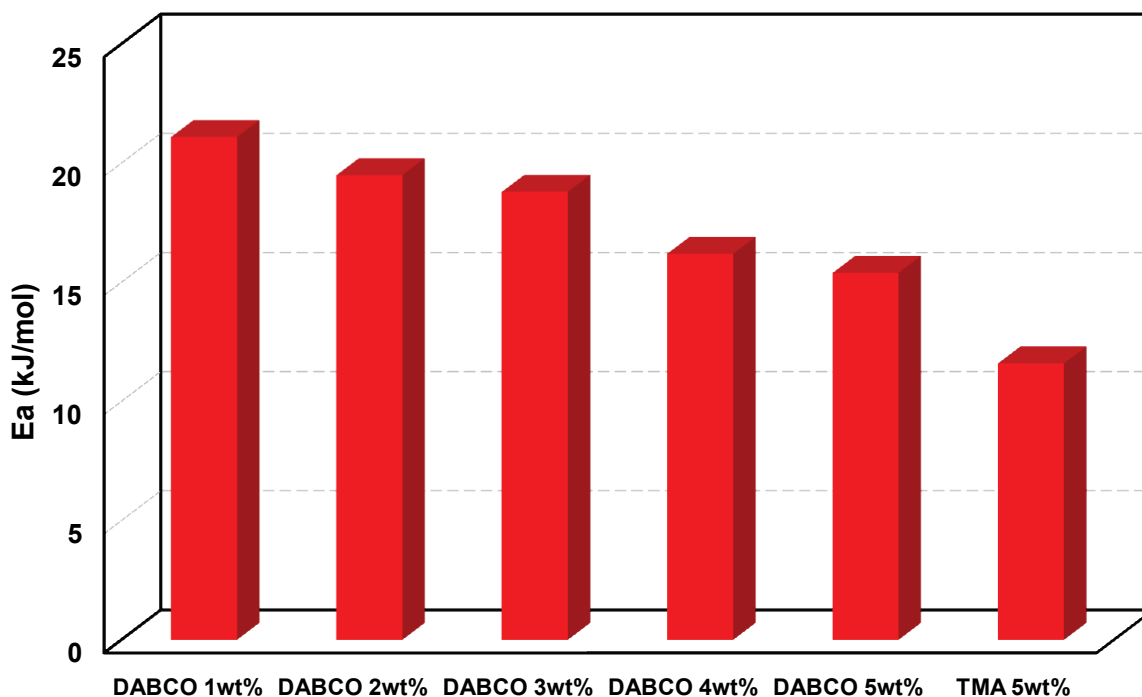


Figure 77. Arrhenius activation energy (E_a) of in-plane conductivities (HCO_3^- -form) for membranes obtained by quaternization reaction between RSBS-F37 films and different amine solutions in methanol

3.2.4 Morphology and transport properties

The relationship between ionomer structure and performance characteristics such as ionic conductivity continues to be a critical driving force for much of the structural research on ionomer membranes and provides the foundation for fundamental modeling work on these materials. For cation-exchange membranes, such as Nafion®, have been proposed several morphological models in order to correlate its structure with its properties, such as water management, hydration stability at high temperatures, electro-osmotic drag, as well as the mechanical, thermal, and oxidative stability. An early and most accepted model is the so called “Cluster-Network” model, consisting in an equal distribution of sulfonate ion clusters, also described as “inverted micelles” (89), with a 4 nm diameter held within a continuous fluorocarbon lattice. Narrow channels about 1 nm in diameter interconnect the clusters. This model, exemplified in Figure 78, is still used to describe the fundamental relationship between ionomer cluster structure and electrochemical properties (24).

Cluster-Network morphology emphasizes the fact that the solvent swelling and ionic conductivity of these ionomers are dominated by the cluster network, while certain other characteristics such as anion exclusion and hydrodynamic permeability are dominated by intra-cluster transport processes (90). These latter processes are presumed to involve transport inside of channels, possibly cylindrical in nature, that connect adjacent clusters.

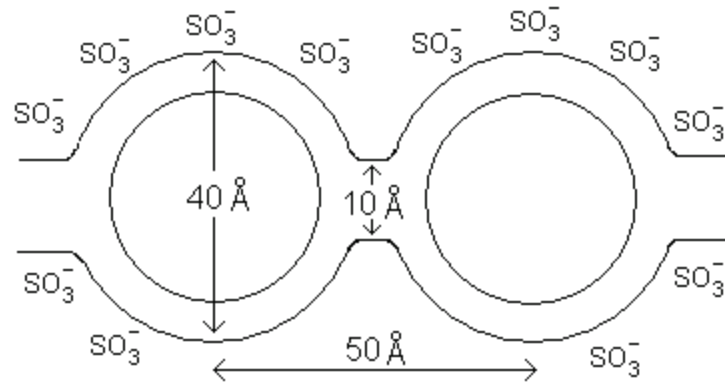


Figure 78. Morphological Cluster-Network model for Nafion® ionomeric membranes

Advanced morphological models include a network of ionic clusters; these models differ in the cluster geometries and distributions.

Assuming an analogous model for anion-exchange materials, consisting in an equal distribution of quaternary ammonium ion clusters, held within a continuous hydrophobic polymeric lattice (e.g. polystyrene for the synthesized SBS-based membranes) and interconnected by narrow cylindrical channels, some transport indexes will be defined, calculated and interpreted in terms of clusters size and interconnection.

Arrhenius-like activation energies reported in Figure 77 for SBS-based membranes suggest that ionic conduction mechanism inside the membrane matrix should be analogous to free ions in water.

In order to evaluate the influence of charged polymer matrix on the ionic mobility, an ionic transport ratio index has been proposed in literature (91). The ionic transport ratio, $\sigma_{\text{ratio}}(X/Y)$, compares the ionic conductivities ratio of two different membranes forms (e.g. hydroxyl and bicarbonate forms) with ionic conductivities ratio in water of the salts used to exchange the membranes counterions at the concentration equivalent to ionic groups density of the swollen membrane:

$$\sigma_{\text{ratio}}(X/Y) = \frac{\sigma_m(X)/\sigma_m(Y)}{\left[C_X \sum_i (n_i \lambda_i^0)_X \right] / \left[C_Y \sum_i (n_i \lambda_i^0)_Y \right]} \quad (3.7)$$

where $\sigma_m(X)$ and $\sigma_m(Y)$ are the ionic conductivities of the membrane exchanged respectively with solutions of salts X and Y, C_X and C_Y are the ionic groups concentration of the swollen membrane respectively on the X and Y forms, calculated scaling the IEC with the volumetric WU of the envisaged form, n_i is the charge of the i -th ion composing the respective salt (X or Y) and λ_i^0 is the respective limiting ionic conductivity. In the ideal case $\sigma_{\text{ratio}}(X/Y)$ should be equal to 1, deviation from this value indicates different interactions of counterions with fixed charges and water. For Nafion®, on the cited paper, is reported a $\sigma_{\text{ratio}}(\text{HCl}/\text{NaCl}) \approx 1$, thus the interaction between counterions and polymer sulfate fixed charge distributed on clusters doesn't affect the transport mechanism. Same index, calculated for crosslinked polysulphonic-based membranes (91) is above one, that is sodium ions mobility is hindered more than hydronium ions one. Comparing to Nafion®, this result is explained in terms of lower ratio between clusters diameter and channels length, that would

result in an increased ion association. For hydronium ions the hindrance is lower probably due to an hop, Grotthus-like, transport mechanism, less affected by an increased charge density of the clusters.

Ionic transport ratio index has been calculated by equation (3.7) for sodium hydroxide and sodium bicarbonate exchanged Tokuyama A-201 benchmark membrane and some of the SBS-based membranes using IEC, WU and ionic conductivities reported in the previous paragraphs:

Sample	IEC (meq/g)	%H ₂ O (vol/vol)	$\sigma_{ratio}(\text{NaOH}/\text{NaHCO}_3)$
Tokuyama A-201	1.84	50	2.1
R-SBS-F13+DABCO	0.52	77	1.5
R-SBS-F16 100%	0.82	116	2.4
R-SBS-F16 75%	0.85	122	2.1
R-SBS-F16 50%	0.83	133	1.8
R-SBS-F16 25%	0.79	137	1.8
R-SBS-F37+DABCO	1.21	154	1.8

Table 29. Ionic transport ratio $\sigma_{ratio}(X/Y)$ of commercial anion-exchange membrane Tokuyama A-201 and SBS-based membranes, having different FD and crosslinking ratio

Both commercial benchmark membrane and synthesized SBS-based membranes show a positive deviation from ideality ($\sigma_{ratio}>1$). Assuming a Cluster-Network-like morphological model a lower ratio between clusters diameter and channels length, compared to Nafion[®] ionomeric membranes, is suggested: hindrance for hydroxyl anion mobility is less than bicarbonate anions one probably due to a Grotthus-like hop transport mechanism for hydroxyl ions. For SBS-based membranes the index is nearer to ideality at lower IEC (R-SBS-F13 based membrane) and decreases increasing the water swelling (i.e. lower crosslinking ratio). During the VBC grafting reaction an higher FD would result in a comb-type polymer having more side chains or longer side chains. In the first case the charges resulting after the quaternization reaction are more distant, i.e. lower charge density, than the side chain grow case. Since the ionic transport ratio increases increasing the FD, an higher charge density is expected inside the clusters due to longer side chains resulting from an increase in radical initiator percentage during VBC grafting. At the same FD, an higher water content would dilute the charge density, increasing clusters diameter, resulting in the observed lower index.

Ionic transport ratio is thus a useful index in order to understand the resulting morphology of the synthesized membrane.

Ions in solution are subjected to an hindrance on their mobility due to by the movement of counter ions, electrophoretic effect, and by the relaxations effect (Debye-Hückel theory of electrolytes, 1923). These effects have not been taken into account in the ionic transport ratio defined by equation (3.7): salts conductivities in water has been calculating assuming no interactions (i.e. no hindrance on the limiting ionic conductivities λ^0). In order to obtain an index that better compare ion transport between solutions and charge fixed on the

membrane matrix, a tortuosity index $\tau(X)$ of the membrane in the X-form can be defined as follow:

$$\tau(X) = \frac{\sigma_w(X)}{\sigma_m(X)} \quad (3.8)$$

where $\tau(X)$ is the tortuosity index and $\sigma_w(X)$ and $\sigma_m(X)$ are the conductivity of the counterion X respectively in water and inside the membrane. In terms of Cluster-Network model this index describes the difference in mean length that ions, subjected to an electric field, have to cover in solution or inside the membrane, due to a tridimensional displacement between the clusters. Hence, the tortuosity index summarize differences in interactions and mean walking distances of the X ions between the membrane and water solution: nearer to one is the tortuosity, better is the interconnection between the clusters and more ideally the interactions between counterions and fixed charges.

Inside the membrane, being the charge fixed onto the polymeric matrix, contribution to the conductivity comes from counterions motion subjected to the electric field. In water solution, instead, due to the electroneutrality is not possible to directly obtain contribution from one ionic species. However it is well known (Kohlraush independent migration of ions, 1874) that equivalent conductivity of an electrolyte at infinite dilution is equal to the sum of the conductances of anions and cations:

$$\Lambda^0 = \lambda_+^0 + \lambda_-^0 \quad (3.9)$$

where Λ^0 is the equivalent conductivity at infinite dilution of the salt, λ_+^0 and λ_-^0 are respectively the equivalent conductivity at infinite dilution of the cation and the anion composing the salt. Equivalent conductivity Λ of a strong electrolyte solution is correlated to the equivalent conductivity at infinite dilution Λ^0 by Onsager limiting law (Onsager & Fuoss, 1932):

$$\Lambda = \Lambda^0 - k\sqrt{C} \quad (3.10)$$

where k is a parameter associated to electrophoretic and relaxation effects and C is the electrolyte equivalent concentration. Equation (3.10) can be applied for low concentration of the electrolyte ($<10^{-4}$ eq/L), application range can be extended (92) using the following modified equation:

$$\Lambda = \Lambda^0 - k \frac{\sqrt{I}}{1 + \sqrt{I}} \quad (3.11)$$

where I is the ionic strength of the solution. In order to estimate contribution from a single ionic species, transport numbers can be used:

$$\begin{aligned} t_{\pm} &= \frac{\lambda_{\pm}}{\Lambda} \\ t_{\pm}^0 &= \frac{\lambda_{\pm}^0}{\Lambda^0} \end{aligned} \quad (3.12)$$

where t_{\pm} and t_{\pm}^0 are cation(+)/anion(-) transport numbers respectively at ionic strength I and at infinite dilution, λ_{\pm} and λ_{\pm}^0 are cation(+)/anion(-) equivalent conductivity respectively at ionic strength I and at infinite dilution.

Assuming that the transport number value is nearly independent by I in the envisaged ionic strength range (i.e. $t_{\pm} \approx t_{\pm}^0$), combining equations (3.9) and (3.11) the following equation is obtained:

$$\lambda_{\pm} \cong \lambda_{\pm}^0 - kt_{\pm}^0 \frac{\sqrt{I}}{1 + \sqrt{I}} \quad (3.13)$$

Values for k parameter were obtained by linear least square fittings of equation (3.11) to experimental conductivity data in water for HCl (hydronium form), NaOH (hydroxyl form) and NaHCO₃ (bicarbonate form) measured at 25°C within the concentration range of 0÷0.2 M. These experimental parameters are reported in Table 30 together with equivalent conductivities and transport numbers at infinite dilution at 25°C (93).

Ion	λ^0 [S cm ² eq ⁻¹]	t^0	k [S cm ^{7/2} eq ^{-3/2}]
H ₃ O ⁺	350	0.82	144
OH ⁻	198.6	0.80	126.5
HCO ₃ ⁻	44.5	0.47	75

Table 30. Equivalent conductivities at infinite dilution, transport numbers at infinite dilution and experimental k parameters at 25°C for hydronium, hydroxyl and bicarbonate ions

Approximated equivalent conductivities λ_X for ion X in solution were then calculated using equation (3.13), from which tortuosity index $\tau(X)$ of membranes in the X-form has been calculated using the following formula, obtained from equation (3.8):

$$\tau(X) = \frac{n_X \lambda_X C_X}{\sigma_m(X)} \quad (3.14)$$

where n_X is the charge of ion X and C_X is the ionic groups concentration of the swollen membrane on the X-form, calculated scaling IEC with volumetric WU of the membrane on X-form. Tortuosity index for Nafion® ionomeric membranes having different IECs has been calculated by means of equation (3.14) using conductivity data of its hydronium form at 22°C reported in literature (94). These data are reported on Figure 79 as function of volumetric water swelling: increasing water content, as effect of higher IEC values, membrane conductivity gets nearer to the corresponding theoretical hydronium conductivity in water solution, most likely due to a better interconnectivity between the clusters. Over 100 vol% WU a slight increase is observed, probably due to an excessive water content inside the clusters resulting in a non-optimal morphology. Most common commercial Nafion® ionomeric membranes (EW1100) have the best trade-off between water content (≈50 vol%) and tortuosity index (≈3.9). Tortuosity for the benchmark Tokuyama A-201 membrane is ≈4.4 at WU ≈50 vol% for both hydroxyl and bicarbonate forms.

On Figure 80 tortuosity index for SBS-based membranes, having different IECs and crosslinking ratio, is plotted against volumetric water swelling: higher the water swelling, both originated from higher IEC or lower crosslinking ratio, lower is the tortuosity index for both bicarbonate and hydroxyl forms of the membranes. A slight increase of the tortuosity index is observed at water swelling of the hydroxyl form higher than 140 vol% (≈120 vol% for the bicarbonate form): these values are referred to R-SBS-based membrane, having the highest IEC.

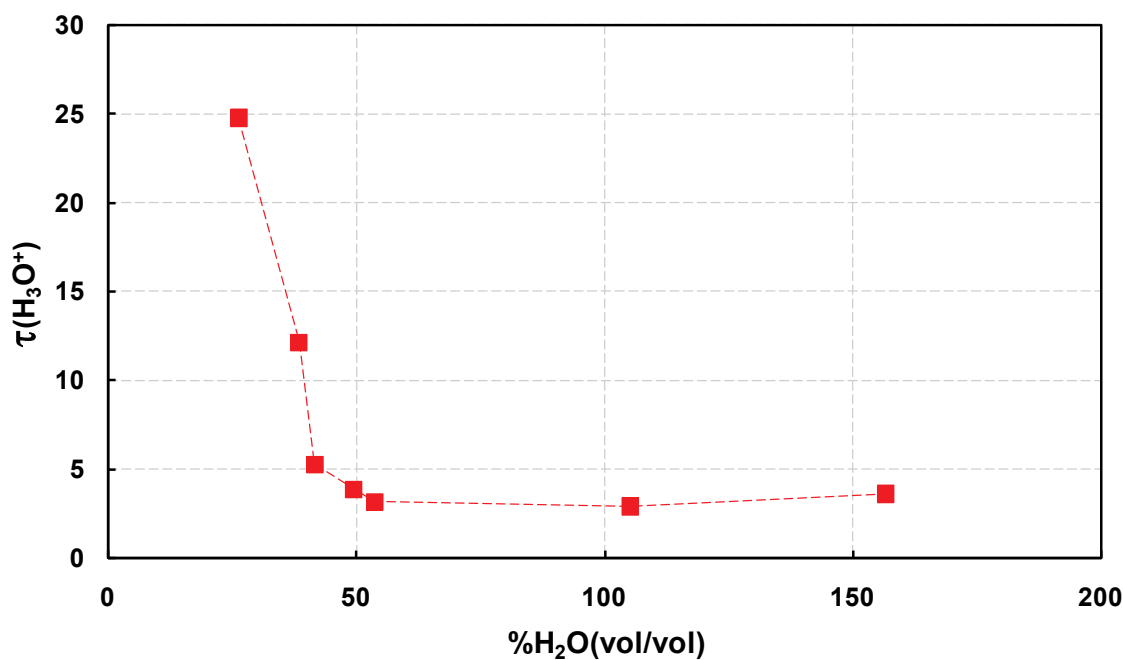


Figure 79. Tortuosity index for Nafion® ionomeric membranes, having different IECs, as function of volumetric water swelling

Increasing the FD an higher charge density is probably present inside the clusters resulting in a stronger interaction between counterions and fixed charge and thus taken into account on the tortuosity index, together with clusters interconnections.

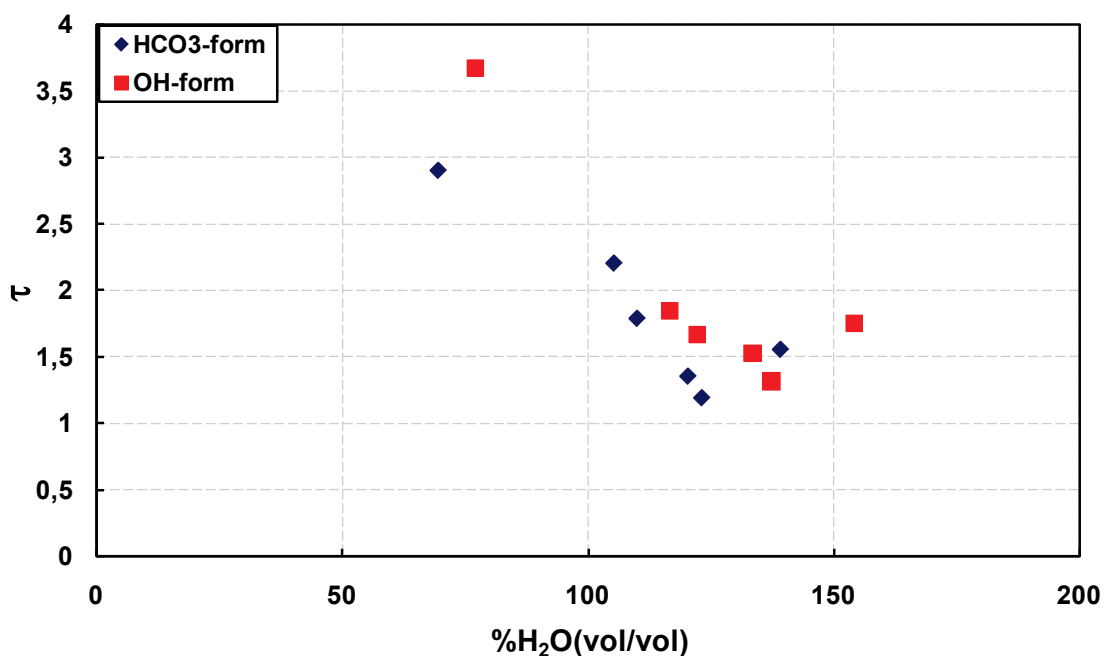


Figure 80. Tortuosity index for SBS-based membranes, having different FD and crosslinking ratio, as function of volumetric water swelling

In order to better understand crosslinking effect on swollen membrane morphology, tortuosity index has been calculated for bicarbonate form of R-SBS-F37 based membranes,

quaternized with TMA or different DABCO percentages (i.e. different crosslinking ratio) and plotted as function of volumetric water swelling on Figure 81 : the shape resemble the one obtained for Nafion[®], shifted on X-axis by ≈ 40 vol%, probably due to a higher charge density inside the clusters for the high FD SBS-based membranes (i.e. stronger interactions between counterions and fixed charges), enhancing the hypothesis of longer quaternized polyVBC side chains formation as FD is increased.

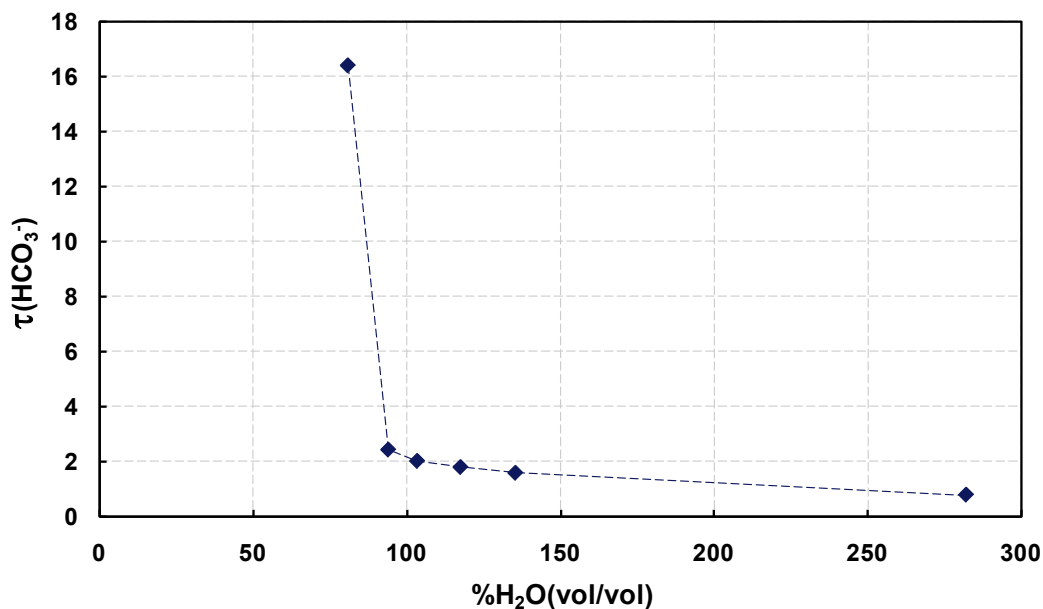


Figure 81. Tortuosity index for R-SBS-F37 based membranes, having different crosslinking ratio, as function of volumetric water swelling

Using the tortuosity indexes it is possible to define and calculate the tortuosity ratio index, analogous to an ionic transport ratio taking into account electrophoretic and relaxation effects:

$$\tau_{\text{ratio}}(X/Y) = \frac{\tau(Y)}{\tau(X)} \quad (3.15)$$

where X and Y are the respective forms of the exchanged membrane. On Table 31 tortuosity ratio is reported for the anion-exchange membranes already studied by means of ionic transport ratio index: all the values are now close to one, confirming a transport mechanism inside the membranes analogous to the water solution one, as already suggested by the previous analysis performed on the activation energies.

Sample	IEC (meq/g)	%H ₂ O (vol/vol)	$\tau_{\text{ratio}}(\text{OH}^-/\text{HCO}_3^-)$
Tokuyama A-201	1.84	50	1.0
R-SBS-F13+DABCO	0.52	77	0.8
R-SBS-F16 100%	0.82	116	1.2
R-SBS-F16 75%	0.85	122	1.1
R-SBS-F16 50%	0.83	133	0.9
R-SBS-F16 25%	0.79	137	0.9
R-SBS-F37+DABCO	1.21	154	0.9

Table 31. Tortuosity ratio $\tau_{\text{ratio}}(X/Y)$ of commercial anion-exchange membrane Tokuyama A-201 and SBS-based membranes, having different FD and crosslinking ratio

Tortuosity parameter has been defined and calculated for Nafion[®] membranes having different IECs and compared with values for SBS-based membranes: the comparison suggested longer quaternized PVBC side chains for the synthesized membrane as IEC is increased. Assuming a cluster-network morphological model this means that clusters diameter for SBS-based membranes is higher, due to the increased charge density. This interpretation would explain why for these membranes an high WU has been measured. Moreover tortuosity parameter ratio between two different counterion forms of the membrane suggested that ion transport mechanism inside the synthesized SBS-based membranes is similar to the water solution one, confirming the activation energy analysis previously performed.

3.2.5 Summary and future works

As shown before water uptake (WU) and ionic conductivity (σ) for SBS-based anion-exchange materials (AMs) can be tuned either by modifying the functionalization degree (FD) or the crosslinking degree. Even though the obtained results are promising in terms of ionic conductivity, water swelling for these materials is way too high compared to the benchmark Tokuyama A-201 membrane, even though the ion exchange capacities for the synthesized SBS-based ionomers are smaller than the benchmark membrane.

Assuming constant overall ion-exchange capacity the ion-exchange groups distribution is not fixed. If VBC grafting on the SBS matrix is preferred over its homopolymerization, the resulting AM will have a random distribution of the ion exchange groups over the butadienic blocks (Figure 82 (a)), i.e. the charge will be evenly distributed and its density minimized. On the other hand if VBC homopolymerization is preferred over its grafting on the SBS matrix, the resulting AM will have a clustered distribution of the ion exchange groups over the butadienic blocks (Figure 82 (b)), i.e. the charge will be unevenly distributed with local peaks of its density.

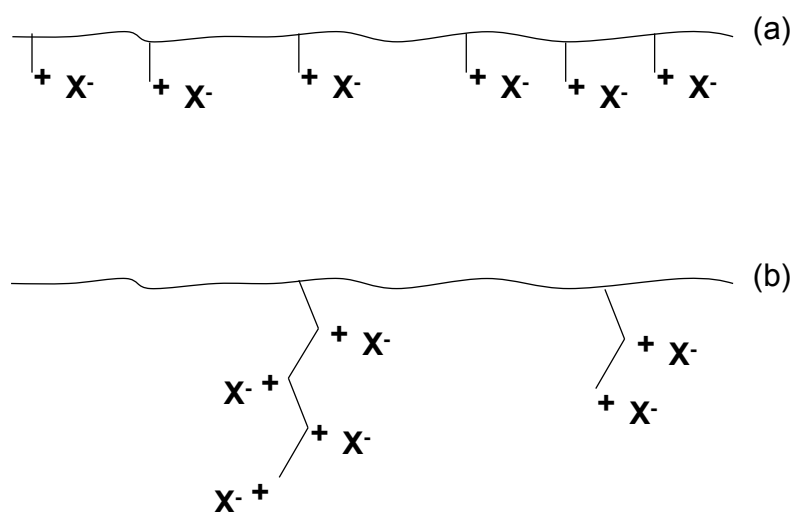


Figure 82. Random (a) and clustered (b) distribution schematics of ion-exchange groups

Tortuosity parameter analysis suggested that increasing the FD the mean cluster diameter in the swollen membrane increases as well, due to the formation of longer

clustered quaternized PVBC side chains. This trend leads to the observed higher WU compared to the benchmark membrane.

Moreover, even though DABCO crosslinking ratio can be controlled by its concentration during the quaternization reaction, as shown in section 3.2.3, crosslinking can be in principle between two different SBS chains (interchain crosslinking), or between two VBC units grafted on the same SBS chain or on the same side chain (intrachain crosslinking), as shown in Figure 83. Clearly, interchain crosslinking is desirable, helping to reduce the AM swelling.

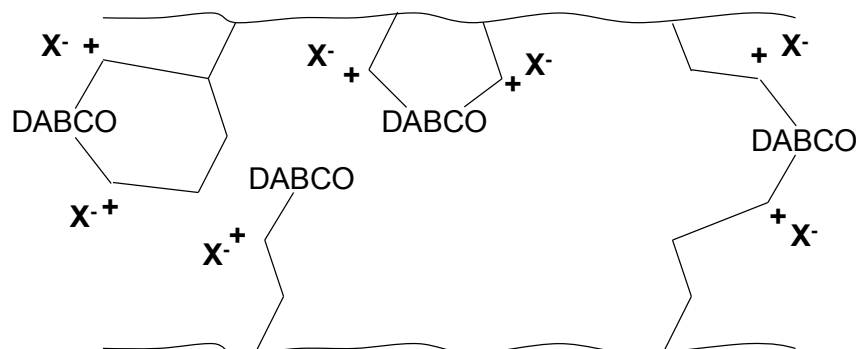


Figure 83. Intrachain and interchain DABCO crosslinking schematics

In order to improve the ion-exchange groups distribution and promote interchain crosslinking the AM synthesis can be modified in one or more of the following ways:

- Usage of a Styrene/VBC mixture during the grafting reaction in order to statistically reduce the charge density of the quaternized membrane;
- Conducting the VBC grafting reaction in a solvent inert to radical reactions (e.g. benzene), slowly adding the VBC in order to work with a defect of VBC. In this way homopolymerization should be less likely, leading to a better side chains distribution over the butadienic blocks;
- Usage of long-chain polyamines for the quaternization reaction in order to promote interchain crosslinking rather than intrachain crosslinking;
- Quaternizing in excess of DABCO an SBS-g-VBC polymer having a low FD (e.g. 1-5%), in order to obtain a crosslinking-free polymer, containing one-side quaternized DABCO molecules. Another SBS-g-VBC polymer having the envisaged FD may then be quaternized with the previous one, obtaining a crosslinked material which can be now fully quaternized with DABCO or trimethylamine.

3.3 Anion-exchange Membrane Fuel Cell (AMFC) applications

Due to reasons of excessive cost and supply limitations of platinum, large-scale application of H₂/O₂ Polymer Electrolyte Membrane Fuel Cells (PEMFCs) would require strongly reduced Pt loadings. To meet this requirement, the Pt specific power density would have to be reduced to <0.2 g_{Pt}/kW at cell voltages of ≥0.6 V (to maintain high fuel cell energy conversion efficiencies of > 55%). State-of-the-art Pt loading are ≈0.4 to 0.5 mg_{Pt}/cm²_{MEA}, corresponding to Pt-specific power densities of ≈0.5 g_{Pt}/kW. Therefore, to reach the above targets, Pt loadings of ≤0.15 mg_{Pt}/cm²_{MEA} are needed, which would require improved cathode catalysts with an approximately four-fold higher activity compared to Pt/C (1).

Anion-exchange membrane fuel cells (AMFCs), on the other hand, promise to enable the use of Platinum Group Metal (PGM) free catalysts. In the last 6 years, novel anion-exchange polymers (membranes and solubilized ionomers) have been developed, opening a new challenge to develop ionomer-bonded Anion-exchange Materials (AMs) based Membrane Electrode Assemblies (MEAs) analogous to PEMFCs, and recent literature results are promising (5; 6).

In the next paragraphs H₂/O₂ AMFC performances using Tokuyama commercial AMs will be evaluated and compared to kinetic and ohmic projections in order to estimate the potential of this technology. Diagnostics by means of in-situ Electrochemical Impedance Spectroscopy (EIS) will be presented in order to study MEA stability, comparing previously reported AMs ex-situ parameters (i.e. conductivity and water uptake) with values measured in an operating AMFC. At last SBS-based AMs will be used to prepare an MEA and evaluate their suitability and performance in H₂/O₂ AMFC.

3.3.1 AMFC performances using commercial AMs

In the present paragraph Tokuyama benchmark materials and Acta's Platinum Group Metal (PGM) free Oxygen Reduction Reaction (ORR) catalysts "K14" and "K18" will be evaluated. Catalyst Coated Membranes (CCMs) using Tokuyama A-201 membrane and AS-4 solubilized anion-exchange ionomer were prepared with either conventional Pt/C or non-PGM K14 and K18 catalysts and evaluated in a H₂/O₂ AMFC. In order to estimate the potential of this technology H₂/O₂ AMFC measured performances will be compared with theoretical performance projections.

Pt-Pt CCMs

Figure 84 shows the measured performance (squares) of a H₂/O₂ AMFC at 80°C using a Pt/C-based CCM, prepared as described in the experimental section. At 0.6V the measured power density is ≈140mW/cm². While this is ≈10 times smaller than what one would get with Nafion[®] 111 based PEMFCs under similar conditions (95), this result is very promising considering the early stage of this technology, and also compares very well with recent literature data for AMFCs (96). The triangles in Figure 84, on the other hand, is the estimated AMFC performance for perfectly designed MEAs, based on the known kinetic and ohmic losses (see below). The difference between the actual and the projected performance is

indicated as “transport losses”, which are currently undefined losses. They could arise from gas transport resistances, ion transport resistances in the electrode and pH gradients originating from foreign anions (97).

The estimated kinetic and ohmic limit discussed above is obtained by considering that the cell potential, E_{cell} , can be defined by the following equation:

$$E_{cell} = E_{cathode} - E_{anode} - i \cdot R_{\Omega} - \eta_{tx} \quad (3.16)$$

where $E_{cathode}$ is the O₂ cathode potential, E_{anode} is the H₂ anode potential, i is the current density, R_{Ω} is the ohmic resistance (arising from contact and membrane resistances), and η_{tx} is the transport overpotential, which is considered to be zero for the “ideal” electrode. The ohmic resistance was calculated using the following equation:

$$R_{\Omega} = \frac{t_{wet}}{\sigma_{membrane}} + R_{contact} \quad (3.17)$$

where t_{wet} is the wet thickness of the membrane ($\approx 40 \mu\text{m}$), $\sigma_{membrane}$ is the membrane conductivity ($\approx 70 \text{ mS/cm}$ at 80°C from Figure 39), and $R_{contact}$ is the electric contact resistance between current collector and gas diffusion layer, measurable assembling the cell without the membrane ($\approx 0.025 \Omega \cdot \text{cm}^2$). The anode potential was calculated using the following equation:

$$E_{anode} = 0V + \eta_{anode} \quad (3.18)$$

where η_{anode} is the anodic kinetic overpotential, calculated from the Butler-Volmer equation:

$$i = i_{0V} \left[e^{\frac{\alpha F}{RT} \eta_{anode}} - e^{-\frac{(1-\alpha)F}{RT} \eta_{anode}} \right] \quad (3.19)$$

where F is the Faraday constant, R is the gas constant, T is the temperature in Kelvin, α is the transfer coefficient and i_{0V} is the current density at 0V vs. RHE (reversible hydrogen electrode potential) at the operating conditions (80°C , 50kPa H₂ partial pressure). To estimate i_{0V} at the cell conditions, rotating disk electrode data at 21°C and 100kPa H₂ were used (15). The catalyst mass activity is estimated to be about the same at AMFC test conditions (i.e., $i_{0V} \approx 0.35 \text{ A/mg}_{\text{Pt}}$ with a transfer coefficient $\alpha \approx 0.5$), assuming that the hydrogen oxidation reaction (HOR) activity is first order with respect to the H₂ partial pressure (i.e. 0.5x activity from 100kPa p_{H2} rotating disk electrode conditions to 50kPa p_{H2} in the AMFC) and that the activation energy at 0V reported in literature for Pt/C is $\approx 29.5 \text{ kJ/mol}$ (i.e., $\approx 7.5\text{x}$ activity from 21°C RDE to 80°C AMFC) (15).

The cathode potential was calculated, assuming simple Tafel kinetics, i.e. only one Tafel slope, using the following equation:

$$E_{cathode} = 0.9V - TS \cdot \log\left(\frac{i}{i_{0.9V}}\right) \quad (3.20)$$

where TS is the Tafel Slope and $i_{0.9V}$ is the current density at 0.9V vs. RHE (reversible hydrogen electrode potential) at the operating conditions (80°C , 50kPa O₂ partial pressure). To estimate $i_{0.9V}$ at the cell conditions, rotating disk electrode data at 25°C and 100kPa O₂ were used (20). The catalyst mass activity is estimated to be about the same at AMFC test conditions (i.e., $\approx 0.03 \text{ A/mg}_{\text{Pt}}$ at 0.9V vs. RHE with a Tafel slope of $\approx 100 \text{ mV/dec.}$), assuming that the ORR activity is first order with respect to the O₂ partial pressure (i.e. 0.5x activity

from 100kPa p_{O_2} rotating disk electrode conditions to 50kPa p_{O_2} in the AMFC) and that the activation energy at 0.9V is similar to what was measured in PEMFCs for Pt/C, namely ≈ 10 kJ/mol (i.e., 2x activity from 25°C RDE to 80°C AMFC) (98).

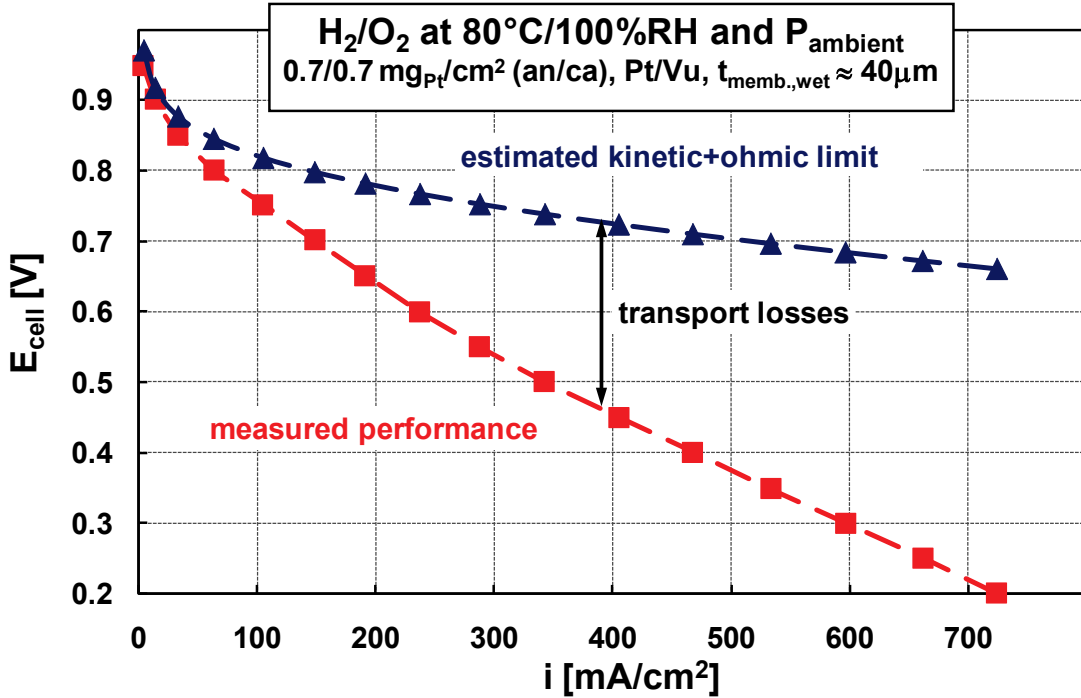


Figure 84. AMFC performance with fully humidified H_2/O_2 (70/140 sccm flows) at ambient pressure and 80°C. Ionomer-bonded 5 cm² CCMs were based on a commercial benchmark membrane ($t_{wet} \approx 40 \mu m$) with catalyst loadings of 0.7/0.7 mg_{Pt}/cm² (anode/cathode), using a 40%wt. Pt/C catalyst. Data were obtained after 3 minutes hold at each potential. Square symbols denote the measured performance, while triangles represent the approximate kinetic and ohmic limit

Combining equations (3.16), (3.17), (3.18) and (3.20), we obtain the expression for the kinetically and kinetically-ohmically limited cell potential based on the catalyst and membrane properties:

$$\begin{cases} E_{kin} = 0.9V - TS \cdot \log\left(\frac{i}{i_{0.9V}}\right) - \eta_{anode} \\ E_{kin+\Omega} = 0.9V - TS \cdot \log\left(\frac{i}{i_{0.9V}}\right) - \eta_{anode} - i \cdot \left(R_{contact} + \frac{t_{wet}}{\sigma_{membrane}}\right) \end{cases} \quad (3.21)$$

As can be seen, the actual (squares in Figure 84) and the projected (triangles in Figure 84) performance coincide at low current density, demonstrating that the ionomer does not poison the ORR/HOR kinetics. At higher current densities, transport losses make the experimental curve deviate from the projected limit.

A decay on performances ($\approx 10\%$) has been observed repeating the voltage scan after a while. In order to study this degradation process, diagnostics by means of EIS will be presented on the next paragraph.

Pt-K14 CCMs

In Figure 85, the same analysis has been applied to an AM-CCM using a non-PGM ORR catalyst (ACTA's K14) and tested in a H_2/O_2 AMFC. Compared to Figure 84, the power density at 0.6V is not so different (110 vs. 140 mW/cm^2), which to our knowledge is the highest performance ever reported for an AMFC using a non-PGM cathode catalyst, clearly demonstrating the high potential of the AMFC technology to reduce the PGM content by a large factor, or even to eliminate it. However, a limiting current appears at $\approx 0.2A/cm^2$, which is probably due to non-optimized MEA design. At the same time the theoretical curve based on the RDE kinetics of K14 (triangles) does not match with the experimental data (squares) at low current density (20). This behavior could be due to significant kinetic dependence of the non-PGM ORR catalyst on pH, contrary to a Pt catalyst (99), to AMs thermal degradation, or to ionomer poisoning of the catalyst at the operating temperature. Further tests at lower temperature have been conducted in order to investigate this difference and to optimize the structure of the electrodes.

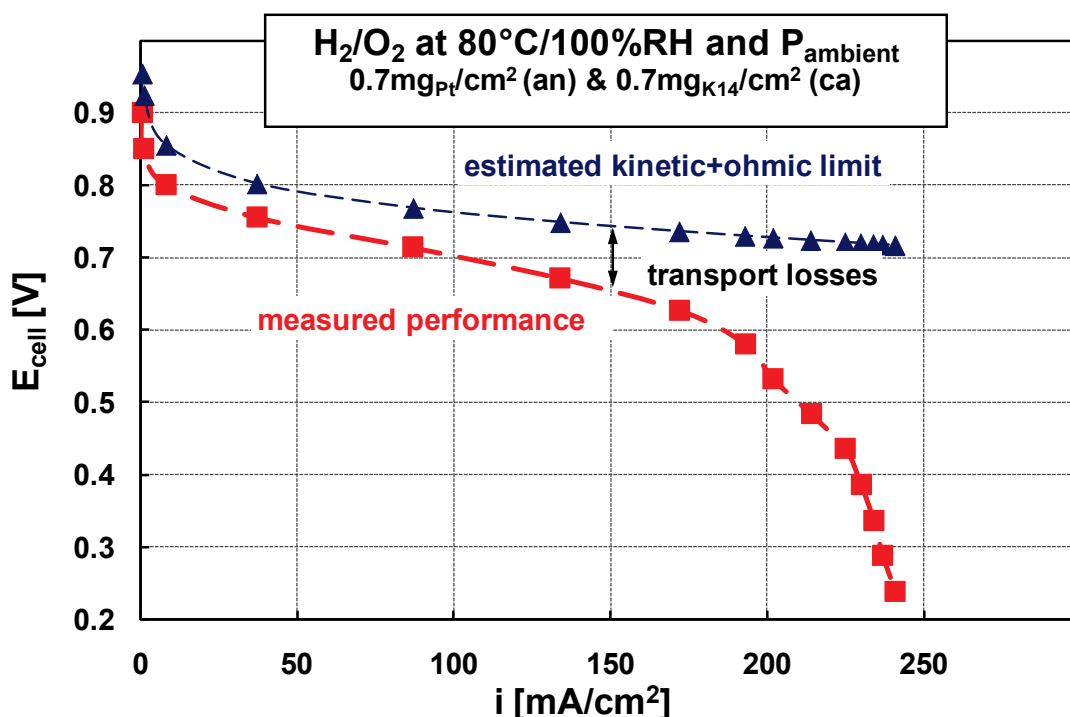


Figure 85. AMFC performance with fully humidified H_2/O_2 (70/140 sccm flows) at ambient pressure and $80^\circ C$. Ionomer-bonded $5 cm^2$ CCMs were based on a commercial benchmark membrane ($t_{wet} \approx 40 \mu m$) with anode loadings of $0.7 mg_{Pt}/cm^2$ (40%wt. Pt/C) and cathode loadings of $0.7 mg_{catalyst}/cm^2$ using Acta's non-PGM K14 cathode catalyst. Data were obtained after 3 minutes hold at each potential. Square symbols denote the measured performance, while triangles represent the approximate kinetic and ohmic limit

Pt-K18 CCMs

In Figure 86, the same analysis has been applied to an AM-CCM using another non-PGM ORR catalyst (ACTA's K18) and tested in a H_2/O_2 AMFC at $30^\circ C$, in order to determine whether the discrepancy on Figure 85 between measured and theoretical performances at low current density is due to thermal instability of the CCM. At this temperature theoretical and experimental curves match at low current density, moreover repeating the measurement after 30' no performance decay is observed. Increasing the temperature at $50^\circ C$ a small decay ($\approx 5\%$) is observed, at $80^\circ C$ the decay is far higher and faster ($<100 mA/cm^2$ at 200mV after 10'). Hence at temperature higher than $50^\circ C$ the prepared MEAs aren't stable, the degradation process will be further investigated on the next paragraph.

In Figure 87 H_2/O_2 AMFC performances obtained at $30^\circ C$ using ACTA's K18 non-PGM ORR catalyst are compared with performances obtained by a Pt/Pt MEA ($0.5 mg/cm^2$ for both anode and cathode) showing similar results.

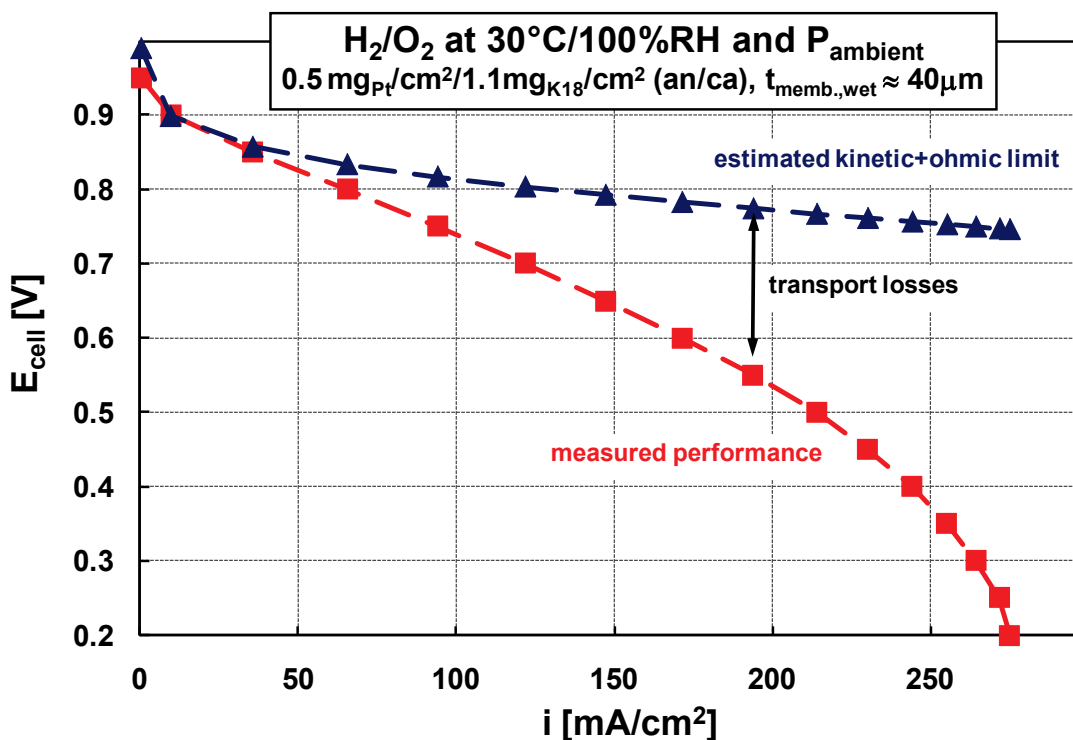


Figure 86. AMFC performance with fully humidified H_2/O_2 (200/200 sccm flows) at ambient pressure and $30^\circ C$. Ionomer-bonded $5 cm^2$ CCMs were based on Tokuyama A-201 membrane with anode loadings of $0.5 mg_{Pt}/cm^2$ (60%wt. Pt/C) and cathode loadings of $1.1 mg_{catalyst}/cm^2$ using Acta's non-PGM K18 ORR catalyst. Data were obtained after 3 minutes hold at each potential. Square symbols denote the measured performance, while triangles represent the approximate kinetic and ohmic limit

Tough CCM design has yet to be improved in order to minimize transport losses and thermal stability, these results are encouraging since similar performances are obtained both using Pt and non-PGM ORR electrocatalysts.

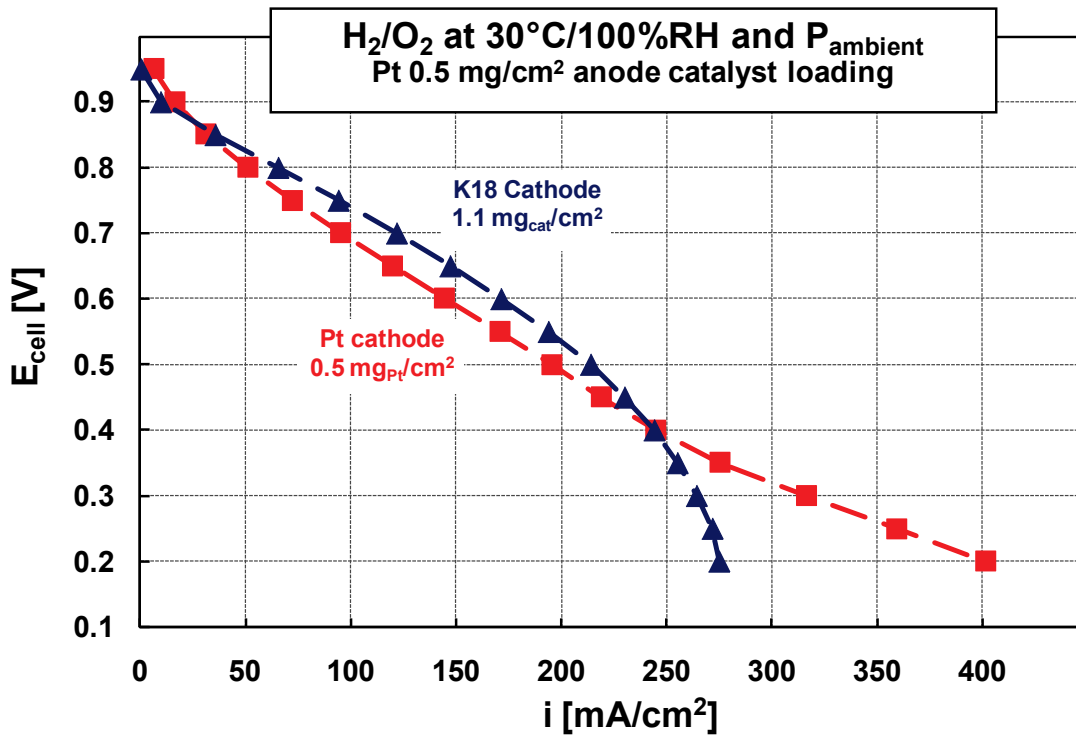


Figure 87. AMFC performances with fully humidified H₂/O₂ (200/200 sccm flows) at ambient pressure and 30°C. Ionomer-bonded 5 cm² CCMs were based on Tokuyama A-201 membrane with anode loadings of 0.5 mg_{Pt}/cm² and cathode loadings of 1.1 mg_{K18}/cm² (triangles) or cathode loadings of 0.5 mg_{Pt}/cm² (squares). Data were obtained after 3 minutes hold at each potential

3.3.2 Electrochemical Impedance Spectroscopy in-situ diagnostics

On the previous paragraph despite the encouraging performances obtained using both Pt and non-PGM ORR catalysts, some decay was observed at temperatures higher than 50°C. In order to study whether this decay is due to catalyst poisoning, AMs degradation or other sources impedance spectra were collected at each constant voltage step during voltage/current measurements for a H₂/O₂ AMFC at 50°C using a Pt/C-based CCM (0.5mg_{Pt}/cm² loading for both anode and cathode) prepared as described in the experimental section.

Collected impedance data are reported for three voltage steps on Figure 88 as Nyquist plot (i.e. Impedance imaginary part Z'' vs. Impedance real part Z'). Extrapolating high frequency impedance data at zero imaginary part by a 45° line, the so-called High Frequency Resistance (HFR) is obtained. Extrapolated HFR is 110 mΩ·cm² and doesn't change with AMFC operating DC voltage. The HFR take into account both membrane ionic resistance and contact resistance:

$$HFR = R_{membrane} + R_{contact} \quad (3.22)$$

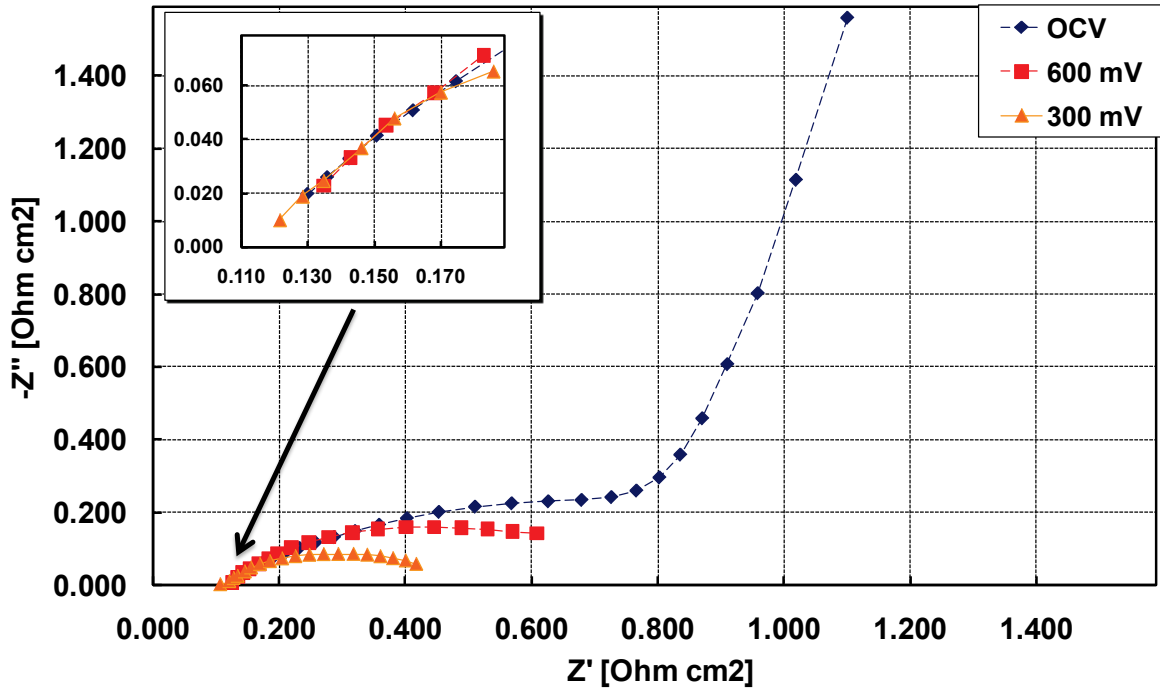


Figure 88. Nyquist plot at different DC voltages of an AMFC operating with fully humidified H_2/O_2 (200/200 sccm flows) at ambient pressure and 50°C. Ionomer-bonded 5 cm² CCMs were based on Tokuyama A-201 membrane with catalyst loadings of 0.5/0.5 mg_{Pt}/cm² (anode/cathode), using a 60%wt. Pt/C catalyst. Data at Open Circuit Voltage (OCV) obtained between 100kHz-1Hz applying 4mV amplitude AC perturbations. Data at 600 and 300mV obtained between 100kHz-100Hz applying 1mV amplitude AC perturbations. Magnification of high frequency range impedance data is reported on the top left corner of the graph

Since $R_{\text{contact}} \approx 25 \text{ m}\Omega \cdot \text{cm}^2$, as reported in the previous paragraph, measured membrane resistance is $\approx 85 \text{ m}\Omega \cdot \text{cm}^2$, resulting in a conductivity of 47 mS/cm at 50°C for a 40 μm wet thickness membrane. This value compare well to the ex-situ through-plane conductivity of the hydroxyl form reported in Figure 39 for the Tokuyama A-201 membrane ($\approx 50 \text{ mS/cm}$). Hence the membrane is healthy and no CO_2 contamination occur at the operating conditions. On Figure 89 obtained performance data are reported along with kinetic projection, calculated by equation (3.20), and ohmic-loss free performance:

$$E_{iR\text{-free}} = E_{\text{cell}} + i \cdot HFR \cong E_{\text{kin}} \quad (3.23)$$

Assuming that the HOR activity is first order with respect to the H_2 partial pressure and taking into account the reported activation energy, an exchange current density of 0.92A/mg_{Pt} is calculated at 50°C and 88kPa H_2 .

At 0.9V an iR -free current density of 45mA/mg_{Pt} is measured. From equation (3.19) a negligible anodic overpotential of 1.5mV is calculated, i.e. $E_{iR\text{-free}} \cong E_{\text{cathode}}$ at this current density.

Assuming the ORR is of the first order to O_2 partial pressure, a current density of 52mA/mg_{Pt} is calculated from experimental data at 50°C and 100kPa O_2 partial pressure. In literature (20) a mass activity of 35mA/mg_{Pt} is measured at 25°C, 100kPa O_2 partial pressure and 0.1M KOH by means of Rotating Disk Electrode (RDE) voltammetry. Comparing the two mass activities at 25°C (RDE) and 50°C (AMFC) would result in an activation energy of $\approx 12 \text{ kJ/mol}$, comparable to Pt/C in PEMFC (98).

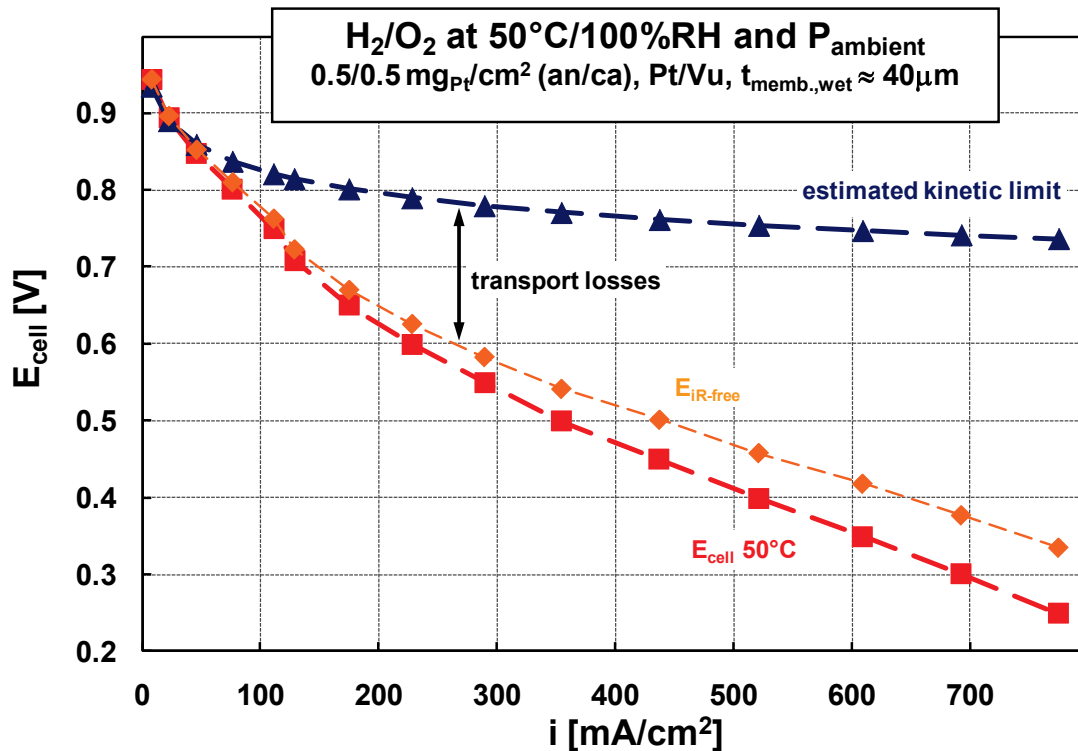


Figure 89. AMFC performance with fully humidified H₂/O₂ (200/200 sccm flows) at ambient pressure and 50°C. Ionomer-bonded 5 cm² CCMs were based on a Tokuyama A-201 membrane (t_{wet} ≈ 40 μm) with catalyst loadings of 0.5/0.5 mg_{Pt}/cm² (anode/cathode), using a 60%wt. Pt/C catalyst. Data were obtained after 3 minutes hold at each potential. Red line denote the measured performance, orange line the ohmic loss-free performance and blue line represent the approximate kinetic limit

Therefore the transport losses are not due to CO₂ contamination, membrane degradation or catalyst poisoning. Most likely these voltage drop are due to a non-optimized MEA design, resulting in a slow gas diffusion and/or slow ion transport inside the catalyst layer.

In order to better understand the previously observed performance decay, the measurements were repeated three times at 50°C and once at 80°C using the same MEA.

On Figure 90 performance data together with extrapolated HFR are reported for the subsequent measurement cycles. After two measurement cycles at 50°C a small performance drop is observed, this decay is not due to catalyst deactivation (current density at 0.9V doesn't change) neither to membrane deactivation (similar HFRs data). At 80°C a huge performance decay can be observed: membrane conductivity calculated by HFR data is ≈ 72 mS/cm and is comparable to the ex-situ conductivity measured at 80°C for the hydroxyl form of the membrane (68 mS/cm). Since platinum catalyst deactivation is unlikely something should change on the catalyst layer structure, such as ionomer dissolution or degradation. On Figure 91 HFR data for the previously described measurement cycles are reported together with the real part of impedance at 1 kHz (Z'_{1kHz}), commonly used by commercial test stations and milliohmeters: while HFR data are consistent with ex-situ conductivity at each AMFC operating DC potential and cycle, Z'_{1kHz} increases at each cycle. Since at 1 kHz impedance data take into account in a certain measure also the catalyst layer

ionic resistance, the ionic conductivity of the ionomer inside the catalyst layer decreases at temperature higher than 50°C confirming ionomer dissolution or degradation.

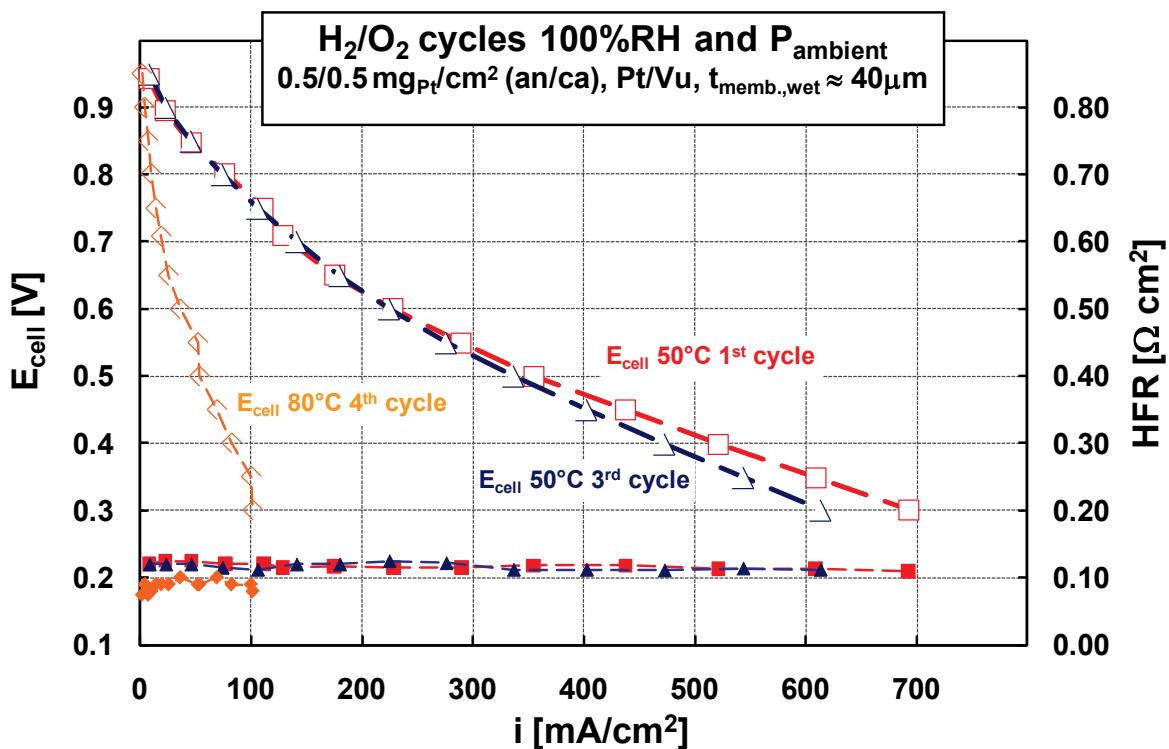


Figure 90. AMFC performances (hollow symbols) and HFRs (full symbols) with fully humidified H₂/O₂ (200/200 sccm flows) at ambient pressure for subsequent measurement cycles at 50°C and 80°C. Ionomer-bonded 5 cm² CCMs were based on a Tokuyama A-201 membrane (t_{wet} ≈ 40 μm) with catalyst loadings of 0.5/0.5 mg_{Pt}/cm² (anode/cathode), using a 60%wt. Pt/C catalyst. Data were obtained after 3 minutes hold at each potential, high frequency resistances were extrapolated by impedance data (see text)

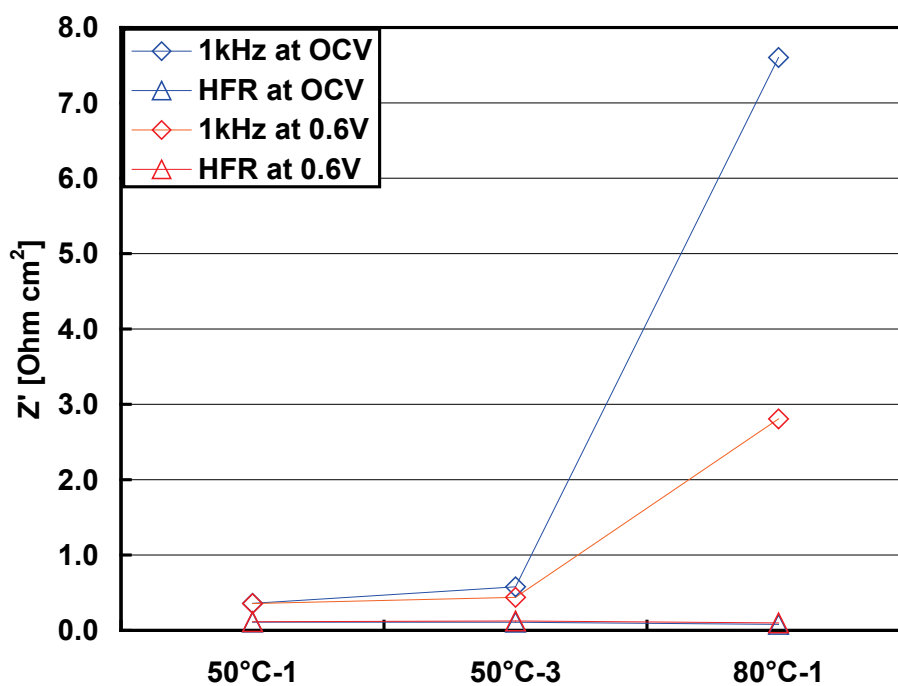


Figure 91. AMFC HFR and impedance real part at 1kHz measured both at Open Circuit Voltage (OCV) and 0.6V operating DC voltage for subsequent measurement cycles reported on Figure 90

On Figure 92 a picture of the bottle used to collect water vapor coming out the cathode side of the AMFC used for the previously described measurement cycles is reported: water is yellowish-brown and a yellow deposit is present. FT-IR analysis of this dried water sample confirmed that ionomer has been dissolved at 80°C.

Ionomer dissolution is probably due to the high water uptake (250wt% at 30°C) measured for the Tokuyama AS-4 AM (Figure 36).



Figure 92. Picture of the bottle collecting condensed water vapor coming out the cathode side of the AMFC used for subsequent measurement cycles reported on Figure 90

Thus CCMs prepared using Tokuyama AMs are stable at operating temperatures lower than 50°C and give promising performances in H₂/O₂ AMFC both using Pt/C or PGM-free ORR electrocatalysts, even though a better MEA design is needed in order to be comparable with PEMFC performances.. Moreover Electrochemical Impedance Spectroscopy (EIS) has been proved as viable technique for AMFC in-situ diagnostics confirming no CO₂ contamination, no membrane degradation and suggesting usage of ionomeric polymer having low water swelling in order to extend AMFC operating temperature range.

3.3.3 AMFC performances using SBS-based AMs

An R-SBS-F37 film (FD 11.6%), previously quaternized in methanol with trimethylamine, was dissolved in methanol at 120°C in an autoclave for 1h, obtaining a 4wt% ionomeric solution. In-plane conductivity and water uptake of a membrane obtained recasting this ionomer solution in a PTFE petri dish were measured in order to verify that no degradation occurred during the heat treatment. In-plane conductivity of the bicarbonate form (11.9 mS/cm) and water swelling (305 wt%) are comparable with values reported on Section 3.2.3 for the untreated membrane.

An ink was prepared dispersing Pt/C 40wt% (BASF®) catalyst into a portion of the ionomer solution (50 wt% Ionomer to Carbon ratio). The ink was then casted on expanded PTFE (ePTFE) film using a Mayer rod, obtaining a catalyst layer having $0.45 \text{ mg}_{\text{Pt}}/\text{cm}^2$ loading. The catalyst layer was then decal transferred by means of hot pressing (105°C , 60bar) onto a DABCO quaternized R-SBS-F37 membrane (1M DABCO in methanol), obtaining a Catalyst Coated Membrane (CCM). The CCM was exchanged into the OH-form soaking it in a 1M KOH solution for 1 h.

At 30°C in an H_2/O_2 AMFC the CCM showed no performances (peak current density $<2 \text{ mA}/\text{cm}^2$) and very high impedance at 1kHz ($>10\Omega$). By means of EIS an HFR of $\approx 390 \text{ m}\Omega$ was extrapolated, obtaining a conductivity of $\approx 8 \text{ mS}/\text{cm}$ for the SBS-based membrane having a wet thickness of $140 \mu\text{m}$. This value compare well with the previously reported ex-situ conductivity (Figure 73) for the hydroxyl form of this AM: the membrane was not damaged by the hot pressing treatment. The high impedance at 1kHz, being not due to a membrane fault, arises from an high resistance of the catalytic layer, probably due to ionomer dissolution, degradation or segregation.

Ionomer thermal degradation is unlikely, since the hot pressing temperature is far below than the 265°C , first decomposition temperature detected by TGA analysis (Figure 70). Since dissolved ionomer was not detected on the KOH solution used to exchange the CCM to the hydroxyl form damage on the microphase dispersed ionomer/catalyst structure most likely occurred.

Scanning Electron Microscopy (SEM) analysis was performed on the catalytic layer before and after the decal transfer. On Figure 93 SEM micrographs are reported for the catalytic layer before and after the decal transfer: at lower magnification ($\times 1,000$) catalyst layer surface is smoother and less porous after the hot pressing, at higher magnification ($\times 10,000$) a clear segregation of the ionomer (brighter spots) can be observed.

Ionomer segregation would explain the recorded high impedance and poor performances, resulting in a poor interconnection between the three phases (i.e. pores for reactants transport, carbon for electrons transport and ionomer for ionic transport).

Segregation most likely occurred due to the huge water uptake of the ionomer ($\approx 300\text{wt}\%$): since the coating is prepared in humid open air the ionomer is partially swollen, when heated during the hot pressing treatment the ionomer turn to the dry form and then absorb again water from air when cooled to room temperature. These volume changes stress the microphase dispersed ionomer/catalyst structure leading to the observed ionomer segregation.

In order to confirm that ionomer segregation occurs after the hot pressing treatment, the ink previously prepared was casted, using a Mayer rod, directly on the Gas Diffusion Layer (GDL), obtaining an MEA onto the Gas Diffusion Electrode (GDE) configuration having $0.4 \text{ mg}_{\text{Pt}}/\text{cm}^2$ loading.

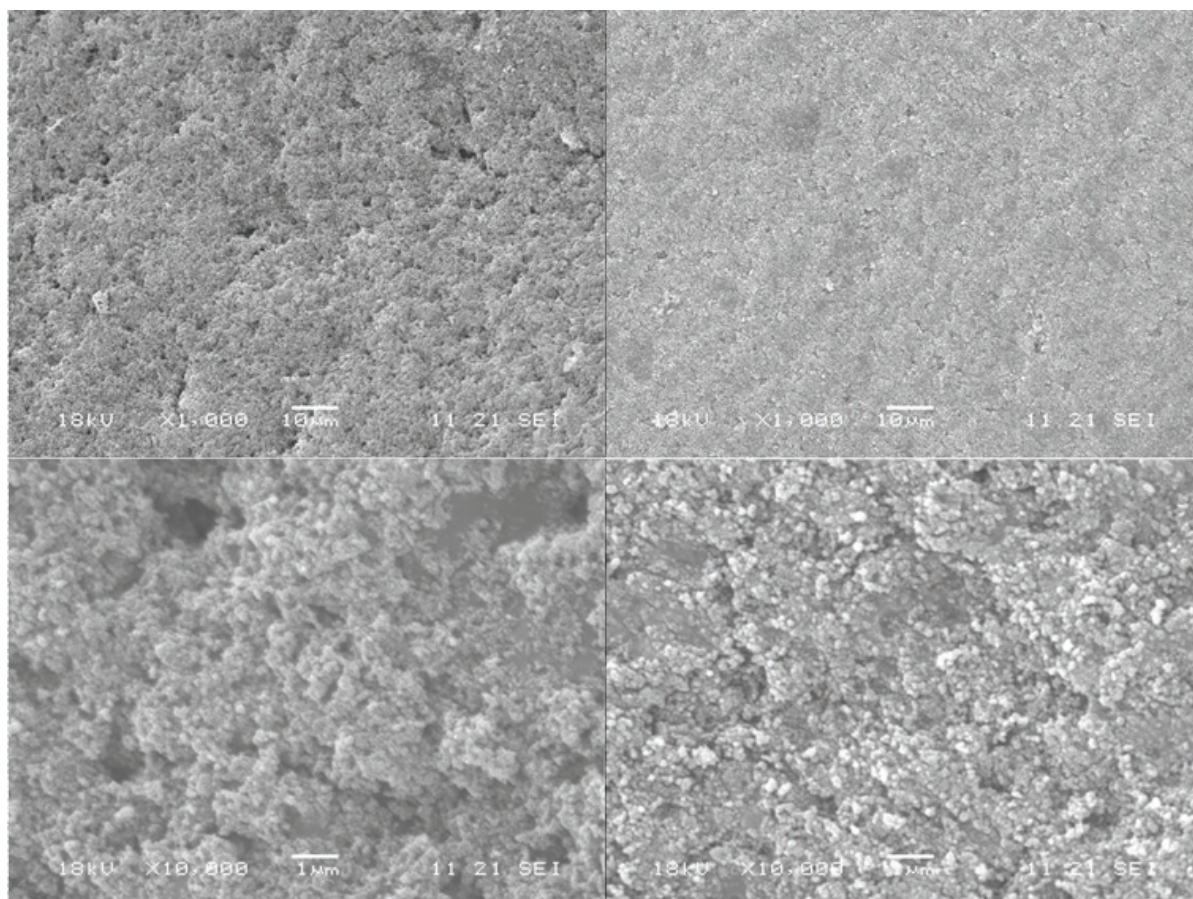


Figure 93. SEM micrographs having $\times 1,000$ magnification (top micrographs) and $\times 10,000$ magnification (bottom micrographs) of a catalyst layer before (left micrographs) and after (right micrographs) the decal transfer from ePTFE to a DABCO quaternized R-SBS-F37 membrane (see text)

The MEA was then tested at $50^{\circ}\text{C}/80\%$ relative humidity in order to reduce the ionomer swelling. In an H_2/CO_2 -free Air (obtained using a carbon dioxide scrubber) AMFC the GDEs showed low performances (Figure 94). Measuring the in-situ membrane conductivity by means of EIS showed no CO_2 contamination. Increasing temperature or relative humidity of the supplied gases resulted in a progressive, irreversible, decay in performances, probably due to modification on the catalyst layer as for the CCM case.

Using a ionomer/carbon weight ratio of 0.5/1 at approximate densities of $0.9\text{g}/\text{cm}^3$ for the ionomer and $2\text{g}/\text{cm}^3$ for carbon, the dry ionomer/carbon volume ratio would be 1.1/1. Considering the carbon volume fraction of $\approx 20\%$ for Vulcan and Ketjen based electrodes (100), the volume fractions under dry conditions would be 20% for carbon, 21% for the ionomer, and 59% for the void volume. In the presence of liquid water, the volume of the ionomer would expand by a factor of ≈ 4 (300% volume uptake), which means that there would be no void volume left for gas diffusion, explaining the low measured performances. Decreasing the ionomer/carbon ratio to 0.25/1, the volume fractions under dry conditions would be 22% for carbon, 11% for the ionomer, and 67% for the void volume. Even though some void volume would be left in presence of liquid water, measured performance were similar to the previous layer, probably due to low ionic conductivity of the catalyst layer.

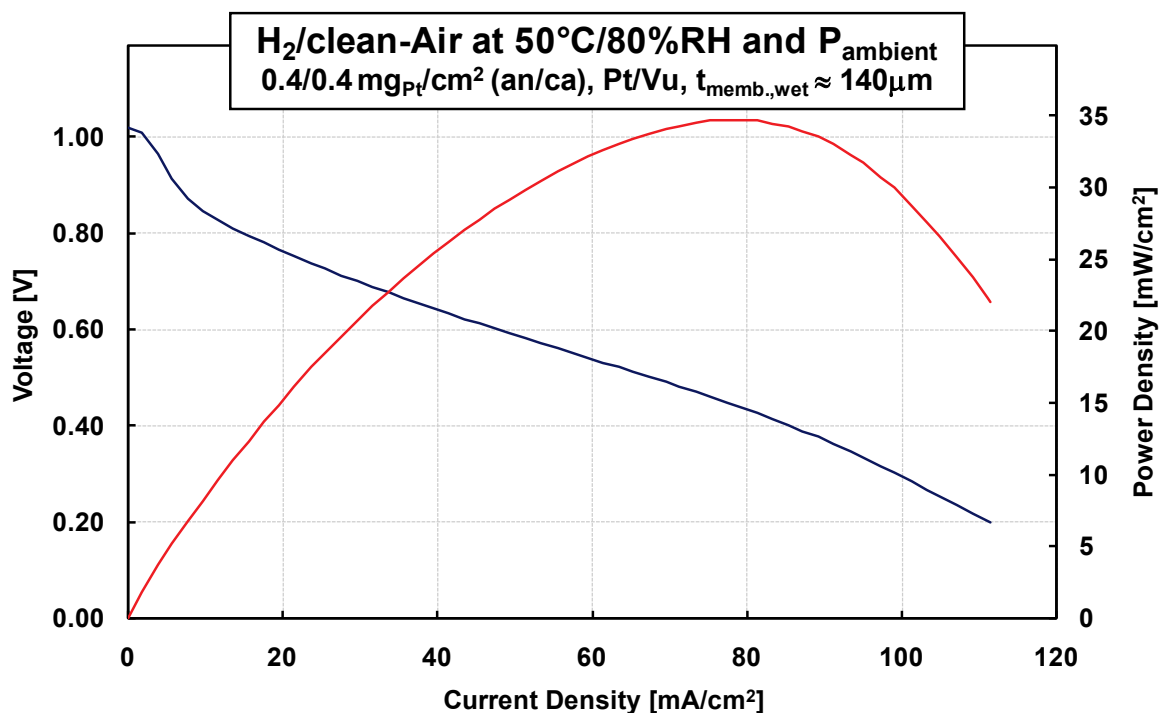


Figure 94. AMFC performance with 80% relative humidity H₂/CO₂-free Air (100/1000 sccm flows) at ambient pressure and 50°C. Ionomer-bonded 5 cm² GDEs were based on a DABCO quaternized R-SBS-F37 membrane (t_{wet} ≈ 140 μm) with catalyst loadings of 0.4/0.4 mg_{Pt}/cm² (anode/cathode), using a 40%wt. Pt/C catalyst. Data were scanning the current at 10mA/s. Blue line denote the polarization curve, red line power density curve

In order to improve performance and durability of the MEAs water swelling of the ionomer should be reduced.

As shown before water uptake and ionic conductivity for SBS-based anion-exchange materials can be tuned either by modifying the functionalization degree (FD) or the crosslinking degree. Unfortunately at lower FD the ionomer conductivity would be too low and crosslinking would make it insoluble. In order to reduce the ionomer swelling without decreasing its conductivity, a better distribution of VBC over the butadienic blocks of SBS is desirable and could be achieved as suggested in chapter 3.2.5.

4 Final remarks

In the last few years a number of new anion-exchange polymers (5; 6; 7; 8; 9; 10; 11; 12; 13; 14) have been developed, offering the possibility of assembling Membrane Electrode Assemblies (MEAs) to develop Anion-exchange Membrane Fuel Cells (AMFCs) and Anion-exchange Membrane-based Electrolyzers (AMEs).

The current technologies of Anion Exchange Materials (AMs) for electrochemical application shows several limitations relate to the possibility of obtaining a reasonable low cost membrane having: high ionic conductivity, chemical stability in strong alkaline media, low permeability, low water swelling and good mechanical properties.

For cation-exchange materials a block copolymer having side chain ionic functionalities shows favorable combination of high conductivity and low water swelling compared to random copolymers having ion-exchange groups in the main chain (68).

The purpose of this study was to develop and characterize AMs based on Styrene-butadiene-styrene (SBS) copolymer, a thermoplastic material with a block structure widely employed in the rubber industry. Electrochemical properties were measured and correlated with synthetic parameters. Commercial materials were also evaluated and used as benchmarks. The relationship between ionomer structure and performance characteristics, such as ionic conductivity, is a critical driving force for much of the structural research on ionomer membranes and provides the foundation for fundamental modeling work on these materials. Cluster-Network morphology model is widely used to describe the fundamental relationship between ionomer structure and electrochemical properties (24). This morphology model consists in an equal distribution of ion-exchange groups clusters held within a continuous polymeric backbone lattice. Narrow channels interconnect the clusters, explaining the transport properties. Correlations between transport properties and synthetic parameters were thus explained in terms of Cluster-Network morphological parameters (i.e. clusters diameter and interconnecting channel length). Performance of the obtained materials were then evaluated in a working AMFC and compared with commercial AMs. Diagnostics on AMFCs, by means of electrochemical impedance spectroscopy (EIS), were performed in order to evaluate measured performances.

On the following paragraphs obtained results will be summarized for each research steps focusing on the correlations between structure and properties.

4.1 Grafting reaction

In order to introduce ion-exchange groups on the SBS backbone a synthetic protocol was developed to graft vinylbenzyl chloride via a bulk radical functionalization, initiated either by benzoyl peroxide (BPO) or α,α' -azo-bis-isobutyronitrile (AIBN), of SBS with vinylbenzyl chloride (VBC). Along with the envisaged grafted SBS copolymer (SBS-g-VBC) poly(vinylbenzyl chloride) (PVBC) homopolymer was obtained. Separation of PVBC homopolymer from the grafted copolymer via acetone extraction was complete (FT-IR, $^1\text{H-NMR}$, $^{13}\text{C-NMR}$ and GPC

data). At radical initiator percentage higher than 1.1 mol% SBS-g-VBC was partially soluble in chloroform suggesting that crosslinking reactions between different SBS matrix chains occurred.

Extracted (PVBC) and residual (SBS-g-VBC) phases were weighted in order to measure reaction products ratio: a different behavior of the reaction products ratio respect to radical initiator amount is observed, depending on its type. Using BPO the residual phase percentage increases as radical initiator amount increases. On the contrary, reactions conducted using AIBN do not show net change in reaction products ratio varying the initiator amount.

Functionalization degree data, determined by $^1\text{H-NMR}$, were compared with free radical initiator percentage: at the same initiator molar percentage grafting efficiency is higher using BPO rather than AIBN.

Weight average molecular weight \overline{M}_w , determined by GPC analysis, of extracted homopolymer phases showed a positive correlation with BPO initiator percentage. On the contrary, using AIBN as free radical source the weight average molecular weight is nearly independent from the initiator percentage obtaining homopolymers having $\overline{M}_w \approx 10700$ amu. By means of deconvolution analysis on GPC chromatograms it was possible to obtain weight average molecular weight of the grafted copolymer: increasing BPO amount \overline{M}_w increases, on the contrary increasing AIBN amount no change was observed in \overline{M}_w .

Therefore BPO initiator promotes grafting reaction of VBC on SBS more than VBC homopolymerization and the obtained grafted product has higher FD and \overline{M}_w compared to AIBN, making the latter more suitable to produce VBC homopolymer rather than the envisaged VBC grafting reaction.

Decomposition temperature, determined by TGA analysis, showed a positive correlation with BPO percentage used for the grafting reaction. Considering that higher BPO percentage produces a grafted copolymer having higher functionalization degree, the positive correlation can be explained in terms of thermal stabilizing effect of VBC fragments which can delocalize free radicals generated on polymer matrix at high temperature.

Physical and chemical homogeneity of grafted copolymer casted films has been confirmed by means of SEM and optical microscopies respectively coupled with spatially resolved EDS and FT-IR spectroscopies.

4.2 Quaternization reaction

To ensure anionic conduction properties the polymer matrix must incorporate cationic functionalities. Quaternary ammonium groups grafted onto the polymer matrix exhibit the best thermal and chemical stabilities (85). Benzyl chloride groups in the synthesized SBS-g-VBC copolymers can be converted into quaternary ammonium groups via quaternization reaction with a tertiary amine.

In an alkaline medium quaternary ammonium groups can be very sensitive to Hoffman degradation (86), leading to the formation of a tertiary amine and a non-charged olefin. This reaction implies the presence of an hydrogen atom in beta position respect to the nitrogen

atom of the quaternary ammonium group and need an anti-periplanar (180°) or syn-periplanar (0°) conformation, easily obtained at room temperature due to the low rotational barrier between the conformations. In order to avoid Hoffmann degradation the tertiary amine used for the quaternization reaction should have no β -hydrogens (such as trimethylamine), or an high rotational barrier (such as strained cyclic amines). An interesting tertiary amine is the 1,4-diazabicyclo[2.2.2]octane (DABCO): even though there are several β -hydrogens its bicyclic structure prevents interconversion between conformers, moreover being a diamine can produce crosslinked structure during the quaternization reaction.

Films of the residual phases were prepared and reacted with a methanol solution of the envisaged tertiary amine for 72h at 60°C .

Comparing FT-IR spectra before and after quaternization reaction, peak at 1265 cm^{-1} , associated to $\text{CH}_2\text{-Cl}$ wagging, disappears, confirming thus that the reaction was complete for all the synthesized samples.

On films quaternized with trimethylamine, soluble in CDCl_3 , $^1\text{H-NMR}$ signal at 4.5 ppm related to chloromethylene units disappears, confirming that the quaternization reaction was complete, as already stated by FT-IR analysis. NMR analysis was not performed on films quaternized with DABCO due to their insolubility in common deuterated solvents.

Since after quaternization with a tertiary amine the polymer assumes a positive charge, its increased swelling in polar solvents such as methanol or water may damage its morphology. However SEM and optical microscopies, respectively coupled with spatially resolved EDS and FT-IR spectroscopies, confirmed physical and chemical homogeneity for quaternized films: quaternization reaction and subsequent higher solvent swelling didn't damage their structure.

Thermogravimetric analysis of quaternized polymeric films showd two decomposition temperatures. First decomposition temperature at 270.5°C is most likely due to quaternary ammonium decomposition. Second decomposition temperature at 447.5°C is due to SBS matrix degradation. Since both decomposition temperatures are far above the operating temperature range ($25\text{-}80^\circ\text{C}$) of the envisaged electrochemical applications, obtained AMs are thermally stable.

DSC analysis of raw SBS and R-SBS-F11 DABCO quaternized film, showed that grafting and subsequent quaternization reactions do not affect thermal properties: butadienic block glass transition temperature (T_g1) changes aren't sensible, suggesting that VBC grafting on this block didn't stiffen the polymer chain.

Summarizing, the reported three-steps synthetic protocol, i.e. VBC grafting, purification and quaternization reaction with a tertiary amine, leads to a chemically and thermally stable anion-exchange membrane, both chemically and physically homogeneous, based on a cheap commercial SBS triblock copolymer. Moreover the functionalization degree (FD), calculated by $^1\text{H-NMR}$ data and confirmed by elemental analysis, is highly tunable being positively correlated to the starting percentage of radical initiator. Quaternization reaction using diamine such as DABCO introduces a certain crosslinking degree between different chains, in

fact the resulting films were not soluble in chloroform and other common solvents. The introduced crosslinking should help to obtain materials having better mechanical properties.

4.3 Electrochemical characterization

In the first chapter were discussed the required properties for an ion-exchange membrane in order to improve its performance and durability on the envisaged low temperature electrochemical applications.

Protocols to measure main electrochemical properties (ion-exchange capacity, water uptake and ionic conductivity) were developed and validated for commercial ion-exchange materials. Tuneable synthetic parameters, i.e. functionalization degree (FD) and crosslinking ratio (x_{link}), have been correlated to measured transport properties in order to improve and better understand the morphology of these novel SBS-based AMs.

4.3.1 Functionalization degree (FD)

As mentioned before the FD can be easily tuned varying free radical initiator molar percentage during the grafting reaction. Electrochemical parameters were evaluated for DABCO quaternized SBS-g-VBC grafted copolymers having different FDs, and compared with a commercial benchmark membrane measured properties.

Experimental ion-exchange capacity (IEC) is positively correlated with FD. This correlation was expected since complete quaternization was previously confirmed (FT-IR and $^1\text{H-NMR}$). All the SBS-based AMs exhibit lower IECs compared to the benchmark.

A positive correlation was also noticed between FD and both water swelling and ionic conductivity. These trends were also predictable: an higher FD (i.e. higher IEC) would result in a comb-type polymer having more side chains or longer side chains, increasing ionic species concentration inside the swollen polymer.

Nevertheless R-SBS-F37 (FD 11.6 mol%) based membrane IEC is lower than the Tokuyama benchmark membrane one, its ionic conductivity at 30°C is higher in both bicarbonate and hydroxyl forms. Ionic conductivities for bicarbonate forms are ≈ 4 -fold lower than that of the hydroxyl form, consistent with the approximately 4-fold lower equivalent ionic conductance in water of bicarbonate ions compared to hydroxide, suggesting an ion transport mechanism similar to water solutions. Moreover in-plane and through-plane conductivities of SBS-based membranes is the same, i.e. the materials exhibit an isotropic behavior.

Best trade-off between ionic conductivity and water swelling was found for R-SBS-F16 based membrane, having FD 8.1 mol%, which conductivity is comparable with the benchmark one and water uptake is slightly higher but still acceptable.

Thus, simply tuning the FD of these SBS-based membranes, ionic conductivities higher than a commercial benchmark membrane has been obtained, though water uptake is still higher than the benchmark membrane one.

Correlations between transport properties and FD gave hints to understand the morphology of water swollen SBS-based membranes: since IEC, WU and σ nearly linearly

increases as FD increases, all the ionic clusters are properly interconnected and reachable by the solvent. Moreover ionic conductivity isotropy suggests an homogeneous clusters distribution.

4.3.2 Crosslinking ratio

Other than FD, another tunable parameter during the described SBS-based membrane synthesis is the crosslinking ratio. Its tuning can be achieved modifying the quaternization reaction conditions.

Amines mixing

A first attempt was made quaternizing four R-SBS-F16 (FD 8.1 mol%) films with a solution obtained mixing different amounts of 1M DABCO (diamine) solution in methanol and 1M N-methylimidazole (monoamine) solution in methanol. Theoretical crosslinking percentage was defined, assuming that DABCO quaternization always give raise to crosslinking and quaternization probability with an amine type is given by the normalized product of its concentration and the number of amine groups per molecule

Even though the crosslinking percentage is a pure theoretical data, based on the arguable assumption of complete crosslinking by DABCO, a perfectly negative linear correlation was observed for both WU and σ , confirming a change in the real crosslinking ratio. Therefore the crosslinking ratio can be effectively modified mixing DABCO with a monoamine, such as N-methylimidazole or trimethylamine (TMA), in order to tune the electrochemical parameters.

Dabco concentration

In literature (88) is reported that an important parameter to tune DABCO crosslinking during the quaternization reaction is its molar fraction relative to the chlorobenzyl groups: lower the relative molar fraction, higher the crosslinking degree. Thus, in principle, there's no need to mix DABCO with a monoamine in order to tune the resulting crosslinking ratio: DABCO concentration is correlated to this parameter.

In order to study this correlation five R-SBS-F37 films (FD 11.6 mol%) have been quaternized with methanol solutions of DABCO having concentration ranging from 1wt% to 5wt%.

As expected both water swelling and conductivities are positively correlated with DABCO concentration, confirming that decreasing its value increase the crosslinking ratio of the resulting membranes. Contrarily to the case where crosslinking was tuned by mixing DABCO with a monoamine, discussed in the previous paragraph, the way water uptake and conductivity increase with DABCO concentration are different: while water swelling increases linearly, conductivity increases asymptotically to the crosslinking-free value, obtained quaternizing R-SBS-F37 film with TMA.

These results suggested that tuning crosslinking degree using different concentration of DABCO in the quaternizing reaction solution would result in a large water swelling decrease (e.g. two third using 3 wt% DABCO), with a small decrease in ionic conductivity (e.g. one

third using 3wt% DABCO). Thus, together with the FD, the DABCO concentration can be tuned in order to efficiently obtain an SBS-based membrane having high ionic conductivity and small water swelling.

4.4 Morphology

Assuming a Cluster-Network morphology model for anion-exchange materials, consisting in an equal distribution of quaternary ammonium ion clusters held within a continuous hydrophobic polymeric lattice (e.g. polystyrene for the synthesized SBS-based membranes) and interconnected by narrow cylindrical channels, some transport indexes have been defined, calculated and explained in terms of clusters size and interconnection.

As discussed before a higher FD would result in a comb-type polymer having more side chains or longer side chains. On the first case increasing the FD would result in an AM having more and better interconnected clusters with nearly the same mean diameters. On the second case increasing FD would result in an AM having larger clusters due to the higher charge density of the quaternized PVBC side chains which cannot be shared between different clusters.

Ionic conductivity Arrhenius-like activation energies for SBS-based membranes suggested that ionic conduction mechanism inside the membrane matrix should be analogous to free ions in water.

In order to evaluate the influence of charged polymer matrix on the ionic mobility a tortuosity index $\tau(X)$ of the membrane in the X-form has been defined as the ratio between X ion conductivity inside the membrane and an approximated theoretical contribution of the X ion in water solution. In terms of Cluster-Network model this index describes the difference in mean length that ions, subjected to an electric field, have to cover in solution or inside the membrane, due to a tridimensional displacement between the clusters. Hence the tortuosity index summarizes both difference in interactions and mean walking distance of the counterion inside a membrane: nearer to one is the tortuosity, better is the interconnection between the clusters and more ideally the interactions between counterions and fixed charges.

Tortuosity parameter has been calculated for Nafion® membranes having different IECs and compared with values obtained for SBS-based membranes, the comparison suggested longer quaternized PVBC side chains for the synthesized membrane as IEC is increased. Assuming a cluster-network morphological model this means that clusters diameter for SBS-based membranes is higher, due to the increased charge density inside the clusters. This interpretation would explain why for these membranes a higher WU has been found compared with the benchmark membrane. Moreover tortuosity parameter ratio between two different counterion forms of the membrane suggested that ion transport mechanism inside the synthesized SBS-based membranes is similar to the water solution one, confirming the activation energy analysis previously performed.

4.5 AMFC performances and diagnostics

4.5.1 Commercial materials

Tokuyama A-201 AM and Acta's Platinum Group Metal (PGM) free Oxygen Reduction Reaction (ORR) catalysts "K14" and "K18" were used and evaluated, showing promising performances in AMFC applications. In order to estimate the potential of this technology kinetically and ohmically limited theoretical performance projections were calculated, using the measured ex-situ properties of the benchmark AM and Acta's K14 and K18 catalysts kinetic activity data (20).

Projected performances coincide at low current density with measured ones, demonstrating that the commercial ionomer does not poison the ORR kinetics. At higher current densities transport losses make the experimental curve deviate from the projected limit.

Tough membrane electrode assembly (MEA) design has yet to be improved in order to minimize transport losses, these results are encouraging since similar performances are obtained both using Pt and non-PGM electrocatalysts for the ORR.

Diagnostics

Despite the encouraging performances obtained using both Pt and non-PGM ORR catalysts, some decay was observed at temperatures higher than 50°C. In order to study whether this decay is due to catalyst poisoning, AMs degradation or other sources electrochemical impedance spectroscopy (EIS) analysis was performed.

EIS analysis showed that MEAs prepared using Tokuyama AMs aren't stable at operating temperatures higher than 50°C due to ionomer dissolution, confirming on the contrary no CO₂ contamination and no membrane degradation. Thus EIS has been proved as viable technique for AMFC in-situ diagnostics.

4.5.2 SBS-based AMs

A trimethylamine quaternized VBC grafted R-SBS-F37 based AM was dissolved in methanol at 120°C in an autoclave for 1h, obtaining a 4wt% ionomeric solution. In-plane conductivity and water uptake of a membrane obtained recasting this ionomer solution in a PTFE petri dish were measured, confirming that no degradation occurred during the high temperature dissolution. An ink was prepared dispersing Pt/C 40wt% (BASF®) catalyst into a portion of the ionomer solution (50 wt% dry ionomer to carbon ratio).

Catalyst coated membrane (CCM)

CCM obtained by decal transfer showed no performances in H₂/O₂ AMFC (peak current density <2mA/cm²) and very high impedance at 1kHz (>10Ω). EIS analysis confirmed that the membrane was not damaged by the hot pressing treatment. The high impedance at 1kHz, being not due to a membrane fault, arises from an high ionic resistance of the catalytic layer, probably due to ionomer dissolution, degradation or segregation. Ionomer thermal degradation is unlikely, since the hot pressing temperature is far below than decomposition

temperature detected by TGA analysis. Dissolved ionomer was not detected on the KOH solution used to exchange the CCM to the hydroxyl form.

Scanning Electron Microscopy (SEM) analysis was performed on the catalytic layer before and after the decal transfer showing a clear segregation of the ionomer.

Segregation most likely occurred due to the huge water uptake of the ionomer ($\approx 300\text{wt}\%$ in liquid water at room temperature): since the coating is prepared in humid open air the ionomer is partially swollen, when heated during the hot pressing treatment the ionomer turn to the dry form and then absorb again water from air when cooled to room temperature. These volume changes stress the microphase dispersed ionomer/catalyst structure leading to the observed ionomer segregation.

Gas diffusion electrode (GDE)

In order to confirm that ionomer segregation occurs after the hot pressing treatment, the ink previously prepared was casted directly on the Gas Diffusion Layer (GDL), obtaining a Gas Diffusion Electrode (GDE).

At 50°C H_2/CO_2 -free Air AMFC showed low performances. Measuring the in-situ membrane conductivity by means of EIS confirmed no CO_2 contamination. Increasing temperature or relative humidity of the supplied gases resulted in a progressive, irreversible, decay in performances, probably due to modification on the catalyst layer as for the CCM case.

In the presence of liquid water the volume of the ionomer would expand by a factor of ≈ 4 , leaving no void volume left for gas diffusion, thus explaining the low measured performances.

In order to improve performance and durability of the MEAs water swelling of the crosslinking-free ionomer should be reduced.

4.6 Future works

Assuming constant overall ion-exchange capacity the ion-exchange groups distribution is not fixed. If VBC grafting on the SBS matrix is preferred over its homopolymerization, the resulting AM will have a random distribution of the ion exchange groups over the butadienic blocks, i.e. the charge will be evenly distributed and its density minimized. On the other hand if VBC homopolymerization is preferred over its grafting on the SBS matrix, the resulting AM will have a clustered distribution of the ion exchange groups over the budadienic blocks, i.e. the charge will be unevenly distributed with local peaks of its density.

Morphology analysis suggested that increasing the FD the cluster diameter in the swollen membrane increases as well, due to longer clustered quaternized PVBC side chains formation. This trend leads to the observed higher WU compared to the benchmark membrane.

Moreover, even though DABCO crosslinking ratio can be controlled by its concentration during the quaternization reaction, crosslinking can be between two different SBS chains (interchain crosslinking), or between two VBC units grafted on the same SBS chain or on the

same side chain (intrachain crosslinking). Clearly interchain crosslinking is desirable rather, helping to reduce the AM swelling.

In order to improve the ion-exchange groups distribution and promote interchain crosslinking the AM synthesis can be modified in one or more of the following ways:

- Usage of a Styrene/VBC mixture during the grafting reaction in order to statistically reduce the charge density of the quaternized membrane;
- Conducting the VBC grafting reaction in a solvent inert to radical reactions (e.g. benzene), slowly adding the VBC in order to work with a defect of VBC. In this way homopolymerization should be less likely, leading to a better side chains distribution over the butadienic blocks;
- Usage of long-chain polyamines for the quaternization reaction in order to promote interchain crosslinking rather than intrachain crosslinking;
- Quaternizing in excess of DABCO an SBS-g-VBC polymer having a low FD (e.g. 1-5%), in order to obtain a crosslinking-free polymer, containing one-side quaternized DABCO molecules. Another SBS-g-VBC polymer having the envisaged FD may then be quaternized with the previous one, obtaining a crosslinked material which can be now fully quaternized with DABCO or trimethylamine.

5 Bibliography

1. Gasteiger, H.A., et al. 56, 2005, Appl. Catal. B: Env., p. 9.
2. Miles, M.H., et al. 6, 1977, Electrochimica Acta, Vol. 23, pp. 521-526.
3. Gülzow, E. and Schulze, M. 127, 2004, J. Power Sources, pp. 243-251.
4. Komkova, E.N., et al. 244, 2004, J. Membr. Sci., pp. 25-34.
5. Varcoe, J.R., Slade, R.C.T. and Lam How Yee, E. 2006, Chem. Commun., p. 1428.
6. Adams, L.A., et al. 1, 2008, ChemSusChem, Vol. 1, pp. 79-81.
7. Kang, J.J., et al. 15, 2004, Polym. Adv. Technol., p. 61.
8. Danks, T.N., Slade, R.C.T. and Varcoe, J.R. 13, 2003, J. Mater. Chem., p. 712.
9. Fang, J. and Shen, P.K. 285, 2006, J. Membr. Sci., p. 317.
10. Li, L. and Wang, Y.X. 262, 2005, J. Membr. Sci., p. 1.
11. Wan, Y., et al. 162, 2006, J. Power Sources, p. 105.
12. Honga, J., Lia, D. and Wang, H. 318, 2008, J. Membr. Sci., p. 441.
13. Wua, L., et al. 310, 2008, J. Membr. Sci., p. 577.
14. Li, Y., Xu, T. and Gong, M. 279, 2006, J. Membr. Sci, p. 200.
15. Sheng, W., Gasteiger, H.A. and Shao-Horn, Y. 157, 2010, J. Electrochem. Soc., pp. B1529-B1536.
16. Lyons, M.E.G. and Brandon, M.P. 3, 2008, Int. J. Electrochem. Sci., pp. 1386-1424.
17. Lyons, M.E.G. and Brandon, M.P. 1-2, 2010, J. Electroanal. Chem., Vol. 641, pp. 119-130.
18. Singh, R.N., et al. 9, 2007, Electrochem. Comm., pp. 1367-1373.
19. Olivares-Ramírez, J.M., et al. 32, 2007, Int. J. Hydrogen Energy, pp. 3170-3173.
20. Piana, M., Catanorchi, S. and Gasteiger, H.A. 16, 2008, ECS Trans., Vol. 2, p. 2045.
21. Wilhelm, H.M. and Felisberti, M.I. 86, 2002, J. Appl. Polym. Sci., Vol. 2, pp. 366-371.
22. Wilhelm, H.M. and Felisberti, M.I. 87, 2003, J. Appl. Polym. Sci., Vol. 3, pp. 516-522.
23. Cordella, C.D., et al. 87, 2003, J. Appl. Polym. Sci., Vol. 13, pp. 2074-2079.
24. Gierke, T.D., Munn, G.E. and Wilson, F.C. 19, 1981, J. Polym. Sci. Polym. Phys., p. 1687.
25. Debye, P. and Hückel, E. 24, 1923, Physikalische Zeitschrift, pp. 185-206.
26. Harris, Daniel C. *Quantitative Chemical Analysis*. 6th. s.l.: W.H. Freeman & Company, 2003.
27. Bockris, J. O'M., Reddy, A.K.N. and Gamboa-Aldeco, M. *Modern Electrochemistry*. 2nd. : Springer, 1998.
28. Bešter-Rogač, M. and Habe, D. 53, 2006, Acta Chim. Slov., pp. 391-395.
29. Bard, A.J. and Faulkner, L.R. *Electrochemical Methods: Fundamentals and Applications*. New York : Wiley, 2001.
30. Short, G.D. and Bishop, E. 37, 1965, Anal. Chem., pp. 962-967.
31. Bard, A.J. and Faulkner, L.R. *Electrochemical Methods*. s.l. : John Wiley & Sons, 1980.
32. Graham, D.C. 41, 1947, Chem. Rev., p. 441.
33. Parsons, R. 1954, Modern Aspects of Electrochemistry, Vol. 1, p. 103.

34. **Delahay, P.** *Double Layer and Electrode Kinetics*. New York : Wiley-Interscience, 1965.
35. **Mohilner, D.M.** [book auth.] A.J. Bard. *Electroanalytical Chemistry*. New York : Dekker, 1966, p. 241.
36. **Smith, D.E.** [book auth.] A.J. Bard. *Electroanalytical Chemistry*. New York : Dekker, 1966, Vol. 1, p. 1.
37. **Bond, A.M.** *Modern Polarographic Techniques in Analytical Chemistry*. New York : Dekker, 1980.
38. **Doetsch, G.** *Laplace Transformation*. New York : Dover, 1953.
39. **Di Stefano, J.J., Stubberud, A.R. and Williams, I.J.** *Theory and Problems of Feedback and Control Systems*. 2nd. New York : McGraw-Hill, 1990.
40. **Bottelberghs, P.H. and Broers, G.H.J.** 67, 1976, *J. Electroanal. Chem.*, pp. 155-167.
41. **Raistrick, I.D., et al.** 77, 1977, *Electroanal. Chem.*, Vols. 319-337.
42. **Zoltowski, P.** 375, 1994, *J. Electroanal. Chem.*, p. 45.
43. **Matsui, Y., et al.** 16, 2009, *ECS trans.*, Vol. 25, pp. 105-110.
44. **Varcoe, J.R.** 9, 2007, *Phys. Chem. Chem. Phys.*, pp. 1479-1486.
45. **Piana, M., et al.** 18, 2010, *J. Power Sources*, pp. 5875-5881.
46. **Ralph, T.** 41, 1997, *Platinum Metals Review*, pp. 102-113.
47. **Wilson, M. and Gottesfeld, S.** 139, 1992, *J. Electrochem. Soc.*, Vol. 2, pp. L28-L30.
48. **Nasef, M.M. and Hegazy, E.A.** 29, 2004, *Prog. Polym. Sci.*, pp. 499-561.
49. **Perusich, S.A. and Reddy, S.M.** 31, 2001, *J. Appl. Electrochem.*, p. 421.
50. **Grubb, W.T.** *Fuel Cell. US2913511* June 29, 1955.
51. **Grot, W.G.** 82, 1994, *Macromol. Symp.*, p. 161.
52. **Grot, W.G.F., Munn, G.E. and Walmsley, P.N.** Houston, TX : s.n., 1972, 141st National Meeting of Electrochemical Society, Inc., p. Abstract #154.
53. **Ralph, T.** 41, 1997, *Platinum Met. Rev.*, p. 102-113.
54. **Zawodzinski, T.A., et al.** 140, 1993, *J. Electrochem. Soc.*, p. 1042.
55. **Savadogo, O.** 1, 1998, *J. New Mater. Electrochem. Syst.*, p. 47.
56. **Butler, G.B., O'Driscoll, K.F. and Wilkes, G.L.** C34, 1994, *JMS-Rev. Macromol. Chem. Phys.*, Vol. 3, pp. 325-373.
57. **Yeager, H.J. and Eisenberg, A.** *Perfluorinated Ionomer Membranes. ACS Symp. Ser. No.180*. Washington, DC : American Chemical Society, 1982, pp. 1-4,41-63.
58. **Mauritz, K.A.** C28, 1988 : s.n., *JMS-Rev. Macromol. Chem. Phys.*, Vol. 1, pp. 65-98.
59. **Brookman, P.J. and Nicholson, J.W.** [ed.] A.D. Wilson and H.J. Prosser. *Developments in Ionic Polymers*. London : Elsevier Applied Science Publishers, 1986, Vol. 2, pp. 269-283.
60. **Gottesfeld, S. and Zawodzinski, T.A.** *Polymer Electrolyte Fuel Cells*. [ed.] R.C. Alkire, et al. *Advances in Electrochemical Science and Engineering*. New York : Wiley-VCH, 1997, Vol. 5.
61. **Cleghorn, S., Kolde, J. and Liu, W.** *Catalyst Coated Composite Membranes*. [ed.] W. Vielstich, A. Lamm and H.A. Gasteiger. *Handbook of Fuel Cells, Fundamentals,*

- Technology and Applications*. New York : John Wiley & Sons, 2003, Vol. 3, pp. 566-575.
62. *Membranes Performance and Evaluation*. **Zawodzinski, T.A.** Arlington, VA : s.n., 2001. NFS Workshop on Engineering Fundamentals at Low Temperature PEM Fuel Cells.
63. **Ding, J., Chuy, C. and Holdcroft, S.** 35, 2002, *Macromolecules*, p. 1348.
64. **Yang, Y., Shi, Z. and Holdcroft, S.** 35, 2004, *Macromolecules*, p. 1678.
65. **Bai, Z., et al.** 48, 2007, *Polym. Prep.*, p. 508.
66. **Elabd, Y.A., Napadensky, E. and Walker, C.W.** 45, 2004, *Polym. Prep.*, p. 19.
67. **Kreuer, K.D.** 185, 2001, *J. Membr. Sci.*, p. 29.
68. **Gross, M., et al.** Design Rules for the Improvement of the Performance of Hydrocarbon-Based Membranes for Proton Exchange Membrane Fuel Cells. [ed.] W. Vielstich, et al. *Handbook of Fuel Cells*. s.l. : Wiley, 2009, Vol. 5.
69. **Capelhart, T.W. and Soldera, A.** *Unpublished data*.
70. **Xie, Z., et al.** 153, 2006, *J. Electrochem. Soc.*, p. E173.
71. **Doyle, M., et al.** 105, 2001, *J. Phys. Chem. B*, p. 9387.
72. **Buchi, F.N. and Scherer, G.G.** 148, 2001, *J. Electrochem. Soc.*, p. A183.
73. **Rieke, P.C. and Vanderborgh, N.E.** 32, 1987, *J. Membr. Sci.*, p. 313.
74. **Gardner, C.L. and Anantaraman, A.V.** 449, 1998, *J. Electroanal. Chem.*, p. 209.
75. **Parthasarathy, A., et al.** 139, 1992, *J. Electrochem. Soc.*, p. 2530.
76. **Sakai, Takeraka, T.H. and Torikai, E.** 1, 1986, *J. Electrochem. Soc.*, Vol. 133, pp. 88-92.
77. **Kazmaier, P.M., et al.** 30, 1977, *Macromolecules*, pp. 2228-2231.
78. **Lassalle, V.L., et al.** 18, 2004, *J. of Adhesion Sci. and Tech.*, pp. 1849-1860.
79. **Jiang, D.D. and Wilkie, C.A.** 35, 1997, *J. Polym. Sci.*, pp. 965-973.
80. **Brydon, A., Burnett, G.M. and Cameron, G.G.** 11, 1973, *J. Polym. Sci.*, pp. 3255-3269.
81. **Manaresi, P., Passalacqua, V. and Pilati, F.** 16, 1975, *Polymer*, pp. 520-526.
82. **Huang, N.J. and Sundberg, D.C.** 33, 1995, *J. Polym. Sci.*, pp. 2587-2603.
83. **Cameron, G.G. and Qureshi, M.Y.** 18, 1980, *J. Polym. Sci.*, pp. 2143-2153.
84. *Nomenclature of Inorganic Chemistry IUPAC Recommendations*. 2005. p. 66.
85. **Bauer, B., Strathmann, H. e Effenberger, F.** 79, 1990, *Desalination*, p. 125.
86. **House, H.** *Modern Synthetic Reactions*. Paris, 1972.
87. **Katritzky, A.R. and Weiss, D.E.** 57, 2006, *Polym. Bullet.*, pp. 513-524.
88. **Rengan, K. e Engel, R.** 1992, *J. Chem. Soc. Chem. Commun.*, p. 757-758.
89. **Mauritz, K.A. and Moore, R.B.** 104, 2004, *Chem. Rev.*, pp. 4535-4585.
90. **Hsu, W.Y. and Gierke, T.D.** 13, 1983, *J. Membr. Sci.*, p. 307.
91. **Koter, S., Piotrowski, P. and Kerres, J.** 153, 1999, *J. Membr. Sci.*, pp. 83-90.
92. **Merlak, E.** 42, 2009, *Atti e Memorie della Commissione Grotte "E. Boegan"*, pp. 53-65.
93. **Lide, D.R.** *Handbook of Chemistry and Physics*. 78th. s.l. : CRC Press, 1997-1998.
94. **Doyle, M., et al.** 105, 2001, *J. Phys. Chem. B*, p. 9387.

-
95. **Gasteiger, H.A., et al.** 3, 2003, Handbook of Fuel Cells - Fundamentals Technology and Applications (Wiley and Sons), p. 593.
 96. **Lim, P.C., Ge, S.H. and Wang, C.Y.** 2008, 214^o ECS Meeting. Abstract#1073.
 97. **Wang, Y., et al.** 5, 2003, Electrochem. Commun., p. 662.
 98. **Neyerlin, K.C., et al.** 153, 2006, J. Electrochem. Soc., p. A1955.
 99. **Piana, M.** *Unpublished data.* ACTA s.p.a. Crespina (PI).
 100. **Gu, W., et al.** Proton exchange membrane fuel cell (PEMFC) down-the-channel performance model. [ed.] W. Vielstich, H. Yokokawa and H.A. Gasteiger. *Handbook of Fuel Cells - Fundamentals, Technology and Applications.* s.l. : John Wiley & Sons, 2009, Vol. 6, 43.
 101. **Kocha, S.S.** Principle of MEA preparation. [ed.] W. Vielstich, A. Lamm and H.A. Gasteiger. *Handbook of Fuel Cells - Fundamentals, Technology and Applications.* Chichester (UK) : Wiley, 2003, Vol. 3, p. 538 (Chapter 43).